Monitoring and Analysis of Sediment and Nutrients and their Associated Pollutant Load

Pritam Rony[1], Omar Talafha[1], Shubham Gupta[1], Tushar Sinha[1], Jianhong Ren[1] and Jong-Won Choi[2]

[1]Department of Environmental Engineering, Texas A&M University-Kingsville

Kingsville, TX 78363

[2]Department of Civil and Architectural Engineering, Texas A&M University-Kingsville, Kingsville, Texas

This report was funded in part by a Texas Coastal Management Program grant approved by the Texas Land Commissioner, providing financial assistance under the Coastal Zone Management Act of 1972, as amended, awarded by the National Oceanic and Atmospheric Administration (NOAA), Office for Coastal Management, pursuant to NOAA Award No. NA23NOS4190249. The views expressed herein are those of the author(s) and do not necessarily reflect the views of NOAA, the U.S. Department of Commerce, or any of their subagencies.

TABLE OF CONTENTS

PROJECT SUMMARY

The Nueces River Watershed is a major hydrologic system in South Texas that provides freshwater inflow to the Nueces Bay and Corpus Christi Bay system in a subtropical, semi-arid climate with variable rainfall. Transport of sediment and nutrients from the watershed affects reservoir storage, stream channel stability, aquatic habitat, turbidity, and downstream estuarine water quality. The Nueces/Corpus Christi Bay system frequently undergoes significant wet-dry cycles and issues related to eutrophication, hypoxia, and legacy pollutant loading. However, the impact of the seasonal variations on water quality and sediment properties has not been fully addressed.

This study undertook a year-long field investigation (September 2024 – August 2025) in five representative locations, gathering bimonthly water and sediment samples by quantifying conventional water quality parameters, sediment parameters, nutrient forms (nitrogen and phosphorus), and trace metals in dissolved, particulate, and bed sediment phases. Statistical investigation was also conducted to assess temporal and spatial variations, and principal component analysis and cluster analysis to identify co-variation patterns.

Analysis of the field data revealed unique seasonal patterns. During dry months, salinities were elevated, and nitrate and phosphate concentrations accumulated in bed sediments, while wet months experienced significant freshwater inflows that resulted in peaks of suspended sediment concentration (SSC > 600 mg/L) and nutrient influxes (e.g., ammonium load reached 7,650 kg/day in April). These pulses were associated with reduced dissolved oxygen levels, frequently below 3 ppm during the wet season. Spatial variations were minimal; only water-column NH_4^+ exhibited significant differences among locations. Heavy metal concentrations in the water exceeded chronic guideline thresholds at most sampling times. Episodic spikes were observed, and arsenic and selenium peaked during the dry season, whereas summer storms induced elevated levels of dissolved lead and mercury

(Hg reached around 2 mg/L in August). Metal concentrations in sediment surged, particularly mercury, which reached over 600 mg/kg in June.

Multivariate studies revealed that rainfall and flow dictate the primary variable, associating sediments and elevated nutrients with high-flow conditions, whereas metals were categorized by their sources (natural Fe and Al versus anthropogenic trace metals). The comprehensive seasonal analysis in this study indicates a significant deficiency in the comprehension of semi-arid estuaries. Results will guide management methods, including the optimization of freshwater flows and stormwater controls, to alleviate nutrient load surges and avert hypoxia.

Monitoring sediment concentration is essential for assessing water quality, as sedimentation impacts aquatic ecosystems and increases flood risks by reducing reservoir capacities. This study utilized remote sensing to estimate total suspended sediment (TSS) concentration based on the principle that higher sediment loads in water increase surface reflectance. Using MODIS (2000 – 2025) and Landsat-8 (2013 – 2025) datasets, this study analyzed reflectivity in the visible and infrared bands to estimate TSS levels in the Nueces River and its associated bays. The analysis of the satellite data aims to establish a relationship between satellite reflectance and in-situ data, map the spatiotemporal patterns of TSS in the Nueces River and the Nueces/Corpus Christi Bay system, and evaluate the influence of hydroclimatic factors on sediment loading.

The analysis results showed that the MODIS-based Random Forest model for the bays achieved the highest predictive power with an R^2 of 0.87, validating the hypothesis that satellite-derived relationships were stronger in bay environments than in river segments. While MODIS excelled in capturing bay-wide dynamics, Landsat achieved an R^2 of 0.53 for the river segments. Analysis of the 25-year dataset (2000 – 2025) revealed a system characterized by long-term stability disrupted by sharp seasonal variations; monthly mean

TSS ranged from a minimum of 19.95 mg/L (December 2011) to a historical peak of 43.00 mg/L (April 2022) in the Bays. The peak TSS occurred primarily between March and May, indicating recurring seasonal processes and possibly the effect of flush and dilution. The findings of this study are important for estimating the timing and spatial patterns of TSS spikes, providing decision-makers with a tool to manage the environmental and infrastructural impacts of sediment accumulation.

Since sediment and nutrient transport in the Nueces River Watershed is strongly influenced by episodic rainfall, runoff generation, reservoir routing, land cover, soil properties, and management practices, a process-based watershed model is needed to evaluate pollutant loading and potential reduction strategies. Therefore, in this study, the Soil and Water Assessment Tool (SWAT) was employed to simulate streamflow, sediment, total nitrogen, and total phosphorus loading in the Nueces River Watershed and to assess the effects of selected best management practice (BMP) scenarios. An existing SWAT model was refined using updated watershed input data, reservoir parameters, streamflow records, and observed sediment and nutrient data. Major spatial inputs included elevation, land use, soil, and stream network data, while climate and hydrologic inputs included precipitation, temperature, streamflow, and water-quality observations. Observed sediment and nutrient concentrations were converted to monthly loads using measured concentrations and streamflow records so that observed and simulated values could be compared consistently.

Model calibration and validation were conducted at the monthly time scale using SWAT-CUP. Calibration followed a sequential approach in which streamflow was calibrated first, followed by loading for sediment, total nitrogen, and total phosphorus. The calibrated model produced acceptable to strong performance for monthly streamflow, loading for sediment, nitrogen, and phosphorus during the calibration period. Validation results were generally acceptable for flow, sediment, and nitrogen, although uncertainty remained in the magnitude and variability of nutrient loads. Phosphorus calibration was strong, but validation performance was weaker, indicating that phosphorus results should be interpreted cautiously, especially for absolute load prediction.

The calibrated model was then used to evaluate management scenarios relative to a selected baseline condition. Results indicated that sediment and nutrient loading in the Nueces River Watershed is highly event-driven, with a limited number of wet months and high-flow periods contributing disproportionately large sediment and nutrient loads. Sediment-control practices were most relevant for reducing sediment and sediment-associated phosphorus delivery during high-flow conditions. Nutrient-management scenarios provided a basis for evaluating reductions in nitrogen loading, while brush-clearing scenarios showed potential hydrologic effects but should not be treated as stand-alone water-quality practices unless paired with erosion control, soil protection, or revegetation. Therefore, the reported scenario results should be interpreted as responses to the corresponding management practice assumptions used in the SWAT model.

Overall, the SWAT model provides a useful process-based framework for evaluating relative changes in sediment and nutrient loading under corresponding management practice scenarios. The results support the use of targeted sediment-control and nutrient-management practices to reduce pollutant delivery to the Nueces Bay and Corpus Christi Bay system, particularly during high-runoff periods that dominate annual loads. However, uncertainties associated with limited observed water-quality data, simplified management assumptions, reservoir representation, and phosphorus validation should be considered when interpreting the results. Therefore, the model is most appropriate for corresponding management responses and identifying priority processes rather than predicting exact future pollutant loads.

NOMENCLATURE

ADCP	Acoustic Doppler Current Profiler
B_i	Surface reflectance of spectral band i (unitless).
CBBEP	Coastal Bend Bays & Estuaries Program
DIW	Deionized Water
DO	Dissolved Oxygen
D_{10}, D_{30}, D_{60}	Effective sediment particle diameters at 10%, 30%, and 60%
EPA	Environmental Protection Agency
GEE	Google Earth Engine, the platform used for all satellite data pre-processing.
GC	Gas Chromatography
HDPE	High-Density Polyethylene
ICP-MS	Inductively Coupled Plasma Mass Spectrometry
KCl	Potassium Chloride
LOI	Loss on Ignition
MAE	Mean absolute error.
MODIS	Moderate Resolution Imaging Spectroradiometer satellite sensor.
NIST	National Institute of Standards and Technology
OLI	Operational Land Imager, the multispectral sensor aboard Landsat 8.
pH	Measure of hydrogen ion concentration
$r_{i/j}$	Band ratio between spectral bands i and j.
R^2	Coefficient of determination (variance explained).
RMSE	Root-mean-square error.
SSC	Suspended Sediment Concentration
SWQMIS	Surface Water Quality Monitoring Information System, the TCEQ's data repository.

TAMU	Texas A&M University
TCEQ	Texas Commission on Environmental Quality
TDS	Total Dissolved Solids
TSS	Total Suspended Solids
USGS	United States Geological Survey
UTMSI	University of Texas Marine Science Institute, source of validation data.
YSI ProDSS	Multi-parameter field water quality probe

Chapter 1. Introduction

Coastal ecosystems are essential for preserving water quality by regulating nutrients, metals, pesticides, and sediment (Barbier et al., 2011. These ecosystems play a crucial role in nutrient cycling, which helps maintain the balance of nitrogen and phosphorus levels in the water (Robert, 1988). Urban development in coastal regions interferes with natural sediment transport and elevates stormwater runoff, which carries pollutants such as heavy metals, fertilizers, pesticides, and organic contaminants into nearby water bodies (Howarth et al., 2002). This surge in flow erodes riverbanks and transports larger volumes of sediment downstream, eventually depositing them in downstream water bodies. Excessive nutrients like nitrogen and phosphorus, often from agricultural runoff, can lead to harmful algal blooms, which deplete oxygen levels and harm aquatic life (Wakwella et al., 2023). These situations, sometimes termed "dead zones," have been documented in coastal systems worldwide, with certain areas exhibiting a persistent increase in their occurrence, extent, and duration (Stramma et al., 2008). Metals, both naturally occurring and anthropogenic, can accumulate in coastal waters, posing toxicity risks to marine organisms and potentially entering the food chain through bioaccumulation (Dai et al., 2023).

Sediment, carried by rivers and runoff, can cloud water, reduce light penetration, and smother habitats, impacting the overall health of coastal ecosystems (Pacific Coastal and Marine Science Center, 2021). Depletion of oxygen causes biodiversity loss, habitat degradation, and food web instabilities (Rensselaer Polytechnic Institute, 2024). The consequences endanger both the biological integrity of the bay and the economic pursuits of coastal communities, such as fisheries and tourism (Cloern, 2001; Paerl et al., 2011). Increasing ocean temperatures further exacerbate coral bleaching incidents, compromising the structural integrity of reef systems that function as natural barriers (Hughes et al., 2018).

Corpus Christi Bay is a large water body covering 370 km^2, while Nueces Bay covers approximately 93 km^2. Both are located along the Gulf Coast of Texas, United States, as part of the Nueces River estuary (Figure 1.1). The Corpus Christi Bay is one of the largest bays in the United States by total revenue tonnage, which is defined as the amount of cargo transported (USACE, 2022).

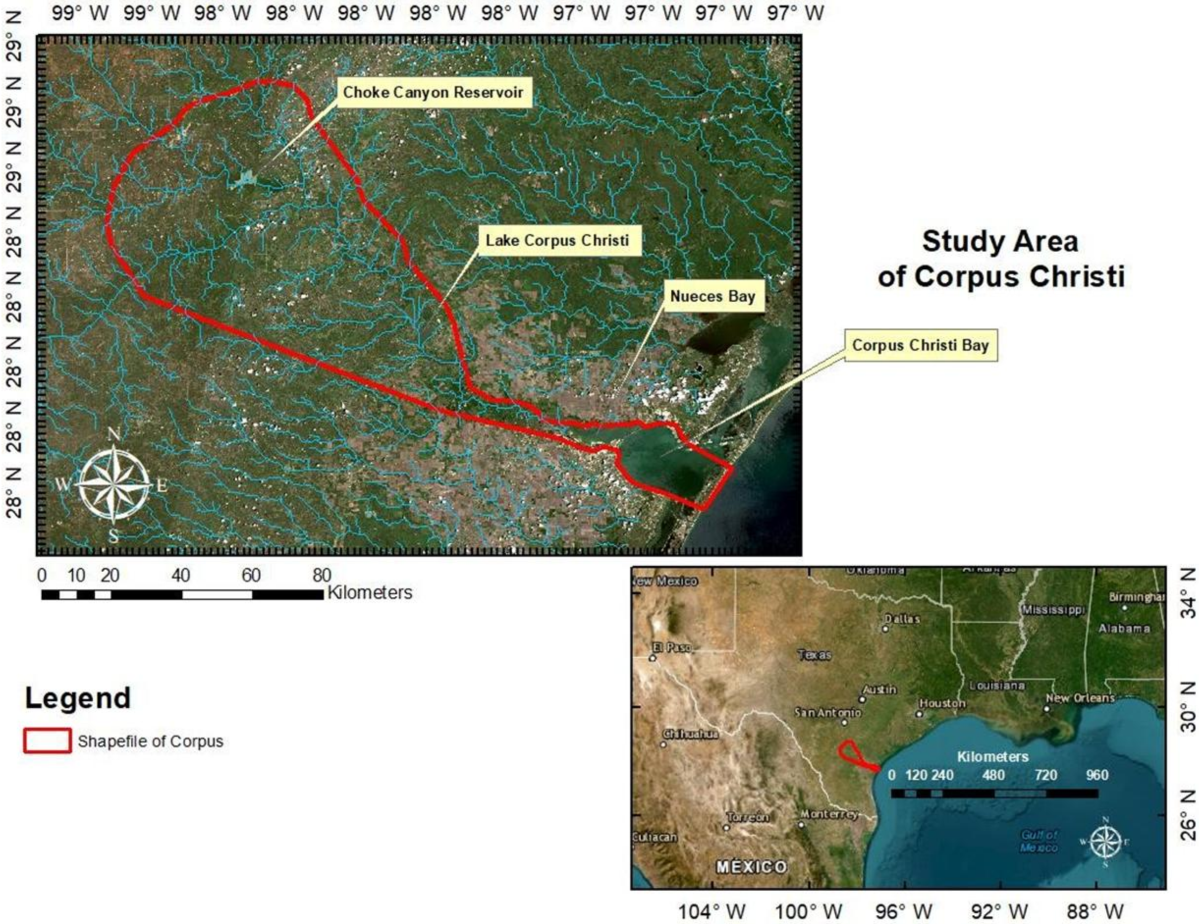

Figure 1.1. Study Area, showing Corpus Christi Bay, Nueces Bay, Lake Corpus Christi, and Choke Canyon Reservoir.

The hydrological and climatic characteristics of the Nueces River estuary play a fundamental role in governing sediment transport and deposition within Corpus Christi and Nueces Bays. The region is characterized by a subtropical semi-arid climate, with mean annual precipitation ranging from approximately 700 to 900 mm, although rainfall is highly variable and often concentrated in high-intensity storm events, including tropical storms and hurricanes. Mean annual air temperatures typically range from 20°C to 24°C, contributing to high evaporation rates that influence salinity and water balance within the estuarine system.

The Nueces River, which serves as the primary freshwater inflow to the bays, originates in central Texas and drains a watershed dominated by rangeland, agricultural areas, and localized urban development. Land use within the basin significantly affects sediment yield, as agricultural practices and soil disturbances increase erosion potential, while regulated flows from upstream reservoirs such as Choke Canyon Reservoir and Lake Corpus Christi modify natural discharge patterns. Tidal exchanges via Packery Channel and Aransas Pass affect salinity, establishing a dynamic freshwater-marine interface (Montagna et al., 2012; Palmer et al., 2011). The bay sustains essential ecosystems, such as seagrass meadows, salt marshes, tidal flats, and oyster reefs, which offer nursery habitats, biodiversity, and coastal protection (Beck et al., 2011; Waycott et al., 2009), so that it enhances local economies via fishing, recreation, and ecotourism. Meanwhile, the adjacent Port of Corpus Christi functions as one of the major gateways for liquefied natural gas (LNG) export in the United States.

1.1 Sediment, Nutrients, and Associated Pollutant Loading

The Nueces/Corpus Christi Bay system illustrates the difficulties encountered by numerous estuary systems. This semi-enclosed bay holds significant ecological and economic value, supporting a variety of marine species, sustaining fisheries, and offering leisure activities (Chong, 2024). Nonetheless, human activities, such as urbanization, agriculture, and industrialization, have profoundly modified the natural hydrodynamics and water quality of these coastal ecosystems (Nicolau & Hill, 2013). Excessive nutrient loading and heavy metal contamination have resulted in water quality deterioration, affecting the biological equilibrium and long-term viability of the bays (Harrison & Martin, 1982). The adjacent watersheds, encompassing urban areas (e.g., Corpus Christi), agricultural territories, and industrial sectors, significantly contribute pollutant loads to the bay, particularly during storm events (Schoenbaechler et al., 2011). The watersheds in this region, such as Oso Bay (a closed shallow water body located along the southern Corpus Christi Bay), exhibit indications of nutrient pollution resulting from wastewater flows (Bugica et al., 2020). Persistent heavy metal pollutants, such as mercury and lead, have been identified in sediments and aquatic creatures. These contaminants present a risk of bioaccumulation, potentially impacting marine organisms and human seafood consumers (Jiang et al., 2021).

Nutrient-induced hypoxia has been reported as a growing environmental problem in the Gulf of America, particularly Nueces/Corpus Christi Bay (Rabalais et al., 2002). A previous study (Paudel et al., 2019) showed that nutrient concentrations and transport are significantly influenced by hydrologic flow patterns, hence influencing estuaries' condition in South Texas. Applebaum et al. (2005) also reported a notable long-term drop in dissolved oxygen (DO) levels in Corpus Christi Bay, underscoring the need for monitoring ongoing hypoxia events. Montagna et al. (2021) found that freshwater inflows affect salinity, which in turn drives nutrient changes and algal blooms — highlighting the need for coordinated watershed management in the coastal bend. Their follow-up study (Montagna & Douglas, 2021) also linked rising salinity levels to shifts in sediment deposits and habitat changes across the region.

A United States Geological Survey study in 2014 found that in Oso Creek's (a creek that flows into the Oso Bay) agricultural sub-watersheds, most runoff and pollutants are delivered in short bursts during intense storms rather than steadily over time (U.S. Geological Survey, 2014). A study on nutrient transport in Nueces Bay by the Texas Water Development Board (TWDB) in 2017 found that changes in freshwater imports have gradually shifted the bay's salinity and nutrient balance (Nueces River Authority, 2018). In this semi-arid region, the cycle is straightforward but damaging — dry periods allow nutrients to build up, then heavy storms flush large pulses into the bays. Droughts reduce river flow and spike salinity, while heavy rain dumps significant nutrient loads all at once (TWDB, 2017).

The Nueces River was once the primary source of freshwater and nutrients for Nueces Bay, but dam and reservoir construction has significantly reduced that flow — cutting nitrogen loads by roughly 75% due to lower water volume and concentration (TWDB, 2017). Unlike temperate estuaries with consistent seasonal flows, nutrient loading here is event-driven, spiking during spring and fall storms and dropping off during dry stretches. According to the Coastal Bend Bays & Estuaries Program (CBBEP), the Corpus Christi Bay system receives around 15,000 kg of nitrogen and 3,100 kg of phosphorus daily from rivers, runoff, wastewater, and Gulf water exchange (Montagna et al., 1995).

Bighash & Murgulet (2015) highlighted the importance of understanding sediment movement and deposition in the Texas coastal region for effective water quality management. In the Nueces Estuary, sediment loads vary dramatically — ranging from just 3.8 tons per day during low-flow periods to 2,490 tons per day during high flows (Ockerman et al., 2013). Droughts and water withdrawals sharply reduce sediment delivery, while major storms drive large spikes in sediment flux. From 1958 to 2010, roughly 98% of the suspended sediment reaching the estuary consisted of fine silt and clay particles (Ockerman et al., 2013).

Paudel et al. (2019) underline even further how variation in freshwater inflows directly influences total suspended solids (TSS) and nitrogen distributions, therefore impacting water quality in the Nueces Estuary. Yeager et al. (2006) observed that the sediment cores from Nueces Bay have a higher proportion of sand compared to those from Corpus Christi Bay, and this sand is distributed at a wider range of depths, possibly attributable to geographic and physiographic influences. Ockerman et al. (2013) observed that whereas yearly suspended-sediment loads in the Nueces Estuary can vary significantly between low- and high-flow years, the seasonal variations in these loads are inadequately constrained due to infrequent sampling.

The Nueces/Corpus Christi Bay system carries a legacy of heavy metal contamination, including zinc, mercury, and lead, from past industrial activity, though current levels in fish, crab, and oyster tissue remain below thresholds considered harmful to human health. A report by the Texas Commission on Environmental Quality (TCEQ) found that zinc levels in Nueces Bay from 2008 to 2014 were generally safe for oyster harvesting, but stressed the importance of ongoing monitoring given the risks from industrial discharges and urban runoff (Hill & Nicolau, 2016). Sampling in 2005 also detected arsenic, copper, mercury, and selenium in local seafood, though mostly at levels not considered a concern for consumption (TCEQ, 2005).

For long-term trend analysis for nutrients and metals, data collection and analysis methods should be consistent. However, available data, like TCEQ's 30-year records, may include methodological flaws (TWDB, 2017). A previous study (Hill & Nicolau, 2016) reveals that historical data on heavy metals and pesticides in the Nueces Bay area were gathered inconsistently throughout time, constraining the identification of seasonal trends, without clearly stating a deficiency in seasonal data.

1.2 Monitoring Sediment Concentration and Turbidity with Remote Sensing Data

Morphologically, Corpus Christi Bay is a relatively shallow, wind-driven estuary with an average depth of approximately 3 to 4 m, while Nueces Bay is even shallower, with average depths generally less than 2 m. These shallow depths enhance sediment resuspension through wind-induced wave action and tidal mixing, thereby amplifying turbidity and influencing the spatial distribution of suspended sediments. Collectively, these hydroclimatic conditions, watershed characteristics, and geomorphological features establish the physical framework within which sediment dynamics operate in the Nueces River–bay system.

Sediment dynamics, precipitation rates and patterns, and streamflow discharge rates are key factors affecting the ecosystem in the Corpus Christi and Nueces bays. Such factors control the fate of coastal morphology and aquatic habitats and influence water quality. Understanding how these factors correlate with sediment distribution and concentration helps find solutions and pave the way for better coastal and bay management.Numerous studies have used remote sensing to investigate sediment dynamics. The satellite images were used to estimate total suspended sediment (TSS) values by developing algorithms relating reflectivity to TSS (Reisinger et al., 2017), while other studies expanded to include chlorophyll concentration and colored dissolved organic matter (CDOM) absorption coefficients, in addition to TSS (Binding et al., 2005). Doxaran et al. (2009) used a similar approach, in which sediment concentration was estimated from Terra and Aqua satellites and correlated with the reflectance ratio of MODIS bands.

The Corpus Christi Bay supports commercial fishing of several species (e.g., red fish, black drum, flounder, etc.) and recreational fishing, providing job opportunities in the area, both of which are an integral part of the City's economy. The increased sediment loading may reduce light penetration into the water column. As a result, aquatic plants (e.g., algae and seaweed) can be affected, disrupting the local food chain. In other words, if the aquatic plants are affected, other species that rely on them as a food source are affected as well. Similarly, high turbidity levels can limit the fishing of aquatic species, reduce visibility, and thereby disrupt their reproductive rates (Berry et al., 2003).

Because of their minute size and low density, suspended sediments have low settling rates, as their physical properties effectively counteract gravity. These particles, typically ranging from 0.002 mm to 0.2 mm, remain buoyant long enough to infiltrate and obstruct the respiratory systems of various aquatic organisms (Yuliati et al., 2024). Sediments can also carry pollutants (e.g., heavy metals) and cause severe damage to both fish and humans that consume them (Kadim et al., 2026). In addition, sediments reduce water capacity in dams and reservoirs (Patro et al., 2022). Accumulation of sediments can reduce the bay's storage capacity, especially in the estuary. For example, when floodwaters from rivers carrying finer sediment particles drain into the bays, heavier particles sink to the bottom, resulting in higher sediment deposition in the upper reaches of the bays (McHugh et al., 2004).

Corpus Christi includes many industrial facilities, such as refineries and petrochemical plants, which, in addition to urban and agricultural runoff, threaten the bay's water quality through pollutant loading. Such pollutants can bind to sediments and be carried to the bottom of the water column or transported along with the sediments.

Ockerman & Heitmuller (2010) used the Hydrological Simulation Program–FORTRAN (HSPF) and reported that the average daily sediment load discharged into the Nueces Bay was 117 tons/day from croplands, 98 tons/day due to releases from the Corpus Christi Lake, 55 tons/day from erosion, 37 tons/day from other land types, and 9.6 tons/day via unspecified sources during 1958-2008. Stormwater runoff, industrial discharge, and dredging activities all contribute to sediment concentration. Dredging represents a significant recurring economic burden for coastal management; for instance, maintaining Navigational Channels in the Corpus Christi Ship Channel requires millions of dollars in annual expenses to combat siltation (Rosati, 2005; TxDOT, 2021).

Remote sensing has been widely used in sediment studies, especially satellite-based images, due to its high temporal resolution. Compared to other remote sensing modes, satellites frequently cover a large spatial extent at regular intervals (revisit period), unlike aerial images. Remote sensing provides geospatial data with resolutions ranging from 31 cm (e.g., WorldView-4) to a few hundred meters (e.g., MODIS). Compared with aerial photography and in situ sampling, satellite imagery is cost-effective.

Recent advances in machine learning are enhancing its application in remote sensing analysis. For instance, Imen et al. (2015) presented a model for forecasting TSS in Lake Mead, located in Nevada and Arizona, during 2003 – 2009 using machine learning and high-resolution satellite data. They built a relationship between TSS concentration field data collected in the Boulder basin, Colorado, and reflectivity data extracted from satellite imagery, obtaining an R^2 of 0.98. Prediction models can vary depending on the inputs used to build them, such as field sample size, the sensor used, and the study period.

A similar approach was adopted by Silva et al. (2015) to study TSS in the Parnaíba River using CBERS-2B (China-Brazil Earth Resources Satellite 2B), Landsat 5-TM, and Tassan's algorithm. Their study showed that the seasonal precipitation strongly impacted the TSS and yielded an R^2 of 0.93 (for band 3) and 0.90 (for band 2) between TSS field measurement and satellite-derived TSS. Hossain et al. (2021) used Landsat 8 imagery to develop a model for the Tennessee Riverand its tributaries to estimate turbidity. They also used ground truth data and achieved a high coefficient of determination (R^2) of 0.97 using a red band. Their model also covered different temporal ranges and achieved an R^2 of 0.94. Wu et al. (2014) developed empirical models using MODIS sensor scenes and 95 field samples collected from Dongting Lake, China, and derived 6 models relating the predicted suspended particle matter (SPM) concentration (CSPM) to the SPM field data. These 6 models, with R^2 values ranging from 0.69 to 0.75, were selected from 12 trial models. Some models can achieve higher accuracy in predicting a specific water quality parameter, while the same model may not exhibit similar higher accuracy on other parameters. In other words, the good model for predicting TSS may not be equally good at predicting chlorophyll or turbidity.

Given that the MOD09GA (MODIS) product has a spatial resolution of 500 m, it is a reasonable product since daily coverage is suitable for monitoring dynamic processes such as the transportation of sediments, and its large swath width can include both upstream and downstream areas in one scene (i.e., the Nueces River basin and the bays). Previous studies have demonstrated that the MOD09GA product provided sufficient accuracy for estimating suspended sediment concentrations (SSCs) in large estuarine and coastal systems due to its high signal-to-noise ratio and frequent temporal revisit (Petus et al., 2010). MOD09GA also includes multispectral bands that are sensitive and well-suited for water quality studies.

Landsat 8 OLI provides high spatial resolution imagery, making it ideal for capturing changes and variations in water quality parameters in the Nueces River system. Specifically, Landsat 8 OLI provides 185 km × 185 km area spatial coverage and 30 m spatial resolution in the visible, Short-Wave Infrared (SWIR), and Near-Infrared (NIR) bands. A combination of both MODIS and Landsat sensors offers better insights at higher spatio-temporal scales. Multi-spectral satellites have been widely used in such research (Ayana et al., 2015), and by studying sediment reflectivity, suspended sediment concentrations can be estimated.

1.3 Modeling of Nutrient and Sediment Loading

The movement of sediment and nutrients from watersheds to downstream receiving water bodies is a major concern in water resources management. Sediment transport influences stream channel stability, reservoir storage, aquatic habitat quality, turbidity, and the delivery of sediment-associated pollutants. Nutrient enrichment, particularly from nitrogen and phosphorus, can accelerate eutrophication, increase algal productivity, reduce dissolved oxygen, and degrade aquatic ecosystem functions in rivers, reservoirs, and coastal receiving waters. Because sediment and nutrient transport are strongly controlled by rainfall, runoff generation, land use, soil properties, channel routing, and watershed management, process-based watershed models are useful tools for evaluating the sources, transport pathways, and potential reduction strategies for nonpoint-source pollution.

The Nueces River Watershed is an important hydrologic system in South Texas and provides freshwater inflow to the Nueces/Corpus Christi Bay system. The watershed is characterized by semi-arid to subtropical climatic conditions, seasonal rainfall variability, extensive rangeland, agricultural areas, urban development, and major reservoir operations. These watershed characteristics create complex interactions among streamflow, sediment transport, and nutrient loading. During high-rainfall periods, increased runoff and streamflow can mobilize sediment from upland areas, channel banks, and streambeds, while also transporting dissolved and particulate forms of nitrogen and phosphorus downstream. In dry periods, low streamflow conditions may limit transport but can increase the sensitivity of downstream water bodies to nutrient enrichment and water-quality degradation.

The Nueces/Corpus Christi Bay system is also sensitive to the balance between sediment supply and pollutant loading. Adequate sediment delivery can contribute to maintaining coastal morphology, but sediment may also act as a carrier for nutrients, pesticides, metals, bacteria, and other associated pollutants. Therefore, evaluating sediment loading alone is not sufficient. A watershed-scale assessment must also consider the relationship between sediment transport, nutrient dynamics, and management actions that may reduce pollutant delivery to the bay system. This is particularly important because nutrient enrichment can contribute to algal blooms, dissolved oxygen impairment, and broader ecological stress in estuarine environments.

Watershed models provide a practical framework for evaluating these processes because field monitoring alone is often limited by sparse sampling frequency, spatial variability, and the difficulty of capturing high-flow events. Physically based, continuous-time models can simulate long-term hydrologic and water-quality responses under different climate, land use, soil, and management conditions. Among available watershed models, the Soil and Water Assessment Tool (SWAT) has been widely used to simulate streamflow, sediment yield, nutrient cycling, pesticide transport, crop growth, and the effects of agricultural and watershed management practices (Arnold et al., 1998; Gassman et al., 2007; Neitsch et al., 2011). SWAT divides a watershed into subbasins and hydrologic response units (HRUs), which represent unique combinations of land use, soil type, slope, and management conditions. This structure allows the model to simulate spatially distributed hydrologic and pollutant-generation processes while routing water, sediment, and nutrients through the stream network.

In this study, SWAT was applied to evaluate streamflow, sediment, total nitrogen, and total phosphorus loading in the Nueces River Watershed. The model was developed from an existing calibrated Nueces watershed SWAT model and refined for sediment and nutrient simulation. Calibration and validation were conducted using observed streamflow and water-quality data at a monthly time scale. Flow simulation was evaluated first because sediment and nutrient transport depend strongly on the timing and magnitude of runoff and channel flow. Sediment calibration was then conducted to improve the representation of upland erosion and channel sediment transport. Nitrogen and phosphorus simulations were subsequently evaluated to estimate nutrient loading and to examine the role of hydrology and sediment transport in nutrient delivery.

The calibrated model was also used to evaluate selected management scenarios intended to reduce sediment and nutrient loading to the Nueces/Corpus Christi Bay system. These scenarios included brush-clearing or flow-response scenarios, sediment-control scenarios such as grassed waterways, and nutrient-management scenarios related to fertilizer application and land-use assumptions. Scenario results were compared with a calibrated baseline condition to estimate relative changes in sediment and nutrient loading. Because the observed water-quality record is limited and nutrient validation uncertainty remains, the model results are interpreted primarily as a basis for comparing relative management responses rather than as exact predictions of absolute future loads.

The Nueces River Watershed contributes freshwater, sediment, nutrients, and other associated pollutant loads to the Nueces Bay and Corpus Christi Bay system. Although sediment supply is a natural component of riverine and coastal geomorphic processes, excessive sediment delivery can increase turbidity, reduce reservoir and channel storage capacity, degrade aquatic habitat, and transport sediment-bound pollutants downstream. Nutrient enrichment from nitrogen and phosphorus can further contribute to eutrophication, algal growth, dissolved oxygen depletion, and deterioration of water quality in downstream receiving waters. These issues are especially important in semi-arid and subtropical watersheds such as the Nueces River Watershed, where episodic rainfall, high-flow events, reservoir operations, land cover, soil properties, and watershed management practices strongly control sediment and nutrient transport.

Previous monitoring and remote sensing efforts have provided valuable information on sediment concentration, turbidity patterns, and water-quality conditions in the Nueces River and bay system. However, field observations alone are limited in their ability to fully describe long-term watershed-scale loading because water-quality sampling is often discontinuous and may not capture the full range of hydrologic conditions, especially short-duration storm events that can dominate annual sediment and nutrient export. In addition, management decisions such as brush clearing, fertilizer reduction, land-use modification, and sediment-control practices cannot be fully evaluated using observed data alone. A process-based watershed model is therefore needed to integrate climate, soils, land use, streamflow, sediment transport, and nutrient cycling into a single framework for estimating load generation, routing, and management response.

SWAT models may provide a suitable framework for this purpose because they can simulate long-term hydrologic processes, sediment yield, nitrogen and phosphorus cycling, and the effects of land-management practices at the watershed scale. For this project, an existing SWAT model of the Nueces River Watershed was refined to represent flow, sediment, total nitrogen, and total phosphorus loading. The model was calibrated and validated using observed streamflow and water-quality data and then used to evaluate management scenarios relevant to reducing sediment and nutrient delivery to the Nueces/Corpus Christi Bay system. The central problem addressed in this chapter is the need to quantify watershed-scale sediment and nutrient loading and evaluate how selected management decisions may reduce pollutant delivery under variable rainfall and streamflow conditions.

1.4 Objectives of the Study

This study addresses existing knowledge gaps by evaluating the occurrence and distribution of sediments, nutrients, and other pollutants in the Nueces/Corpus Christi Bay. Field observations, laboratory analyses, and pollutant load estimations examine the quality of water and sediments. In the Nueces River, sediment transport is predominantly controlled by upstream freshwater discharge and episodic high-intensity precipitation events. However, as these sediments enter the expansive, shallow bay environment, tidal mixing and wind-induced wave resuspension become the dominant factors. Therefore, it remains unclear whether extreme precipitation, such as flash floods and hurricanes, or localized estuarine processes account for the highest observed sediment concentrations in this specific system. This study also aims to evaluate sediment and nutrient loading in the Nueces River Watershed and to assess the effects of selected management decisions on pollutant delivery to the Nueces Bay and Corpus Christi Bay system.

The specific objectives addressed in this study are as follows:

1) To evaluate nutrient and heavy metal concentrations in waters and sediments and estimate their loads and seasonal and spatial variability, providing insights into water quality around the Nueces/Corpus Christi Bay system,
2) To analyze the physical and chemical properties, concentrations, and loadings of sediments around the Nueces/Corpus Christi Bay system,

3) To establish a relationship between satellite reflectance and in-situ data,
4) To map the spatiotemporal patterns of TSS in the Nueces River and the Nueces/Corpus Christi Bay System,
5) To set up, refine, and update the Nueces River Watershed SWAT model, including watershed delineation, subbasin and HRU development, input data sources, reservoir representation, and management assumptions,
6) To calibrate and validate the model for monthly streamflow, sediment, total nitrogen, and total phosphorus loading using SWAT-CUP and appropriate model performance criteria,
7) To evaluate the influence of streamflow and sediment transport on nitrogen and phosphorus delivery,
8) To simulate selected management scenarios, including brush-clearing or flow-response scenarios, sediment-control practices, and nutrient-management alternatives,
9) To compare scenario results against the selected baseline condition and identify management options that may reduce sediment, nutrient, and associated pollutant loading to the Nueces-Corpus Christi Bay system.

The structure of this report is as follows. In Chapter 2, the collection of field data on sediment, nutrients, and associated Pollutants and the analysis of the acquired data will be discussed. Chapter 3 will describe the remote sensing data collection and analysis with a focus on the spatiotemporal distribution of sediment concentration and turbidity. Chapter 4 will present the results from numerical modeling with the SWAT model. Then, conclusions and recommendations for future work, including the best management options to reduce nutrients and pollutants to the bay system, will be discussed in Chapter 5.

Chapter 2. Sediment, Nutrients, and Associated Pollutants

2.1 Study Area

In this study, water and sediment samples were collected from multiple sites surrounding the Nueces/Corpus Christi Bay during designated sampling trips. The sampling locations include (i) Labonte Park, (ii) Nueces Bay Fishing Site, (iii) Sgt. J.D. Bock Park, (iv) Sugar Tree Apartments, and (v) Ennis Joslin Road (Figure 2.1). These locations were chosen for their biological, hydrological, and anthropogenic importance. The details of each location are described below.

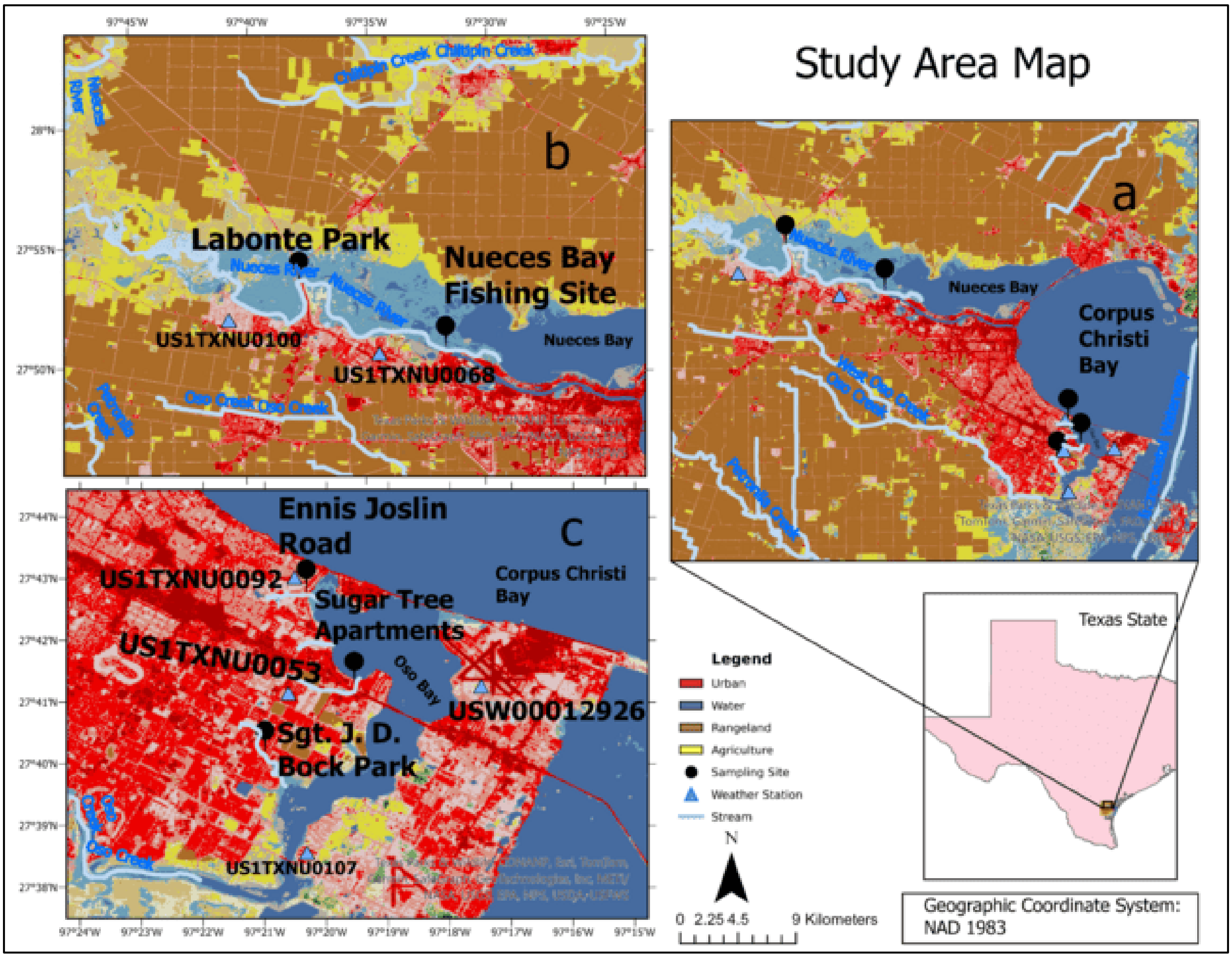

Figure 2.1. Map of sampling locations with land use/ land cover. (a) Overview of sampling sites and weather stations, (b) Focused view of Labonte Park and Nueces Bay Fishing Site with weather station, and (c) focused view of Ennis Joslin, Sugar Tree Apartments and Sgt. J. D. Buck Park, with weather stations (blue triangles in the legend).

Labonte Park (27.89152273, -97.6302842)

Labonte Park, located at 14333 Interstate 37, Corpus Christi, TX, which is upstream on the Nueces River (Figure 2.2), functions as a representative location for examining freshwater inputs into the bay. This location is essential for understanding the role of riverine inputs in the transport of sediments, nutrients, and pollutants downstream into the estuary system. Investigation at this site helps in assessing the impact of upstream activities on the bay's overall health of the ecosystem.

Figure 2.2. Sampling Site at Labonte Park, picture taken by Victor Garcia (a graduate student at TAMUK) on November 23, 2024.

Nueces Bay Fishing Site (27.84670635, -97.5279371)

The Nueces Bay fishing site, as an industrial center (Hill & Nicolau, 2016) in the region, significantly impacts the water and sediment quality of the bay (Figure 2.3). Many oil and gas companies are located on the southern shore of the bay. These businesses support economic growth but also pose environmental risks. This site was chosen to investigate the impacts of industrial effluents, heavy metal pollution, and sediment dynamics in a highly exploited region. It also assesses the influence of port operations on adjacent ecosystems and water quality.

Figure 2.3. Sampling Site at Nueces Bay Fishing Site, picture taken by Victor Garcia on November 23, 2024.

Sgt. J.D. Bock Park (27.669026, -97.349941)

Sgt. J.D. Bock Park is a tranquil outdoor space located at 7323 Canadian Dr, Corpus Christi, TX 78414 (Figure 2.4). This site is situated adjacent to a vital canal that connects sections of the bay system, rendering it an important location for comprehending sediment transport and water exchange. Nearby Oso Bay Wetlands Preserve has trails, places to watch birds, and conducts educational events about the local ecosystems. Observation at this location offers insights into the interplay between freshwater influx and tidal dynamics.

Figure 2.4. Sampling Site at Bock Park, picture taken by Victor Garcia and Pritam K. Rony (a graduate student at TAMUK) on November 23, 2024, and April 16, 2025.

Sugar Tree Apartments (27.687665, -97.325817)

The Sugar Tree Channel is a small urban tributary near Sugar Tree Apartments at 8050 South Padre Island Drive in Corpus Christi, draining into Oso Bay (Figure 2.5). It primarily carries urban runoff, while the nearby Oso Wastewater Treatment Plant (OWWTP) contributes treated effluent – both influencing the bay's water quality (Texas Commission on Environmental Quality, 2005). This site is particularly useful for assessing nutrient and pollutant inputs from residential and commercial development, and its proximity to urban infrastructure makes it well-suited for studying human-driven pressures on the estuarine system.

Figure 2.5. Sampling Site at Sugar Tree Apartments, picture taken by Pritam K Rony on November 23, 2024.

Ennis Joslin Bridge (27.712518, -97.338756)

This location, situated near a critical bridge crossing, proves itself as an ideal place for observing the interplay among urban runoff, tidal effects, sediment, and pollutant distribution (Figure 2.6). The bridge is accessible via Ennis Joslin Road, an important road providing direct access to multiple residential and commercial areas. Adjacent landmarks comprise La Joya Bay Resort Apartments (1514 Ennis Joslin Rd) and The Shores Apartments (1515 Ennis Joslin Rd), both providing waterfront residences. The bridge is close to the Texas A&M University–Corpus Christi campus. The site's accessibility and strategic positioning make it advantageous for monitoring water transport in a semi-enclosed section of the bay. The Ennis Joslin Bridge region serves as a transitional zone where freshwater from urban runoffs converges with the saltwater of Oso Bay, which generates gradients that substantially affect the nutrient cycle, sediment transport, and ecological dynamics (Conrads et al., 2018; Masterson, 2004).

Figure 2.6. Sampling site at Ennis Joslin Road, picture taken by Victor Garcia on November 23, 2024**.**

2.2 Field Data Collection Methods

Precipitation data for the study period at stations close to the sampling sites were available from the National Oceanic and Atmospheric Administration (NOAA). For the Labonte site, the closest station used in the data analysis was Station US1TXNU0100; for the Nueces site, US1TXNU0068; and for Ennis Joslin, US1TXNU0092. For the Bock Park site, although Station US1TXNU0053 is geographically closer, it lacked complete monthly precipitation records for the study period. Therefore, Station US1TXNU0107 was selected to ensure full temporal coverage. For the Sugar Tree site, precipitation records were compiled from two nearby stations to ensure complete temporal coverage, with most months sourced from NOAA Station USW00012926 and June 2025 from US1TXNU0053 (Figure 2.1).

Multiple water quality parameters, including pH, temperature, conductivity, total dissolved solids (TDS), salinity, and dissolved oxygen (DO) (Table 2.1), were measured in-situ using a YSI ProDSS meter (YSI, Xylem brand, 1700/1725 Brannum Lane, Yellow Springs, OH 45387, USA). Measurements were conducted bimonthly on September 29 and November 23, 2024, February 6, April 16, June 28, and August 16, 2025, to account for seasonal fluctuations and ensure representative results. Measurements were collected bimonthly over one year.

Table 2.1. Summary of methods and references used for testing all parameters.

Parameters	Matrix	Method / Instrument
pH, Temperature, Conductivity, TDS, Salinity, Dissolved Oxygen (DO)	Water	Field measurement using a YSI ProDSS meter
Dissolved Ammonium	Water	Colorimetric determination with a V-1200 spectrophotometer
Nitrate, Nitrite, Phosphate	Water	Ion Chromatography using a Dionex ICS-5000 system
Heavy Metals	Water	Inductively Coupled Plasma Mass Spectrometry (ICP-MS)
Suspended Sediment Concentration (SSC)	Water	Vacuum filtration using 0.40-µm glass membrane filters followed by oven-drying at 105°C
Total Phosphorus	Sediment	Colorimetric method using a V-1200 spectrophotometer, ICP-MS
Nitrate, Phosphate	Sediment	Ion Chromatography using a Dionex ICS-5000 system
Heavy Metals	Sediment	Acid digestion (EPA Method 3052) followed by ICP-MS analysis
Grain Size Distribution	Sediment	Sieve analysis and hydrometer
Organic Carbon Content	Sediment	Loss-on-ignition (LOI) method
Discharge / Flow Rate	Water	Acoustic Doppler Current Profiler (ADCP) – Rio Grande StreamPro ADCP operating at 2000 kHz

Channel flow rates were determined using an Acoustic Doppler Current Profiler (ADCP) (Rio Grande StreamPro ADCP, operating at 2000 kHz, manufactured by Teledyne RD Instruments, 14020 Stowe Drive, Poway, CA 92064, USA). The ADCP measured the cross-sectional area of the channel as it traversed across it. Using the velocity measurements and the cross-sectional profile obtained from the ADCP, flow rates were calculated (flow rate

= flow velocity × cross-sectional area). Flow data on November 23, 2024, and April 16, 2025, were collected using the ADCP. On February 6, June 28, and August 16, 2025, velocity measurements were conducted using a SonTek® SL1500 Side-Looking Doppler Current Meter, manufactured by Xylem Inc., 9845 Carroll Park Drive, San Diego, CA 92121, USA. These velocity values were then multiplied by the cross-sectional area previously measured by the ADCP on Nov 23, 2024, and April 16, 2025, resulting in flow rates for those months.

Water and sediment samples were collected at five locations (Figure 2.1) on September 29 and November 23, 2024, and February 6, April 16, June 28, and August 16, 2025. Water samples were taken six inches below the surface using a high-density polyethylene (HDPE) container mounted on an extendable sampling pole. HDPE was chosen for its durability and low risk of chemical leaching (USEPA, 1993a; 1993b). All plastic bottles and amber glass jars were cleaned using a strict decontamination protocol: soaked in phosphate-free laboratory detergent for 30 minutes, rinsed with tap water, soaked in 10% nitric acid (HNO_3) for 30 minutes to remove trace metals (Demutskaya & Kalinichenko, 2010), and triple-rinsed with deionized water (Turk, 2001). Amber glass jars were then filled with deionized water and held for at least 48 hours before use to confirm the absence of residual contaminants (Wilde et al., 2004).

Powder-free gloves were worn at all sampling sites to minimize contamination. Before collection, the deionized water in the pre-cleaned amber glass jars was discarded and each jar was rinsed three times with sample water (Turk, 2001; Wilde et al., 2004). Three water samples were collected per site by stepping 3 m upstream between each collection to better capture suspended sediment concentration (SSC). Samples were transferred into amber glass jars, which were chosen for their chemical inertness and ability to block UV light and protect light-sensitive analytes (Richardson, 2009). Jars were sealed with Teflon®-lined caps, placed in plastic bags, and kept in an ice-cooled cooler at near-freezing temperatures to prevent degradation during transport to the laboratory (Turk, 2001; Wilde et al., 2004).

For sediment sample collection, stainless-steel scoops and amber glass containers were cleaned using the same protocol applied to the amber glass jars used for water sample storage. Sediment samples were collected using a stainless-steel scoop due to its non-reactive and contamination-resistant properties (Shelton & Capel, 1994). The sediment samples were placed in the pre-cleaned amber glass jars, sealed with Teflon®-lined tops, placed in plastic bags, and stored in a cooler with ice at slightly above freezing temperatures to prevent degradation before analysis (Turk, 2001; Wilde et al., 2004), after which they were transported to the laboratory for further analysis.

Before each sampling event, the YSI ProDSS meter was calibrated according to the manufacturer's guidelines. That is, pH sensors were calibrated using NIST-traceable pH 4, 7, and 10 buffers; DO sensors were calibrated with air-saturated water or a zero-oxygen solution; and conductivity/TDS/salinity sensors were calibrated using a standardized conductivity solution (YSI, 2021). All sensors were rinsed with deionized water between locations to prevent cross-contamination. Data were stored immediately in the sensors' internal memory and simultaneously backed up to a field laptop for real-time verification. Additional QA/QC procedures included adherence to standard field protocols, collection of multiple measurements at each site to ensure instrument stability and reproducibility, and routine inspection of equipment for cleanliness and proper function. All sample handling and processing were conducted in a clean laboratory environment with strict cross-contamination prevention measures, including the use of clean gloves, acid-washed containers, and dedicated workspaces for different sample types.

2.3 Field Data Analysis

2.3.1 Nutrients, Metals, and Suspended Sediment in Water Samples

Dissolved ammonium concentrations in water samples were determined using a V-1200 spectrophotometer (VWR International, Researchpark Haasrode 2020, Geldenaaksebaan 464, B-3001 Leuven, Belgium), employing a colorimetric method based on Nessler's reagent (Bower & Holm-Hansen, 1980; Demutskaya & Kalinichenko, 2010; Searle, 1984). Water samples were filtered in the laboratory through 0.45 µm Mixed Cellulose Esters membrane filters (MilliporeSigma, Burlington, MA, USA) to remove particulates and prevent analytical interference before the analysis. Other nutrients, including nitrate and phosphate in water samples, were analyzed using a Dionex ICS-5000 Ion Chromatography (IC) system (Thermo Fisher Scientific, 168 Third Avenue, Waltham, MA 02451, USA). Water samples were filtered through 0.45 µm membrane filters to remove suspended particles and subsequently diluted with ultrapure water to ensure concentrations fell within the linear range of the IC calibration curve. However, due to instrumental issues encountered with the IC system during June and August 2025, nitrate and phosphate concentrations for samples collected in these sampling periods were determined using color disc test kits manufactured by Hach Company (Loveland, Colorado, USA). Specifically, nitrate was analyzed using the Hach Nitrate and Nitrite Color Disc Test Kit (Model 1408100), and phosphate was measured using the Hach Phosphate Test Kit (Model PO-23).

Heavy metal concentrations in water and suspended sediment samples were determined using Inductively Coupled Plasma Mass Spectrometry (ICP-MS). Water samples were filtered through 0.45 µm membrane filters to remove suspended particles, and the resulting filtrate was acidified to a pH below 2 using concentrated nitric acid (HNO_3) for preservation, following EPA Method 200.8 (United States Environmental Protection Agency, 1994). Acidified water samples were stored in pre-cleaned polyethylene containers and analyzed at the Elemental Analysis Laboratory, Department of Chemistry, Texas A&M University (TAMU) using ICP-MS (PerkinElmer Inc, 710 Bridgeport Avenue, Shelton, Connecticut 06484, United States).

To analyze metals associated with suspended sediment, suspended solids (SS) were obtained by centrifuging water samples using a Heraeus Megafuge 8 Centrifuge (Thermo Fisher Scientific, 168 Third Avenue, Waltham, MA 02451, USA). The centrifuge was operated at 3000 RPM for approximately 8 minutes, a duration calculated based on Stokes' law and centrifugal acceleration to ensure effective settling and separation of particulate matter. After centrifugation, the supernatant was discarded, and the solids were collected, air-dried, and homogenized for further analysis (Association et al., 2017; Droppo et al., 1992). Before analysis, suspended solids samples were digested following EPA Method 3052 (USEPA, 1996) using an Anton Paar Multiwave GO microwave digestion system (Anton Paar GmbH, Anton-Paar-Straße 20, 8054 Graz, Austria). The digestion mixture consisted of 9 mL of nitric acid (68% HNO_3), 3 mL of hydrochloric acid (37% HCl), and 2 mL of hydrogen peroxide (30% H_2O_2). The digested mixture was filtered through a 0.45 µm membrane filter, stored in pre-cleaned polyethylene containers, and sent to TAMU for ICP-MS (PerkinElmer Inc, 710 Bridgeport Avenue, Shelton, Connecticut 06484, United States) analysis.

SSCs were determined using a vacuum filtration system equipped with a 0.40 µm glass membrane filter to separate sediment from known volumes of water samples. The sediment retained on the filters was dried in an oven at 105 °C for a minimum of 1 hour or until a constant weight was achieved (APHA, 2017; Groten et al., 2023). The mass of the filters with and without dried sediment was measured, and the SSCs were calculated using the following equation:

$$SSC\ (mg/L) = \frac{m_{fs} - m_f}{V_{sample}} \quad (2.1)$$

where m_{fs} is the mass of the filter with dried sediment, m_f is the mass of the dry filter, and V_{sample} is the volume of the water sample.

2.3.2 Sediment Samples

For particle-size analysis, sediment samples were air-dried to remove surface moisture and gently disaggregated using a mortar and pestle to break down aggregates without damaging individual grains. Samples were then rinsed with distilled water to remove soluble salts and subsequently oven-dried at 105 °C for 24 hours following ASTM standards (ASTM International, 2007, ensuring complete moisture removal and consistent analytical conditions. In cases where drying caused hardening or clumping, samples were lightly rehydrated to soften aggregates and re-dried to achieve an optimal texture for sieving.

For heavy metal analysis, sediment samples were air-dried, homogenized, and sieved through a 2 mm mesh to remove coarse debris and ensure uniformity. Acid digestion was performed according to U.S. EPA Method 3052 (USEPA, 1996) using an Anton Paar Multiwave GO microwave digestion system (Anton Paar GmbH, Graz, Austria). Each sample was digested in a mixture of 9 mL nitric acid (68% HNO_3), 3 mL hydrochloric acid (37% HCl), and 2 mL hydrogen peroxide (30% H_2O_2), allowing for complete breakdown of mineral matrices and release of trace metals for subsequent instrumental analysis. After cooling, the digested mixture was filtered through a 0.45 µm membrane filter, stored in pre-cleaned polyethylene containers, and sent to TAMU for ICP-MS analysis.

For analyzing nutrients such as nitrate and phosphate, collected sediments were extracted using potassium chloride (KCl), following US EPA Method 300.0 (1993a; 1993b). In detail, for each analysis, 1 g of air-dried and sieved (through a 2 mm mesh) sediment sample was placed into clean centrifuge tubes, and a 2 N KCl solution, prepared with analytical-grade reagents, was added at a 1:10 (w/v) sediment-to-solution ratio. The mixture was stirred on an orbital shaker for 30 minutes at room temperature to facilitate nutrient extraction. After shaking, samples were centrifuged at 3,000 rpm for 10 minutes to separate the supernatant, which was then filtered through a 0.45 µm membrane filter. Filtered extracts were stored at 4 °C in labeled amber jars and analyzed for nutrients within 24 to 48 hours. For analyzing organic carbon, sediment samples were homogenized, coarse debris was removed, and a subsample was dried at 105 ˚C to a constant mass following ASTM D2974.

Sediment particle size distribution and texture were determined using sieve analysis and hydrometer testing following ASTM D422 guidelines (ASTM International, 2007). The organic carbon content of the air-dried and homogenized sediments was analyzed using the ignition method, following ASTM D2974 protocols (ASTM International, 2014). Extracted sediments were analyzed for nitrate and phosphate using a Dionex ICS-5000 Ion Chromatography (IC) system (Thermo Fisher Scientific, 168 Third Avenue, Waltham, MA 02451, USA) (USEPA, 1993). Nitrite could not be detected due to high chlorine concentrations in the samples.

Additionally, due to the IC instrumental issues during the June and August 2025 sampling periods, nitrate was analyzed using the Hach Nitrate and Nitrite Color Disc Test Kit, Model 1408100, and phosphate was measured using the Hach Phosphate Test Kit, Model PO-23 (Hach Company, Loveland, Colorado, USA). Total phosphorus in sediment samples was measured using a V-1200 spectrophotometer (VWR International, Researchpark Haasrode 2020, Geldenaaksebaan 464, B-3001 Leuven, Belgium), employing a colorimetric method based on the ascorbic acid–molybdenum blue reaction (de Morais et al., 2021; USEPA, 1993a; 1993b; Wang et al., 2013) for samples collected in September and ICP-MS analysis for samples collected in the remaining months. Heavy metal concentrations in sediment samples were determined using Inductively Coupled Plasma Mass Spectrometry (ICP-MS) (PerkinElmer Inc, 710 Bridgeport Avenue, Shelton, Connecticut 06484, United States).

The sediment, nutrient, and metal loads were estimated using the measured SSC, nutrient concentration, metal concentration in water, and the corresponding discharge values determined at each sampling site. The sediment load was calculated by multiplying the concentration (i.e., SSC) and nutrient and metal concentrations by discharge using the relationship:

$$Q_s = Q \times C \tag{2.2}$$

where Q_s is the sediment load (kg/day), Q is the discharge, and C is the concentration (mg/L).

2.4 Results

2.4.1 Precipitation and Flow Rate

Figure 2.7 shows that across all stations, rainfall remained very low and sporadic from September 2024 through early March 2025, with only small, isolated events. Beginning in April 2025, precipitation increased sharply, marked by several high-intensity rainfall peaks. From May to August 2025, rainfall became more frequent, more clustered, and overall, much higher, with multiple notable storm events contributing to the majority of annual precipitation. For classification purposes, September, November, February, and April were considered dry months, while June and August were categorized as wet months.

Discharge (Figure 2.8) varied substantially across sites and seasons. Bock Park and Sugar Tree showed consistently low flows with only minor fluctuations throughout the year. Ennis Joslin exhibited moderate, relatively stable discharge across all sampling dates. Labonte Park displayed the highest variability, with a pronounced peak in April 2025. The Nueces Bay Fishing Site showed extreme episodic behavior, with very high discharge in November 2024 and April 2025, while the remaining months weren't measured due to the current meter limitations; specifically, the channel cross-section at this site was wider and deeper than the operational range of the SonTek® SL1500 Side-Looking Doppler current meter used.

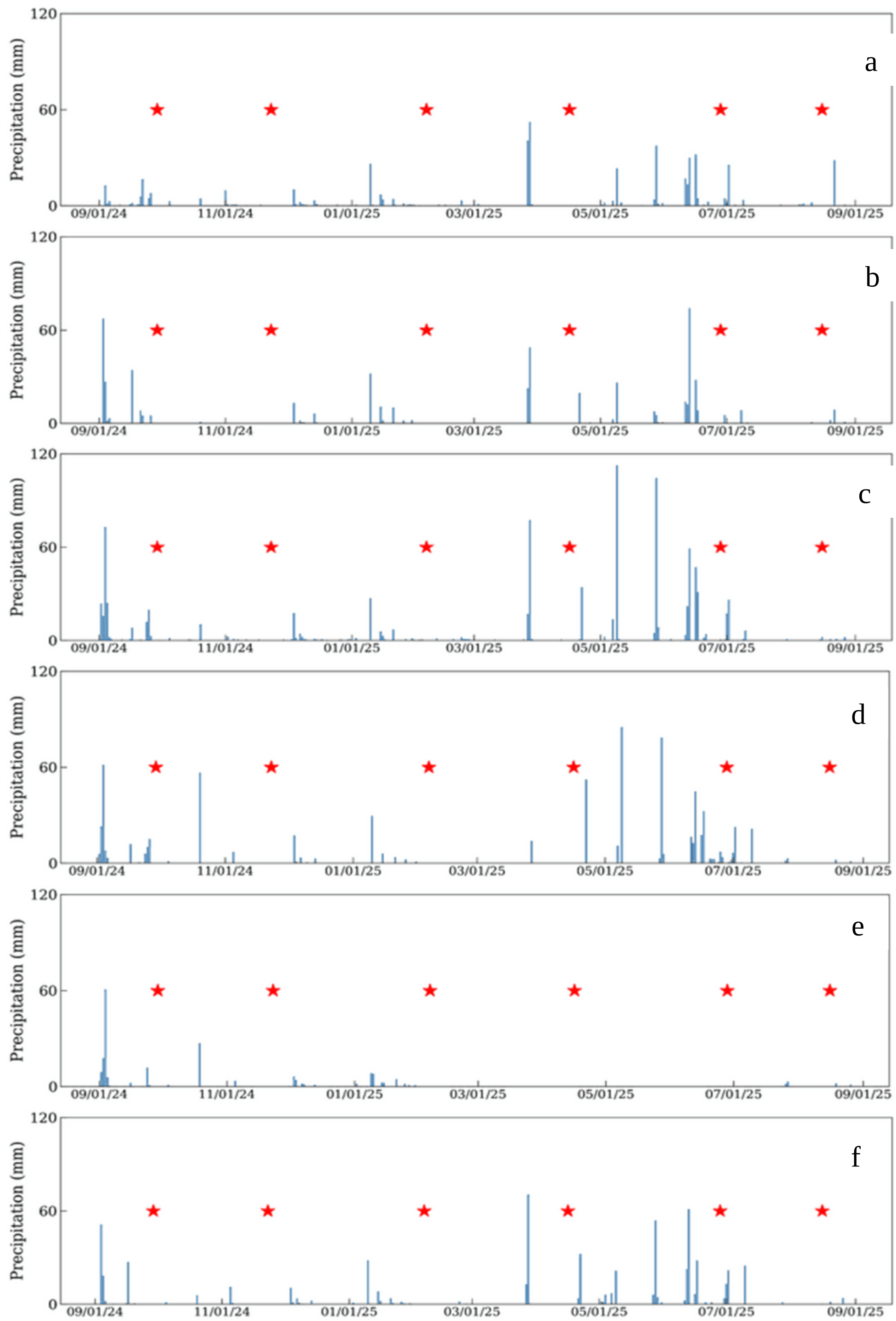

Figure 2.7. Precipitation across monitoring stations between September 2024 and August 2025: (a) US1TXNU0100 (Labonte Park), (b) US1TXNU0068 (Nueces Bay Fishing Site), (c) US1TXNU0107 (Bock Park), (d) US1TXNU0053 (Sugar Tree), (e) USW00012926 (Sugar Tree), and (f) US1TXNU0092 (Ennis Joslin). Note that the red stars in the figures indicate the sampling dates.

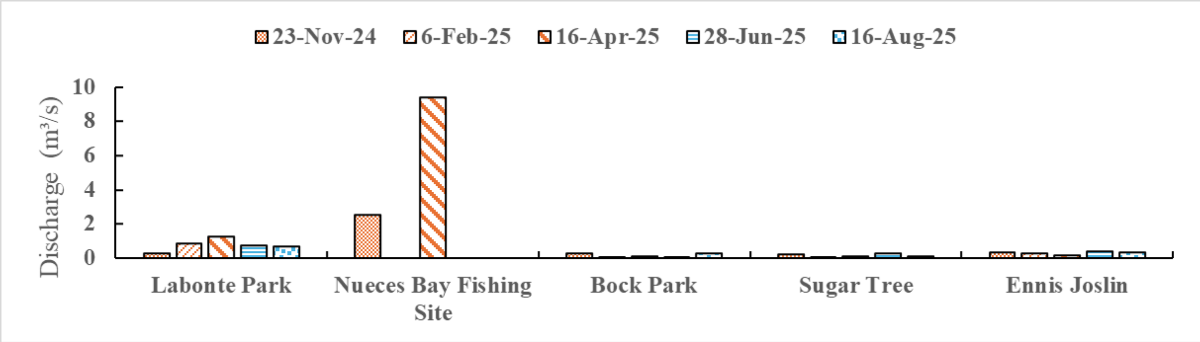

Figure 2.8. Discharge measured/estimated across five sampling sites on sampling dates.

2.4.2 Water Quality Parameters

The measured pH values (Figure 2.9a) indicate that the water at the study sites remained consistently alkaline across all sites, ranging between 6.5 and 11.6, with two very high values observed at Nueces Bay (10.8 in September 2024) and Bock Park (11.6 in November 2024). During the wet months (June – August), pH stabilized around 8.0 – 8.6. Temperature exhibited a distinct seasonal trend, ranging from ~19 to ~32 °C across sites (Figure 2.9b). During the dry months (September, November, February, and April), temperatures ranged from approximately 19.4 °C to 31.4 °C, with the lowest values observed in November and February. In contrast, the wet months (June and August) exhibited consistently higher temperatures across all sites, generally exceeding ~29 °C.

For salinity (Figure 2.9c) across the six sampling dates, Nueces Bay consistently exhibited the highest salinity values, with a steady increase with a peak in August. Sugar Tree Apartments also maintained high salinity levels throughout the study period, with a notable rise in August 2025. Labonte Park showed moderate fluctuations, dipping in April before rising sharply by August. Sgt. J.D. Bock Park remained low but displayed a gradual upward trend. Ennis Joslin Road started with moderate salinity but dropped significantly after November, remaining low through August.

DO concentrations across the five sites ranged from 2.2 to 29.9 ppm, showing clear spatial and seasonal variations (Figure 2.9d). During the cooler dry months (November –

April), DO values were generally high, reaching 20.52 ppm at Nueces Bay, 16.26 ppm at Sugar Tree Apartments, and a maximum of 29.9 ppm at Ennis Joslin Road in April. In contrast, during the wet months (June – August), DO levels decreased markedly, with the lowest concentrations recorded at Sugar Tree Apartments (2.2 ppm) and Bock Park (3.9 ppm).

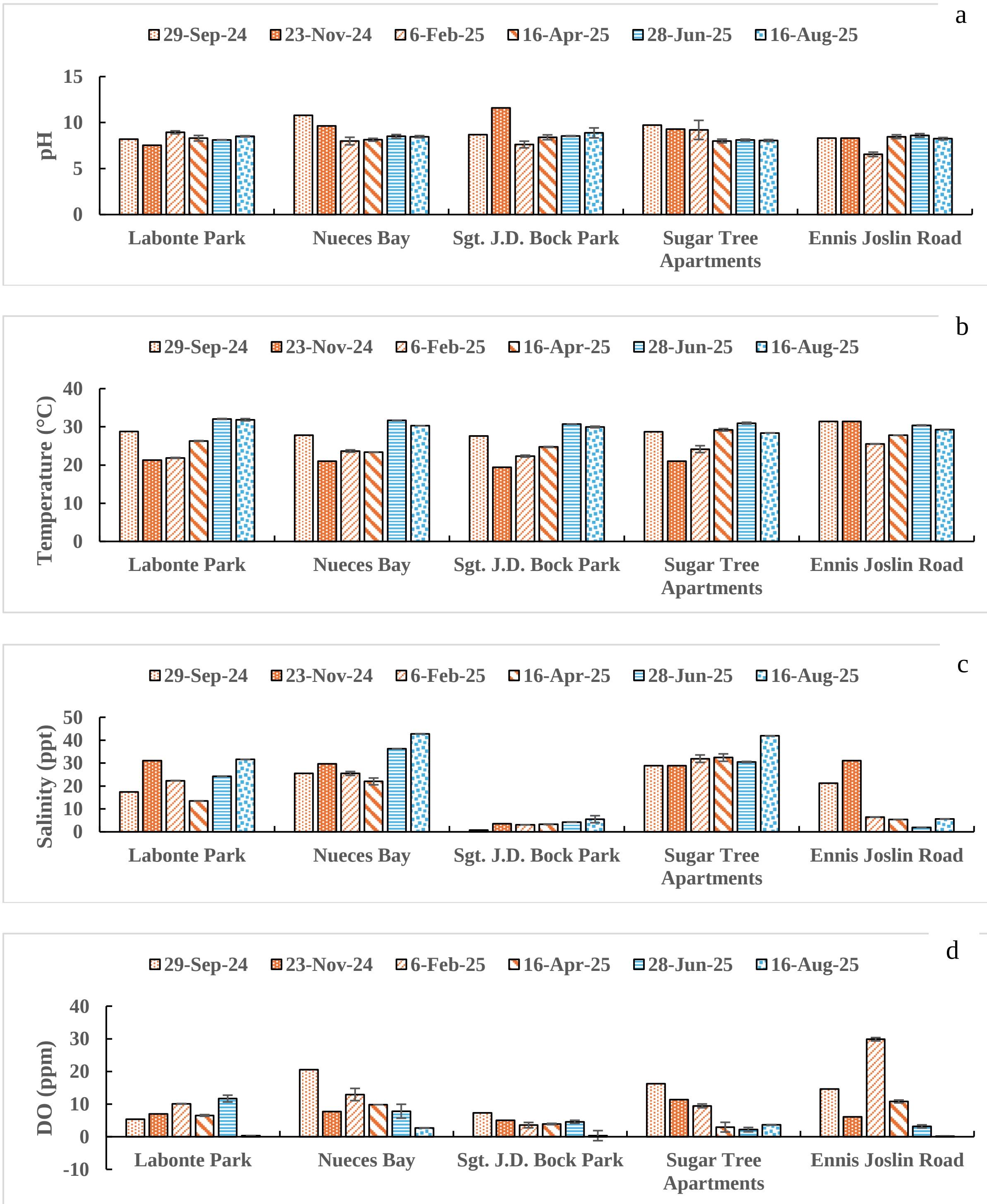

Figure 2.9. Comparison of water quality parameters: (a) pH, (b) temperature, (c) salinity, and (d) DO. Error bars are standard deviations for three measurements, and triplicate measurements were taken for sampling from February and continued in the subsequent months.

2.4.3 Suspended Sediment Concentration

SSC trends varied notably across sites (Figure 2.10). Labonte Park showed a consistent increase, culminating in the highest SSC value in August (135.4 mg/L), indicating rising sediment loads over time. Nueces Bay exhibited fluctuating SSC levels, with a spike in June (626.8 mg/L), followed by a decline, suggesting episodic sediment influx. Sgt. J.D. Bock Park maintained low SSC throughout the study period, with only slight increases during summer. Sugar Tree Apartments showed moderate SSC values, peaking in February before tapering off. Ennis Joslin Road displayed irregular fluctuations, with elevated values in February and August.

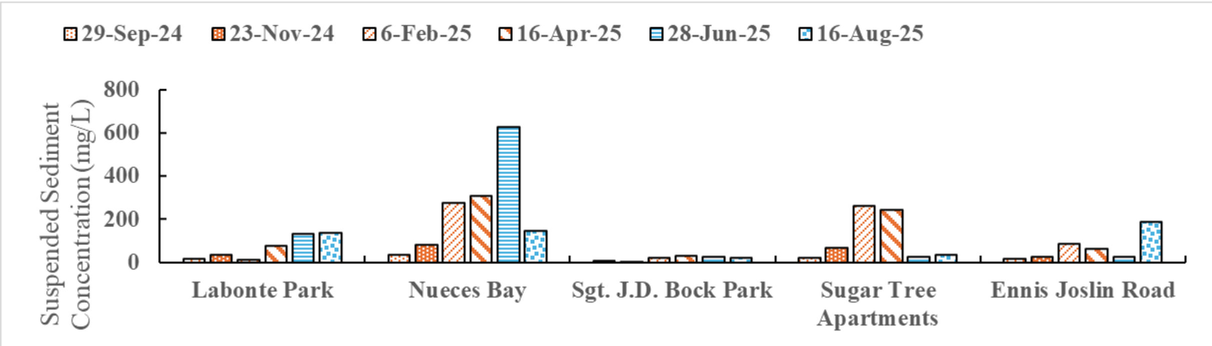

Figure 2.10. SSC comparison at the study sites.

2.4.4 Sediment Characteristics

Figure 2.11 presents the particle size distribution curves of the sediment samples from the study sites, indicating that sediments were predominantly sand throughout the sampling period, with noticeable fluctuations of coarser sand fractions (i.e., shifting of the particle size distribution curves in up and down directions). At Labonte Park (Figure 2.11a), sediments become progressively finer from September to February (i.e., curves shift upward). From April through August, the curves shift downward, indicating coarser textures. Nueces Bay Fishing Site (Figure 2.11b) sediments show relatively smaller variations among months. June and February 2025 show slightly higher coarse fractions, whereas September 2024 and November 2024 exhibit finer sand fractions. Bock Park (Figure 2.11c) sediments show notable seasonal variations. In September 2024, the particle size distribution curve shows a higher coarser fraction, whereas June 2025 and November 2024 exhibit finer sand fractions. At Sugar Tree (Figure 2.11d), the particle size distribution curves remained closely grouped across months. August 2025 had the coarser sample, showing a higher % passing, while September and November 2024 displayed finer textures. At Ennis Joslin (Figure 2.11e), sediments show larger seasonal shifts than at other sites. April 2025 had the coarser sample, with a higher % passing, while September had the finer samples.

The grain size characteristics (D_{10}, D_{30}, and D_{60}) revealed a mix of fine to moderately coarse sediments (Figure 2.12). Overall, D_{10} values ranged from 0.07 to 0.17 mm, D_{30} from 0.12 to 0.95 mm, and D_{60} from 0.23 to 2.5 mm, indicating predominantly sandy to silty textures. D_{10} values across sites and dates indicate temporal shifts in soil texture, with the highest D_{10} (up to 0.17 mm) at Nueces Bay and Ennis Joslin Road. Sugar Tree Apartments also exhibited increased D_{10} in April and August, while Labonte Park remained relatively stable. D_{30} values varied relatively less notably across sites and seasons except at Ennis Joslin Road, with a peak of 0.95 mm in April 2025. Nueces Bay and Sugar Tree Apartments showed relatively consistent increases (up to 0.28 mm), while Labonte Park and Sgt. J.D. Bock Park displayed more stability. D_{60} values reveal significant temporal and spatial variation, with Ennis Joslin Road peaking at 2.5 mm in April 2025. Nueces Bay also showed elevated D_{60} values in summer (up to 2 mm). In contrast, Sgt. J.D. Bock Park exhibited the lowest and most stable D_{60} values except in September 2024.

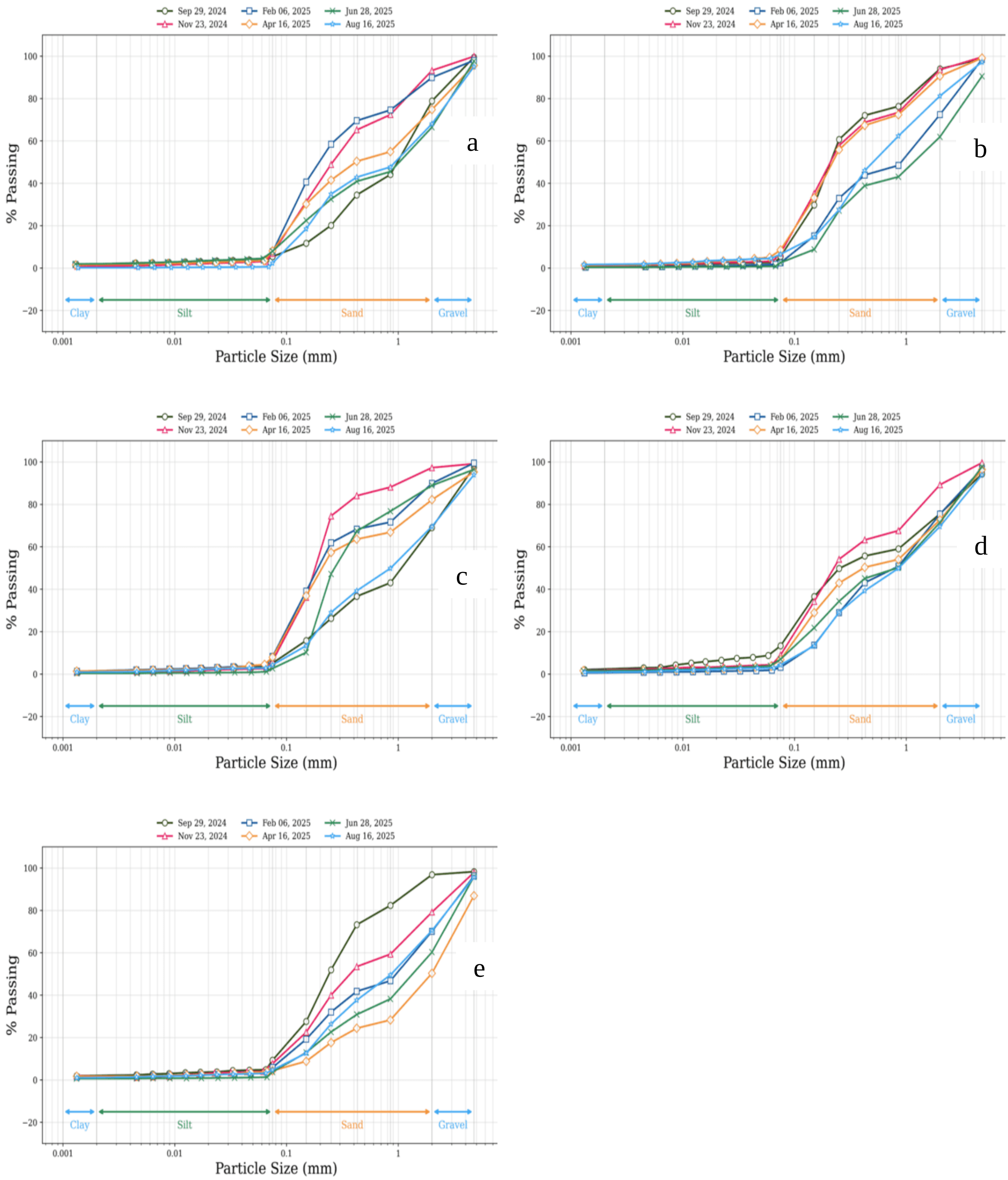

Figure 2.11. Comparison of particle size distributions at the study sites: (a) Labonte Park, (b) Nueces Bay Fishing Site, (c) Bock Park, (d) Sugar Tree, and (e) Ennis Joslin.

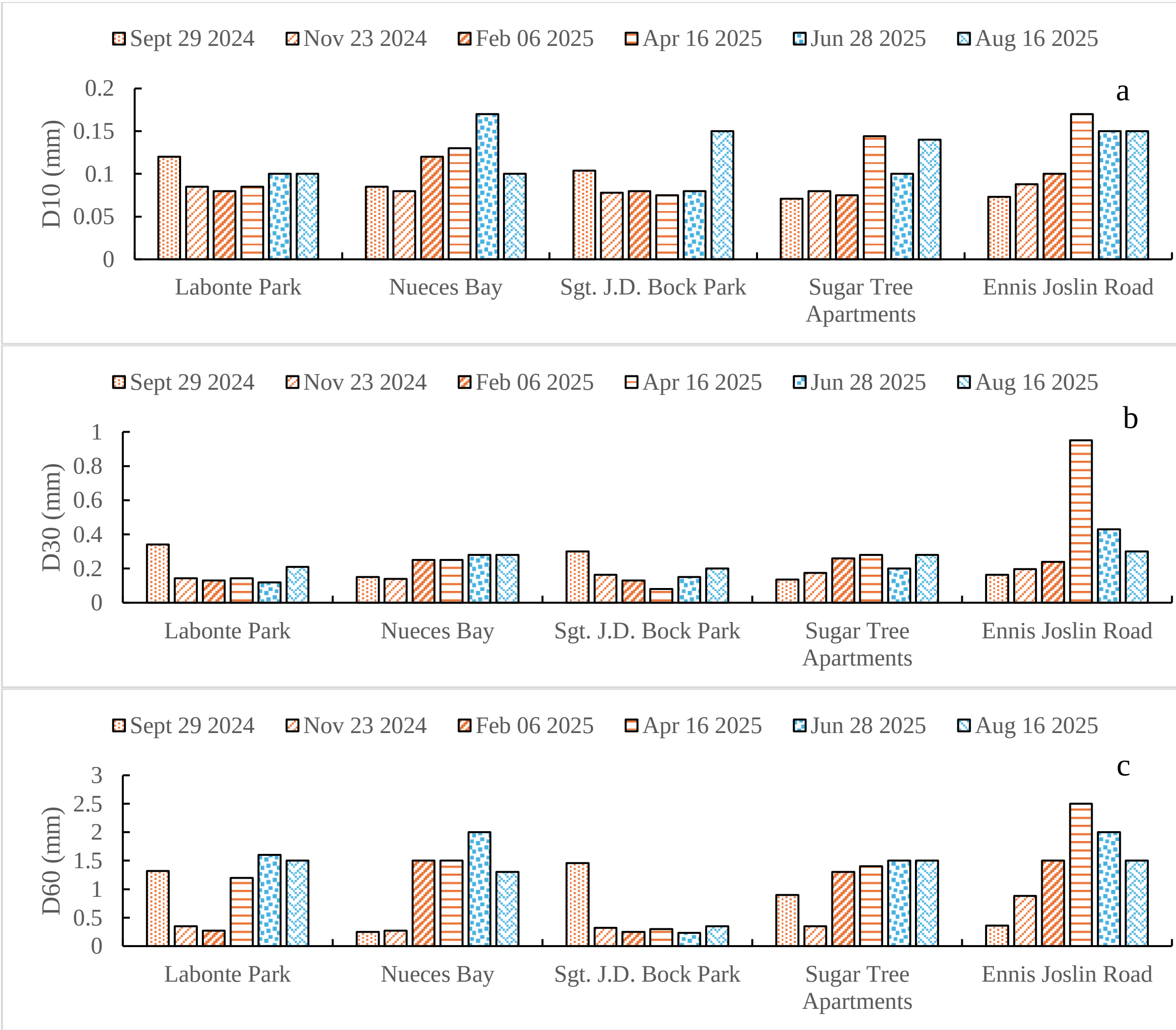

Figure 2.12. Comparison of particle size parameters: (a) D_{10}, (b) D_{30}, and (c) D_{60} at the study sites.

Organic Carbon showed seasonal variation (Figure 2.13) over the six sampling dates. Labonte Park maintained relatively stable values across all sampling dates, with measurements ranging from 8.67% to 12.5%. Nueces Bay showed a gradual increase over time, peaking at 15.33% in June and maintaining elevated levels in August. Sgt. J.D. Bock Park had relatively stable but lower values, with a notable increase in June (14%). Sugar Tree Apartments showed a sharp spike in February (18.67%), the highest single value across all sites, followed by moderate levels in June and August 2025. Ennis Joslin Road displayed fluctuating carbon content, with a dip in June 2025 (2%) followed by a recovery in August

2025. Overall, carbon content varied seasonally and spatially, with February and June showing the most pronounced site-specific peaks.

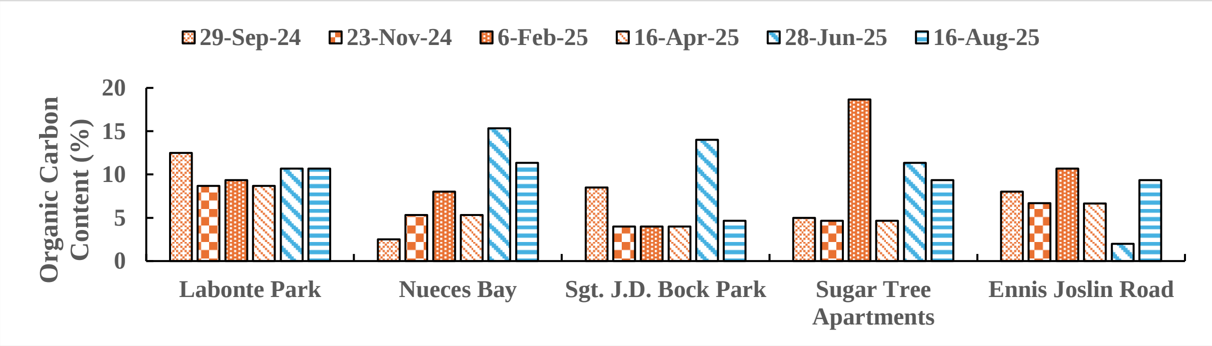

Figure 2.13. Comparison of organic carbon content in the sediment samples.

2.4.5 Nutrient Parameters

During the dry months (September – April), high nitrate levels were recorded across all sites (Figure 2.14a). Phosphate followed a similar pattern, except at the Sugar Tree and Ennis Joslin sites, where the phosphate concentrations were high in June and August 2025 (Figure 2.14b). Notably, nitrate was not detected at Labonte Park and Nueces Bay Fishing Sites in February, April, June, and August, while phosphate was not detected across all sites in November, February, and April. Ammonium concentrations were generally higher in the earlier sampling months (Figure 2.14c). Most sites showed irregular peaks, while Sgt. J.D. Bock Park remained consistently low throughout. It should be noted that nutrients associated with suspended sediments were not measured in this study, as the focus was on dissolved fractions to better capture the water-column dynamics and site-specific variability.

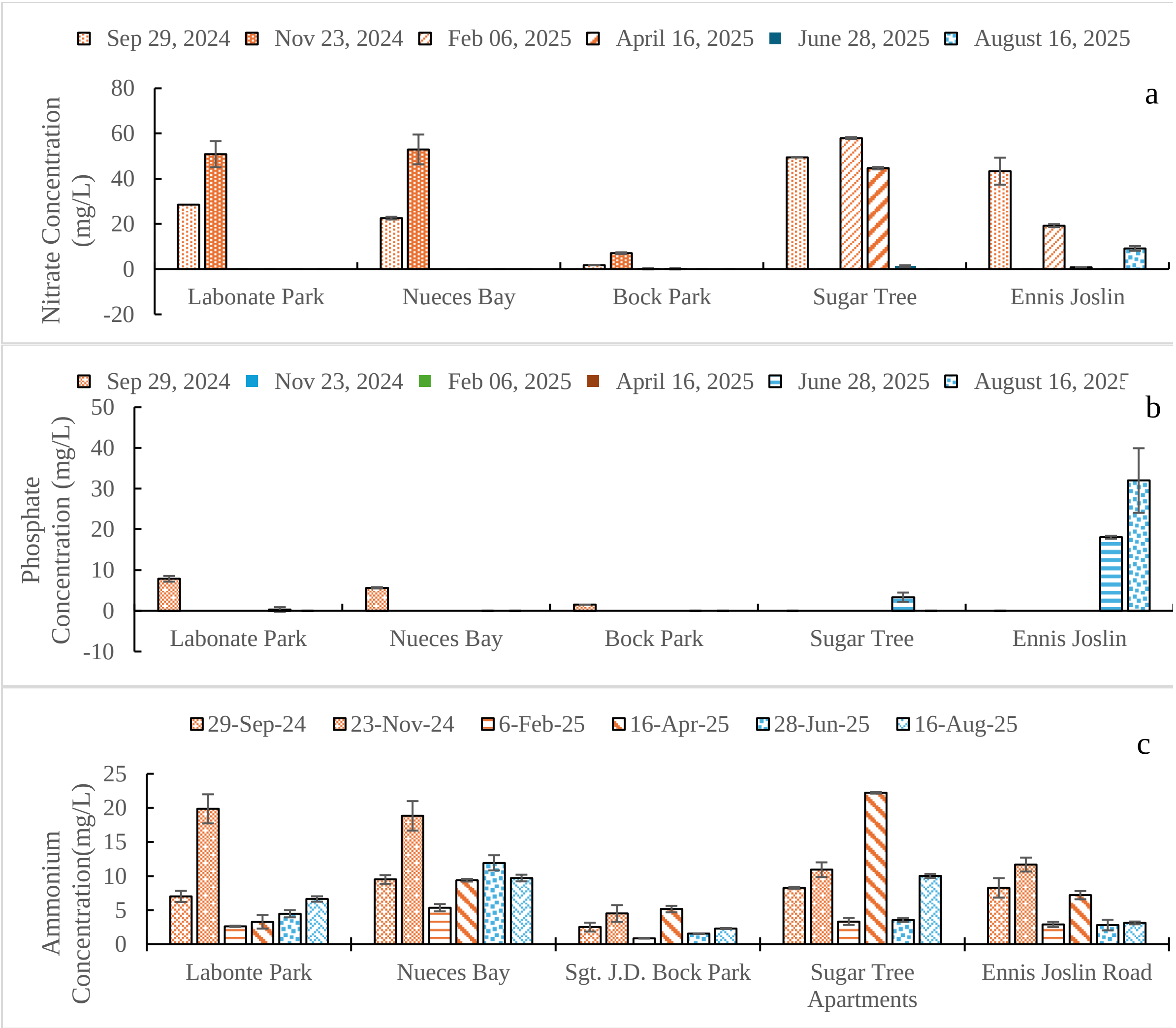

Figure 2.14. Comparison of nutrient concentrations measured in waters at study sites: (a) dissolved nitrate, (b) dissolved phosphate, and (c) dissolved Ammonium. Error bars are standard deviations for three measurements. Note that nitrate and phosphate were below detection limits during some sampling trips.

During the dry season (September – April), nitrate, phosphate, and total phosphorus (TP) concentrations in sediments were elevated across all sites (Figure 2.15). Concentrations declined in the wet months (June – August). Notably, nitrates were not detected at Labonte Park, Bock Park, and Ennis Joslin sites in February, June, and August. Phosphate concentrations in sediments were undetectable at all sampling sites, except for Sgt. J.D. Bock Park in November 2024.

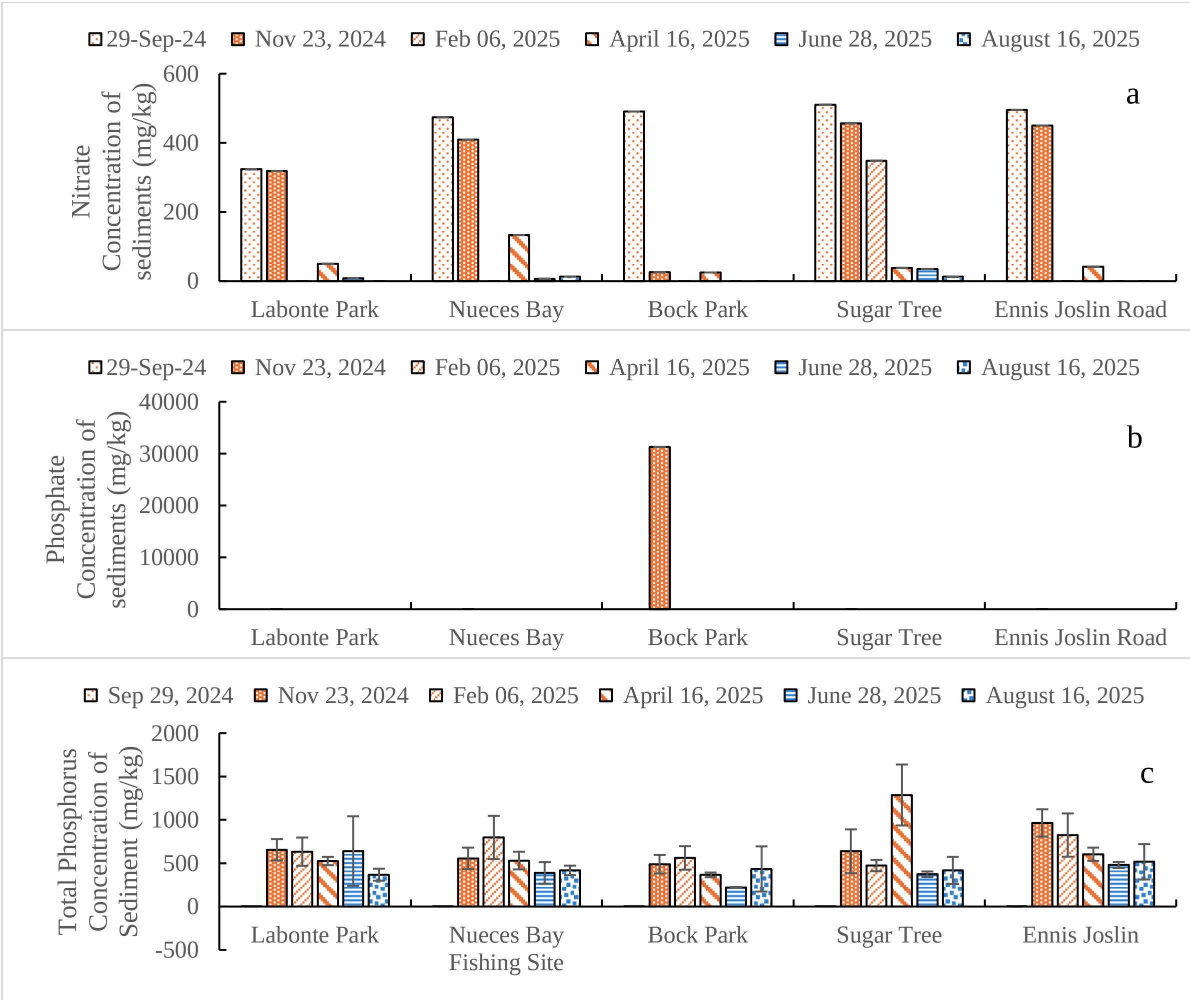

Figure 2.15. Comparison of nutrient concentrations measured in sediments collected at the study sites: (a) Nitrate, (b) Phosphate, and (c) Total Phosphorous. Error bars are standard deviations for three measurements.

2.4.6 Heavy Metal Concentrations in Water and Sediments

A total of 24 metals were detected in this study including Be, Al, V, Cr, Mn, Fe, Co, Ni, Cu, Zn, As, Se, Rh, Pd, Ag, Cd, Sn, Sb, W, Pt, Hg, Tl, Pb, and U. Among the detected metals, arsenic (10 µg/L), copper (1.3 mg/L), lead (1.15 µg/L), mercury (0.0122 µg/L), selenium (50 µg/L), and iron (1 mg/L) exceeded their respective Texas Surface Water Quality Standards as noted in the parentheses (Texas Surface Water Quality Standards, 2018). For sediments, arsenic (5.9 mg/kg), cadmium (0.6 mg/kg), chromium (37.3 mg/kg), copper (35.7 mg/kg), and mercury (0.17 mg/kg) were selected for focused evaluation because their concentrations exceeded the established ecological benchmark thresholds as noted in the parentheses (MacDonald et al., 2000).

Figure 2.16a shows that arsenic concentrations exhibited pronounced seasonal and spatial variability across the study sites. The highest levels were recorded in February 2025 at Sugar Tree (0.434 mg/L) and Nueces Bay (0.397 mg/L), while Labonte Park also showed elevated arsenic in the same month (0.210 mg/L). In contrast, Bock Park and Ennis Joslin consistently displayed lower arsenic concentrations. Copper concentrations peaked in November 2024, with Sugar Tree (2.826 mg/L) and Nueces Bay (2.948 mg/L) showing the highest values (Figure 2.16b). Nueces Bay also exhibited a strong secondary peak in June, the highest among all sites and months. Labonte Park displayed elevated copper concentrations in November 2024 and in June and August 2025, whereas Bock Park and Ennis Joslin maintained consistently low concentrations except for a pronounced November surge in 2024, reaching 0.772 mg/L and 1.923 mg/L, respectively.

Lead levels spiked sharply in June 2025 at Labonte Park (0.00914 mg/L), the Nueces Bay Fishing Site (0.00649 mg/L), and Sugar Tree (0.00772 mg/L), far exceeding values from other months (Figure 2.16c). Bock Park and Ennis Joslin exhibited relatively stable and low lead concentrations throughout the study period. High mercury concentrations were observed in August 2025 at most sampling sites, particularly at Sugar Tree (2.120 mg/L), Nueces Bay (2.016 mg/L), Bock Park (1.468 mg/L), and Labonte Park (1.253 mg/L), while Ennis Joslin showed lower but still detectable levels (Figure 2.16d). Selenium concentrations were elevated during dry months at all sites and peaked in February 2025 at Sugar Tree (0.304 mg/L), Nueces Bay (0.271 mg/L), and Labonte Park (0.214 mg/L) (Figure 2.16e). Bock Park and Ennis Joslin exhibited comparatively lower selenium levels throughout the year. Iron concentrations peaked in September 2024 at Nueces Bay (≈ 7.893 mg/L), Labonte Park (≈ 7.663 mg/L), Sugar Tree (≈ 7.400 mg/L), and Ennis Joslin (≈ 6.573 mg/L) (Figure 2.16f).

Levels declined during winter and reached minimum values during the wet season. Iron concentrations remained generally higher at Nueces Bay and Sugar Tree and consistently lower at Bock Park.

Figure 2.17a shows that arsenic concentrations in suspended solids were generally low from September to November 2024 across all sites (< 0.04 mg/L), followed by a major system-wide spike in February 2025. The highest February (2025) levels occurred at Nueces Bay (0.847 mg/L) and Sugar Tree (0.648 mg/L), with additional elevations at Labonte Park (0.175 mg/L), Bock Park (0.284 mg/L), and Ennis Joslin (0.065 mg/L). Moderate increases also appeared in April and June 2025 at all sites (0.04 – 0.07 mg/L), with a secondary rise in August 2025 (0.06 – 0.08 mg/L). Copper remained low (< 0.01 mg/L) across all stations from September 2024 through February but exhibited strong system-wide spikes in April 2025 (Figure 2.17b). The highest April concentration occurred at Ennis Joslin (0.251 mg/L), followed by Sugar Tree (0.105 mg/L), Bock Park (0.0995 mg/L), Nueces Bay (0.0843 mg/L), and Labonte Park (0.0766 mg/L). A smaller secondary rise was observed in June 2025, especially at Bock Park (0.0835 mg/L), Labonte Park (0.0760 mg/L), and Sugar Tree (0.0569 mg/L), before decreasing again in August 2025.

Lead concentrations remained very low during most sampling months, with one notable spike at Ennis Joslin in February (0.02179 mg/L) (Figure 2.17c). Additional moderate increases were observed in June 2025 at Nueces Bay (0.00861 mg/L) and Ennis Joslin (0.00493 mg/L), and in August 2025 at Ennis Joslin (0.00451 mg/L) and Nueces Bay (0.00317 mg/L). Mercury in suspended solids showed pronounced month-to-month variability, with sharply elevated concentrations in April 2025 – most prominently at Bock Park (3.62 mg/L) – and strong November (2025) peaks at Labonte Park (2.60 mg/L) and the Nueces Bay Fishing Site (1.56 mg/L) (Figure 2.17d). Other months (September 2024, February, and June 2025) remained uniformly low across sites, while August 2025 showed moderate increases at all locations. Selenium remained consistently low across all sites and months (0.0025 – 0.008 mg/L) (Figure 2.17e). Labonte Park displayed the greatest variability and occasional small peaks, whereas the other sites exhibited minimal fluctuation and uniformly low concentrations. Iron associated with suspended solids exhibited a clear seasonal variation. The highest levels occurred at the Nueces Bay site, reaching 7.39 mg/L in June 2025 and 5.15 mg/L in February 2025. Ennis Joslin, Sugar Tree, and Labonte Park showed moderate peaks (3 – 4 mg/L) in February 2025, while Bock Park remained low (~0.4 – 1.5 mg/L) with only slight increases during February 2025.

The fraction (%) of dissolved-phase metal varied substantially across sites and sampling months (Figure 2.18). Arsenic, copper, lead, and mercury generally exhibited high dissolved fractions at most locations, while selenium and iron showed lower dissolved proportions and high SS percentages with noticeable site-dependent differences. Meanwhile, Labonte Park and Nueces Bay Fishing Site displayed the greatest temporal variability.

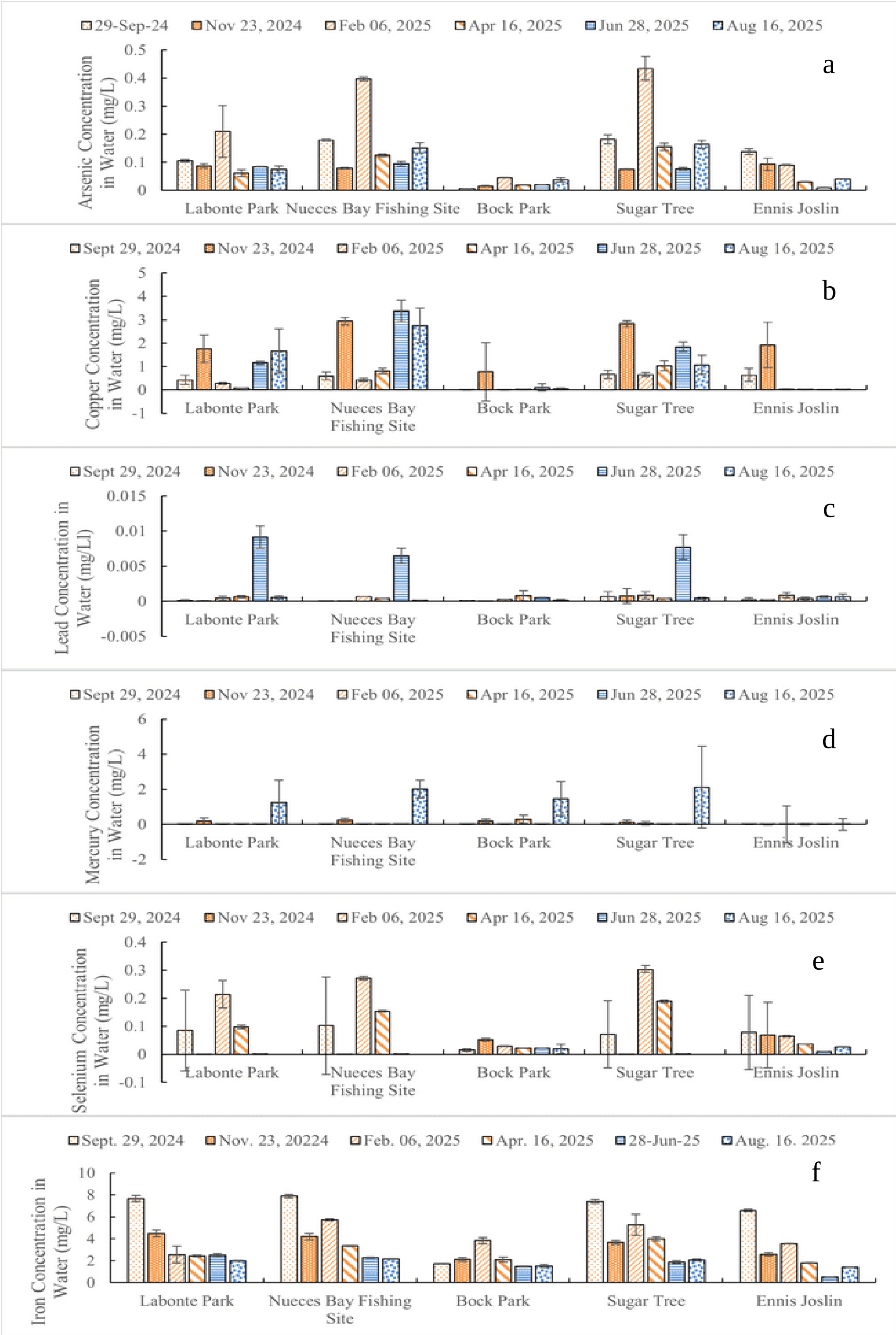

Figure 2.16. Comparison of dissolved heavy metals in water samples collected at study sites: (a) Arsenic, (b) Copper, (c) Lead, (d) Mercury, (e) Selenium, and (f) Iron. Error bars are standard deviations for three measurements.

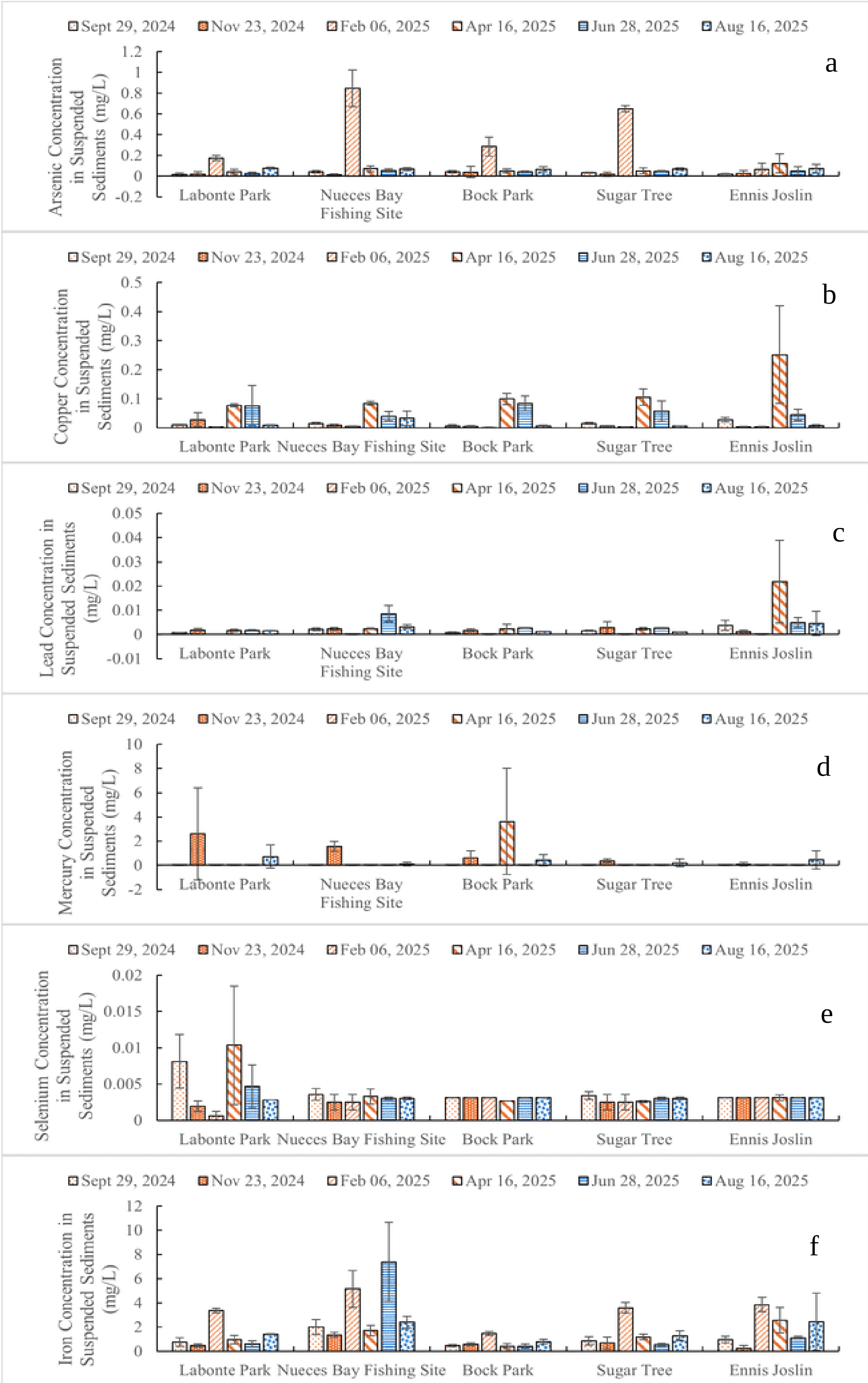

Figure 2.17. Comparison of heavy metals associated with suspended sediment at study sites. (a) Arsenic, (b) Copper, (c) Lead, (d) Mercury, (e) Selenium, and (f) Iron. Error bars are standard deviations for three measurements.

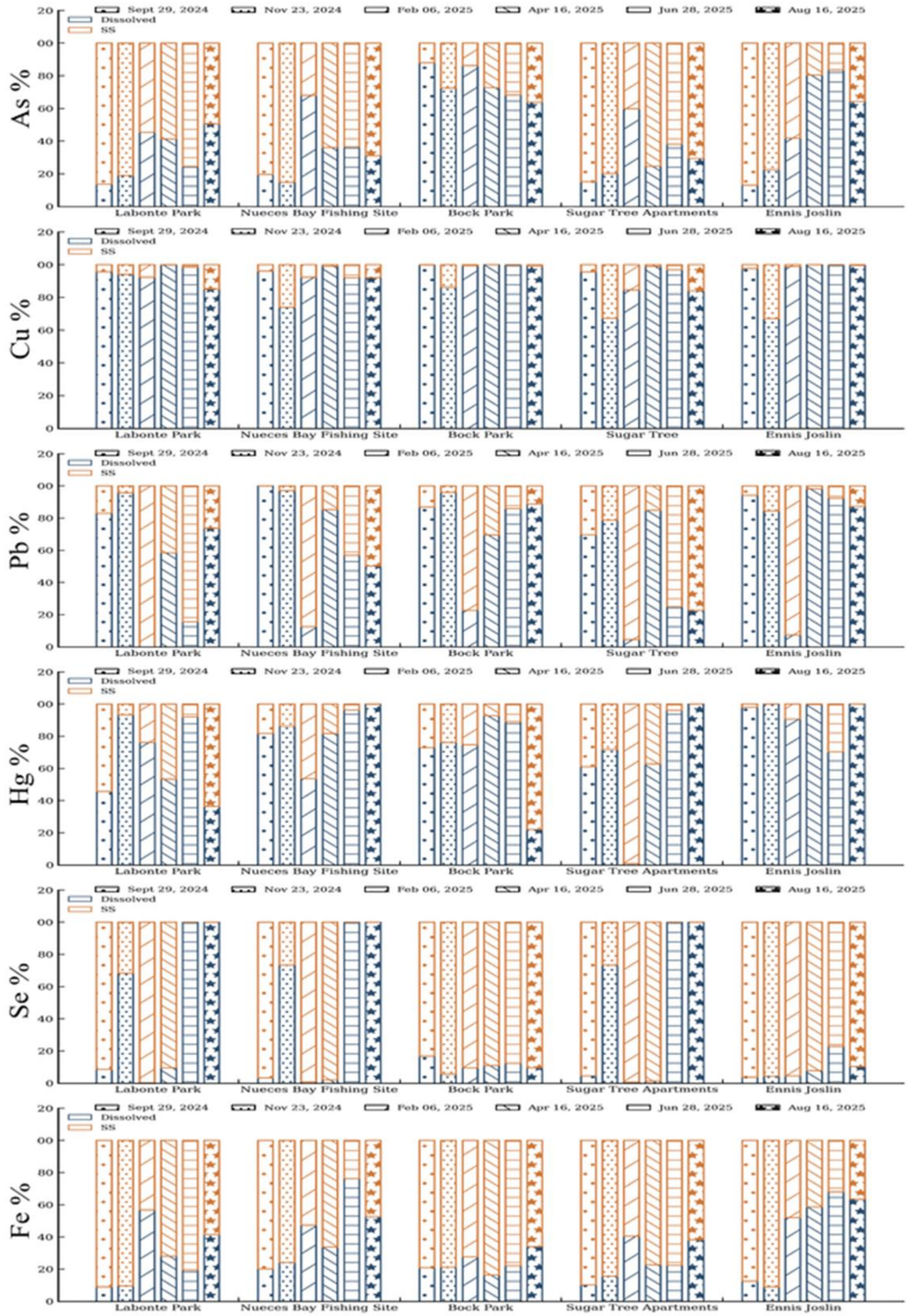

Figure 2.18. Metal % in dissolved and particulate (associated with SS) phases.

Figure 2.19a shows that arsenic levels peaked at all sites in February, with the highest concentration observed at the Nueces Bay site (130.9 mg/kg). Cadmium levels in sediment stayed low across all sites and dates, with only one major spike at Bock Park in September 2024 (Figure 2.19b). Most of the other measurements were below 1 mg/kg with small standard deviations, indicating stable and consistently low contamination over time. Chromium concentrations were highest at Sugar Tree in April 2025 (28.7 mg/kg) and February 2025 (25.6 mg/kg), while other sites showed moderate levels (Figure 2.19c). Copper concentration peaked in April 2025 at Sugar Tree (22.3 mg/kg) and Nueces Bay (19.9 mg/kg) (Figure 2.19d). Bock Park showed the highest copper concentration level in September 2024 (43.9 mg/kg) across all sites and sampling dates, and a sharp drop from September 2024 to February 2025, while other sites showed moderate seasonal variations. Mercury concentrations in sediment surged sharply in June 2025, with extreme values at Labonte Park (653.9 mg/kg), Bock Park (602.4 mg/kg), and Ennis Joslin (374.9 mg/kg), marking clear outliers relative to other months (Figure 2.19e).

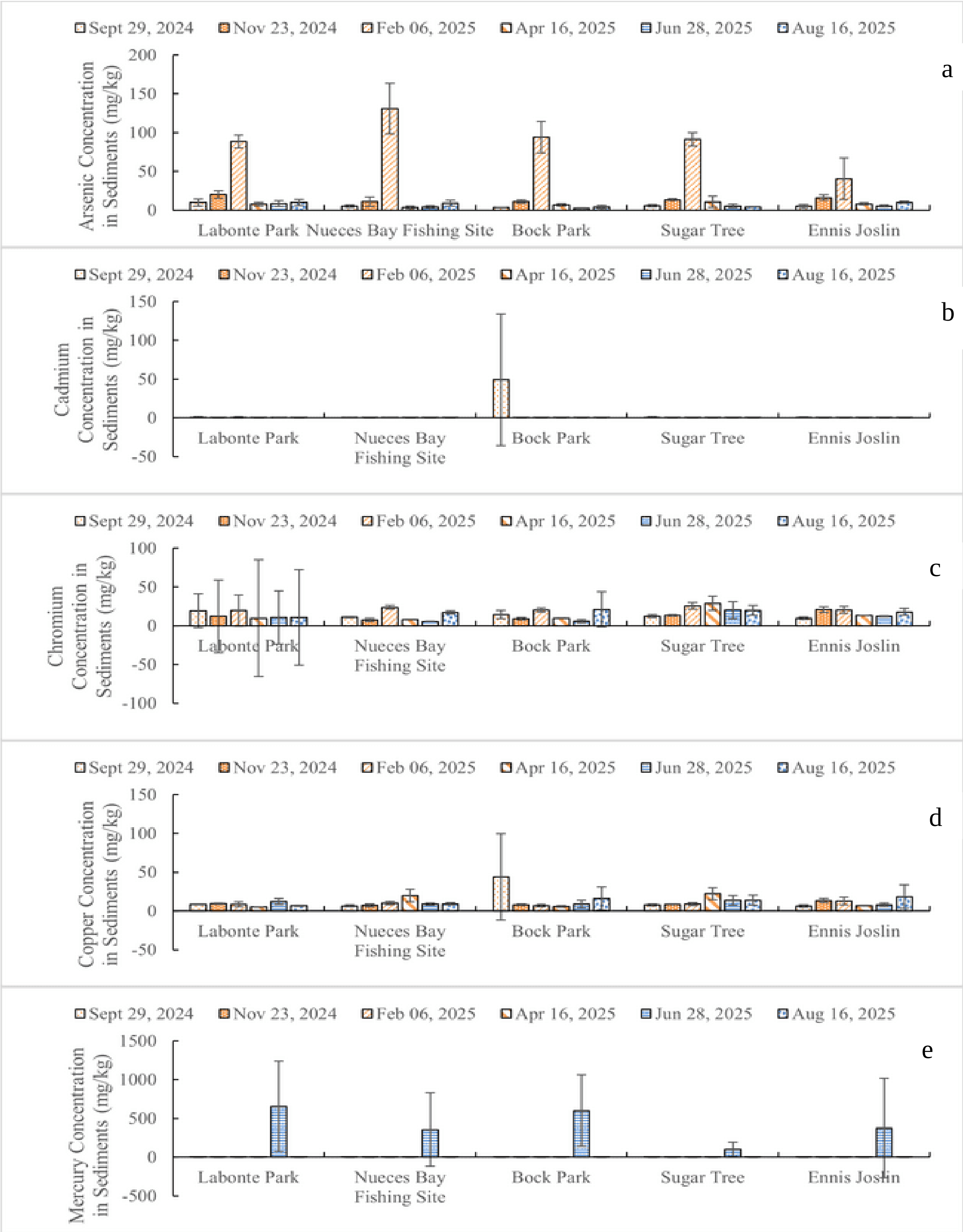

Figure 2.19. Comparison of bed sediment heavy metal concentrations at study sites: (a) Arsenic, (b) Chromium, (c) Copper, (d) Mercury, and (e) Cadmium. Error bars are standard deviations for three measurements.

2.4.7 Sediment, Nutrient, and Metal Loading

Figure 2.20 shows that sediment loading at the Nueces Bay site peaked at 252,468 kg/day in April 2025, while Labonte Park also showed seasonal surges above 8,000 kg/day in April and June 2025 and August 2025. For nutrients, ammonium loading also peaked at the Nueces Bay site, reaching 7,650 kg/day in April 2025 and at Labonte Park, the ammonium loading gradually increased to over 400 kg/day in August 2025 (Figure 2.21a). For nitrate and phosphate loadings (Figures 2.21b and 2.21c), Nueces Bay and Labonte Park sites exhibited high loading values in November 2024, with noticeable spikes in August 2025 at Ennis Joslin for phosphate and in June 2025 at Sugar Tree for nitrate. In Figure 2.22, metal loading for copper, selenium, mercury, lead, arsenic, and iron remained low, with occasional elevations, particularly copper in Nueces Bay in November 2024 and February 2025 (~0.65 kg/day), selenium in Nueces Bay in April 2025 (0.12 kg/day), mercury at Labonte Park in August 2025 (0.0759 kg/day), lead in Labonte Park in June 2025 (0.00056 kg/day), arsenic at Nueces Bay in April 2025 (0.0173 kg/day), and iron at Nueces Bay in April 2025 (2.72 kg/day).

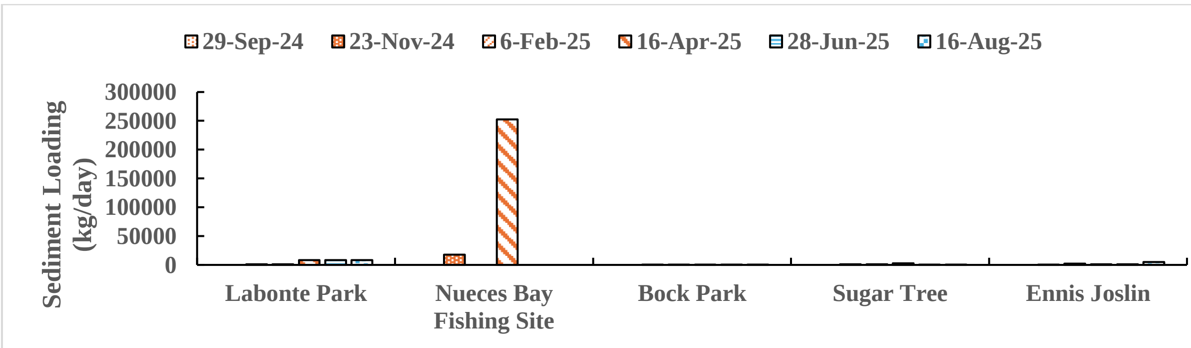

Figure 2.20. Estimated sediment loading at study sites.

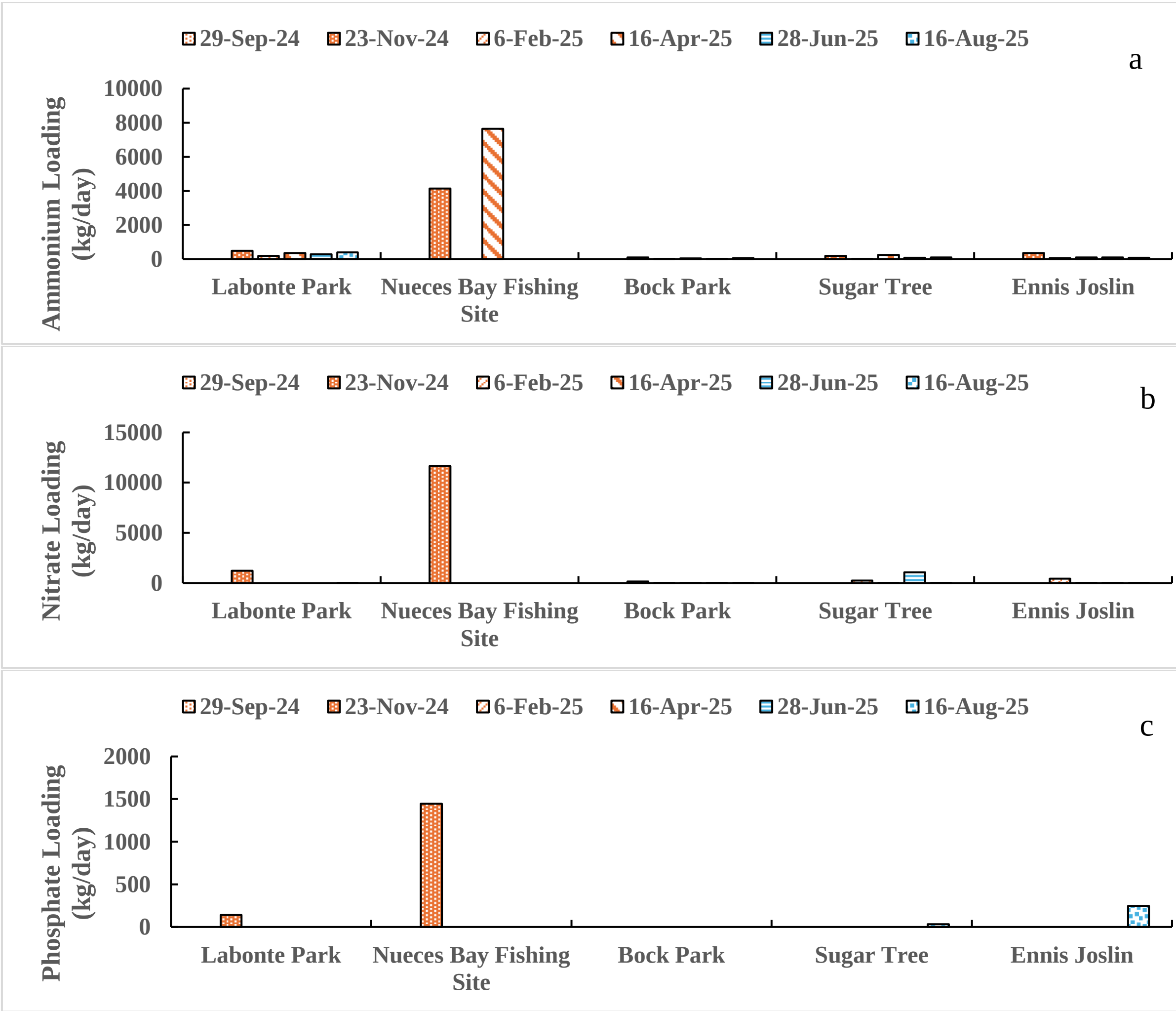

Figure 2.21. Estimated nutrient loading at study sites: (a) Ammonium, (b) Nitrate, and (c) Phosphate.

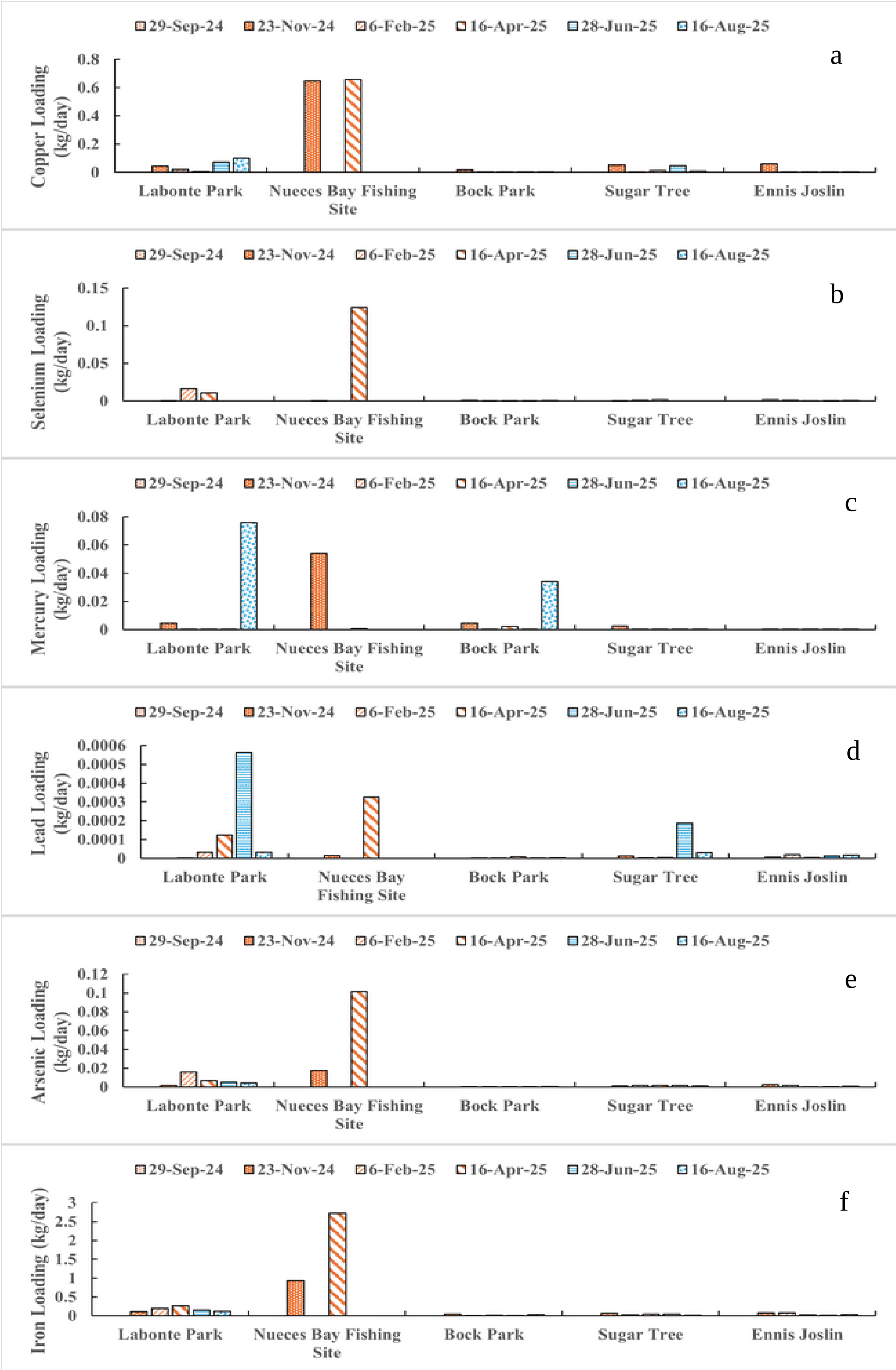

Figure 2.22. Estimated metal loading at study sites: (a) Copper, (b) Selenium, (c) Mercury, (d) Lead, (e) Arsenic, and (f) Iron.

2.4.8 Statistical Data Analysis

To assess spatial and temporal variations in water quality and sediment characteristics, Analysis of Variance (ANOVA) was conducted to compare pollutant concentrations across various locations and sampling periods (Darji & Lodha, 2025). Principal Component Analysis (PCA) was conducted to identify dominant environmental patterns and to reveal how water quality parameters, sediments, nutrients, and metals correlate across sites. Cluster analyses of water and sediment metal concentrations were carried out across sampling sites and months to identify groupings (Maitra et al., 2022). Such groupings are important for tracing pollution sources, understanding seasonal trends, and guiding targeted monitoring and remediation efforts.

For sediment parameters, the ANOVA test was conducted only for D_{60} and organic carbon content because only these two parameters passed the normality and equal variance criteria required for a valid comparison. Results (Table 2.2) showed that no significant difference among the sampling dates was found for these two parameters, and D_{60} and organic carbon content were statistically uniform across sampling months. Among nutrients, only dissolved ammonium passed the normality and equal variance tests, and a significant temporal difference was found for dissolved ammonium in water. For metals that passed both the normality and equal variance tests, dissolved iron in water, chromium, and nickel associated with bed sediments, and iron associated with suspended sediments exhibited significant variations among sampling dates. Among all sediment, nutrient, and metal parameters analyzed using ANOVA across the sampling sites, ammonium in water was the only variable that showed a statistically significant difference among locations (Table 2.3).

Table 2.2. ANOVA test results of nutrients and heavy metals of water and sediment samples across the study period.

Difference among sampling months	**Datasets analyzed based on results of normality and equal variance tests**	**F-Value**	**F-crit Value**
Sediment Parameters			
D_{60}	Sept 24, Apr 25, June 25	1.12	3.89
Organic Carbon Content	Sept 24, Nov 24, Feb 25, Apr 25, June 25, Aug 25	1.59	2.62
Nutrients			
Dissolved Ammonium in Water	Sept 24, Nov 24, Feb 25, Apr 25, June 25, Aug 27	**2.85**	2.62
Metals			
Dissolved Fe in Water	Nov 24, Feb 25, Apr 25, June 25, Aug 25	**6.38**	2.87
Dissolved Ni in Water	Nov 24, Feb 25, Apr 25, June 25, Aug 26	2.5	2.87
Dissolved Se in Water	Sept 24, Feb 25, Apr 25	2.12	3.89
Cr associated with Bed Sediment	Sept 24, Nov 24, Feb 25, Apr 25, June 25, Aug 25	**5.08**	2.87
Ni associated with Bed Sediment	Sept 24, Nov 24, Feb 25, June 25, Aug 28	**4.05**	2.87
Fe Associated with Suspended Sediment	Sept 24, Nov 24, Feb 25, Apr 25, Aug 25	**8.71**	2.87

Note: Bold F-values indicate statistically significant differences among sampling months (F > F-crit) based on one-way ANOVA results.

Table 2.3. ANOVA test results of nutrient and heavy metals of water and sediment samples across the sampling sites.

Difference among sampling sites	Datasets analyzed based on results of normality & equal variance tests	F-Value	F-crit Value
Sediment Parameters			
D_{10}	Ennis Joslin, Labonte Park, Nueces Bay Fishing Site, Sugar Tree	0.88	3.1
D_{30}	Bock Park, Nueces Bay Fishing Site, Sugar Tree	1.25	3.68
D_{60}	Ennis Joslin, Labonte Park, Nueces Bay Fishing Site, Sugar Tree	0.47	3.1
Organic Carbon Content	Ennis Joslin, Labonte Park, Nueces Bay Fishing Site, Sugar Tree	0.58	3.1
Nutrients			
Nitrate associated with Bed Sediment	Nueces Bay Fishing Site, Sugar Tree Apartments	0.22	4.96
Total Phosphorus associated with Bed Sediment	Bock Park, Ennis Joslin, Labonte Park, Nueces Bay Fishing Site, Sugar Tree	0.46	2.76
Dissolved Ammonium in Water	Bock Park, Ennis Joslin, Nueces Bay Fishing Site, Sugar Tree	**3.8**	**3.1**
Metals			
Dissolved Al in Water	Nueces Bay Fishing Site, Sugar Tree	1.15	4.96
Dissolved Cu in Water	Labonte Park, Nueces Bay Fishing Site, Sugar Tree	0.78	3.68
Dissolved Fe in Water	Ennis Joslin, Nueces Bay Fishing Site, Sugar Tree	0.89	3.68
Dissolved Zn in Water	Bock Park, Ennis Joslin, Labonte Park	1.86	3.68
Dissolved Pb in Water	Bock Park, Ennis Joslin, Sugar Tree	2.55	3.68
Cr associated with Bed Sediment	Bock Park, Ennis Joslin, Nueces Bay Fishing Site, Sugar Tree	1.88	3.1
Ni associated with Bed Sediment	Nueces Bay Fishing Site, Sugar Tree	3.06	4.96
Al associated with Bed Sediment	Bock Park, Ennis Joslin, Labonte Park, Nueces Bay Fishing Site, Sugar Tree	1.94	2.76
Fe associated with Bed Sediment	Bock Park, Ennis Joslin, Nueces Bay Fishing Site, Sugar Tree	1.02	3.1
Cu associated with Bed Sediment	Ennis Joslin, Labonte Park, Sugar Tree	1.28	3.68
Fe associated with Suspended Sediment	Ennis Joslin, Nueces Bay Fishing Site	1.72	4.96

Note: Bold F-values indicate statistically significant differences among sampling months (F > F-crit) based on one-way ANOVA results.

PCA results of conventional water quality and sediment parameters highlight key factors driving site variability (Figure 2.23). At Labonte Park, PC1 (44.3%) is defined by strong positive loadings of rainfall variables (P_3, P_4, P_7, and P_8), which represent precipitation that occurred 3, 4, 7, and 8 days before the sampling date, as well as fine sediment fractions (D_{10} and D_{30}) and Organic Carbon (OC). In contrast, discharge and DO load on the positive PC2 axis. The SSC and Q_s load high on positive PC2, while salinity and pH lie near the origin. At Nueces Bay, PC1 (49.6%) is strongly controlled by sediment and organic matter processes, with D_{10}, D_{30}, D_{60}, SSC, and OC all clustering on the far positive PC1 side. Q_s also loads positively on PC1 and strongly on PC2.

At Bock Park, PC1 (37.2%) is driven by sediment structure and antecedent rainfall, with D_{60}, loading strongly on the positive side, where rainfall lags (P_3, P_4, P_5), defined as the days of precipitation occurring before the sampling date, also exhibit strong positive loadings, indicating that multi-day antecedent rainfall enhances the transport and deposition of coarser sediment fractions at this site. P_0 and P_1, zero and one day after precipitation and before sampling, align closely with D_{10} in the upper-right quadrant along PC2. At Sugar Tree, D_{10}, D_{30}, and salinity are all positioned in the upper-central region. Precipitation variables (P_2, P_6, P_7, P_8, and P_3) cluster strongly with discharge on the positive PC1 side. At Ennis Joslin, PC1 (34.4%) is primarily defined by sediment texture, with D_{10}**,** D_{30}**,** and D_{60} loading strongly on the positive PC1 side. Immediate rainfall (P_0), SSC, and Q_s load strongly on the positive PC2 axis.

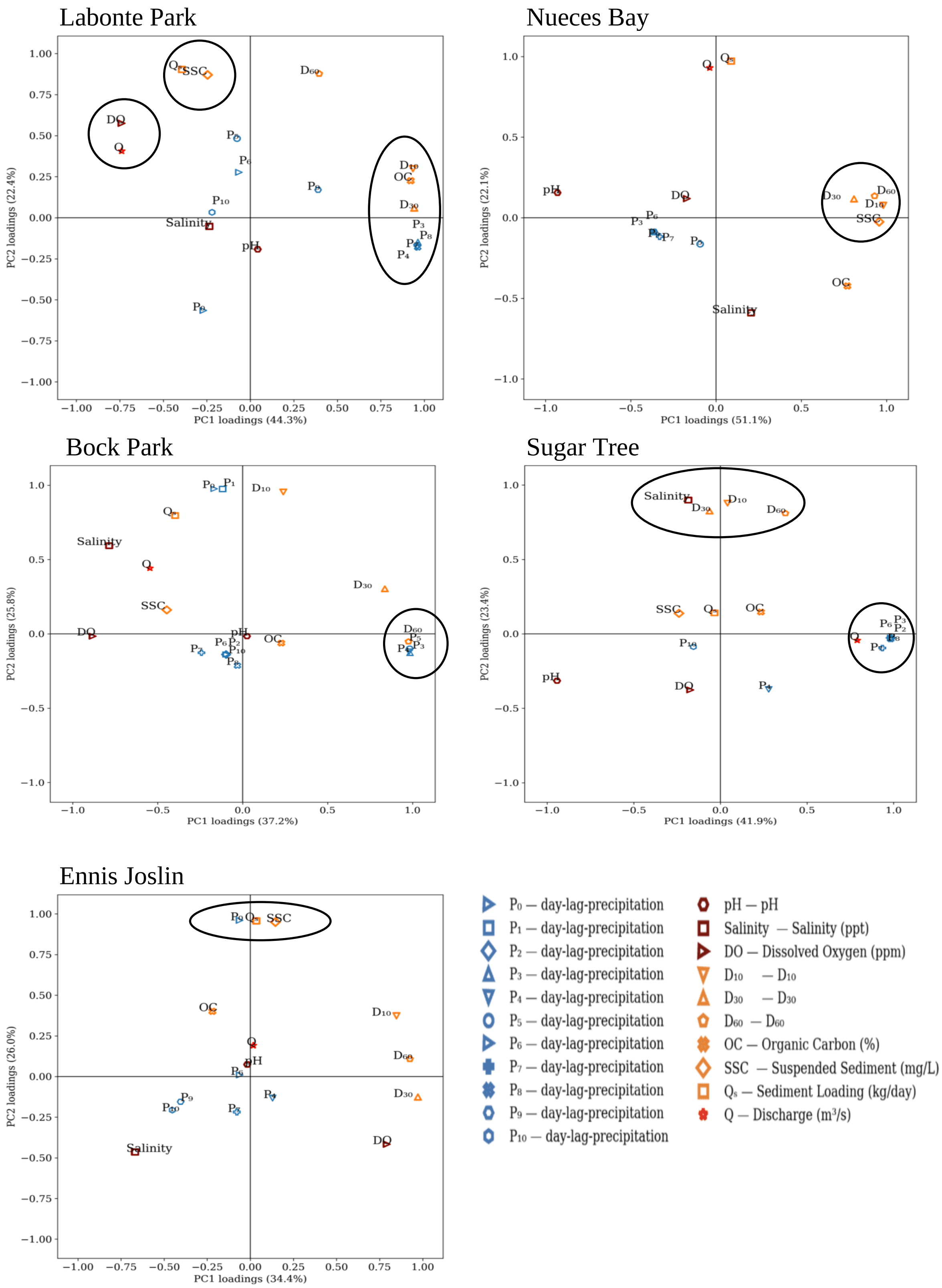

Figure 2.23. Principal Component Analysis (PCA) of water quality parameters and sediment characteristics across all sampling sites.

PCA of water parameters, nutrients and sediments highlights key factors driving site variability (Figure 2.24). At Labonte Park, the PCA shows clear groupings among variables. Water-column nutrients NO_3^-(W) and NH_4^+(W) cluster tightly together on the highly positive PC2. These nutrient concentrations are closely aligned with nitrate loadings (Q_n) and phosphate loadings (Q_p). Fine sediment fractions (D_{10} and D_{30}) and OC also form a cluster on the positive PC1 side, along with several rainfall variables (P_3, P_7, P_8, and P_4). In Nueces Bay, water-column nutrients NO_3^-(W)**,** PO_4^{3-}(W) form a tight cluster in the upper-right quadrant together with nitrate loading (Q_n), phosphate loading (Q_p), and ammonium loading (Q_a). These are positioned opposite sediment particles D_{10}, D_{30}, and D_{60}, which cluster on the far negative PC1 side together with SSC and Organic OC. pH stands separately on the far positive PC1 side, opposite the sediment cluster. At Bock Park, water-column nutrient NO_3^-(W) and its associated loading Q_n, Q_a, and discharge cluster tightly in the upper-right quadrant. Coarse sediment fractions, D_{30} and D_{60}, sit on the far positive PC1 side, together with rainfall variables P_3, P_4, and P_5, and nitrate in sediments (NO_3^-(S)) and dissolved phosphate (PO_4^{3-}(W)) in water. In contrast, SSC lies strongly on the negative PC1 and negative PC2 side.

Salinity, Total phosphorus in bed sediments (TP(S)), and DO cluster on the left side of PC1, opposite the coarse sediment and nutrient group. At Sugar Tree, D_{10}, D_{30}, together with SSC, Q_s, and the sediment nutrient TP(S) all positioned in the upper-left to upper-central region. Water-column ammonium NH_4^+(W) also joins this group, linking ammonium availability to sediment-driven conditions. In contrast, rainfall variables P_2, P_3, P_6, P_7, and P_8 cluster tightly with nitrate loading (Q_n), and discharge on the far positive PC1 side. At Ennis Joslin, nutrient variables, NO_3^-(W)**,** NO_3^-(S), NH_4^+(W), and salinity cluster together on the negative PC1 axis. In contrast, SSC, Q_s, water-column phosphate PO_4^{3-}(W) and Phosphate Loading (Q_p) cluster in the upper-right region.

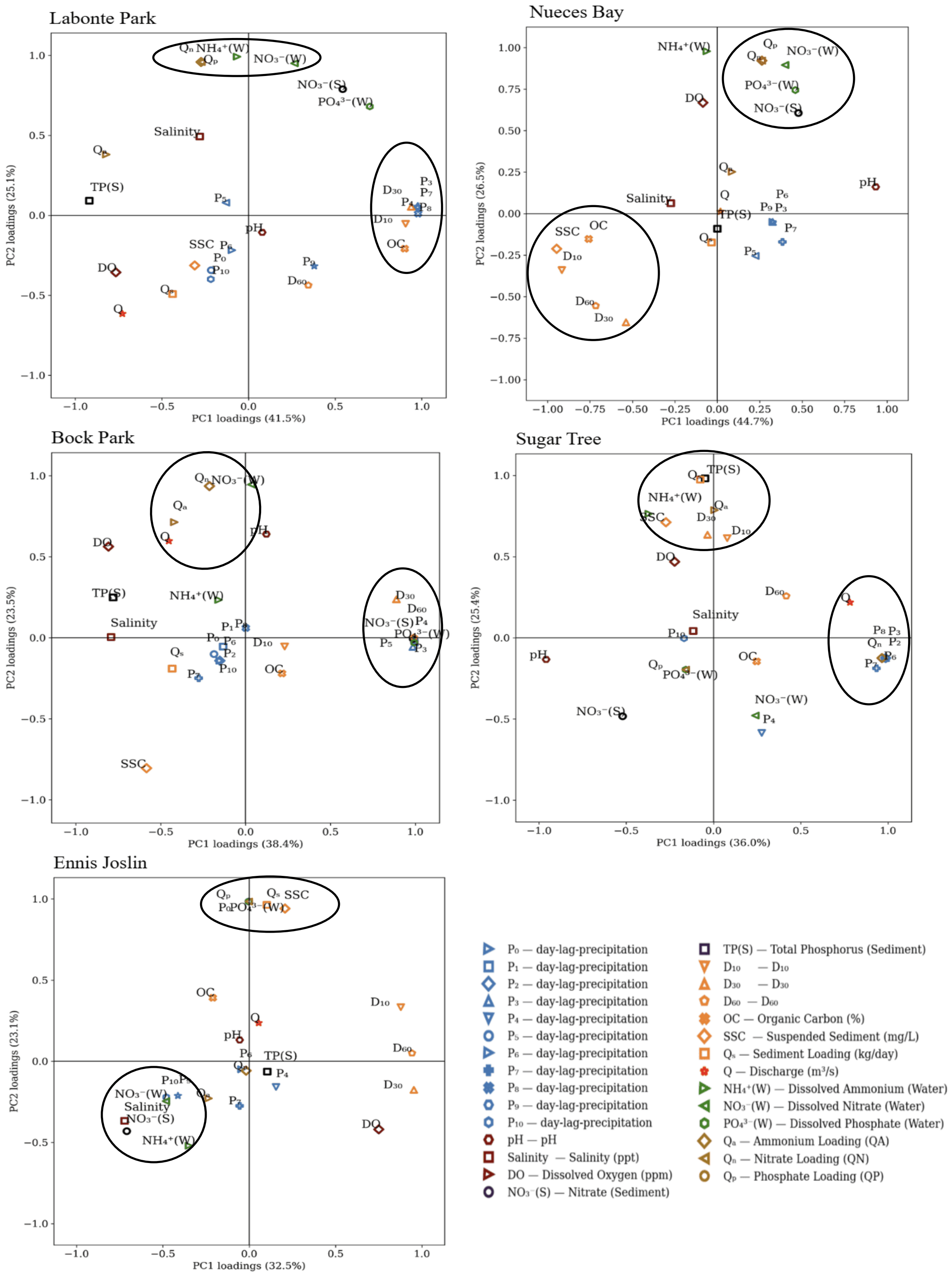

Figure 2.24. Principal Component Analysis (PCA) of water quality parameters, nutrients and sediment characteristics across all sampling sites.

Figure 2.25 shows three clear metal-behavior clusters at Labonte Park. Water-phase metals, As(W), As(S), As(SS), Se(W), Fe(SS), and P_0, cluster strongly in the positive PC2 region, indicating similar behavior. A second cluster appears on the right side, where OC, D_{30}, D_{10}, Fe (W), and rainfall variables (P_3, P_4, P_7, and P_8) group together, representing a rainfall–fine-sediment-metal–organic matter process. In contrast, Pb(SS) lies far on the negative PC2 side, separating strongly from all other metals. Cr(S) and Cd(S) form their own cluster on the far-right positive PC1 side. DO, and discharge sit in the far-left negative PC1 region, directly opposite the sediment/metal clusters. At the Nueces Bay site, the PCA separates metals into two dominant groups. Cr(S), Cd(S), and Arsenic and selenium across all phases, including As(W), As(S), As(SS), Se(W), cluster tightly in the strongly positive PC2, forming a strong dissolved–sediment–suspended metal group.

On the far positive PC1 side, sediment variables (D_{10}, D_{30}, and D_{60}), Fe(SS), Pb (W), Hg (S), and OC linked the group together, forming a metal-sediment–organic matter cluster. Finally, pH stands isolated on the far negative PC1 side, directly opposite the sediment-metal group. At Bock Park, the PCA reveals three major metal clusters. As(W), As(S), As(SS), Fe(W), and Fe(SS) form a tight group in the strongly positive PC2. A second cluster emerges along the strongly positive PC1 axis, characterized by elevated Se(W) and DO levels in association with salinity. While Pb(SS) is separated in the lower-right far quadrant. On the opposite side of the plot (negative PC1), P_3, P_4, P_5, Cd(S), Cu(S), D_{60}, D_{30}, and D_{10} cluster together, forming a sediment–rainfall-metal group. At Sugar Tree, the PCA shows a strong arsenic–iron–selenium cluster across all phases – As(W), As(S), As(SS), Fe(SS), Fe(W), OC, P_{10}, and Se(W) – grouped in the positive PC2. Rainfall variables (P_2 – P_8), Hg(S), and Pb(W) cluster in the far-right region, opposite to pH. At Ennis Joslin, SSC, Hg(SS), Hg(S), Q_s, and P_0 cluster tightly in the far positive PC2. On the other hand, D_{10}, D_{30}, D_{60}, Pb(SS), Cu(SS), DO, and Se(SS) form a group on the far positive PC1.

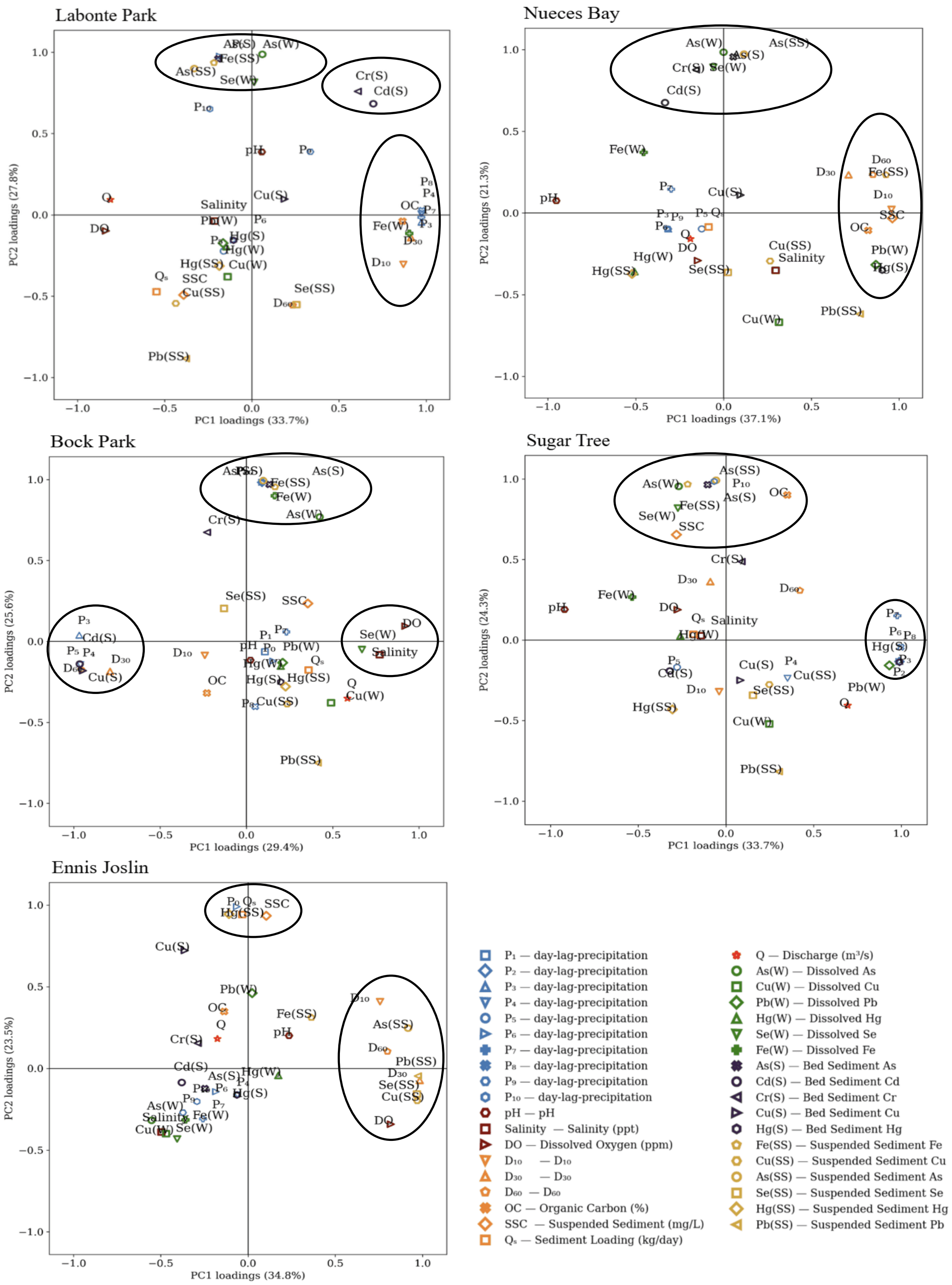

Figure 2.25. Principal Component Analysis (PCA) of water quality parameters, metals, and bed sediment characteristics across all sampling sites.

Across all sites and sample types, the metals of interest show a remarkably consistent pattern of association. In water (Figure 2.26), As, Cu, Pb, Hg, and Se all group with a large suite of trace metals—including Cd, Ni, Cr, V, Sb, and others, whereas Fe, and occasionally Cu or Pt, form a group. For suspended sediments (Figure 2.27), results show a similar pattern: As, Cu, Pb, Hg, and Se cluster with the broad trace-metal group, while Fe (and sometimes Sn or Hg) align with Al in a mineral-associated cluster. In sediments (Figure 2.28), As, Cd, Cr, Cu, and Hg always fall within the broad trace-metal cluster (Be–Hg), while Fe and Al remain isolated in their own lithogenic cluster.

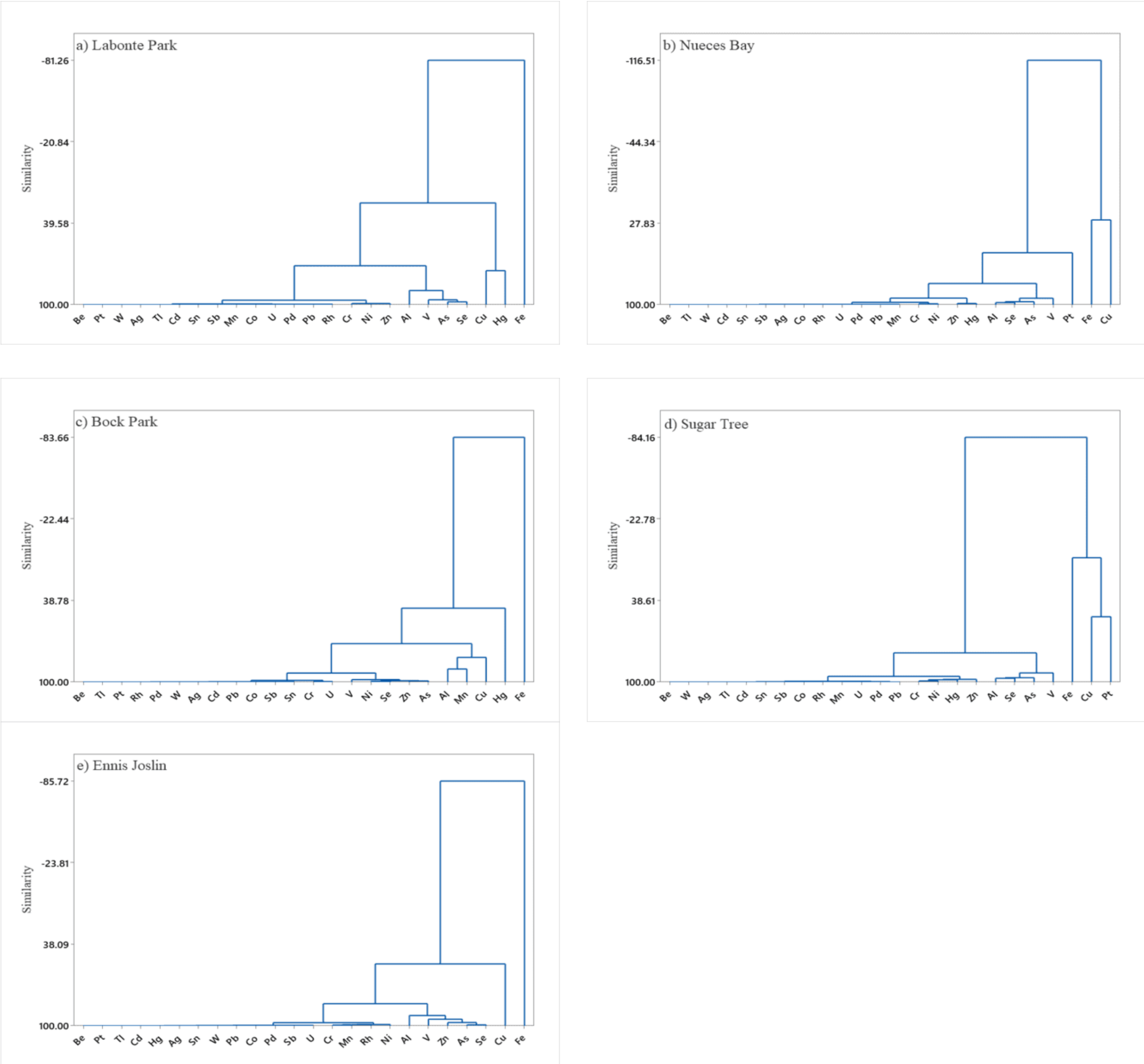

Figure 2.26. Cluster Analysis of Dissolved Metals of Sept 29, 2024, Nov 23, 2024, Feb 06, 2025, April 16, 2025, June 28, 2025, and August 16, 2025.

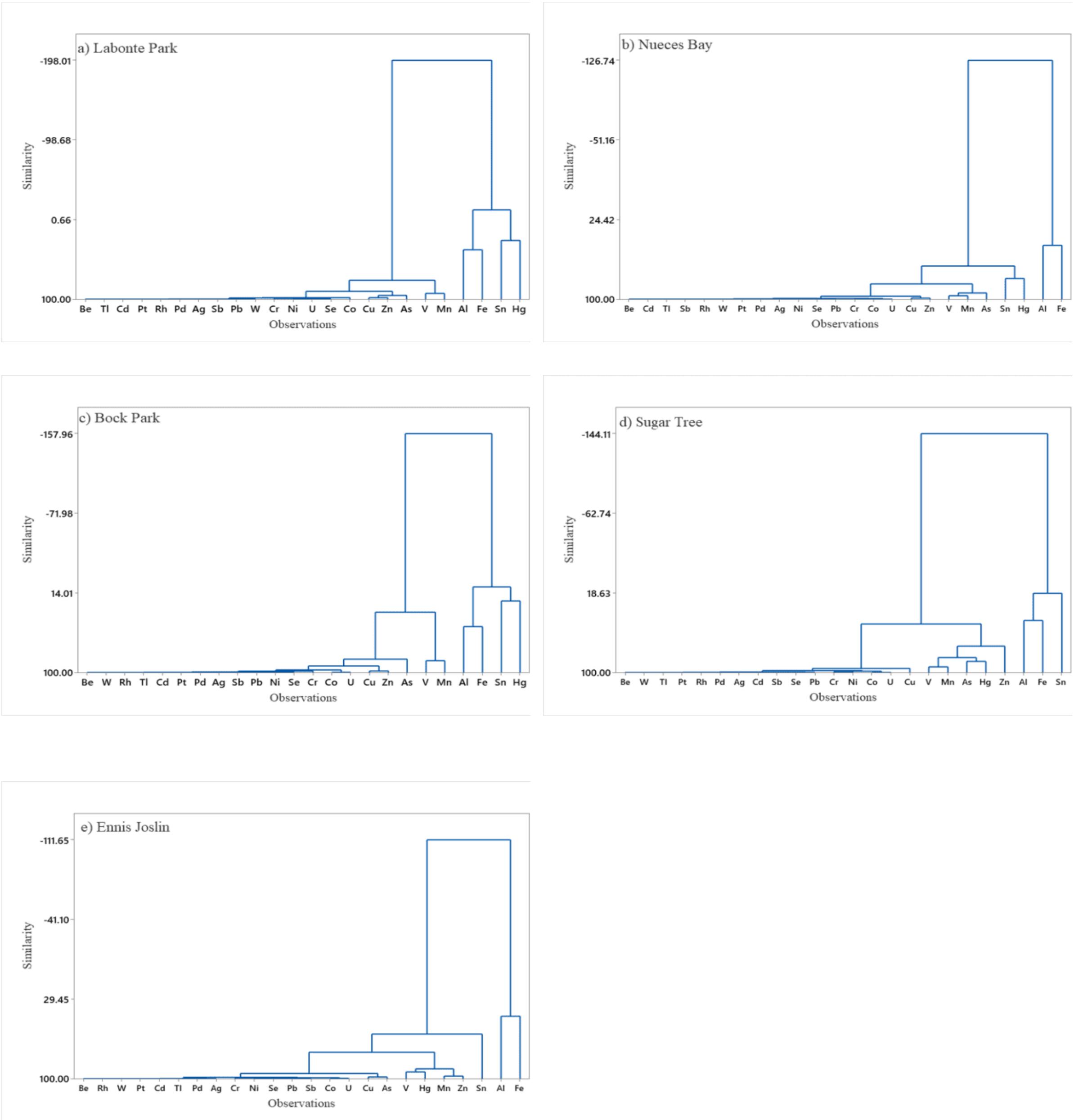

Figure 2.27. Cluster Analysis of metals associated with Suspended Sediment Samples of Sept 29, 2024, Nov 23, 2024, Feb 06, 2025, April 16, 2025, June 28, 2025, and August 16, 2025.

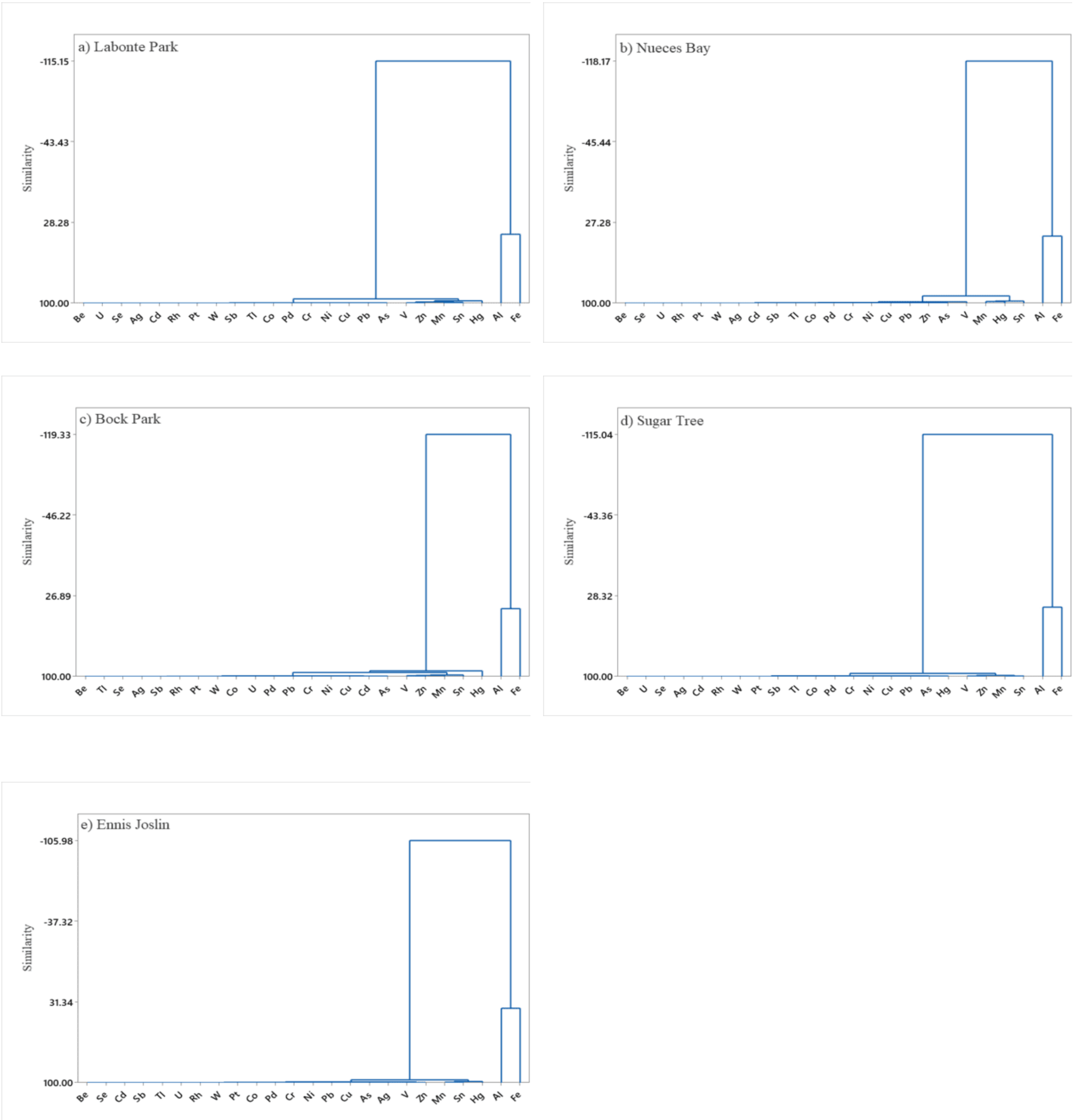

Figure 2.28. Cluster Analysis of metals associated with Bed Sediment Samples of Sept 29, 2024, Nov 23, 2024, Feb 06, 2025, April 16, 2025, June 28, 2025, and August 16, 2025.

Chapter 3. Spatiotemporal Distribution of Sediment Concentration and Turbidity

This study employed MODIS and Landsat data sets to leverage their complementary spatiotemporal characteristics, and they are publicly available and free. MODIS offers daily coverage, which can be useful for observing seasonality and changes in TSS patterns at high temporal resolution. Its large swath width (2,330 km) also allows it to cover extended areas in a single pass, with 36 bands with 250 m –1 km resolution, which is critical for capturing high-dynamic suspended sediment events that often occur between the 16-day Landsat overpasses (Sahoo et al., 2022; Miller & McKee, 2004). Landsat was chosen for this study due to its long history of data archiving, dating back to 1972. In addition, Landsat offers 30 m resolution with 12 bits per pixel, which is a reasonably high resolution for detecting changes in Total Suspended Solids (TSS).

Landsat imagery (30 m resolution) is essential for resolving fine-scale sediment plumes and navigating the complex geometries of the Nueces River and Bay system (Wang et al., 2017). Conversely, this dual-sensor approach has been successfully implemented in various TSS applications to balance the trade-offs between spatial detail and temporal monitoring (Brian & Chuanmin, 2016; Hu et al., 2004).

3.1 Study Area, Workflow, and Model Validation

Sediments on water surfaces exhibit a unique reflectance signature; for instance, turbid water reflects mostly in the red and near-infrared (NIR) bands, enabling remote sensing of sediment concentration in coastal environments. Therefore, the primary goal of this research was to estimate Total Suspended Solids (TSS) concentrations in the Corpus Christi Bay and Nueces Bay.

The comprehensive research framework, from data acquisition to model implementation, is shown in Figure 3.1. This flowchart illustrates the processing of Landsat 8 and MODIS satellite imagery alongside in-situ field data using Google Earth Engine. It further details the data fusion process that supports model selection and validation, ultimately leading to TSS predictions and spatial hotspot mapping.

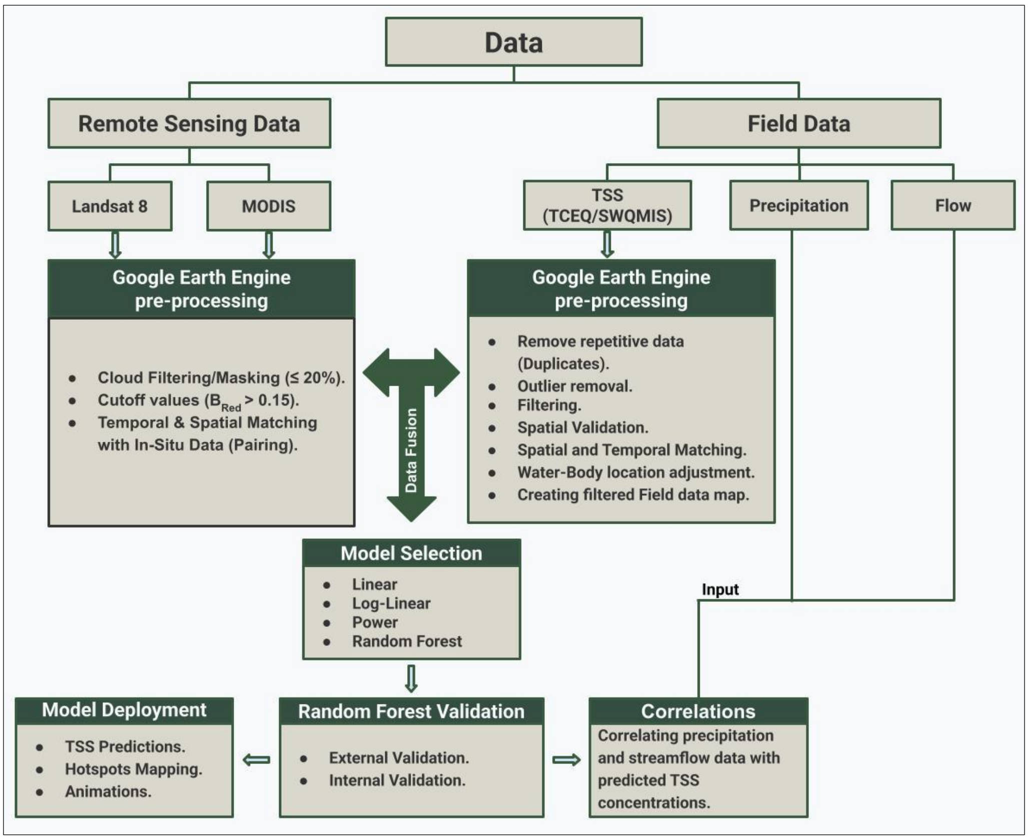

Figure 3.1. Methodological framework for TSS estimation and analysis.

3.2 Ground Truth Data and Pre-Processing

Field observations were obtained from the TCEQ Surface Water Quality Monitoring Information System (SWQMIS). Table 3.1 shows data availability for the selected SWQMIS monitoring stations, as obtained from the TCEQ database. The table reports the period of record for each station, providing an overview of the temporal coverage used in this study. This summary describes the extent of data considered and highlights that only a subset of the full available record was utilized for analysis.

Table 3.1. Data Availability and Period of Record for SWQMIS Monitoring Stations.

Waterbody	Parameter	Station Count	Recording Date		Span Years
			First	Last	
Nueces and Corpus Christi Bays	TSS	9	5/22/1969	12/16/2024	~56
Nueces River	TSS	13	2/9/1972	11/28/2023	~52

Figure 3.2 shows the spatial distribution of the monitoring stations in the study area. The initial dataset included many repetitive point locations. To identify unique monitoring sites, all coordinates were uploaded to Google Earth Engine (GEE) for filtering and spatial validation.

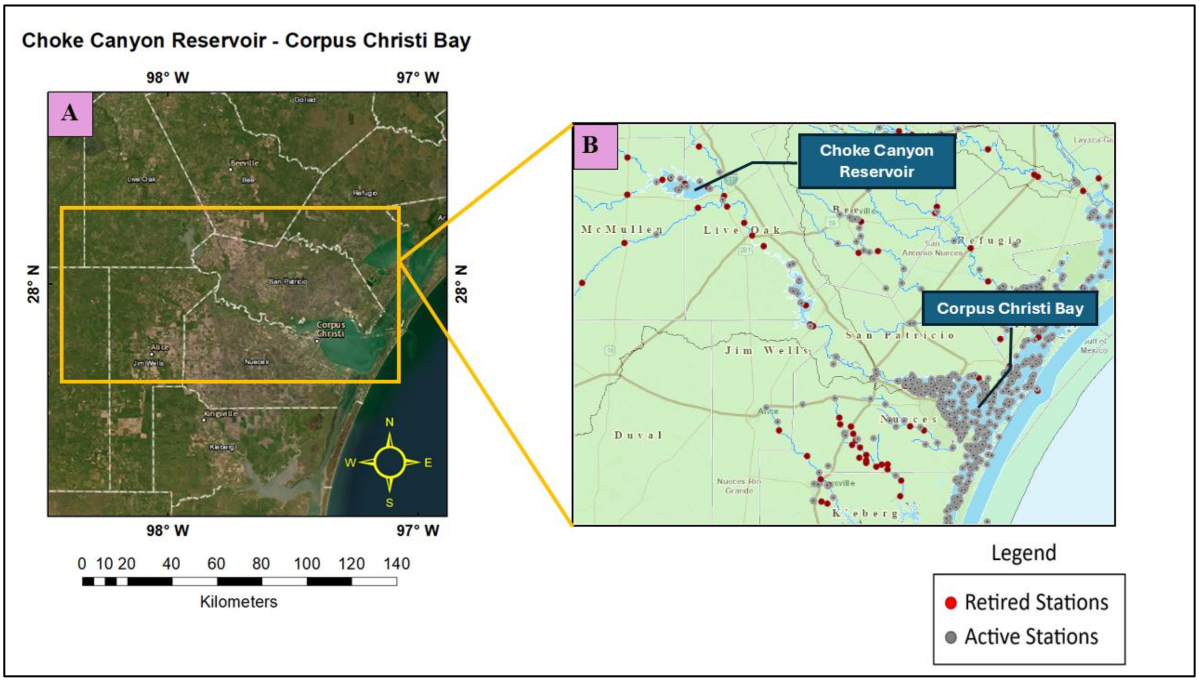

Figure 3.2. Map of the study area: (a) a sample satellite (realistic) image of the study area, and (b) a detailed map illustrating the geographic locations of water monitoring stations, sourced directly from the TCEQ SWQMIS website, including active and retired stations.

To support sediment model development, several automated processes were implemented for data integration, quality control, spatial accuracy, and interactive visualization, as follows:

1) Ground truth data consolidation: Field observation files from SWQMIS were aggregated into a single unified dataset for the Bays and Nueces River locations. Duplicate records, both by file source and content, were removed. This ensured a clean and consistent dataset for further filtering, standardization, and integration with remote sensing data.

2) Parameter identification matching: The ground truth dataset included measurement variables with both descriptive names and associated numerical codes. A lookup process was conducted to pair each parameter name with its corresponding code, creating a list of distinct variables for subsequent modeling and analysis. The spatial accuracy of the field locations was evaluated by calculating the precise surface distance between any two geographic points using an ellipsoidal earth model (WGS84). This calculation was performed using Vincenty's inverse formula, which accounts for the Earth's oblateness to provide high-precision geodetic distances (Vincenty, 1975). This method provided high-precision estimates in meters, enabling accurate filtering and validation of monitoring points.

3) Mapping of ground truth points: Figure 3.3 shows an interactive digital map to visualize the spatial distribution of water quality sampling points across the river and bay system. Each point was color-coded by category (bay or river) and displayed with user-friendly markers and tooltips. The map allowed for dynamic exploration of the field dataset and helped ensure accurate placement of points on water bodies.

4) Mapping the satellite pixels to represent water bodies: Following the initial visual overlay of coordinates on a simple map to confirm general proximity to waterways, the next step was to precisely adjust each point to the nearest open-water pixel using high-resolution imagery to ensure accurate satellite measurement of the water surface. Subsequently, each point was manually inspected on Google's high-resolution satellite basemap, and those falling on land/bridges were assigned to the nearest open-water pixel. This manual

adjustment ensured that all extracted spectral samples accurately represented water-surface reflectance.

5) Google Earth Engine (GEE) was utilized to automate the extraction of satellite reflectance data. First, the validated ground truth coordinates were converted into GEE feature sets. Subsequently, two parallel workflows were developed to process Landsat 8 and MODIS (MOD09GA) surface reflectance products. This process resulted in a consolidated dataset of spatially and temporally matched spectral samples, which were exported for subsequent model development.

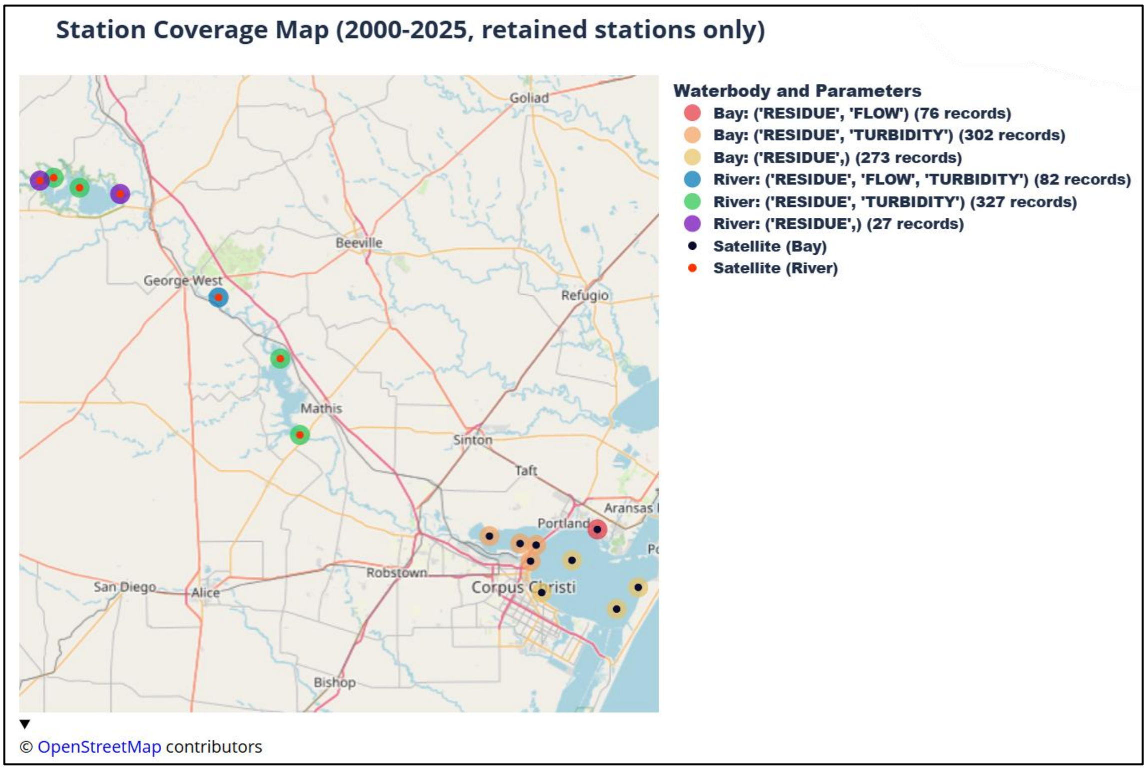

Figure 3.3. Locations of the in-situ monitoring stations selected after data quality checking in the Nueces River and Coastal Bays. Satellite data were obtained for these observed locations to develop suspended-solids models.

This process filtered Landsat 8 Collection 2 Level-2 surface reflectance data by date and spatial extent. These data were pre-processed by the U.S. Geological Survey (USGS, 2021). A standard scale-and-offset transformation was applied to the pixel values, multiplying by 0.0000275 and adding -0.2, to convert the digital numbers to unitless surface reflectance values, as defined in the Landsat 8-9 Calibration and Validation specifications (USGS, 2022). This calibration step is a standard requirement for converting raw digital numbers into scientific reflectance values and has been widely implemented in similar water quality studies using Google Earth Engine (Gorelick et al., 2017; Page et al., 2019).

The images were then sampled at the defined coordinates, paired with metadata, and exported for analysis. The MODIS Workflow followed a similar structure but incorporated additional quality control. It included a highly configurable bitwise quality assurance (QA) -masking function to filter for QA flags, applied optional atmospheric corrections, scaled reflectance by 0.0001, and sampled at 500 m resolution.

Google Earth Engine scripting was used to convert the geographic coordinates from Table 3.2 into feature collections, specialized data structures for managing and processing groups of geographic data points. By grouping these individual sampling features into a unified collection and applying coding, we were able to run concurrent extraction routines simultaneously that analyzed all sampling locations to extract spectral data from Landsat 8 and MODIS MOD09GA surface reflectance products. This process facilitated the spatial and temporal mapping of the satellite and the ground observations together.

As detailed later in Tables 3.15 (MODIS Matchups) and 3.16 (Landsat Matchups), these consolidated datasets were filtered and prepared for modeling by combining compiled satellite band data with field measurements collected during the June 2023 sampling trips conducted by the University of Texas Marine Science Institute (UTMSI). To ensure the integrity of these matchups, strict synchronization logic was applied: the satellite reflectance values were manually adjusted to the nearest open-water pixel and paired with ground samples within a one-day window for MODIS or a ±7-day window for Landsat.

To ensure data integrity, two key terms are important for understanding the output: Surface Reflectance is the measure of light reflected from the Earth's surface, corrected for atmospheric interference (such as haze or clouds). Meanwhile, QA Flags (Quality Assurance Flags) are numerical codes included with satellite data that indicate whether a pixel is of good quality (e.g., clear view) or poor quality (e.g., cloud-covered or a bad sensor reading).

Figure 3.4 illustrates the data used to develop the sediment estimation model and details the sources used to verify the model's accuracy. This framework specifically integrates independent field samples from the University of Texas Marine Science Institute (UTMSI) and 10 % of the historical records from the TCEQ Surface Water Quality Monitoring Information System (SWQMIS).

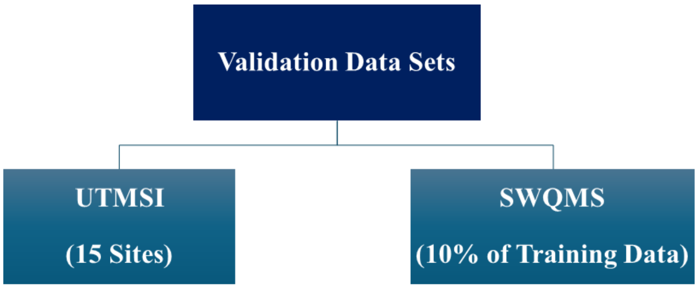

Figure 3.4. The datasets used for the model's validation.

The following steps show how each data set was acquired:

1) Marine Science Institute, University of Texas at Austin (UTMSI)

The data collected by Dr. Mark Alexander Lever, Marine Science Institute, University of Texas at Austin (UTMSI) in June 2023 (June 19, 21, and 22) during 3 sampling trips were used for model validation. It consists of 15 data points spanning Nueces Bay and Corpus Christi Bay. Figure 3.5 illustrates the location, parameter values, and other information.

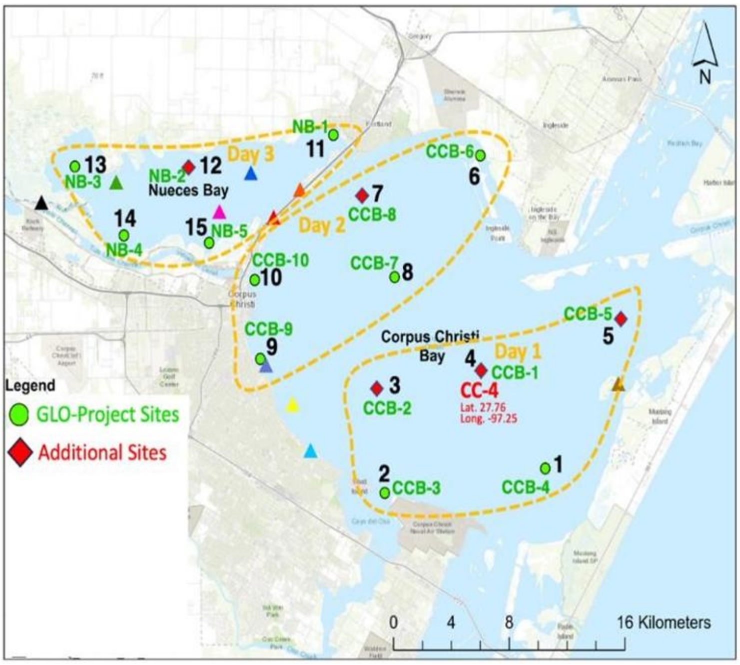

Figure 3.5. Map showing the Corpus Christi Bay and the Nueces Bay, where a total of fifteen sampling points were collected for TSS in June 2023 (UTMSI).

Following the geographical overview provided in Figure 3.5, Table 3.2 details the essential "ground truth" for each water sample. The latitude and longitude coordinates were vital, providing the exact geographic location needed to extract corresponding satellite pixel data from the Landsat and MODIS images. The sampling date and sampling day define the crucial temporal match. Finally, the Water depth (m) and Water column position provided a hydrographic context, and the TSS (mg/L seawater) column provided the core ground-measured TSS, which were used to calibrate and validate the satellite models. Water samples were collected at both the surface and the bottom of the water column. These two discrete measurements were subsequently averaged to yield a representative mean for Total Suspended Sediment (TSS) concentration for each station. This integrated "Residue average", also referred to as the TSS value, served as the primary input for the validation process, which is detailed in the subsequent sections (Section 3.1) of this study to assess the predictive accuracy of the satellite-derived models.

Table 3.2. Locations and Metadata for In-Situ Sampling. (CBB and NB refer to the Corpus Christi Bay and the Nueces Bay, respectively, as monitored by UTMSI.)

Station Name	Station #	Water column position	Water depth (m)	TSS (mg/L seawater)	Latitude	Longitude	Sampling Day	Sampling Date
CCB-1	4	Surface	0.26	37.1	27°46′26″ N	97°14′35″ W	Day 1	6/19/2023
		Bottom	3.82	43.6				
CCB-2	3	Surface	0.29	42.3	27°45′19″ N	97°18′34″ W	Day 1	6/19/2023
		Bottom	3.09	22.5				
CCB-3	2	Surface	0.1	26	27°42′41″ N	97°18′23″ W	Day 1	6/19/2023
		Bottom	0.69	20.4				
CCB-4	1	Surface	0.16	25.9	27°43′14″ N	97°12′29″ W	Day 1	6/19/2023
		Bottom	3.93	195.8				
CCB-5	5	Surface	0.22	29.5	27°47′30″ N	97°09′53″ W	Day 1	6/19/2023
		Bottom	3.1	130.8				
CCB-6	6	Surface	0.1	27.2	27°52′14″ N	97°14′55″ W	Day 2	6/21/2023
		Bottom	2.26	41.8				
CCB-7	8	Surface	0.1	40	27°48′20″ N	97°17′52″ W	Day 2	6/21/2023
		Bottom	4.4	44				
CCB-8	7	Surface	0.1	54.4	27°51′16″ N	97°19′12″ W	Day 2	6/21/2023
		Bottom	3.86	241.2				
CCB-9	9	Surface	0.1	39.5	27°46′08″ N	97°22′48″ W	Day 2	6/21/2023
		Bottom	2.82	61.7				
CCB-10	10	Surface	0.1	20.9	27°48′45″ N	97°23′23″ W	Day 2	6/21/2023
		Bottom	2.96	25.7				
NB-1	11	Surface	0.14	76.3	27°52′02″ N	97°22′06″ W	Day 3	6/22/2023
		Bottom	0.23	71				
NB-2	12	Surface	0.15	50.1	27°51′45″ N	97°25′44″ W	Day 3	6/22/2023
		Bottom	1.26	47.6				
NB-3	13	Surface	0.05	46.3	27°51′31″ N	97°29′49″ W	Day 3	6/22/2023
		Bottom	0.97	41.3				
NB-4	14	Surface	0.16	38.7	27°50′06″ N	97°28′11″ W	Day 3	6/22/2023
		Bottom	0.87	51				
NB-5	15	Surface	0.07	68	27°49′44″ N	97°25′02″ W	Day 3	6/22/2023
		Bottom	0.82	75.6				

2) Surface Water Quality Monitoring Information System (SWQMIS)

Data from the TCEQ's Surface Water Quality Monitoring Information System (SWQMIS) and satellites (Landsat and MODIS) were used to develop the prediction model. Ninety percent of the data was used to develop the prediction model, while the remaining ten percent was used for model validation. Separate models were developed for the Nueces River and the Bays (including the Nueces and the Corpus Christi bays) using Landsat and MODIS data.

3.3 Remote Sensing Data and Pre-Processing

Remote sensing data provided the basis for estimating TSS by offering spatially distributed observations of surface reflectance. Multispectral imagery from two satellite platforms was used to capture both spatial variability and temporal dynamics in sediment concentrations. This section outlines the datasets used, along with the procedures for cloud masking and quality control, and concludes with a summary of the datasets and their limitations.

Before developing the predictive models, it was necessary to quantify the physical and temporal reliability of the available satellite data. Because the Nueces River and Bay system is a dynamic environment, a sensor's ability to capture sediment pulses is heavily influenced by its revisit frequency and local cloud cover. The following section describes the analysis of the spatial density in the Landsat and MODIS datasets and performance metrics.

3.3.1 Landsat and MODIS Data

Landsat 8

Landsat 8's Operational Land Imager (OLI), launched on 11 February 2013 and operational since April 2013, delivers global multispectral imagery at a 16-day revisit interval. OLI scenes are freely accessible via the USGS Earth Explorer and provide consistent coverage from 2013 to the present. The spectral bands for Landsat 8 are shown in Table 3.3.

Table 3.3. Spectral Band Specifications and Typical Use for Landsat 8 OLI Sensor (Adapted from USGS, 2022).

Band	Designation	Wavelength (μm)	Resolution (m)	Typical Use
1	Coastal Aerosol	0.43 – 0.45	30	Water-column studies, coastal mapping, aerosol detection, and correction.
2	Blue	0.45 – 0.51	30	Bathymetry (shallow water depth), distinguishing soil and vegetation.
3	Green	0.53 – 0.59	30	Vegetation vigor and health assessment (chlorophyll absorption).
4	Red	0.64 – 0.67	30	True-color composites, analysis of chlorophyll absorption features.
5	Near-Infrared (NIR)	0.85 – 0.88	30	Biomass/vegetation health (high reflectance), water body boundaries.
6	SWIR 1	1.57 – 1.65	30	Soil and vegetation moisture content, burn severity mapping, and cloud penetration.
7	SWIR 2	2.11 – 2.29	30	Geological mapping, mineral/rock discrimination, and vegetation senescence.
8	Panchromatic (Pan)	0.50 – 0.68	15	Image sharpening and visual detail enhancement.
9	Cirrus	1.36 – 1.38	30	Detecting thin, high-altitude cirrus clouds for quality masking and filtering.
10	TIRS 1	10.60 – 11.19	100	Land surface temperature and thermal mapping.
11	TIRS 2	11.50 – 12.51	100	Atmospheric correction for thermal data.

For every individual Landsat scan, a pixel-level screening process was applied. All pixels spatially intersecting the river polygon were extracted and evaluated for data validity using a reflectance-based condition. Only pixels with surface reflectance values ≥ zero were classified as valid observations to eliminate erroneous or masked measurements. This filtering step was critical for removing unrealistic data prior to the coverage assessment.

The total number of cells within the river segment was set as a static spatial reference; a 30 m × 30 m grid was used to ensure consistent spatial alignment across different dates. Using this fixed grid, the analysis maintained a uniform baseline, allowing direct comparison of data availability across different satellite overpasses. For every scan, a cell was classified as "valid" if it intersected at least one usable Landsat pixel. Coverage was then quantified using the following metrics:

1) Granular-Level Metrics (Data Density)

The analysis was performed at the most granular level by recording the raw count of total and valid 30 m × 30 m pixels. This provided a direct measure of data density, identifying exactly how much raw spectral information was successfully retrieved during the scan.

2) Area-Based Metrics (Spatial Completeness)

To ensure mathematical consistency across different dates, individual pixels were evaluated relative to the total area of the river polygon. The spatial completeness of each scan was determined by the ratio of valid pixels to the total potential observations within the segment boundaries. This metric served as a primary indicator of spatial uniformity, accounting for gaps caused by cloud cover or sensor swathing.

3) Segment-Scale Metrics (Total Monitored Area)

Finally, valid pixel counts were converted into physical surface area measurements. Since each Landsat pixel covered 900 m^2, this conversion enabled the calculation of the total water surface area successfully monitored within the segment. This metric expresses the coverage as a percentage of the entire river segment's physical area.

The quantitative results of these calculations are detailed in Table 3.4, which provides a sample scan-by-scan breakdown of the pixel-level density, polygon-based completeness, and total surface area coverage statistics throughout the analysis period.

Table 3.4. Sample Data Showing Computed Pixel-Level Density, Polygon-Based Completeness, and Surface Area Coverage Statistics per Scan.

Date	Data Density			Spatial Completeness			Total Monitored Area		
	Total Pixels (Density)	**Valid Pixels (Density)**	**Polygon Coverage % (Completeness)**	**Total Pixels**	**Valid Pixels**	**Polygon Coverage %**	**River Total Area Km^2**	**River Covered Area (m^2)**	**Area Coverage %**
3/27/2013	84,034.00	0	0	340	0	0	75.66	0	0
4/18/2013		0	0	2,992.00	0	0		0	0
5/4/2013		1,191.00	1.42	2,970.00	1,389.00	46.77		1,250,100.00	1.65
…		…	…	…	…	…		…	…
5/12/2025		34,980.00	41.63	83,458.00	35,099.00	42.06		31,589,100.00	41.75
5/12/2025		34,772.00	41.38	73,480.00	34,880.00	47.47		31,392,000.00	41.49
5/21/2025		0	0	2,720.00	0	0		0	0
Average		24,988.89	29.74	49,902.24	25,166.32	40.79	-	22,649,684.02	29.94
Min		0	0	0	0	0		0	0
Max		76,413.00	90.93	84,020.00	77,806.00	94.74		70,025,400.00	92.55

After scan-level processing, all successful observations were grouped by acquisition date. A temporal aggregation procedure was then applied to the 30 m river grid to estimate the long-term data availability for each location within the river segment. For each grid cell, the total number of unique days on which valid data existed was computed. This resulted in a spatial coverage map that described not only the location of the data but also the observation frequency for each 30 m cell throughout the study period. This temporal fusion transformed individual satellite passes into a long-term observability dataset. Each 30 × 30 m grid cell was further classified into diagnostic categories based on its long-term observation behavior:

- Observed: The cell was covered by a valid pixel at least once during the study period.
- Outside Study Extent: The cell was never intersected by a Landsat pixel during any overpass.
- Data Gaps: The cell was within the study area but was obscured (e.g., by clouds) during every overpass.

Table 3.5 summarizes the data availability and the classification of cells of interest within the Nueces River system. This classification enables the identification of persistent data gaps, sensor limitations, or chronic atmospheric interference zones within the river corridor.

Table 3.5. Summary of Landsat Data Availability for the Nueces River Study Area.

Scan Category	Count	Description
Observed Scans	677	Scans contain valid surface reflectance data within the river segment.
Outside Study Extent	28	Scans where the satellite path did not intersect the defined river boundaries.
Data Gaps	27	Scans missing the required surface reflectance (spectral) attributes.
Total Scans	732	

MODIS

The Moderate Resolution Imaging Spectroradiometer (MODIS) sensors, carried aboard the Terra (launched in 1999) and Aqua (launched in 2002) satellites, were utilized. These platforms offer continuous global imagery from 2000 to the present, with a wide 2,330 km swath and a high revisit frequency of 1 to 2 days. In this research, the MODIS/Terra Surface Reflectance Daily L2G Global (MOD09GA) product was used, and it is available via Google Earth Engine. This daily product, which generated surface reflectance estimates since February 2000 and provided gridded 500-meter-resolution data for the seven key reflective bands (Bands 1–7), is detailed in Table 3.6.

Table 3.6. Spectral Band Specifications and Applications for MODIS Sensors (the spatial resolution is 500 m).

<table>
<tr><th>Band</th><th>Designation</th><th>Wavelength (μm)</th><th>Primary Use</th></tr>
<tr><td>1</td><td>Red</td><td>0.620–0.670</td><td rowspan="2">Land/cloud/aerosols boundaries</td></tr>
<tr><td>2</td><td>Near-Infrared (NIR)</td><td>0.841–0.876</td></tr>
<tr><td>3</td><td>Blue</td><td>0.459–0.479</td><td rowspan="5">Land/cloud/aerosols properties</td></tr>
<tr><td>4</td><td>Green</td><td>0.545–0.565</td></tr>
<tr><td>5</td><td>SWIR 1</td><td>1.230–1.250</td></tr>
<tr><td>6</td><td>SWIR 2</td><td>1.628–1.652</td></tr>
<tr><td>7</td><td>SWIR 3</td><td>2.105–2.155</td></tr>
</table>

The Key pre-processing steps regarding these satellites include:

1) Cloud Control: Automated cloud screening was performed using a custom script developed in the Google Earth Engine (GEE) JavaScript Application Programming Interface (API). This algorithm integrated GEE’s built-in cloud mask layers along with a scene-wide maximum cloud cover filter of ≤ 20%. Additionally, a stricter spectral cutoff threshold was applied: pixels with Band 4 (Red) reflectance > 0.15 (B4 for Landsat) (Zhu & Woodcock, 2012)

and Band 1 reflectance > 1.5 (MODIS) were excluded to remove high-cloud reflectance artifacts (Vermote et al., 2002). Manual visual inspection was performed to verify the efficacy of this threshold. By coding this logic directly into the GEE processing pipeline, the filtering of localized cloud artifacts was fully automated across the multi-year dataset. This validation confirmed that even when scene-wide cloud coverage fell below 20%, pixels where the red band exceeded 0.15 consistently represented local cloud interference rather than water bodies. This ensured that all points sampled were from water bodies only. Figure 3.6 shows an example of this automated filtering process. While the cloud coverage metadata feature was specific to Landsat, MODIS was filtered in the same manner using the corresponding red band (i.e., Landsat B4 was similar to MODIS B1) to maintain cross-platform consistency.

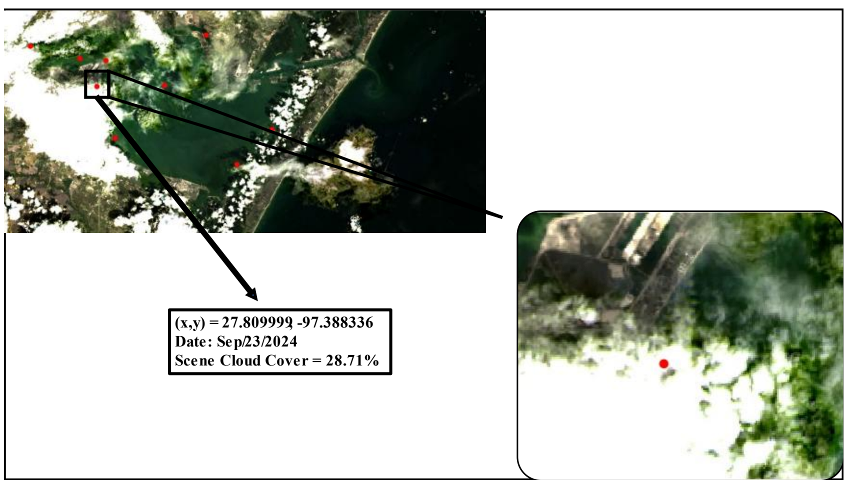

Figure 3.6. Cloud Coverage filtering process with an example: a point completely covered by cloud.

2) Temporal Matching:

- MODIS: Daily reflectance values were matched with field sampling dates with a 1-day time window (Bailey & Werdell, 2006; Feng et al., 2012). This window is commonly used in satellite-to-in-situ matchups for inland and coastal waters to maximize data density while ensuring that the water body's physical properties remain relatively stable between the overpass and the sampling event.

- Landsat: Reflectance was matched within a ±7-day window (Kloiber et al., 2002; Olmanson et al., 2008) due to the 16-day revisit period. This expanded temporal window is commonly used in Landsat water-quality studies to increase the number of valid matchups, particularly in systems where water-quality parameters remain relatively stable over short periods. Only cloud-free matches were retained.

3) Spatial Matching and Mapping: Satellite pixel values were matched with the closest validated observation site. Consolidated reflectance datasets were filtered and prepared for modeling by combining the assembled satellite band data with in-situ field measurements, ensuring one-to-one alignment between them (Tables 3.7 and 3.8).

Table 3.7. River In-Situ Stations and Satellite Matches.

Station ID	Latitude	Longitude	Record Count	Satellite Match
12968.0	28.105556	-97.8875	10	0.0 m
13019.0	28.49	-98.24861	79	0.0 m
13020.0	28.501389	-98.33389	217	0.0 m
17384.0	28.185556	-97.91306	82	0.0 m
17389.0	28.52	-98.38805	148	74.3 m
17648.0	28.298832	-98.04255	147	20.9 m
22328.0	28.514482	-98.417084	6	0.0 m

Table 3.8. Summary of In-Situ Stations and Satellite Matches across the Nueces and Corpus Christi Bay Systems.

Station ID	Latitude	Longitude	Record Count	Satellite Match
13407.0	27.811388	-97.301476	191	0.0 m
13409.0	27.868889	-97.248222	171	0.0 m
13410.0	27.809999	-97.388336	157	0.0 m
13411.0	27.751389	-97.364998	174	0.0 m
13421.0	27.839722	-97.376663	195	0.0 m
13422.0	27.842501	-97.410332	187	0.0 m
13425.0	27.856388	-97.474495	131	0.0 m
14355.0	27.76111	-97.162498	88	0.0 m
17791.0	27.720833	-97.207779	43	0.0 m

3.3.2 Cloud Control and Masking

A robust filtering methodology was established to isolate clear-water pixels from atmospheric and terrestrial interference, ensuring high data reliability across both sensors. This process leverages specific spectral indices and reflectance thresholds to distinguish valid aquatic signals from cloud cover and land features.

The cloud filtering process used MODIS spectral bands (Red, NIR, Blue) and the Normalized Difference Vegetation Index (NDVI) to distinguish water pixels from non-water pixels. Li et al. (2015) used MODIS-derived spectral indices to monitor the presence of water in a seasonally flooded wetland in southern Spain. They focused on time-series analysis of indices such as the NDVI and Normalized Difference Water Index (NDWI) to infer hydrological changes. Water pixels were identified by temporal patterns in NDWI values, with higher NDWI typically indicating water. The study also employed ground truth data and high-resolution imagery to validate the spectral thresholds, thereby separating water from non-water classes.

Mondejar and Tongco (2019) used Landsat 8's Near Infrared (NIR) band as a single-band water index to classify water bodies around Cordova and Lapu-Lapu City in the Philippines. Since water strongly absorbs NIR light, they identified water pixels by setting a reflectance threshold: Band 5 (NIR) pixels with reflectance values below a threshold (~0.1) were classified as water, while higher reflectance indicated non-water features. Their classification was supported by visual interpretation of Google Earth imagery and cross-validation with known water bodies.

To isolate valid water pixels from satellite-derived surface reflectance datasets (Landsat 8 and MODIS), a filtering procedure was applied based on spectral reflectance thresholds and NDVI criteria. Pixels were classified as "Water" if they satisfied the conservative thresholds (Table 3.9) designed to reject cloud-contaminated and vegetated pixels while retaining highly turbid water.

Table 3.9. Spectral Filtering Thresholds for Cloud- and Vegetation-Free Water Pixels.

Satellite	Blue	Red	NIR	NDVI
Landsat	B2 ≤ 0.18	B4 ≤ 0.20	B5 ≤ 0.20	NDVI ≤ 0.10
MODIS	B3 ≤ 0.18	B1 ≤ 0.20	B2 ≤ 0.20	NDVI ≤ 0.10

This approach removed clouds and vegetation from the satellite reflectance datasets while preserving signals associated with high-sediment or turbid water bodies. Following this atmospheric and land-masking process, the remaining cloud-free reflectance values were matched with validated in-situ observation sites to ensure one-to-one alignment.

3.3.3 Data Summary and Limitations

The final number of matched datasets between in-situ TSS measurements and satellite observations is summarized in Table 3.10. Due to Landsat's fixed 16-day revisit interval, opportunities to pair satellite overpasses with field measurements were severely limited when compared to MODIS's 1–2-day frequency. Therefore, in the bay dataset, Landsat matched only 61 TSS measurements, whereas MODIS yielded 1049 TSS observation pairings. While in the river dataset, Landsat matched with 112 TSS observations, whereas MODIS yielded 664 TSS data pairings.

Table 3.10. Summary of Valid Matched Observations by Dataset and Variable.

Sensor	Scope	Residue In Situ
Landsat	Bay	61
	River	112
MODIS	Bay	1049
	River	664

Figure 3.7 illustrates the acquisition timelines for MODIS and Landsat data alongside the in-situ sampling scheduled at nine bay and eight river stations. MODIS and Landsat overpasses appear as dense, regularly spaced markers, yet the corresponding field measurements (green squares in the bay; cyan circles in the river) are both sparse and unevenly distributed. Furthermore, many locations (Stations) in the river and the bay had no ground truth data for several years (e.g., 2016-2025 in the bays) or no samples at all (e.g., the Nueces River). This and the noticeable offset between the high-potential satellite revisit frequency and the limited, irregular in-situ sampling patterns substantially reduced the number of valid satellite–

measurement pairs and, in turn, posed constraints on model calibration, validation, and the reliability of subsequent sediment predictions.

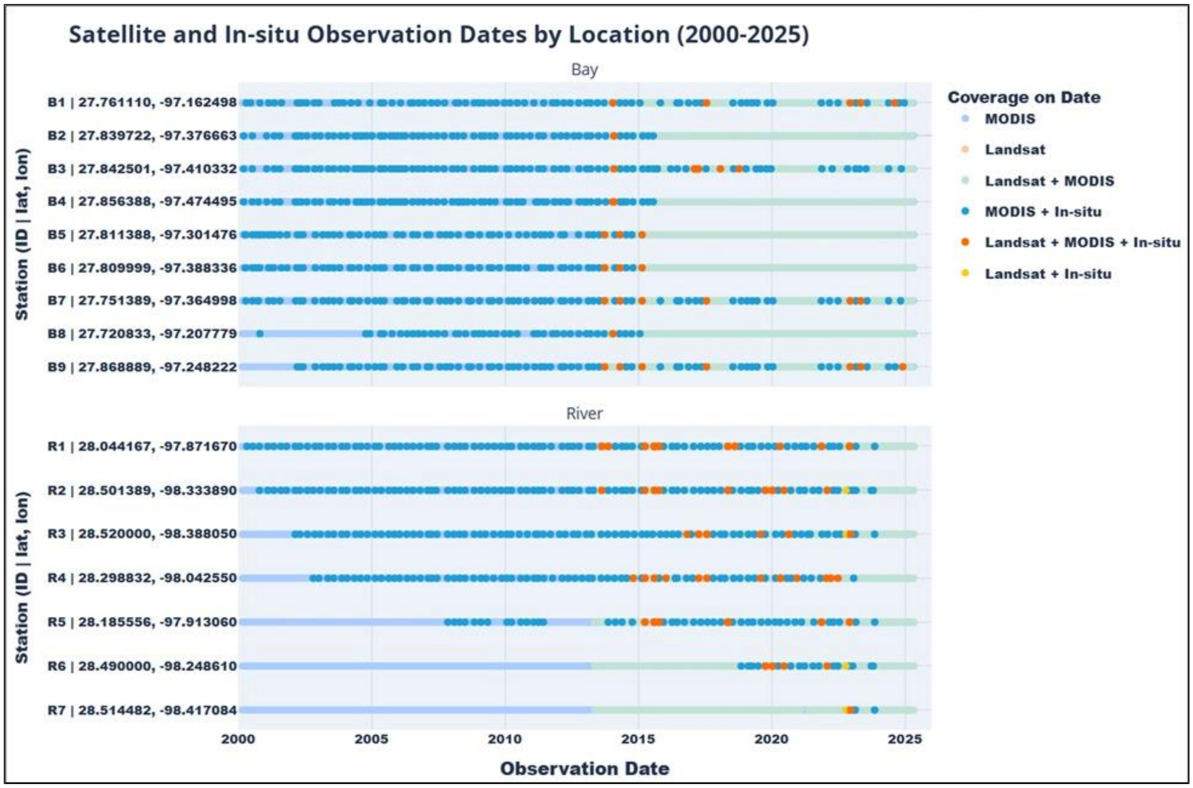

Figure 3.7. MODIS vs Landsat vs. In-Situ Scan Dates by Location.

Table 3.11 presents descriptive statistics for spectral reflectance (B1–B7), TSS, and flow, by sensor (Landsat vs. MODIS) and location (Bay vs. River). In both water bodies, the reflectance bands exhibit very low medians (often zero) but substantial upper-quartile values (e.g., Landsat B3 surface reflectance (sr) in the bay: 50th percentile (pct) = 0.071, 75th pct = 0.092; MODIS B4 sr: 50th pct = 0.103, 75th pct = 0.126), indicating a right-skewed distribution with a long tail of high-reflectance scenes. The spectral standard deviations ($\sigma \approx 0.02$–0.05) are modest, yet the minima of zero and maxima up to 0.454 (MODIS B2 sr in the river) suggest frequent near-zero readings punctuated by occasional high-reflectance outliers. TSS shows similarly wide variation: bay means of 25.7 – 29.7 mg/L, but maxima of 179 mg/L (Landsat) and

810 mg/L (MODIS) point to extreme sediment events that may unduly influence model fits. River TSS is slightly lower on average (≈ 23 – 24 mg/L) but still reaches high values of 236 – 470 mg/L.

Table 3.11. Descriptive statistics for bands 1-7 (Unitless), TSS, and flow, organized by sensor (Landsat vs. MODIS) and (Bay vs. River).

Data-Scope	Statistical Metrics								
	n	μ	σ	min	25%	50%	75%	max	
Features (Bay)									
B1_sr	61	0.028	0.022	0	0.016	0.023	0.034	0.088	**Landsat**
B2_sr		0.046	0.024	0	0.033	0.04	0.052	0.108	
B3_sr		0.076	0.029	0	0.061	0.071	0.092	0.159	
B4_sr		0.045	0.031	0	0.026	0.035	0.056	0.124	
B5_sr		0.014	0.026	0	0	0	0.02	0.096	
B6_sr		0.018	0.029	0	0.001	0.002	0.031	0.107	
B7_sr		0.017	0.026	0	0.002	0.004	0.025	0.102	
Residue in-situ		25.666	23.617	5	16	22	28	179	
Flow in-situ	0	-	-	-	-	-	-	-	
Features (River)									
B1_sr	112	0.029	0.025	0	0.005	0.024	0.049	0.091	
B2_sr		0.041	0.027	0	0.021	0.034	0.063	0.11	
B3_sr		0.07	0.032	0	0.049	0.064	0.09	0.144	
B4_sr		0.063	0.033	0	0.037	0.058	0.088	0.149	
B5_sr		0.05	0.043	0	0.019	0.042	0.074	0.245	
B6_sr		0.035	0.029	0	0.004	0.035	0.058	0.135	
B7_sr		0.026	0.022	0	0.004	0.022	0.044	0.096	

Residue in-situ		23.804	35.455	4	9	15.2	23	236	
Flow in-situ	0	nan	nan	nan	nan	nan	nan	nan	
Features (Bay)									
B1_sr	1049	0.08	0.037	0	0.054	0.078	0.107	0.15	**MODIS**
B2_sr		0.06	0.048	0	0.023	0.051	0.088	0.284	
B3_sr		0.073	0.036	0	0.051	0.072	0.098	0.184	
B4_sr		0.103	0.034	0	0.081	0.103	0.126	0.185	
B5_sr		0.061	0.054	0	0.021	0.047	0.087	0.33	
B6_sr		0.058	0.046	0	0.023	0.046	0.079	0.294	
B7_sr		0.037	0.034	0	0.011	0.026	0.053	0.177	
Residue in-situ		29.672	52.029	4	12	18	29	810	
Flow in-situ	-	-	-	-	-	-	-	-	
Features (River)									
B1_sr	664	0.076	0.032	0	0.054	0.071	0.096	0.15	
B2_sr		0.158	0.101	0	0.073	0.151	0.235	0.454	
B3_sr		0.058	0.033	0	0.036	0.049	0.071	0.188	
B4_sr		0.084	0.031	0	0.064	0.078	0.1	0.176	
B5_sr		0.175	0.112	0	0.08	0.168	0.261	0.465	
B6_sr		0.141	0.091	0.003	0.067	0.132	0.207	0.409	
B7_sr		0.076	0.053	0	0.034	0.072	0.109	0.263	
Residue in-situ		23.295	36.442	3	9	15	25.5	470	
Flow in-situ	6	497.667	800.616	55	104.25	252	252	2120	
Definitions	**n: count; μ: mean; σ: standard deviation; min: minimum; 25%: 1st quartile; 50%: median; 75%:3rd quartile; max: maximum; sr: Surface Reflectivity**								

In contrast, simultaneous flow measurements are entirely missing for Landsat and nearly absent for MODIS (*n* = 6). This scarcity is due to the lack of temporal alignment between satellite overpasses and available discharge data from USGS stream gauges within the defined matchup windows. Taken together, these descriptive statistics underscore that only spectral bands and TSS offer sufficiently dense data for reliable modeling. Conversely, the sparse flow sample counts will necessitate careful preprocessing and may limit their inclusion as a predictive variable in robust modeling.

With the spatial and temporal limitations of the remote sensing platforms established, the next phase of the methodology involved fusing these disparate datasets. By pairing the filtered spectral reflectance values from Landsat and MODIS with simultaneous in-situ TSS measurements from the TCEQ and UTMSI databases, a unified training matrix was constructed. This integrated dataset served as the foundation for evaluating the four distinct models described in the following section.

3.4 Model Building

The matched satellite–field dataset was constrained by the limited number of in-situ measurements collected each year at both bay and river stations. With fewer than ten samples per station annually, episodic sediment pulses (e.g., storm-driven TSS spikes) were not well represented. Furthermore, reflectance bands and TSS exhibited heavy right tails, with rare high values (e.g., MODIS bay TSS max = 810 mg/L). These extreme points, if unfiltered, can dominate least-squares and tree-based (e.g., decision trees and non-parametric models that recursively split data to capture non-linear patterns) models.

To ensure robust parameter estimation, outliers were removed. Figure 3.8 represents Interquartile Range (IQR) boxplots for Landsat and MODIS TSS in the bays and river; red markers denote outliers. Given the overall low sample counts, we adopted a 1.5 × IQR filter, computed between the 25th and 90th percentiles (Helsel et al., 2020), rather than the traditional 25th–75th percentiles, to maximize data retention (blue boxes) and minimize the disproportionate influence of extreme storm events. This wider percentile range retained moderate variability while excluding only the most extreme events with insufficient replication, preserving ~95% of valid matched data points and stabilizing the fitted model against irregular observations (Yetik, 2026).

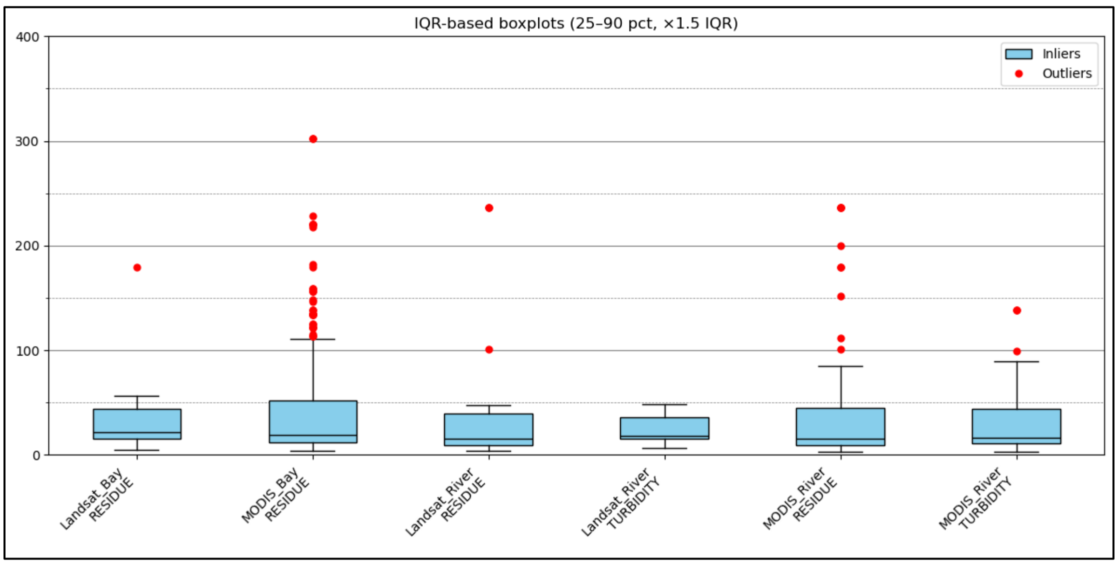

Figure 3.8. Box & Whisker plot showing outlier removal.

Spectral and temporal predictors were derived from the original surface-reflectance bands $B1$ through $B7$. From these, three band ratios ($B5/B3$, $B2/B3$, and $B1/B3$) that normalize illumination effects, were derived (Chen et al., 2021), in addition of a composite scattering index $(\frac{1}{B1} - \frac{1}{B3}) \times B5$. To account for seasonal cycles, the sine and cosine of the monthly phase angle were computed (Brooks et al., 2014; Wilson et al., 2018). This harmonic transformation ensured the model could learn periodic variations without introducing artificial discontinuities at year boundaries. In combination, these eleven features formed the full predictor set used by every model (Equations 3.1 – 3.3), respectively (Alparone et al., 2020; Chen et al., 2021; Stow et al., 2004).

$$r_{i/j} = \frac{B_i}{B_j} \text{for } (i,j) \in \{(5,3),(2,3),(1,3)\} \tag{3.1}$$

where $r_{i/j}$ is the band ratio between bands i and j, B_i is the reflectance of band i (unitless, surface reflectance), and B_j is the reflectance of band j.

$$c_{\text{comp}} = \left(\frac{1}{B1\_sr} - \frac{1}{B3\_sr}\right) \times B5\_sr \tag{3.2}$$

where c_{comp} is the composite reflectance transformation (unitless), B1_sr is the surface reflectance of Band 1 (Blue), B3_sr is the surface reflectance of Band 3 (Red), and B5_sr is the surface reflectance of Band 5 (Near-Infrared).

$$s = \sin\left(\frac{2\pi \text{ month}}{12}\right), c = \cos\left(\frac{2\pi \text{ month}}{12}\right) \tag{3.3}$$

where *s* and *c* are the sine and cosine seasonal components, and month is the month of observation (1 – 12).

In this study, four models were tested and evaluated to determine the most effective approach for TSS retrieval, and the best model was selected for analysis. The three models were based on parametric forms, and the fourth was based on machine learning:

1) Multivariate Linear Regression (MLR): This model assumed a direct weighted sum of features, which provided a baseline for linear relationships between reflectance and TSS (see Equation 3.4) (Gitelson et al., 2008)

$$\hat{y}_{\text{linear}} = a + \sum_{k=1}^{p} b_k \, x_k \tag{3.4}$$

where $\hat{y}_{linear}$ is the predicted target value (e.g., TSS), α is the intercept term, b_k is the coefficient for predictor x_k, x_k is the predictor variable (e.g., band reflectance), and p is the number of predictors.

2) Log-linear Model: This approach applied a logarithmic transformation to the target TSS values before fitting the linear pattern, which accounted for the typical log-normal distribution of water quality parameters (Equation 3.5) (Novo et al., 2006)

$$\log\left(1+\hat{y}_{\mathrm{loglin}}\right)=a\ +\ \sum_{k=1}^{p} b_k\, x_k\,, \hat{y}=\exp\ \left(a+\sum b_k x_k\right)-1 \tag{3.5}$$

where $\hat{y}_{\mathrm{loglin}}$ is the log-transformed predicted value.

3) Power-law Model: This formulation raised each predictor to an estimated exponent before multiplication, which allowed the non-linear relationship often observed in satellite band responses (Equation 3.6) (Dekker et al., 2002)

$$\hat{y}_{\mathrm{power}}=a\prod_{k=1}^{p} {x_k}^{b_k} \tag{3.6}$$

where $\hat{y}_{\mathrm{power}}$ is the predicted value using a multiplicative model, $\prod$ is the product notation, and x_k^{bk} is the predictor x_k raised to the power of bk.

4) Random Forest (RF) Regressor: The Random Forest algorithm is an ensemble learning method that builds a collection of decision trees to achieve superior predictive accuracy and robustness. These "trees" are hierarchical structures that partition data into subsets based on feature thresholds. To ensure diversity and prevent overfitting, each tree is trained on a random sample of the data and considers only a random subset of variables at each split. This decorrelation process ensures that the collective "forest" is not overly sensitive to the noise of any single predictor. Decisions are reached through an aggregation process in which classification tasks rely on a majority vote from all trees, while regression tasks use the average of their numerical outputs. This distinguishes Random Forest from parametric models such as linear, log-linear, or power models, which assume a fixed mathematical relationship and require a specific distributional assumption. While those models seek a global equation, Random Forest is non-parametric and non-linear, allowing it to naturally capture complex interactions and localized

patterns without the rigid constraints of a predefined functional form. This machine-learning suite assembled a forest of 200 decision trees to flexibly capture complex, non-linear interactions among the spectral, ratio, composite, and seasonal predictors (Equation 3.7) (Breiman, 2001).

$$\hat{y}_{\mathrm{RF}} = \frac{1}{T} \sum_{t=1}^{T} f_t(\mathrm{x}) \tag{3.7}$$

where $\hat{y}_{\mathrm{RF}}$ is the Random Forest predicted value, T is the total number of trees in the ensemble, and $f_t(x)$ is the prediction from tree (t) for input features (x).

Each of these formulations was trained on the same feature matrix X and subsequently tested for predictive accuracy. The models' performance was evaluated by three evaluation metrics. We reported the coefficient of determination, R^2, to measure the proportion of variance explained, root-mean-square error (RMSE) for aggregate residual magnitude and mean absolute error (MAE) to guard against the undue influence of large errors. Collectively, these statistics offer a comprehensive perspective on the models' explanatory power and practical precision in estimating suspended-sediment concentrations. Refer to equations (3.8) – (3.10) (Willmott et al., 2012; Chai & Draxler, 2014; Willmott & Matsuura, 2005), respectively.

$$R^2 = 1 - \frac{\sum_i (y_i - \hat{y}_i)^2}{\sum_i (y_i - \bar{y})^2} \tag{3.8}$$

$$\mathrm{RMSE} = \sqrt{\frac{1}{N} \sum_{i=1}^{N} (y_i - \hat{y}_i)^2} \tag{3.9}$$

$$\mathrm{MAE} = \frac{1}{N} \sum_{i=1}^{N} \mid y_i - \hat{y}_i \mid \tag{3.10}$$

Table 3.12 presents the explanatory power (R^2) and absolute errors (RMSE, MAE) of our five models for Bay TSS.

Table 3.12. Models' results for TSS using Landsat and MODIS data across the study area, including both the Nueces/Corpus Christi Bays and the Nueces River segments.

	Model	Landsat			MODIS		
		R^2	**RMSE**	**MAE**	**R^2**	**RMSE**	**MAE**
TSS	**TSS Bay**						
	linear B3	0.049	12.487	9.298	0.016	18.464	12.523
	linear B4	0.083	12.257	9.051	0.024	18.391	12.467
	linear B5	0.048	12.494	9.059	0.012	18.501	12.598
	linear all bands	0.347	10.344	7.896	0.196	16.697	11.147
	Log linear all bands	0.233	11.213	8.035	0.158	17.086	10.54
	power all bands	0.205	11.417	7.4	0.01	18.524	11.483
	Random Forest (RF)	**0.801**	**5.708**	**4.203**	**0.887**	**6.27**	**4.214**
	TSS River						
	linear B3	0.14	10.387	7.82	0.011	14.99	10.774
	linear B4	0.171	10.2	7.644	0.032	14.826	10.595
	linear B5	0.043	10.958	8.415	0.075	14.493	10.392
	linear all bands	0.33	9.166	6.937	0.204	13.448	9.681
	Log linear all bands	0.283	9.487	6.622	0.137	13.998	9.115
	power all bands	0.271	9.565	6.946	0.018	14.936	9.633
	Random Forest (RF)	**0.927**	**3.025**	**2.141**	**0.877**	**5.275**	**3.641**

Initial single-band linear regressions on Landsat B4 yielded R2 = 0.083, RMSE = 12.26 mg/L, and MAE = 9.05 mg/L, all of which were quite low. Their MODIS counterparts performed even lower, achieving $R^2 < 0.03$ and an RMSE of approximately 18.4 mg/L (MAE 12.5 mg/L).

By expanding the feature set to include all seven bands, three band ratios, the composite index, and seasonal sine/cosine components, model performance improved significantly. Specifically, Landsat R^2 rose to 0.347 while RMSE dropped to 10.34 mg/L (MAE = 7.90 mg/L). MODIS similarly improved to an R^2 of 0.196 with an RMSE of 16.70 mg/L (MAE = 11.15 mg/L). Notably, applying log-linear or power-law transforms yielded similar or slightly lower R^2 values (0.158 – 0.233) and higher RMSE (11.21 – 18.52 mg/L), suggesting minimal benefit from the nonlinear scaling of individual bands.

Despite these small incremental improvements, the residual errors and unexplained variances in all the parametric models remained relatively high, indicating poor performance. To address this, we adopted a Random Forest ensemble. Although it functions as a “black box,” it effectively captures complex, context-dependent relationships by partitioning the predictor space via sequential binary splits. This flexibility allows the model to automatically handle thresholds, such as reflectance above a scattering point, and interactions, such as how the effects of B5/B3 vary with seasons.

This approach proved particularly well-suited to our right-skewed, heteroscedastic data. Implementing the Random Forest on the full suite of predictors yielded dramatic improvements. For Bay TSS, we achieved R^2 values of 0.80 for Landsat and 0.89 for MODIS, with RMSE values ranging from 5.71 to 6.27 mg/L (MAE 4.2 mg/L), successfully capturing 80–90% of the variance.

In the River context, the Random Forest achieved R^2 values of 0.93 (Landsat) and 0.88 (MODIS), with RMSE ranging from 3.03 to 5.28 mg/L. These models were trained using historical Total Suspended Solids (TSS) data from the TCEQ-SWQMIS database. Specifically, the training data used 112 valid satellite-to-in-situ matchups for Landsat and 664 for MODIS within the river segments. For the correlation and bay-interaction analysis, the "River" designation was restricted to the river-delta area at the outlet where the Nueces River meets the Bays. Ultimately, the ensemble's ability to aggregate weak predictors into a robust consensus drastically outperformed all parametric models, underscoring its value when sample sizes are sufficiently varied to capture complex relationships.

Surface-reflectance bands (B1–B7) were extracted, and three key band ratios (B5/B3, B2/B3, B1/B3), as well as others, such as seasonal sine/cosine transforms, were constructed. Four parametric models (single-band linear, multivariate linear, log-linear, and power-law) and a Random Forest were applied to predict TSS from Landsat and MODIS data. Performance was quantified using the R^2, RMSE, and MAE, demonstrating that while multivariate linear models explained up to 35 % of the variance, up to 93 % was captured by the Random Forest, hence enhancing the models by nearly 50%.

After the Random Forest model generated Total Suspended Solids (TSS) estimates for individual pixels, a post-processing framework was required to transform these discrete points into continuous geospatial surfaces. This step was essential for visualizing sediment transport patterns and filling data gaps caused by atmospheric interference or sensor constraints.

The spatial coordinates (longitude and latitude) and associated predicted values were extracted per pixel. Any point that did not meet the criteria was not considered a valid water point (cloud/others). Using cubic interpolation, each missing cell was estimated by fitting a smooth, third-degree polynomial curve through its four nearest known neighbors (Keys, 1981). In one dimension, if the four successive sample values were f_1, f_2, f_3, and f_4, and $t \in [0,1]$ was the relative position between the middle two points, the interpolated value was given by equation 3.11.

$$f(t) = (1-t)^3 f_1 + 3t(1-t)^2 f_2 + 3t^2(1-t) f_3 + t^3 f_4 \tag{3.11}$$

By applying equation 3.11 along longitude and then along latitude (two separate interpolations), we obtained a smoothly varying surface over the Area of Interest (AOI). Any internal gaps were filled with appropriate values to improve visual continuity.

3.5 Precipitation and Streamflow Correlation Data and Methodology

Correlations between precipitation and streamflow are important to understanding sediment mobilization, particularly within the river segments of the study area. Precipitation events generate runoffs whose magnitude and intensity directly influence the volume of water entering river channels, which, in turn, governs the capacity of the flow to detach, entrain, and transport sediment particles (Julien, 2010). By quantifying the statistical relationships among precipitation, discharge, and TSS within the Nueces River catchment, it is possible to infer thresholds at which sediment yield sharply increases, thereby improving estimates of sediment yield during rain events. Thus, the statistical relationship between hydrometeorological drivers (i.e., precipitation and streamflow) and sediment transport was analyzed.

Strong flow–sediment correlations enhance model robustness by reducing uncertainty in load estimates under varying hydrometeorological conditions, facilitating sediment budgeting and reservoir siltation forecasting. Furthermore, these correlations guide the design of sampling regimes, ensuring that high-flow periods, which disproportionately contribute to annual sediment yield, are adequately monitored (Syvitski et al., 2005). Ultimately, reliable flow–sediment relationships are indispensable for watershed management strategies aimed at mitigating erosion, maintaining water quality, and preserving aquatic habitats. A study point near the Nueces River delta was selected to develop the correlation.

To summarize, the Nueces River delta polygon was first identified and mapped to establish the study area, after which twenty years of MODIS-based total suspended solids (TSS) data were processed. In parallel, daily river discharge measurements from the nearest upstream USGS gauge and precipitation records from the closest NOAA station (within 10 km) were aggregated at a daily time step. These 3-time series were temporally aligned to create a unified dataset, which was then examined using a stepwise correlation analysis. To this end, the merged series were first evaluated in their entirety. Storm events were then isolated using precipitation thresholds and composited with corresponding Residue windows. Pearson correlation coefficients were calculated across multiple precipitation thresholds, and a regression model was developed for extreme events (≥ 50 mm) to estimate the relationship between sediment concentrations and heavy rainfall. A flow chart of the analysis steps is shown in Figure 3.9.

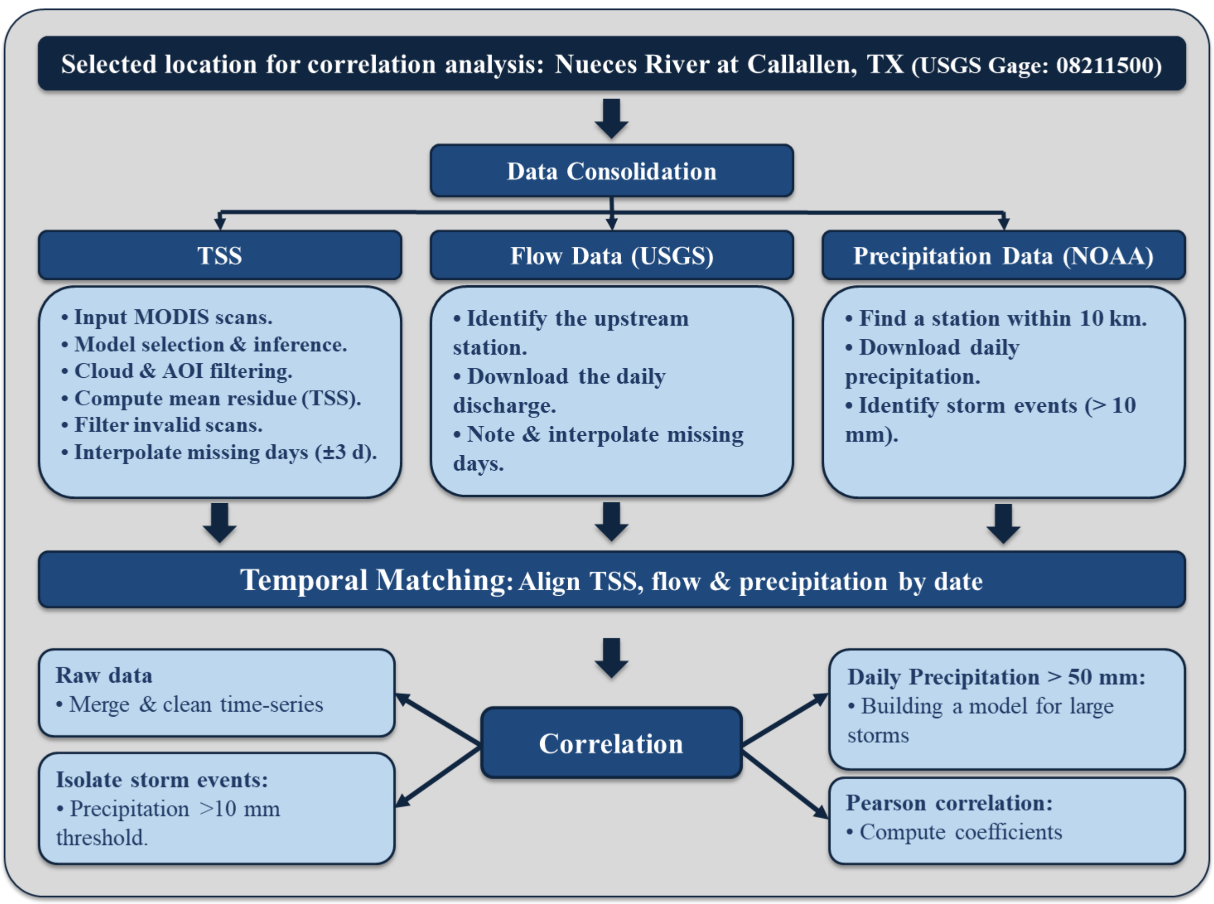

Figure 3.9. Flowchart showing the approach to comparing correlations.

3.5.1 Precipitation and Flow Data

The daily precipitation data were obtained from the Climate Data Online (CDO) website, hosted by the National Centers for Environmental Information (formerly the National Climatic Data Center, ncdc.noaa.gov), which provides an interface for retrieving historical weather and climate records. The website allows users to select from a variety of datasets, including precipitation observations, snowfall, and radar products. Users can define a custom date range and enter search terms, such as station identifiers or geographic names (e.g., city, county, state, or ZIP code), to pinpoint the records they need.

To further investigate the impact of hydrometeorological drivers, discrete storm events were extracted from the daily precipitation time series. A threshold of 10 mm per day was established: any day meeting or exceeding this value was designated as a 'storm' day, and consecutive storm days were grouped into individual events, while all others were classified as 'regular' or 'normal' days. This approach yielded an event catalog, summarized later in Table 3.20, which analyzed Residue trends surrounding specific storm occurrences and the correlations emerging from isolated precipitation events.

Once a query is defined, the tool displays matching stations or data products, which can be added to an order system. In this case, the coordinates of the available weather stations surrounding the related area of interest are shown in Table 3.13. Spatial matching of the target locations with the surrounding weather stations was performed within a 10 km radius. Historical daily discharge records were obtained from the USGS National Water Information System (NWIS) to characterize the fluvial dynamics of the Nueces River. These data were retrieved from the upstream gauging station at Calallen, TX (USGS 08211500), providing the primary metric for analyzing sediment entrainment and transport capacity during storm events.

Table 3.13. Coordination of the available weather stations near the delta of the Nueces River, with codes shown in Figure 3.10.

Station	Code	Latitude	Longitude
USC00412011	P1	27.7793	-97.5055
USW00012924	P2	27.77335	-97.51302
US1TXSP0010	P3	27.924911	-97.534842
US1TXNU0038	P4	27.808389	-97.470553
US1TXNU0068	P5	27.845392	-97.574259

Figure 3.10 illustrates the geographical distribution of the monitoring infrastructure across the Nueces River and bay system.

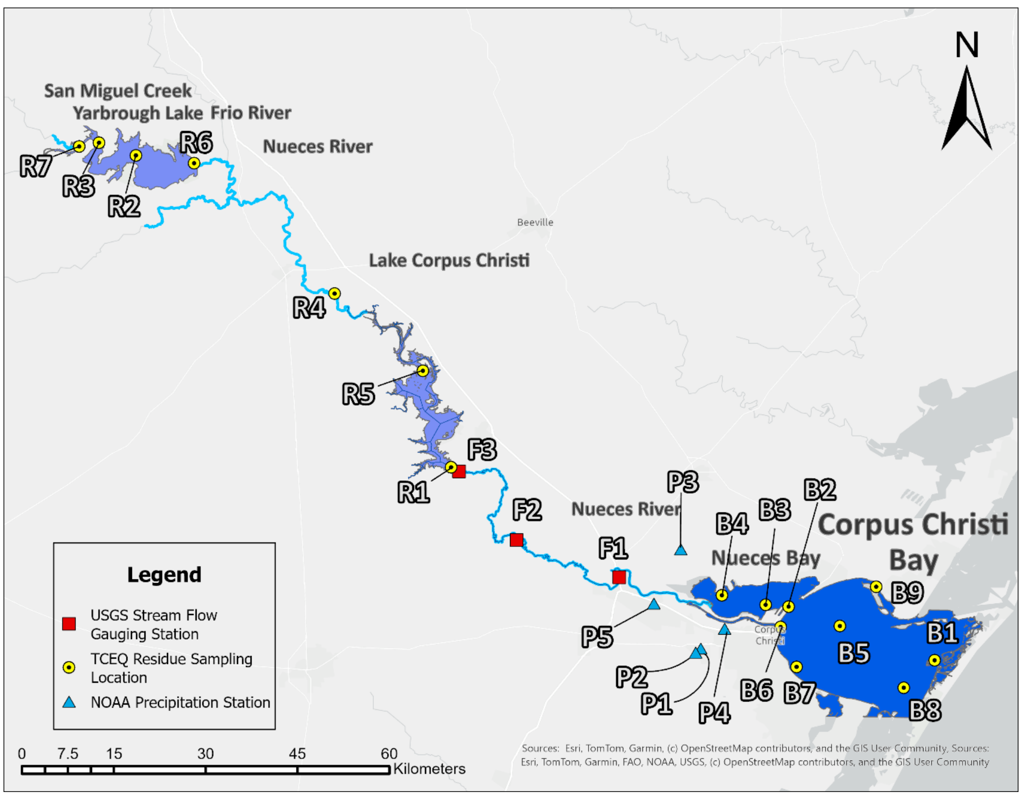

Figure 3.10. Flow, Residue (TSS), and Precipitation stations' location. In this map, B represents Bay monitoring stations, R denotes River segments, P identifies Precipitation records from NOAA, and F indicates USGS Flow gauging stations.

This map shows the specific locations of USGS streamflow gauging stations (only the F1 flow gauge was used), TCEQ residue sampling sites, and NOAA precipitation stations used to analyze the catchment's hydrological response.

3.5.2 Residue (TSS) Data

The Random Forest regression model generated spatially continuous estimates of TSS across the study area. This process transformed the cloud-free reflectance datasets into high-resolution maps, allowing a detailed analysis of sediment distribution patterns within the bays. These resulting spatial products served as the primary basis for the subsequent analysis of sediment hotspots and temporal trends.

To mitigate sub-pixel heterogeneity and mixed-pixel effects inherent to MODIS's 500 m footprint, a polygon delineating the broad river-delta area was defined for model inference (Figure 3.11).

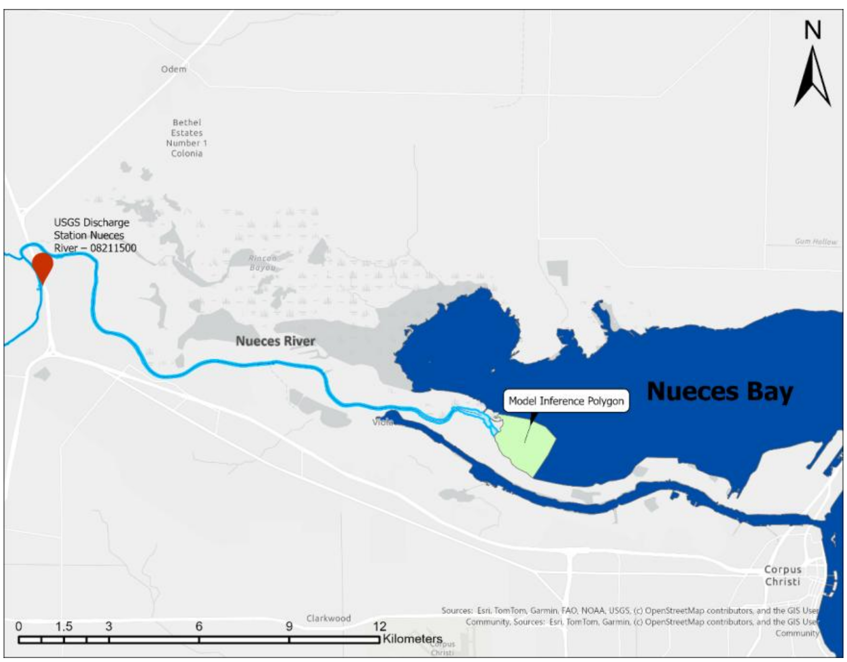

Figure 3.11. Selected area of interest for studying the Correlations between flow, precipitation, and the predicted sediment concentrations, and the monitoring location for station "Nueces River at Calallen, TX – 08211500.

By averaging predicted TSS values (derived from each 500 m pixel within the approximately 2.33 km² polygon) for each acquisition date, a temporally coherent time series was obtained that was less sensitive to individual-pixel noise. A central point at (27.8446559, –97.4936980) was subsequently used to pair these satellite-derived, polygon-averaged TSS estimates with precipitation records from the nearest weather station. This polygonal averaging strategy ensures spatial comparison between satellite data and in situ measurements.

The study point was positioned at the river delta to eliminate mixed-pixel effects associated with MODIS's 500-m footprint, as the river reach is wider than a single MODIS pixel (~500 m × 500 m) and therefore provides estimates in the Bay region. Landsat 8 OLI's finer 30-m resolution can resolve detailed spatial gradients; however, the model built and validated for Landsat-derived reflectance for the Bays achieved a relatively fair R^2 (Table 3.14). Thus, the analysis for the Bays was confined to the delta region based on MODIS-derived TSS.

The operational implementation utilized a Random Forest model trained on native MODIS reflectance bands. Before inference, all input rasters underwent cloud and vegetation screening, as defined by the criteria in Table 3.9. A raster was considered cloud-free when the overall scene cloud coverage was less than 20%, while pixel-level filters identified and retained only clear-water signals. The workflow involved clipping imagery to the specific bay boundary polygons and filtering results using established spectral thresholds (Li et al., 2015; Mondejar & Tongco, 2019). Predictions yielding negative values were flagged as 'invalid,' while valid values were gridded at a 500 m resolution. This automated process independently performed filtering, interpolation, and masking for each date in the archive to ensure consistent geospatial products.

The final filtered daily data includes 6,650 days (i.e., without cloud cover) out of 9,154 raw days, based on the total available data from 2000 to 2025. Figure 3.12 shows estimated

Residue (TSS) values from 27 February, 2000 to 27 May, 2025, where the black strips indicate missing time periods in the MODIS scenes, and the white strips show the data availability.

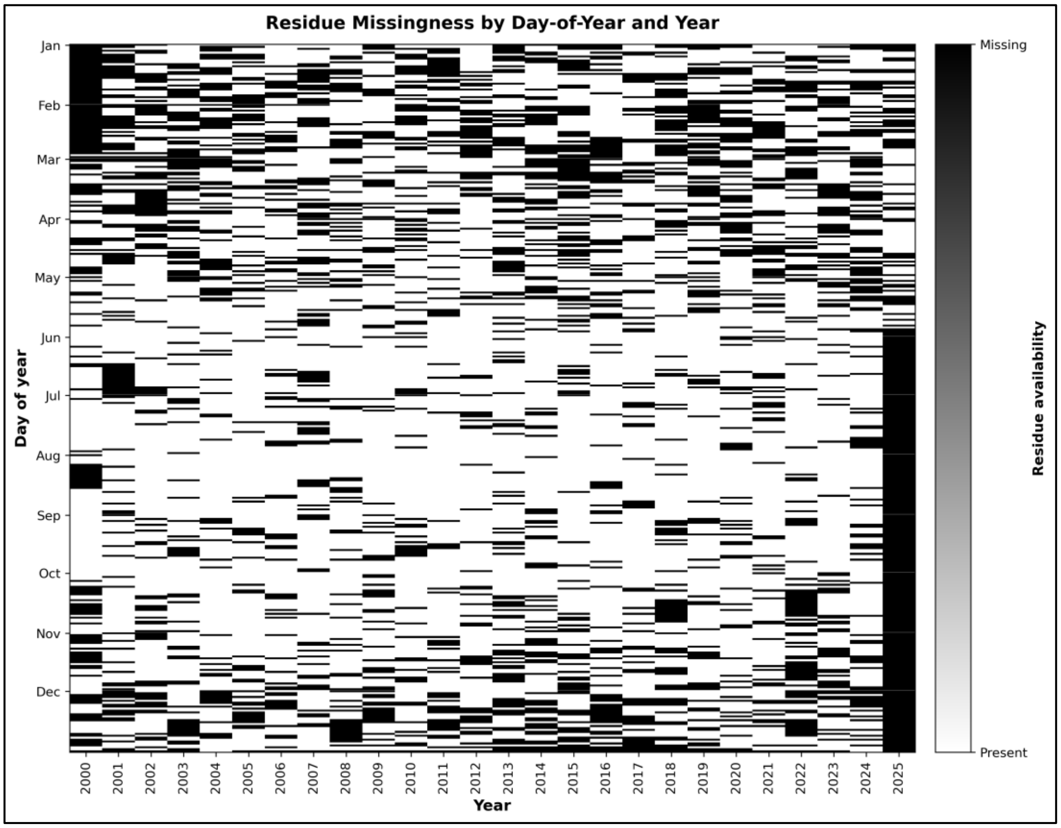

Figure 3.12. Residue (TSS) data availability based on MODIS data availability during the years (2000-2025).

3.6 Results and Analysis

This chapter evaluates the predictive accuracy of the Random Forest models and analyzes the hydro-climatic factors influencing sediment dynamics in the Nueces system. While the previous chapter established the spectral and temporal constraints of the satellite archives, the following sections present the validation of the TSS estimates against independent field datasets.

Furthermore, a stepwise correlation analysis (a statistical method that sequentially adds or removes predictors to identify significant drivers) was used to determine the sensitivity of these sediment concentrations to river discharge and precipitation events, providing a statistical basis for the spatiotemporal trends observed in the final model deployment.

3.6.1 Random Forest Model Validation Results

This section evaluates the predictive performance of the Random Forest models by comparing satellite-derived TSS estimates against independent field observations for both the bay and river systems. Table 3.14 shows the results of the Random Forest validation process using training and observed data sets. The validation results indicate an R^2 of 0.87 for TSS using MODIS data for the Bays. The Landsat data for the Nueces River achieved an R^2 of 0.53 for TSS.

Table 3.14. Random Forest model's validation performance metrics for the bays and the Nueces River in estimating TSS (Residue) using Landsat and MODIS datasets.

Sensor-Scope	Validation Data Source	R^2	RMSE	MAE
Landsat-Bays	TCEQ using 10% of Training data	-0.33	17.61	14.69
	UTMSI data (Averaged TSS)	-1.32	14.10	11.31
	UTMSI data (surface TSS)	-0.64	12.84	10.86
	UTMSI data (Bottom TSS)	-0.65	13.87	12.22
MODIS-Bays	TCEQ using 10% of Training data	0.15	10.25	8.41
	UTMSI data (Averaged TSS)	**0.87**	2.85	2.11
	UTMSI data (surface TSS)	-1.07	11.36	8.99
	UTMSI data (Bottom TSS)	0.65	5.84	4.66
Landsat-River	**TCEQ using 10% of Training data**	**0.53**	5.46	4.46
MODIS-River	TCEQ using 10% of Training data	-0.32	9.98	8.17

Following the spatial interpolation procedure detailed in Section 3.4, a continuous surface map was generated to facilitate analysis of sediment transport dynamics across the bays. The resulting prediction was color-coded on a continuous scale and overlaid on a base map, with values filtered due to cloud cover or missing data colored grey for clarity. A representative sample of this interpolated output is presented in Figure 3.13.

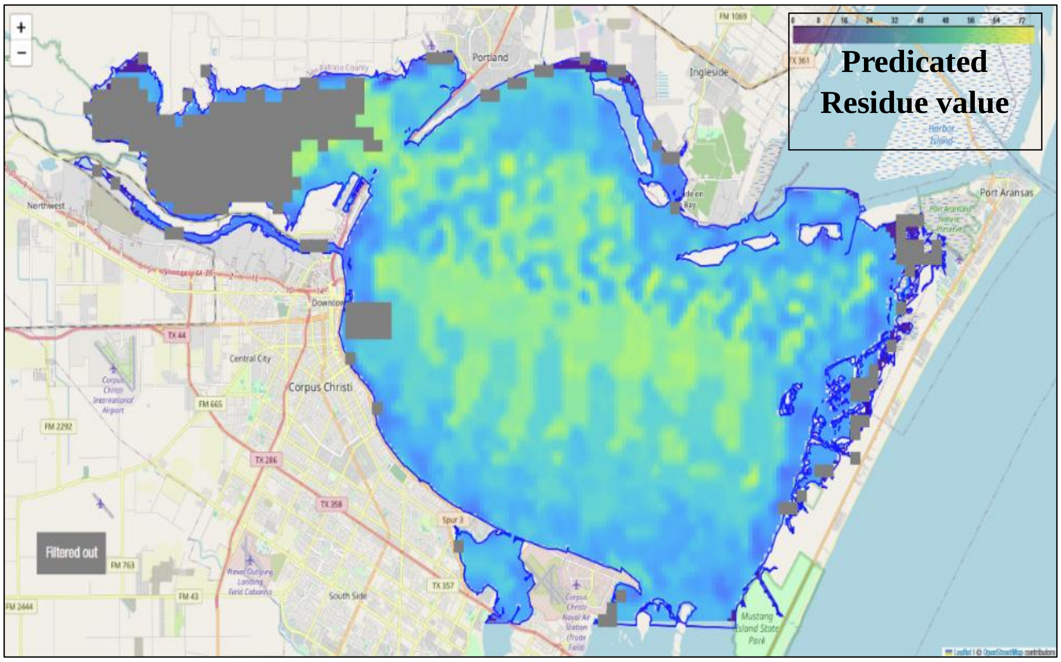

Figure 3.13. Interpolated Sediment Concentration Map from MODIS scene on 6th of March 2025 for Corpus Christi and Nueces Bays as a sample output. Note: the grey pixels indicate invalid points that didn't match the filtering criteria (i.e., clouds).

Although the Random Forest model demonstrates high predictive skill in the bay environment, the statistical validity of these estimates must be evaluated within the larger hydrological cycle. Understanding when and why these sediment spikes occur requires a shift from model validation to an analysis of external drivers.

The following sections investigate the relationships among freshwater inflow, precipitation magnitude, and resulting sediment concentrations in the Nueces River delta.

3.6.2 Correlations Between Flow, Precipitation, and Sediment Concentrations

To understand the physical drivers behind the predicted sediment patterns, the satellite-derived TSS estimates were integrated with synchronous hydrometeorological data. This integration enables a direct comparison between episodic weather events and the resulting sediment mobilization in the river delta. By utilizing the synchronized matchups established in the methodology (Section 3.3.1), the analysis focuses on how freshwater influx and rainfall intensity govern the concentration peaks observed in the bay system. The resulting one-to-one alignment ensures that every spectral sample represents a clear water surface, free from atmospheric interference or land-based noise, providing a robust foundation for the Random Forest algorithm to learn the relationship between light reflectance and observed sediment concentration.

Table 3.15. Summary of Predicted TSS Values and Corresponding Temporal/Spatial Matchups for MODIS across the Nueces and Corpus Christi Bay Systems.

Date	Station Latitude	Station Longitude	Spatial Offset (mm)	RESIDU avg (mg/L)	RESIDUE surface (mg/L)	RESIDUE bottom (mg/L)	Temporal Offset (Days)
6/19/2023	27.71139	-97.3064	0.1	23.2	26	20.4	0
6/19/2023	27.72056	-97.2081	0.6	110.85	25.9	195.8	0
6/19/2023	27.75528	-97.3094	0.5	32.4	42.3	22.5	0
6/20/2023	27.76889	-97.38	0.1	50.6	39.5	61.7	1
6/19/2023	27.77389	-97.2431	0.4	40.35	37.1	43.6	0
6/19/2023	27.79167	-97.1647	0.4	80.15	29.5	130.8	0
6/22/2023	27.80556	-97.2978	0.5	42	40	44	1
6/22/2023	27.8125	-97.3897	0.2	23.3	20.9	25.7	1
6/22/2023	27.82889	-97.4172	0.2	71.8	68	75.6	0
6/22/2023	27.835	-97.4697	0.2	44.85	38.7	51	0
6/19/2023	27.85444	-97.32	0.4	147.8	54.4	241.2	2
6/22/2023	27.85861	-97.4969	0.4	43.8	46.3	41.3	0
6/23/2023	27.8625	-97.4289	0.1	48.85	50.1	47.6	1
6/23/2023	27.86722	-97.3683	0.4	73.65	76.3	71	1
6/20/2023	27.87056	-97.2486	0.5	34.5	27.2	41.8	1

Table 3.16. Summary of Predicted TSS Values and Corresponding Temporal/Spatial Matchups for Landsat across the Nueces and Corpus Christi Bay Systems.

Date	Station Latitude	Station Longitude	Spatial Offset (mm)	RESIDUE avg (mg/L)	RESIDUE surface (mg/L)	RESIDUE bottom (mg/L)	Temporal Offset (Days)
6/17/2023	27.77388889	-97.24305556	0.5	40.35	37.1	43.6	2
6/17/2023	27.75527778	-97.30944444	0.5	32.4	42.3	22.5	2
6/17/2023	27.71138889	-97.30638889	0.2	23.2	26	20.4	2
6/17/2023	27.72055556	-97.20805556	0.6	110.85	25.9	195.8	2
6/17/2023	27.87055556	-97.24861111	0.5	34.5	27.2	41.8	4
6/17/2023	27.80555556	-97.29777778	0.5	42	40	44	4
6/17/2023	27.85444444	-97.32000000	0.5	147.8	54.4	241.2	4
6/17/2023	27.76888889	-97.38000000	0.1	50.6	39.5	61.7	4
6/17/2023	27.81250000	-97.38972222	0.2	23.3	20.9	25.7	4
6/17/2023	27.86722222	-97.36833333	0.4	73.65	76.3	71	5
6/17/2023	27.86250000	-97.42888889	0.1	48.85	50.1	47.6	5
6/17/2023	27.85861111	-97.49694444	0.4	43.8	46.3	41.3	5
6/17/2023	27.83500000	-97.46972222	0.2	44.85	38.7	51	5
6/17/2023	27.82888889	-97.41722222	0.3	71.8	68	75.6	5

Table 3.17 shows a sample of the TSS model inference results across the entire dataset. It includes the averaged TSS and the number of matched pixels within the selected polygon, based on MODIS data availability after cloud filtering (Table 3.9).

Table 3.17. Sample TSS output results based on the MODIS dataset. Only a subset of the output is provided below.

Scan Date	Average TSS (mg/L)	# of pixels averaged per polygon[b]	Total Valid Pixels Over full scan[a]	Valid Data over full scan (%)[a]
2000-02-27	25.40	36	8,324	13.32
2000-03-02	48.05	31	19,682	31.49
2000-03-06	48.94	3	16,520	26.43
2000-03-07	45.31	23	16,309	26.09
2000-03-09	29.47	27	16,758	26.81
…	…	…	…	…
2025-05-10	42.11	37	3,286	5.26
2025-05-16	52.22	19	9,935	15.89
2025-05-17	34.14	37	9,764	15.62
2025-05-18	45.94	36	4,262	6.82
2025-05-19	45.20	5	12,322	19.71

a Statistics for the full scan refer to the entire satellite scene after applying the spectral and cloud-filtering criteria.

b The polygon averaged count refers to the number of cloud-filtered 500 m pixels successfully retrieved.

To address gaps in the MODIS-derived residue time series, short gaps of up to three days were bridged using linear interpolation. The raw and interpolated series were then plotted and visually compared over a representative storm interval to assess their validity against observed data. Accordingly, the interpolated series was selected for inclusion in the analysis.

Over the sample interval shown in Figure 3.14, a three-day linear interpolation was applied to fill short gaps in the Residue record. This interpolation was needed to provide a continuous temporal series required for the subsequent cross-correlation analyses, as missing data points prevent the calculation of consistent lead-lag relationships. In sections where the raw series was complete, the interpolated values closely matched the observations, confirming that the method did not introduce artificial bias. However, to maintain data integrity, longer data gaps in MODIS-derived TSS values were not filled. This three-day linearly interpolated time series served as the basis for all subsequent statistical comparisons.

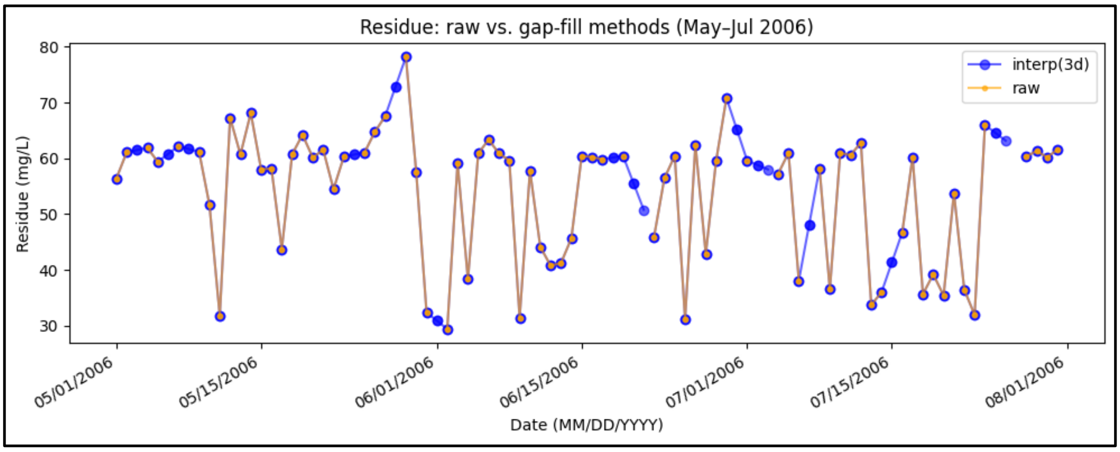

Figure 3.14. Comparison of raw and 3-day linear-interpolated sample Residue time series for the Nueces River delta polygon (Bays), demonstrating the gap-filling method used for the 2000–2025 temporal analysis.

3.6.3 Temporal Matching

Precipitation, flow, and sediment concentration data were aligned to a common daily time step. The initial gaps within each time series were identified and quantified (Table 3.18) before the 3-day linear interpolation. Multiple measurements recorded on the same date were averaged to yield a single daily value, and days lacking any of the three variables were removed. The filtered and merged daily dataset (Table 3.19), comprising days with complete precipitation, flow, and gap-filled Residue measurements, was then used for correlation analysis.

Table 3.18. Summary of initial missing raw daily data (pre-interpolation).

Dataset	Start Date	End Date	Percent of Missing Days %
Precipitation	1/1/2000	6/26/2025	0
Flow	1/1/2000	5/31/2025	0.28
Residue (TSS)	2/27/2000	5/27/2025	17.52

Table 3.19. Descriptive statistics of filtered and merged daily data.

	Count	Mean	σ	Min	P_{25}	Median	P_{75}	Max
Precipitation (mm)	9,222	2.2	8.7	0.0	0.0	0.0	0.3	218.9
Flow (ft3/s)	9,196	417.4	2215.5	0.0	0.0	14.7	81.2	47,800
TSS average (mg/L)	8,206	32.0	8.7	11.6	25.4	30.7	37.5	60.43

The historical relationship between hydrological drivers and sediment response is presented in Figure 3.15. To facilitate a comprehensive comparison of catchment-scale dynamics, Precipitation (mm), River Discharge (ft^3/s), and Average Residue (mg/L) were plotted concurrently. A central objective of this visualization was to examine the temporal relationship between episodic weather events and sediment mobilization. While Figure 3.15 displays concurrent peaks in Residue (TSS) and high-magnitude discharge pulses, particularly in the early 2000s and 2007, statistical analysis revealed that these associations are not sustained across the full dataset. The Pearson correlation between precipitation and Residue was found to be very low at $R = 0.034$ ($p < 0.001$), and Spearman's rank correlation was similarly negligible at $R = 0.036$ ($p < 0.001$). These low values indicate that while extreme events may cause visible spikes, there is no strong relationship between daily hydrometeorological drivers and sediment concentrations in the bay system.

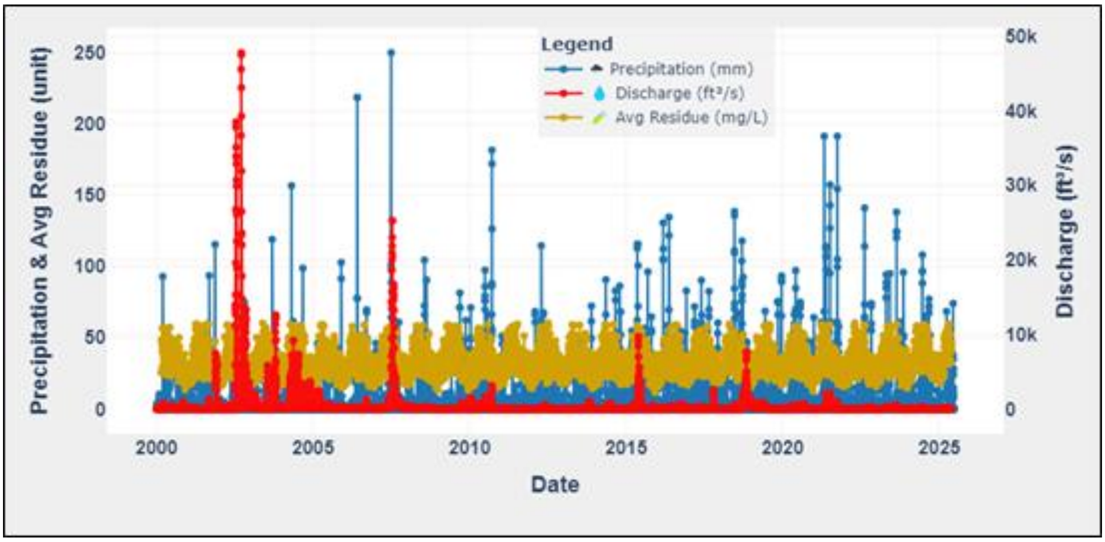

Figure 3.15. Temporal record of precipitation (mm), river discharge (ft^3/s), and predicted average residue (mg/L) from the MODIS-based Random Forest model 2000–2025.

3.6.4 Correlation Analysis

Figure 3.16 presents a scatterplot of daily precipitation versus sediment Residue utilizing the MODIS-derived dataset. Analysis was restricted to days with both measurements, yielding Pearson's correlation $R = 0.034$ ($p < 0.001$) and Spearman's rank correlation $R = 0.036$ ($p < 0.001$). Both coefficients were near zero, indicating a negligible relationship between instantaneous rainfall and Residue, despite the large sample size yielding statistical significance. While this high-frequency analysis relies on near-daily MODIS acquisitions, a similar assessment of Landsat-derived TSS over the Nueces River was constrained by the 16-day Landsat revisit cycle, which often misses the peak of rapid, storm-driven sediment pulses. Consequently, the Landsat data were primarily used for spatial validation rather than for high-resolution temporal correlation.

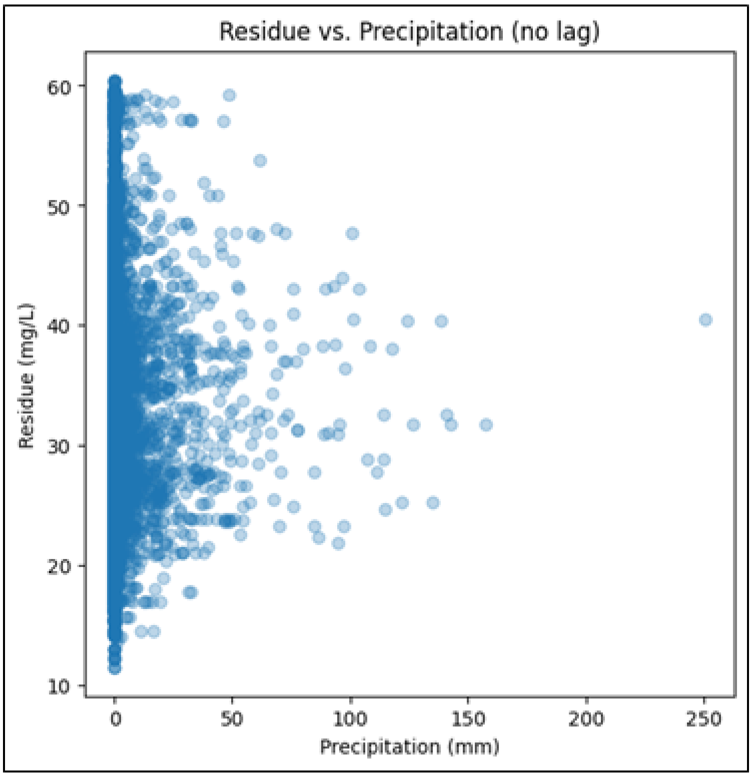

Figure 3.16. Scatterplot of daily MODIS-derived sediment Residue versus precipitation magnitude without temporal lag.

Having found no substantive relationship between daily rainfall and sediment Residue, the analysis was extended to examine lagged effects. As shown in Figure 3.17, log-transformed precipitation and the residue series were cross-correlated over lags of 0 to 30 days. Precipitation gaps were set to zero to retain event signatures. The resulting Pearson coefficients were not statistically significant at various time lags. This pattern suggests that sediment concentration aligned most closely with same-day rainfall and that any delayed response due to precipitation was minimal.

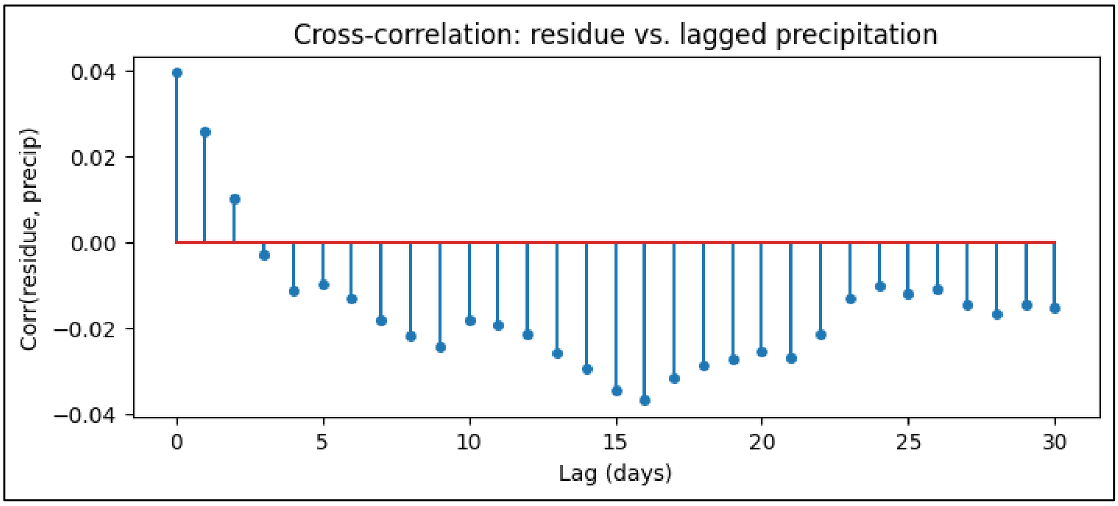

Figure 3.17. Cross-correlation of predicted TSS with lagged log-precipitation (0–30 day lags). The lag indicates the time offset in days between rainfall and sediment response; the results show that sediment concentrations align most closely with same-day rainfall (Lag 0), with no significant delayed response observed.

The following subsections present the results of the sediment analysis for discrete weather events, using the 10 mm precipitation threshold established in the methodology (section 3.5.1). This categorical approach allows for a direct comparison between 'storm' and 'normal' periods, as characterized in the event catalog presented in Table 3.20. These data serve as the basis for evaluating Residue fluctuations and isolated correlations during high-intensity rainfall occurrences.

In this work, for each of the 548 identified precipitation events (days where precipitation met or exceeded the 10 mm threshold), a ±5-day window of Residue values was extracted and aligned. The mean and standard error across all events were then computed to yield the composite response shown in Figure 3.18, which compares residue concentrations in the days leading up to these storms against the concentrations observed during and after the events to isolate the system's hydraulic response. The composite analysis demonstrates a distinct "flush-and-dilute" cycle, characterized by sediment concentrations that peaked immediately prior to a precipitation event and rapidly diluted during and after the storm.

Specifically, mean Residue values increased gradually from approximately 32.9 mg/L five days before a storm to a peak of 33.4 mg/L one day prior, then declined sharply to a minimum near 31.5 mg/L by the third day post-event.

Table 3.20. Characteristics of detected sample rainfall events. Only a subset of data is shown.

Storm Start Date	**Storm End Date**	**Storm Duration Days**	**Total Precipitation (mm)**	**Peak Daily Precipitation During Storm Event (mm)**
2000-03-14	2000-03-14	1	93	93
2000-04-12	2000-04-12	1	23.6	23.6
2000-05-02	2000-05-02	1	10.4	10.4
2000-05-13	2000-05-13	1	32.3	32.3
2000-05-19	2000-05-20	2	65.5	50.8
…	…	…	…	…
2024-12-04	2024-12-04	1	25.9	13.2
2025-01-09	2025-01-09	1	58.4	29.7
2025-01-10	2025-01-10	1	66	34
2025-01-15	2025-01-15	1	10.7	10.7
2025-01-21	2025-01-21	1	10.2	10.2

These pre-precipitation peaks likely resulted from the mobilization of accumulated fine sediments from riverbanks, while the subsequent drop reflected the dilution effect of increased freshwater volume. These results align with observations by Da Silva et al. (2015), confirming that high-magnitude precipitation in this system primarily flushed the channel and diluted existing suspended concentrations.

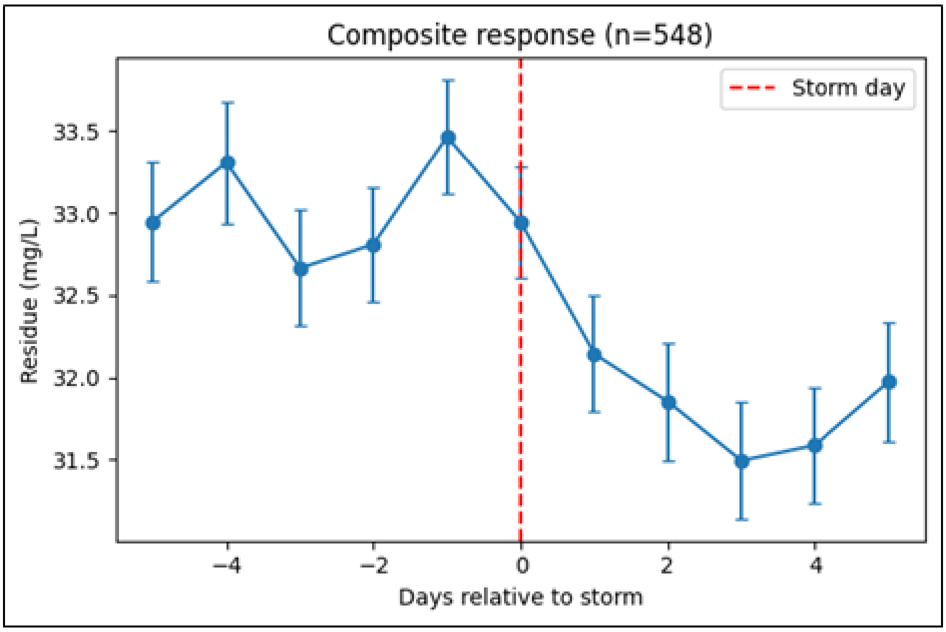

Figure 3.18. Composite residue response (mg/L) from MODIS-based Random Forest predictions during a 10-day window surrounding heavy-precipitation events (Day 0), illustrating the pre-storm peak and post-storm dilution trend over the Nueces River delta polygon.

The observed 'flush-and-dilute' mechanism indicates that moderate meteorological events do not facilitate a sustained increase in net total suspended solids. Instead, the rapid influx of freshwater serves as a temporal hydraulic reset, effectively decreasing TSS concentration following an initial pulse of shore- and bank-side mobilization. These results suggest that the bay's sediment variability is governed by a non-linear response to precipitation, with dilution effects dominating over additional transport during standard storm intervals.

Table 3.21 summarizes how the strength and significance of event-level Residue spikes vary as peak rainfall thresholds increase. At thresholds of 5–20 mm, both Pearson’s R and Spearman’s R remain effectively zero ($|R|<0.05$) and non-significant (p-value > 0.05), indicating no detectable linkages between rainfall and subsequent Residue response for these more frequent, moderate events in the Bays. As the threshold rises to 30 mm, correlations increase slightly (Pearson's R = 0.077; Spearman's R = 0.039), but remain nonsignificant. Only when considering the most intense storms ($\geq$ 50 mm), the coefficients attain values

(Pearson R = 0.145; Spearman R = 0.179), with Spearman's p-value = 0.038, suggesting a weak, but significant monotonic association, although based on a sample (*n* = 134). These findings imply that sediment concentration spikes in the Bays are largely insensitive to rainfall during moderate-to-heavy rainfall events and suggest the dominance of tidal processes.

Table 3.21. Sensitivity of Event-Level Residue (TSS) Correlations to Peak-Rainfall Threshold.

Precipitation Threshold (mm)	Number of Events	Pearson correlation coefficient (R)	Pearson p-value	Spearman correlation coefficient (R)	Spearman p-value
5	811	0.008	0.810	-0.038	0.285
10	811	0.008	0.810	-0.038	0.285
15	618	0.026	0.519	-0.004	0.928
20	477	0.011	0.816	-0.048	0.300
30	318	0.077	0.168	0.039	0.489
50	134	**0.145**	0.094	**0.179**	0.038

Figure 3.19 illustrates the relationship between peak precipitation and the resulting Total Suspended Solids (TSS) spike for high-intensity storms (≥ 50 mm; n = 134). These spikes were defined as the maximum deviation in the Random Forest model-estimated TSS values for the Bays within a ±5-day window around each event. Linear regression yielded a slope of 0.037 and an $R^2 = 0.021$, indicating that peak rainfall magnitude explains only about 2% of the variance in sediment response. Pearson's r (≈ 0.145, p = 0.094) and Spearman's r (≈ 0.179, p = 0.038) both confirm a weak but positive association. Although the correlation is

weak, the consistent upward trend suggests that more intense storms contribute incrementally to sediment mobilization. The broader implications and limitations of this finding will be discussed in the following section.

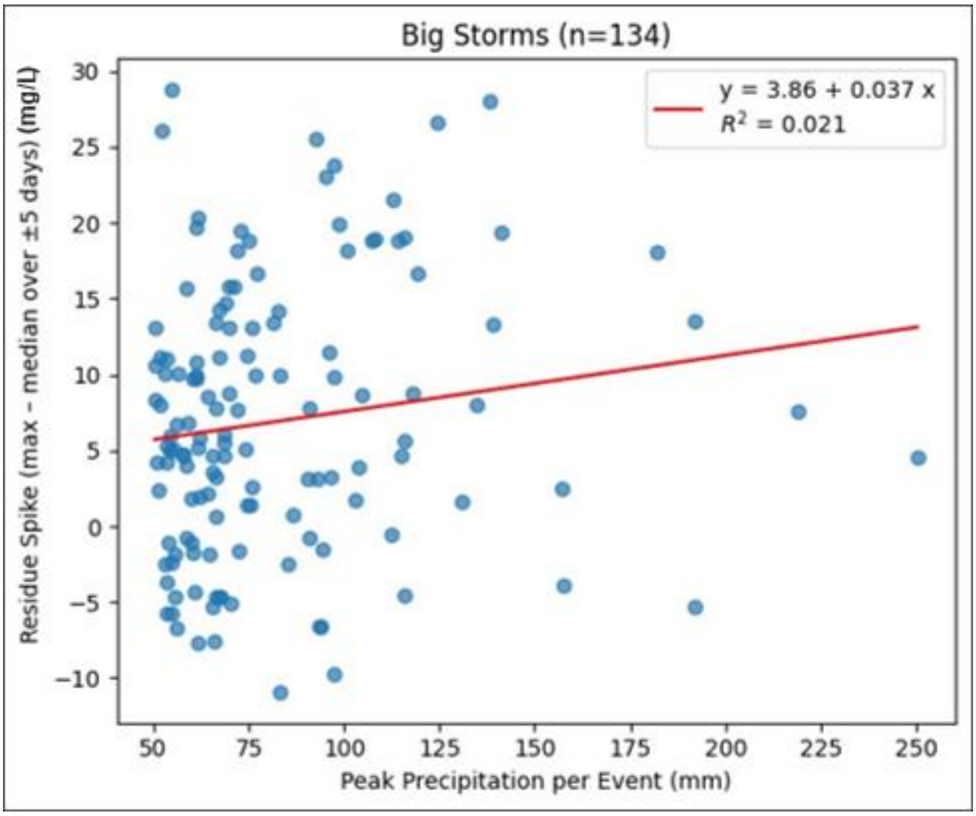

Figure 3.19. Relationship Between Peak Precipitation and Post-Event Residue Spike for High-Intensity Storms (≥ 50 mm; n = 134).

3.6.5 Spatial-Temporal Observability of the Nueces River

This section evaluates the spatial and temporal reliability of the Landsat 8 archive to identify the physical constraints affecting model performance within the Nueces River. By quantifying grid-level coverage and observational density, this analysis justifies the moderate predictive accuracy of the river models compared to broader bay segments.

A statistical summary (Table 3.22) was derived from aggregated grid- and scan-level metrics. This included:

- Mean coverage percentage across successful scans.
- Mean coverage percentage across all scans (including failures).
- Percentage of the river ever observed with valid data.
- Mean, minimum, and maximum number of observation days per grid cell.

These metrics quantify both the spatial extensiveness and the temporal depth of the Landsat archive over the Nueces River system, providing a direct measure of dataset reliability for hydrologic applications.

Table 3.22. Statistical Summarization of Spatial–Temporal Coverage for Landsat Imagery in the Nueces River segment.

Category	Metric	Observed Coverage Value	Units	Description
Area per scan	River total area	75.66	km^2	Total area of the river polygon.
	Mean covered area	24.49	km^2	Mean area covered by valid pixels per successful scan.
	Mean coverage pct (successful scans)	32.37	%	Mean % of river area covered per successful scan (scans with 0% are excluded).
Temporal aggregate	Cumulative area observed	69.84	km^2	Total unique river surface area captured by valid pixels at least once during the study period, representing the cumulative sensor footprint.
	Cumulative coverage pct	92.3	%	% of total river area that had valid data on at least one day.
	Total unique days with data	468	Days	Total number of unique dates with successful scans.
	Mean days per cell	115.38		Mean number of days a grid cell had data (averaged over all in-river cells).
	Min days per cell	0		Minimum number of days any in-river grid cell had data.
	Max days per cell	251		Maximum number of days any in-river grid cell had data.

The reliability of the Landsat 8 archive was assessed across the 75.66 km^2 river polygon. Successful scans yielded a mean area coverage of 24.49 km^2 (32.37%) per overpass. While the cumulative sensor footprint captured 69.84 km^2 (92.3% of the study area), the temporal depth remained limited to 468 unique observation dates.

On a granular level, cells were observed for an average of 115.38 days. However, observational density varied significantly; some cells were captured on 251 dates, while others remained unobserved due to atmospheric interference or sensor swathing constraints. This spatial and temporal fragmentation provides the physical justification for the moderate predictive accuracy of the river-based models

This limited observational frequency was primarily due to the high degree of temporal and spatial fragmentation in the dataset. As illustrated in the Observational Density Map (Figure 3.20), valid observation days were not temporally synchronized among grid cells. Consequently, generating a composite map for any given acquisition date yielded only spatially fragmented, disconnected map portions, with each day representing only a small fraction of the overall study area. Furthermore, because this temporal availability was unevenly distributed across seasons and locations, the dataset lacked the continuous, coordinated patterns necessary to support robust investigations into seasonal dynamics or long-term trends. These data gaps and synchronization issues provided the primary physical justification for the moderate predictive skill ($R^2 = 0.53$) observed in the Landsat river models.

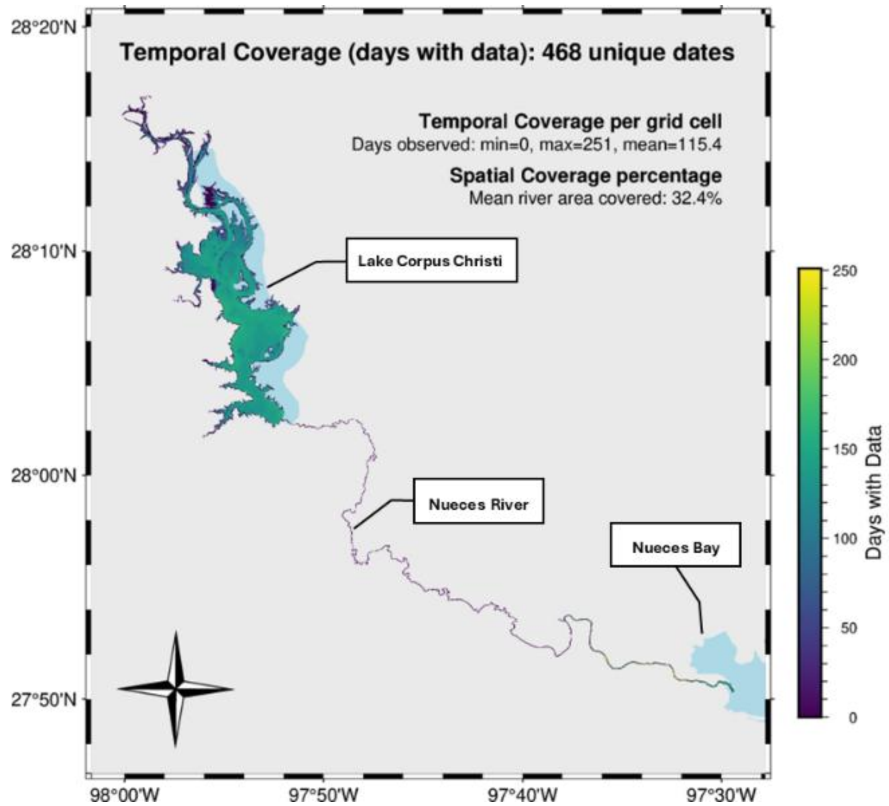

Figure 3.20. The Observational Density Map represents the total number of valid observation days per grid cell.

3.6.6 Summary and Limitations of Correlations

In summary, daily precipitation, flow, and Residue data were aligned and filtered to create a consistent time series for correlation analysis for the Bays. Rescaling each series to a 0–1 range highlighted the continuous variability of sediment Residue, in contrast to the episodic nature of rainfall and discharge. Both Pearson and Spearman correlations between Residue and precipitation (with and without a temporal lag) were negligible, and only the most extreme storms (≥ 50 mm) produced a weak, monotonic association that was not statistically significant, explaining roughly 2% of the variance in sediment spikes in the Bay section. Composite event analysis further revealed a consistent pattern of gradual Residue buildup preceding heavy rainfall and rapid decline afterward, underscoring the dominant influence of same-day hydrodynamics on sediments. This is expected since the Bay Area is significantly affected by tides, whereas precipitation events may not play a major role in TSS concentrations.

Several limitations may have constrained these results. First, in-situ TCEQ measurements were sparse, yielding a small training set and limiting the model's ability to learn extreme Residue values (> 60 mg/L). Second, the infrequent revisit of Landsat, despite its higher spatial resolution, limited synchronous pairing with ground data, forcing reliance on coarser MODIS imagery and further limiting the model's ability to resolve short-lived, high-magnitude events. Third, cloud masking systematically discarded rainy and stormy pixels from both training and inference, creating temporal gaps that may have obscured precipitation–Residue relationships.

Finally, unmodeled basin factors, such as dam operations, land-use change, and in-bay biogeochemical processes, likely contributed to residual variability independent of rainfall. Future work should seek to increase ground sampling density, exploit multi-sensor data (including cloud-penetrating platforms) to recover missing observations, and capture the full suite of controls on sediment transport.

3.7 Model Implementation and Spatio-Temporal Analysis

This chapter describes the operational implementation of the validated Random Forest model to characterize long-term sediment dynamics in the Nueces and Corpus Christi Bays. By deploying the algorithm across the 25-year MODIS archive, point-based spectral observations were transformed into continuous geospatial products that revealed the underlying patterns of sediment transport. The following sections evaluate these results on both monthly and annual scales to identify the recurring seasonal cycles and spatial hotspots that define the system's sediment regime.

3.7.1 Random Forest Inference

After the spatial and spectral filtering described in section 3.5.2, the retained TSS values within the bay boundaries were interpolated using cubic splines to generate continuous surfaces. A consistent color gradient and a rescaled concentration ranging from 0 to 80 mg L^{-1} were applied to facilitate visual comparability across dates. The final maps distinguished between valid pixels, represented by the color scale, and invalid pixels, denoted in grey to indicate the absence or exclusion of data.

Using coding, the workflow starts with importing daily prediction TSS values and a single bay boundary polygon. Plotting parameters were fixed across products, notably a residue concentration ranged from 0 to 80 mg/L and a grid size of 500 m × 500 m. TSS Predictions with negative values were flagged as “invalid,” while non-negative values formed the “valid” subset used in gridding.

Map production was performed for each date, and the script computes summary statistics from the gridded field (minimum, maximum, and mean TSS). Each file was processed independently: reading, filtering, interpolating, masking, and plotting. Figure 3.21 presents a sample of the generated spatiotemporal maps for TSS concentration in the study area.

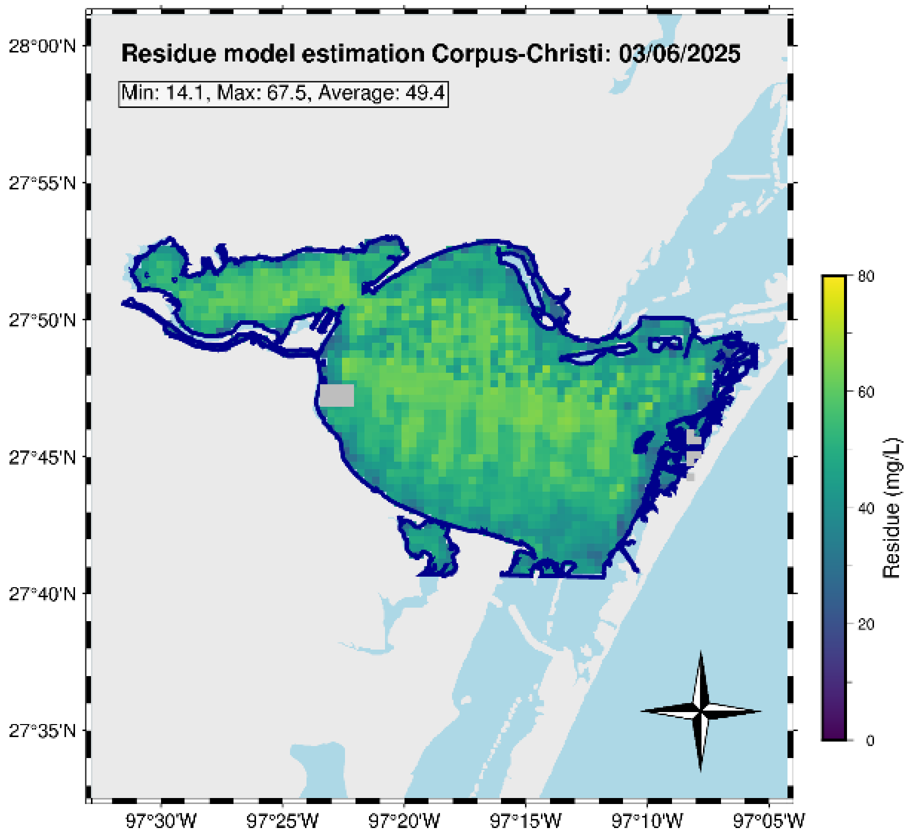

Figure 3.21. Spatio-temporal map for TSS concentration (mg/L) in the Corpus Christi Bay and the Nueces Bay in March/2025.

Figure 3.22 illustrates the key questions guiding the assessment of suspended solid dynamics within the study area. The temporal aspect focused on determining the period during which suspended solids were relatively higher, while the spatial aspect addressed where the highest levels were observed. Together, these components provided a basis for evaluating both seasonal variability and spatial distribution patterns of suspended sediments in the bay system.

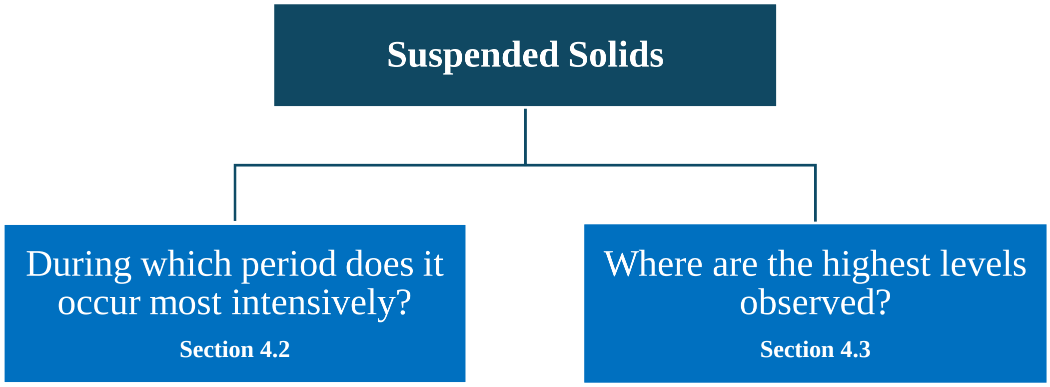

Figure 3.22. Conceptual framework for analyzing suspended solids.

While high-resolution spatial maps provide snapshots of specific environmental conditions, they do not inherently capture the long-term temporal trends that define the system's baseline. To move beyond isolated events, the following assessment shifts to a multi-decadal statistical aggregation. By synthesizing 304 consecutive monthly estimations from 2000 to 2025, it was possible to delineate “normal” background concentrations from episodic spikes, thereby establishing the characteristic seasonal cycle for the Nueces and Corpus Christi Bays.

3.7.2 Assessment of TSS

This assessment quantified the temporal variability of the Residue (TSS) over a 25-year monitoring period (2000–2025). The following subsections detail the statistical properties of the dataset, outline observed temporal extremes, and define the seasonal cycle.

Based on N = 304 consecutive monthly estimations of the mean residue spanning the 25-year period from February 2000 through May 2025 (Table 3.23), the monitoring record indicated a system characterized by long-term stability in the mean, but considerable variability driven by short-duration sediment transport events. Sediment concentrations exhibited a clear seasonal cycle, with the lowest levels occurring during the winter months, particularly in December (22.8 mg/L), and increasing in early spring, peaking in April (36.8 mg/L) and May (35.8 mg/L).

Table 3.23. Bay Monthly Summary for residue in the study period.

Month across study period	Mean (mg/L)	Min (mg/L)	Max (mg/L)	Median (mg/L)	85th Percentile (mg/L)	95th Percentile (mg/L)	Daily grids used (Day)
January	27.199	0.004	92.794	25.700	39.137	47.013	15.400
February	25.564	0.006	90.712	24.682	36.190	43.735	12.320
March	31.770	0.232	93.104	30.840	45.801	53.062	15.760
April	36.850	0.220	193.358	34.372	51.000	59.434	16.880
May	35.821	0.040	140.399	33.959	49.323	58.785	20.680
June	31.229	0.016	237.634	29.053	43.518	51.415	23.520
July	30.058	0.018	158.004	28.409	40.648	49.203	25.240
August	28.254	0.042	199.905	26.623	37.801	47.330	26.280
September	26.902	0.080	103.904	24.669	38.122	46.146	21.560
October	24.358	0.025	90.661	22.576	33.150	39.804	21.080
November	25.497	0.018	90.669	24.255	35.000	41.858	17.800
December	22.835	0.034	84.187	21.270	31.565	38.650	15.160

The analysis of the raw time series revealed the range of average monthly TSS concentrations. Table 3.24 illustrates the Absolute minimums and maximums for the study period, and it is derived from Table 3.23.

Table 3.24. Summary of the Monthly Average TSS across the Nueces and Corpus Christi Bays over the entire 25-year study period.

	Mean Residue	Min Residue	Max Residue	Median Residue	P85 Residue	P95 Residue
Maximum Value (mg/L)	43.003	7.154	237.634	42.958	54.756	60.706
Date (Year-Month)	2022-04	2012-02	2007-06	2022-04	2022-04	2022-04
Minimum Value (mg/L)	19.946	0.004	43.068	18.792	24.875	27.975
Date (Year-Month)	2011-12	2014-01	2012-02	2001-12	2001-12	2018-02

To facilitate the comprehension of Table 3.24, an explanatory example is detailed below:

- Maximum Monthly Mean TSS: The highest monthly mean concentration recorded over the entire 25-year history was 43.003 mg/L, recorded in April 2022.
- Minimum Monthly Mean TSS: Conversely, the lowest recorded monthly average concentration was 19.946 mg/L, observed in December 2011.

3.7.3 Temporal Distribution

A representation of the temporal distribution of TSS concentration in the Corpus Christi and Nueces Bays across the 25-year study period is shown in Figure 3.23, based on the 85th percentile. Notably, April recorded the highest values and frequency across all years of the study period (2000-2025). This peak aligns with the 'Spring Wind Maximum' in South Texas, where the increase of the North Atlantic Subtropical High generates sustained, high-velocity southeasterly winds (Jeter & Wu, 2020). In the shallow environments of the Nueces and Corpus Christi Bays, these powerful spring winds induce the resuspension of fine benthic sediments that remain elevated throughout the season (Vaughan et al., 2021). This wind-driven mechanism, rather than river discharge alone, might explain the high frequency of TSS spikes observed during this window (Conkle et al., 2022).

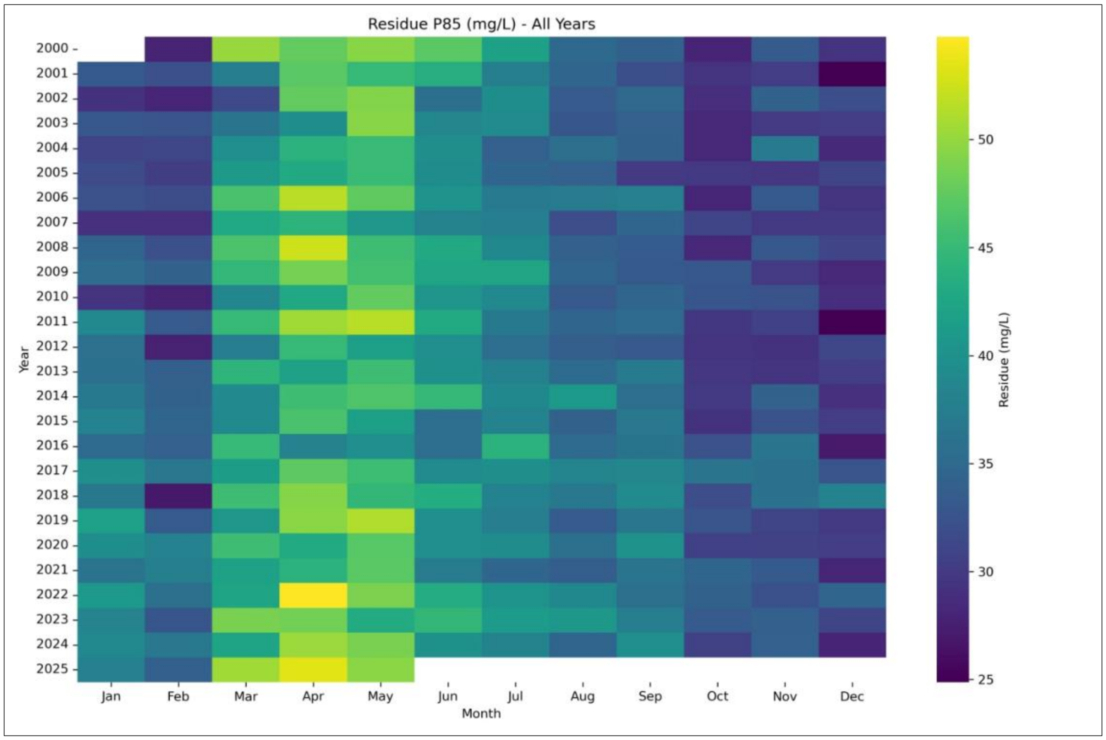

Figure 3.23. Temporal distribution of the TSS concentration in the Corpus Christi and the Nueces Bays across the 25-year study period.

For the 25-year series, the overall mean TSS was established at 29.563 mg/L. The median value was 28.073 mg/L. The overall context of the TSS monitoring is summarized in Table 3.25.

Table 3.25. Overall monthly TSS Descriptive Statistics (2000–2025).

Metric	TSS (mg/L)
Overall Mean	29.563
Median	28.073
Standard Deviation (SD)	5.093

The visualization in Figure 3.24 is based on Table 3.24, which provides a monthly summary of residue across the study period. It can be observed (depending on the 85th percentile) that the spikes exceed 40 mg/L, a threshold that indicates poor water quality, specifically for aquatic life.

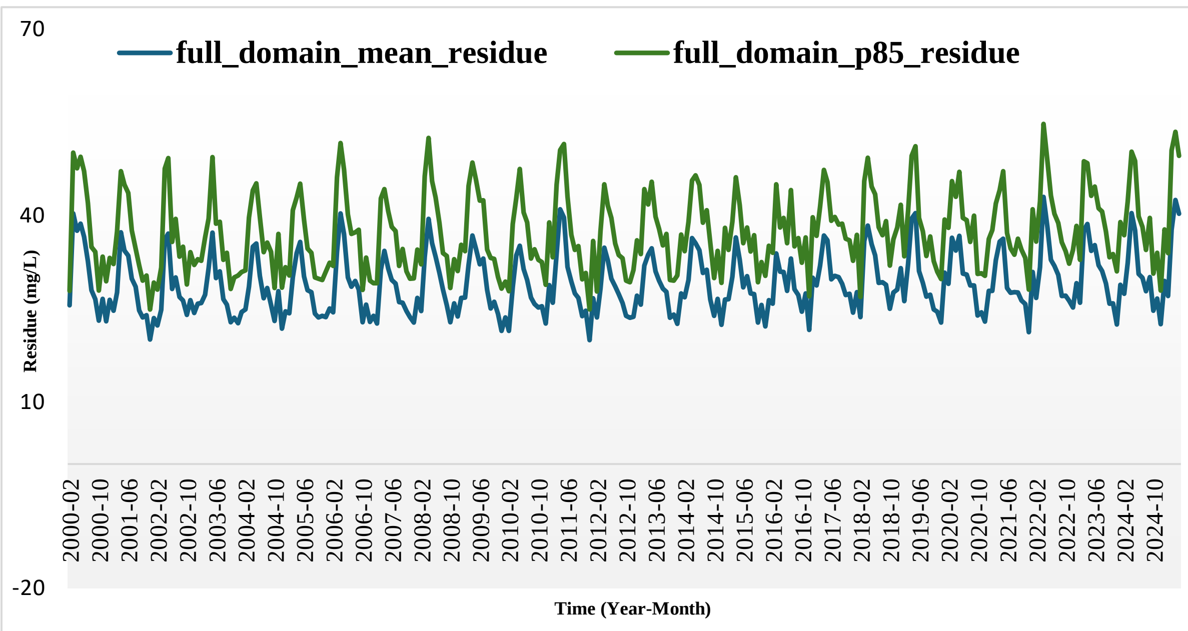

Figure 3.24. Monthly representation of the predicted residue in the study period. The P85 notation refers to the 85th percentile.

Table 3.26 presents the annual summary for the grids covering the Nueces and Corpus Christi Bays for every year of the entire study period. The table contains statistics for suspended solids concentration (e.g., mean, minimum, maximum, 85th percentile, 95th percentile, and the daily grids used).

Suspended sediment data are typically right-skewed due to episodic storm-driven sediment pulses. Therefore, using a high percentile (e.g., the 85th percentile) provides a stable representation of elevated sediment conditions while reducing the influence of extreme outlier events (Horowitz, 2010).

Table 3.26. Annual summary for TSS (mg/L) in the study period (2000-2025).

Year	mean residue	min residue	max residue	85th percentile residue	95th percentile residue	daily grids used
2000	31.85	0.02	134.11	43.84	52.77	186
2001	27.81	0.04	116.57	38.06	47.38	216
2002	28.15	0.04	142.06	38.29	49.01	232
2003	27.77	0.19	132.67	36.70	47.23	224
2004	27.94	0.01	147.47	37.86	47.28	243
2005	27.81	0.16	110.72	36.60	46.71	262
2006	29.31	0.08	157.93	40.58	50.24	240
2007	26.98	0.13	237.63	35.85	45.22	227
2008	29.44	0.30	199.91	40.19	50.17	238
2009	29.69	0.04	157.05	40.97	50.76	250
2010	27.74	0.05	100.98	37.21	47.05	249
2011	29.86	0.02	117.31	41.27	51.26	263
2012	28.02	0.03	101.58	37.05	47.23	241
2013	28.72	0.04	155.90	39.21	48.74	227
2014	30.13	0.00	193.36	41.11	50.76	223
2015	27.81	0.25	110.57	37.27	46.90	207
2016	28.51	0.15	113.75	38.61	48.17	239
2017	30.27	0.01	108.14	40.91	50.22	247
2018	31.09	0.06	115.97	42.37	50.59	216
2019	29.50	0.02	122.24	40.27	49.90	224
2020	29.28	0.03	177.61	39.79	49.67	241
2021	28.30	0.10	108.55	38.23	47.40	229
2022	31.56	0.02	110.09	43.25	53.18	219
2023	30.62	0.04	103.11	41.82	50.69	229
2024	29.28	0.02	140.89	39.61	50.08	205
2025	36.79	0.23	135.86	49.92	57.01	71
All years (Average)	**29.39**	**0.08**	**136.62**	**39.88**	**49.45**	**224.92**

Referring to Table 3.26, the 85th percentile across all years was 39.88 mg/L. This matches the Recent TSS analyses of Corpus Christi Bay, which present median and interquartile concentrations and emphasize percentile summaries to describe typical conditions (Reisinger et al., 2017). Regional USGS monitoring and source studies also provide context for typical and event-driven suspended-sediment concentrations in the Nueces–Corpus system (Ockerman, 2013). Both studies used a percentile-based threshold of ~40 mg/L.

TSS Concentrations begin to increase in late winter, rising sharply through March (32.06 mg/L). The definitive peak occurs in April (37.19 mg/L), followed closely by May (36.31 mg/L). Following the spring peak, TSS levels decline throughout the summer and early fall, reaching their lowest long-term average in October (24.18 mg/L). Specifically, high TSS concentrations during March-May align with the peak spawning and reproductive seasons for many estuarine-dependent species (e.g., Red Drum and Blue Crab) and therefore, are critical. Elevated TSS during these months can significantly influence larval development, as excessive turbidity can impair the foraging efficiency of visual predators or clog the gills of juvenile fish, while simultaneously providing essential cover from larger predators (Ockerman, 2013; Montagna et al., 2013).

While temporal analysis defines the timing of sediment spikes, a comprehensive management framework also requires identification of their spatial distribution. By applying the statistically derived exceedance threshold to the 25-year observational record, the following section translates these temporal trends into a series of spatial heat maps. This approach delineates the specific zones where sediment concentrations chronically exceed typical background levels, providing a geographical basis for analyzing the transport mechanisms within the bay system.

3.7.4 TSS Spatial Trends and Hotspots

According to the Michigan Department of Environment, Great Lakes and Energy (EGLE), the TSS values in water above 40 mg/L tend to appear cloudy and are indicative of impairment for aquatic organisms. Thus, a TSS threshold of 40 mg/L is considered highly elevated or an exceedance event. To ensure the reliability and interpretability of the geospatial visualizations, rigorous data coverage requirements were strictly enforced: a minimum of 70% spatial coverage was required for all long-term map products, while a threshold of 60% was applied to products temporally resolved at a yearly or monthly basis. The analysis was structured into three distinct map categories to characterize both the spatial extent and the temporal distribution of TSS.

First, to summarize the spatial trend over the entire period, two visualizations were produced: The 85th Percentile Map was generated by calculating the 85th percentile of all observed residue values for every grid location (pixel). This visualization identifies areas where the concentration consistently falls in the upper 15% of the total distribution, delineating locations with persistently elevated TSS levels. The Average Exceedance Days per Year Map was produced to quantify the annualized risk and exposure frequency. This was done by counting the annual number of days when the concentration at a given pixel exceeded the 40 mg/L threshold, then calculating the ensemble average across all years. The resulting visualization provides an essential planning and regulatory metric, indicating the typical number of days per year that the elevated concentration standard is not met.

Second, for assessing seasonal variability, a category of Monthly Spatio-Temporal Maps was generated. This included 12 distinct Average Exceedance Days per Month Maps, created by calculating the multi-year average monthly exceedance counts (days > 40 mg/L) for each calendar month.

Figure 3.25 shows the number of days per year that each location typically exceeds the 40 mg/L threshold. This figure is useful for understanding seasonal patterns and for management planning. For each year, exceedance days per pixel were counted, then averaged across all years. pixels with ≥ 60% valid days per year were only included.

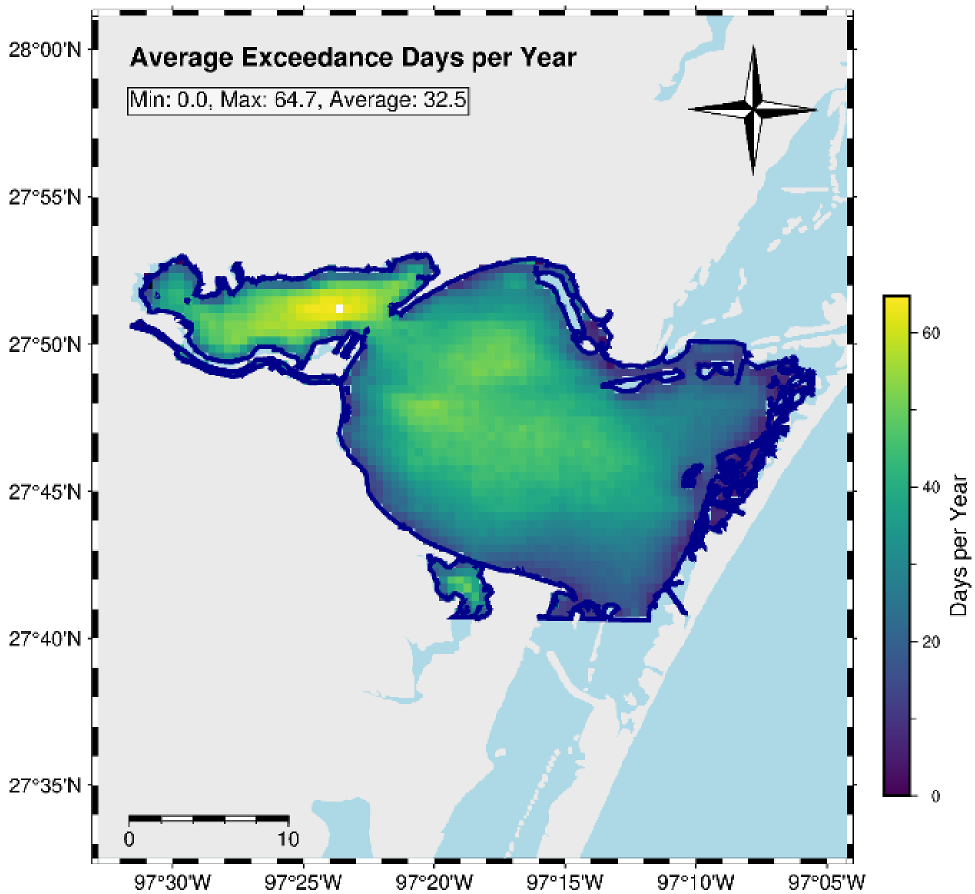

Figure 3.25. Heatmap of the Average Exceedance Days per Year (number of days per year each location that typically exceeds the threshold).

To investigate the hypothesized "flush-and-dilute" mechanism across different bay regimes, Figure 3.26 presents an analysis of TSS concentrations immediately after isolated high-intensity precipitation events. This spatial analysis explicitly compares the bay's response to Hurricane Beryl (July 8, 2024), which produced approximately 100–150 mm of rainfall across South Texas over a 48-hour period, with that of a higher-magnitude (greater than 50 mm) extreme storm event. The subfigures are organized as follows: (a) provides the geographical baseline and the path of the Hurricane Beryl composite; (b) depicts the immediate response to Beryl's passage. Collectively, this figure provides evidence that large-scale freshwater influx from intense events attenuates, rather than elevates, total suspended solids across the wider bay.

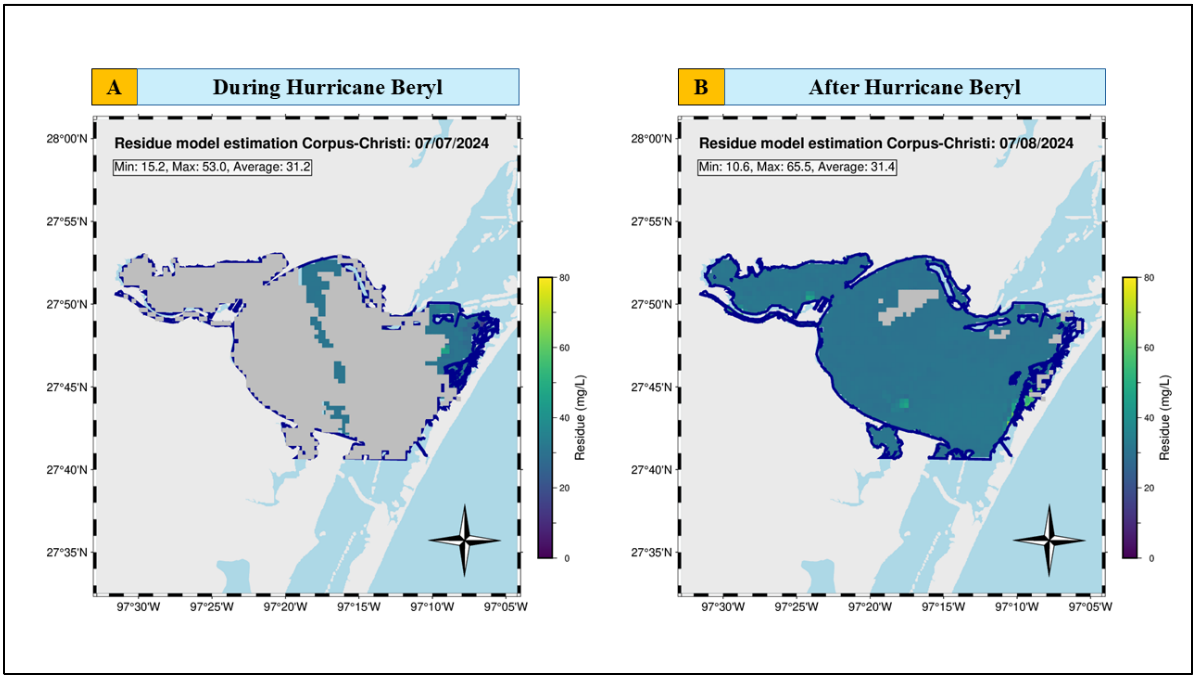

Figure 3.26. Comparative Spatiotemporal Analysis of TSS Dilution Dynamics Following Hurricane Beryl: (a) TSS concentration during the storm event (July 7, 2024), and (b) TSS concentration after the storm event (July 8, 2024). Hurricane Beryl produced approximately 100–150 mm of rainfall across South Texas over 48 hours.

A composite time series of annual sediment transport mechanisms within the Corpus Christi and Nueces Bay system was developed using twelve monthly heatmaps, as shown in Figure 3.27. This spatial matrix illustrates the seasonal relocation of discharged sediments across both bay environments. The visualization suggests that sediments initially aggregate near the Nueces River estuary and then migrate toward the Nueces Bay Causeway. From this point, the material appears to be ultimately discharged into the main Corpus Christi Bay, forming visible sediment plumes that gradually dilute as they spread across the larger bay.

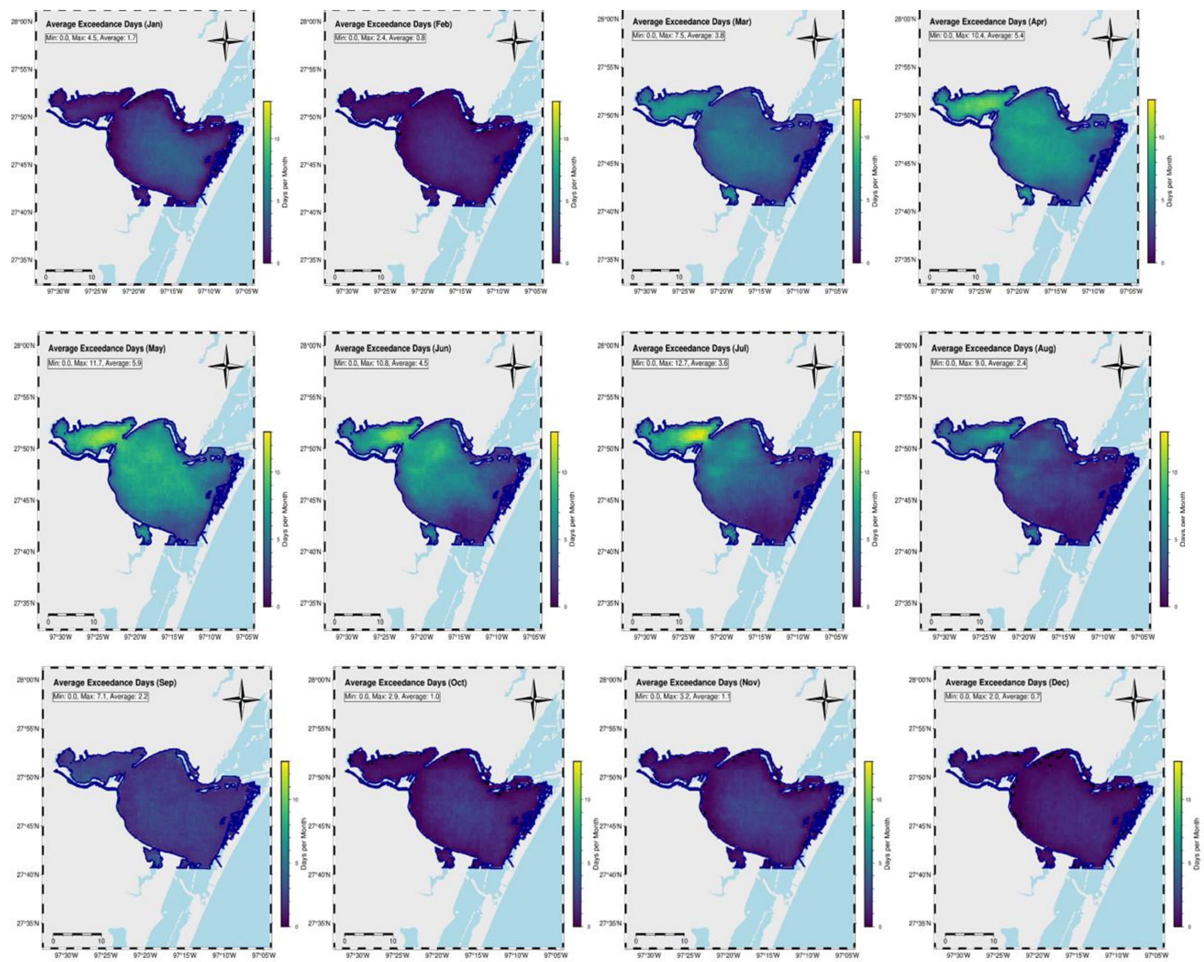

Figure 3.27. Monthly Composite Matrix of Average Exceedance Days (TSS > 39.88 mg/L) across the 25-Year Study Period.

The increase of these transport mechanisms during the March-May transition, peaking in April, is likely influenced by several interacting hydro-climatic factors. One potential driver is the "first-flush" phenomenon, where fine sediments accumulated during the winter dry season are rapidly mobilized by the onset of spring precipitation and increased freshwater discharge.

Furthermore, the system's physical hydrography suggests that wind-driven resuspension may play a critical role in this migration. The shallowness of Nueces Bay, which averages less than 1 meter in depth, allows seasonal wind patterns to keep sediments in suspension, facilitating their transport into the deeper Corpus Christi Bay (Ockerman, 2013; Montagna et al., 2013). Conversely, the lower activity observed in December may correspond to periods of low wind energy and minimal precipitation, potentially allowing a temporary "hydraulic reset" of the system's baseline TSS concentrations (Ward, 2024). Additionally, TSS concentration in the Bays is also affected by tidal hydrodynamic mixing.

Chapter 4. SWAT-Based Hydrological Assessment of Sediment and Nutrient Loads

In this study, SWAT was applied to evaluate streamflow, sediment, total nitrogen, and total phosphorus loading in the Nueces River Watershed. The model was developed from an existing calibrated Nueces watershed SWAT model and refined for sediment and nutrient simulation. Calibration and validation were conducted using observed streamflow and water-quality data at a monthly time scale.

4.1 Introduction

The movement of sediment and nutrients from watersheds to downstream receiving water bodies is a major concern in water resources management. Sediment transport influences stream channel stability, reservoir storage, aquatic habitat quality, turbidity, and the delivery of sediment-associated pollutants (Carpenter et al., 1998). Nutrient enrichment, particularly from nitrogen and phosphorus, can accelerate eutrophication, increase algal productivity, reduce dissolved oxygen, and degrade aquatic ecosystem functions in rivers, reservoirs, and coastal receiving waters (Smith et al., 1999). Because sediment and nutrient transport are strongly controlled by rainfall, runoff generation, land use, soil properties, channel routing, and watershed management, process-based watershed models are useful tools for evaluating the sources, transport pathways, and potential reduction strategies for nonpoint-source pollution (U.S. Environmental Protection Agency, 2026).

The Nueces River Watershed is an important hydrologic system in South Texas and supplies freshwater to Nueces Bay, which forms part of the larger Corpus Christi Bay system (Anchor QEA, 2017). The watershed is characterized by semi-arid climatic conditions, highly variable and seasonal rainfall, extensive rangeland and agricultural areas, localized urban development, and major reservoir operations, particularly those associated with Choke Canyon

Reservoir and Lake Corpus Christi (HDR Engineering, Inc., 2000). These watershed characteristics create complex interactions among streamflow, sediment transport, and nutrient loading. During high-rainfall periods, increased runoff and streamflow can erode upland soils and mobilize sediment from channel banks and streambeds, while transporting dissolved, suspended, and sediment-associated forms of nitrogen and phosphorus downstream (Baird et al., 1996; EPA, 2026). During dry periods, lower streamflow reduces the capacity of the river to mobilize and transport sediment; however, reduced dilution, longer water residence times, and slower water movement can increase the susceptibility of downstream water bodies to nutrient enrichment, algal growth, and related water-quality degradation (EPA, 2000, 2026).

The Nueces–Corpus Christi Bay system is sensitive to both changes in sediment supply and the delivery of pollutants from surrounding watersheds (Ward and Armstrong, 1997). The delivery and deposition of sediment can help form and maintain coastal wetlands, shallow-water habitats, and other geomorphic features; however, transported sediment can also provide a pathway for sediment-associated contaminants (Kirwan et al., 2011; Schoellhamer et al., 2012). Sediment can transport particulate-bound nutrients, metals, pesticides, polycyclic aromatic hydrocarbons, and other contaminants, while runoff carrying sediment may simultaneously deliver bacteria and additional pollutants to estuarine waters (Baird et al., 1996; Ward and Armstrong, 1997).

Therefore, a watershed-scale assessment should also examine interactions among sediment transport, nutrient dynamics, pollutant sources, freshwater inflows, and management actions intended to reduce pollutant delivery to the bay system in addition to evaluating sediment loading (Baird et al., 1996; EPA, 2001). This integrated assessment is particularly important because excessive nitrogen and phosphorus enrichment can stimulate algal blooms, reduce water clarity, contribute to dissolved oxygen (DO) depletion and hypoxia, and produce broad ecological stress in estuarine environments (EPA, 2001).

Watershed models provide a practical framework for evaluating these processes because field monitoring alone is often limited by sparse sampling frequency, limited spatial variability, and the difficulty of capturing high-flow events. Physically based, continuous-time models can simulate long-term hydrologic and water-quality responses under different climatic, land use, soil, and management conditions. Among available watershed models, the Soil and Water Assessment Tool (SWAT) has been widely used to simulate streamflow, sediment yield, nutrient cycling, pesticide transport, crop growth, and the effects of agricultural and watershed management practices (Arnold et al., 1998; Gassman et al., 2007; Neitsch et al., 2011). SWAT divides a watershed into subbasins and hydrologic response units (HRUs), which represent unique combinations of land use, soil type, slope, and management conditions. This structure allows the model to simulate spatially distributed hydrologic and pollutant-generation processes while routing water, sediment, and nutrients through the stream network. (Arnold et al., 1998; Moriasi et al., 2007; Neitsch et al., 2011).

In this study, SWAT was applied to evaluate streamflow, sediment, total nitrogen, and total phosphorus loading in the Nueces River Watershed. The model was developed from an existing calibrated Nueces River Watershed SWAT model and refined/updated for sediment and nutrient simulations. Calibration and validation were conducted using observed streamflow and water-quality data at a monthly time scale. Flow simulation was evaluated first because sediment and nutrient transport depend strongly on the timing and magnitude of runoff and channel flow. Sediment calibration was then conducted to improve the representation of upland erosion and channel sediment transport. Nitrogen and phosphorus simulations were subsequently evaluated to estimate nutrient loading and to examine the role of hydrology and sediment transport in nutrient delivery.

The calibrated model was also used to evaluate selected management scenarios intended to reduce sediment and nutrient loading to the Nueces-Corpus Christi Bay system. These scenarios included brush-clearing or flow-response scenarios, sediment-control scenarios such as grassed waterways, and nutrient-management scenarios related to fertilizer application and land-use assumptions. Scenario results were compared with a selected baseline condition to estimate relative changes in sediment and nutrient loading. Because the observed water-quality record is limited and nutrient validation uncertainty remains, the modeling results presented here are primarily used to demonstrate the corresponding relative responses for the selected management scenarios.

4.1.1 Problem Statement

The Nueces River Watershed contributes freshwater, sediment, nutrients, and other associated pollutant loads to the Nueces and Corpus Christi Bay system. Although sediment supply is a natural component of riverine and coastal geomorphic processes, excessive sediment delivery can increase turbidity, reduce reservoir and channel storage capacity, degrade aquatic habitat, and transport sediment-bound pollutants downstream. Nutrient enrichment from nitrogen and phosphorus can further contribute to eutrophication, algal growth, dissolved oxygen depletion, and deterioration of water quality in downstream receiving waters. These issues are especially important in semi-arid and subtropical watersheds such as the Nueces River Watershed, where episodic rainfall, high-flow events, reservoir operations, land cover, soil properties, and watershed management practices strongly control sediment and nutrient transport.

Previous monitoring and remote sensing efforts have provided valuable information on sediment concentration, turbidity patterns, and water-quality conditions in the Nueces River and bay system. However, field observations alone are limited in their ability to fully describe long-term watershed-scale loading because water-quality sampling is often discontinuous and may not capture the full range of hydrologic conditions, especially short-duration storm events that can dominate annual sediment and nutrient exports. In addition, management decisions such as brush clearing, fertilizer reduction, land-use modification, and sediment-control practices cannot be fully evaluated using observed data alone. A process-based watershed model is therefore needed to integrate climate, soil, land use, streamflow, sediment transport, and nutrient cycling into a single framework for estimating load generation, routing, and management responses.

The Soil and Water Assessment Tool (SWAT) provides a suitable framework for this purpose because it can simulate long-term hydrologic processes, sediment yield, nitrogen and phosphorus cycling, and the effects of land-management practices at the watershed scale. For this project, an existing SWAT model of the Nueces River Watershed was refined/updated to simulate flow, sediment, total nitrogen, and total phosphorus loadings. The model was calibrated and validated using observed streamflow and water-quality data and then used to evaluate management scenarios relevant to reducing sediment and nutrient delivery to the Nueces-Corpus Christi Bay system. The central problem addressed in this chapter is to quantify watershed-scale sediment and nutrient loading and evaluate how selected management decisions may affect pollutant delivery under variable rainfall and streamflow conditions.

4.1.2 Overview of SWAT Model

The Soil and Water Assessment Tool (SWAT) is a physically based, semi-distributed, continuous-time watershed model developed by the United States Department of Agriculture–

Agricultural Research Service to evaluate the long-term effects of land use, climate, soil properties, and management practices on water, sediment, nutrient, and agricultural chemical transport in large and complex watersheds (Arnold et al., 1998; Neitsch et al., 2011). SWAT has been widely applied for watershed-scale hydrologic and water-quality assessment because it can represent spatial variability in topography, land cover, soil characteristics, weather, and management operations while simulating daily hydrologic and pollutant transport processes over long periods (Gassman et al., 2007; Douglas-Mankin et al., 2010).

In SWAT, a watershed is first divided into subbasins based on topography and stream network configuration. Each subbasin is further divided into hydrologic response units (HRUs), which are unique combinations of land use, soil type, slope class, and management condition. The HRU structure allows SWAT to represent different hydrologic and pollutant-generation responses within the same subbasin without requiring a fully distributed grid-based simulation. Water, sediment, and nutrients generated at the HRU level are aggregated to the subbasin scale and routed through the channel network to the watershed outlet (Arnold et al., 1998; Neitsch et al., 2011).

The hydrologic component of SWAT is based on a soil-water balance that accounts for precipitation, surface runoff, infiltration, evapotranspiration, percolation, lateral flow, groundwater recharge, and return flow. Surface runoff can be estimated using the Soil Conservation Service Curve Number method or the Green-Ampt infiltration method, while channel routing is used to simulate flow movement through the stream network (Neitsch et al., 2011). These hydrologic processes are critical because sediment detachment, nutrient mobilization, and pollutant routing are strongly controlled by the timing and magnitude of runoff and streamflow.

Sediment yield in SWAT is commonly estimated using the Modified Universal Soil Loss Equation (MUSLE), which relates sediment generation to runoff energy, peak runoff rate, soil erodibility, slope length and steepness, land cover, and support practice factors (Williams, 1975; Neitsch et al., 2011). After sediment is generated from upland HRUs, SWAT routes sediment through channels, reservoirs, and reaches, where deposition and re-entrainment can occur depending on flow conditions and channel characteristics. This makes SWAT suitable for evaluating both upland erosion and in-stream sediment transport processes.

SWAT also simulates nitrogen and phosphorus cycling through soil, plant, groundwater, and channel processes. Nitrogen is represented in organic and mineral forms and is affected by mineralization, immobilization, plant uptake, denitrification, volatilization, leaching, lateral flow, surface runoff, and groundwater movement. Phosphorus is represented through organic, labile, active mineral, and stable mineral pools and can be transported in dissolved form with surface runoff or in particulate form attached to eroded sediment (Neitsch et al., 2011). Because nitrogen and phosphorus respond differently to hydrologic pathways, soil conditions, plant uptake, fertilizer application, and sediment transport, both nutrient systems must be evaluated in relation to flow and sediment simulation.

For this study, SWAT was selected because the project required a watershed-scale model capable of estimating streamflow, sediment, nitrogen, and phosphorus loading and evaluating management alternatives. The Nueces River Watershed contains diverse land uses, soil types, reservoir systems, and climatic variability, making a process-based model appropriate for linking watershed conditions to downstream pollutant delivery. In addition, SWAT allows management scenarios such as land-cover modification, brush management, sediment-control practices, and nutrient-management alternatives to be compared against a calibrated baseline condition.

4.1.3 Relevance of Flow, Sediment, Nitrogen, and Phosphorus Simulation

Accurate simulation of streamflow is the foundation for sediment and nutrient modeling because runoff generation and channel discharge control the movement of sediment, dissolved nutrients, and sediment-associated pollutants through the watershed. In semi-arid and subtropical watersheds such as the Nueces River Watershed, annual pollutant loading can be strongly influenced by a small number of high-flow events. During these events, increased runoff can detach soil particles from upland areas, erode channels, resuspend previously deposited sediment, and transport nitrogen and phosphorus downstream (Neitsch et al., 2011; Williams, 1975). Therefore, the model must first provide a reasonable representation of streamflow before sediment and nutrient loading can be interpreted with confidence.

Sediment simulation is important because sediment affects both physical habitat and water quality. Excess sediment can increase turbidity, reduce light penetration, alter channel morphology, reduce reservoir storage, and degrade aquatic habitat. Sediment can also function as a transport medium for particulate phosphorus, organic nitrogen, metals, pesticides, and other associated pollutants. For the Nueces-Corpus Christi Bay system, sediment delivery has a dual role. Sediment supply can contribute to maintaining coastal and estuarine geomorphology, but excessive or contaminated sediment delivery may contribute to water-quality degradation. As a result, sediment simulation is necessary not only for estimating sediment loading, but also for understanding sediment-associated nutrient and pollutant transport.

Nitrogen simulation is relevant because nitrogen is a key nutrient controlling primary productivity and water-quality response in many aquatic systems. In SWAT, nitrogen can move through surface runoff, lateral flow, percolation, groundwater return flow, and plant uptake pathways. Nitrate is highly mobile and can be transported with percolating water and subsurface flow, while organic nitrogen is more closely associated with soil organic matter and sediment movement. Because the project objective includes evaluation of management decisions on nitrogen loads under different rainfall and streamflow conditions, nitrogen simulation provides a direct basis for assessing how land use, fertilizer management, and hydrologic variability influence nutrient export from the watershed.

Phosphorus simulation is also necessary because phosphorus is often transported in both dissolved and particulate forms. Dissolved phosphorus may be transported in surface runoff, while particulate phosphorus is commonly attached to eroded soil particles and transported with sediment. This makes phosphorus closely linked to erosion and sediment-routing processes. In watersheds where sediment transport is episodic and storm-driven, phosphorus loading may also be concentrated during high-flow months. Therefore, phosphorus simulation provides an important connection between sediment control practices and nutrient reduction. Even where phosphorus validation is uncertain, phosphorus modeling can still provide useful insight into the relative effects of sediment-related management practices when results are interpreted cautiously.

The combined simulation of flow, sediment, nitrogen, and phosphorus is essential for evaluating management options in the Nueces River Watershed. Flow simulation identifies hydrologic periods and conditions that drive pollutant transport. Sediment simulation identifies erosion and routing processes that influence turbidity and particulate pollutant movement. Nitrogen simulation supports evaluation of nutrient-management alternatives, especially those related to fertilizer input and land-use assumptions. Phosphorus simulation helps evaluate sediment-associated nutrient transport and the potential benefits of erosion-control practices. Together, these model components provide a process-based framework for comparing management scenarios and identifying practices that may reduce sediment and nutrient delivery to the Nueces-Corpus Christi Bay system.

4.2 Theory

Streamflow simulation was the first component evaluated in the SWAT modeling sequence because flow controls the transport capacity of the watershed. Sediment detachment, channel sediment routing, nitrate movement, organic nutrient transport, and phosphorus export are all influenced by the timing and magnitude of runoff and stream discharge. Therefore, calibration and simulations of monthly streamflow were completed before sediment, nitrogen, and phosphorus calibration and simulations. This sequential approach follows the general SWAT modeling procedure in which hydrology is first examined to provide a physically reasonable foundation for subsequent water-quality simulation.

4.2.1 Flow Processes in SWAT

The hydrologic routines in SWAT are based on a daily soil-water balance that accounts for precipitation, surface runoff, infiltration, evapotranspiration, soil-water redistribution, lateral flow, percolation, groundwater recharge, return flow, channel routing, and reservoir routing. The fundamental water balance equation used in SWAT is (Arnold et al., 1998; Neitsch et al., 2011):

$$SW_t = SW_0 + \sum_{i=1}^{t}\left(R_{day} - Q_{surf} - E_a - W_{seep} - Q_{gw}\right) \tag{4.1}$$

where SW_t is the final soil water content (mm H_2O), SW_0 is the initial soil water content (mm H_2O), R_{day} is the daily precipitation (mm H_2O), Q_{surf} is the surface runoff (mm H_2O), E_a is the evapotranspiration (mm H_2O), W_{seep} is the percolation from the root zone (mm H_2O), and Q_{gw} is the return flow or baseflow (mm H_2O).

SWAT uses several simplifying assumptions to represent watershed hydrology at large spatial scales. First, each subbasin is divided into hydrologic response units (HRUs), which represent unique combinations of land use, soil, slope, and management. Hydrologic processes are calculated at the HRU level and then aggregated to the subbasin scale. Second, SWAT assumes that HRUs are not spatially connected within a subbasin, meaning that runoff, sediment, and nutrient contributions from each HRU are added together before being routed through the channel network. Third, soil-water movement is represented through layered soil profiles, where water may infiltrate, be stored, be removed by evapotranspiration, move laterally, percolate to lower layers, or recharge groundwater. These assumptions allow SWAT to simulate long-term hydrologic response across large watersheds while maintaining reasonable computational efficiency.

The primary input driving the hydrologic cycle is precipitation. Rainfall may be intercepted by vegetation canopy, infiltrate into the soil, become surface runoff, or contribute to evaporation. Canopy interception can be approximated as (Neitsch et al., 2011):

$$I = \min(P, I_{max}) \tag{4.2}$$

where I is the intercepted rainfall (mm), P is the precipitation (mm), and I_{max} is the maximum canopy storage (mm). Temperature, solar radiation, wind speed, and relative humidity influence potential evapotranspiration and plant-water demand. Surface runoff in SWAT is commonly estimated using the Soil Conservation Service Curve Number (SCS-CN) method (Neitsch et al., 2011):

$$Q_{surf} = \frac{\left(R_{day} - 0.2S\right)^2}{R_{day} + 0.8S}, \quad R_{day} > 0.2S \tag{4.3}$$

$$S = \frac{25400}{CN} - 254 \tag{4.4}$$

where Q_{surf} is the surface runoff (mm), R_{day} = rainfall (mm), S is the retention parameter (mm), and CN is the curve number. Higher CN values increase surface runoff, while lower values increase infiltration and soil-water storage. In semi-arid watersheds such as the Nueces River

Watershed, runoff is often episodic, with large responses occurring during intense rainfall events and limited runoff during dry periods (Neitsch et al., 2011; Thomas et al., 2019).

Infiltrated water enters the soil profile and is redistributed among soil layers. Soil available water capacity controls the amount of water that can be stored for plant use, while saturated hydraulic conductivity (K_{sat}) controls the rate at which water moves through the soil. Percolation through soil layers can be approximated using (Neitsch et al., 2011):

$$W_{seep} = K_{sat} \times \frac{SW - FC}{SAT - FC} \tag{4.5}$$

where W_{seep} is the percolation (mm), K_{sat} is the saturated hydraulic conductivity, SW is the soil water content, FC is the field capacity, and SAT is the saturation water content.

Water stored in the soil profile may be removed through soil evaporation and plant transpiration. Actual evapotranspiration is typically estimated as (Neitsch et al., 2011):

$$E_a = K_c \times ET_0 \tag{4.6}$$

where E_a is the actual evapotranspiration (mm), K_c is the crop coefficient, and ET_0 is the reference evapotranspiration (mm). These parameters are important in the Nueces River Watershed because evapotranspiration and soil-water storage strongly influence runoff generation under semi-arid climatic conditions (Bassam and Ren, 2018; Thomas et al., 2019).

Lateral flow occurs when water moves downslope through the soil profile and enters the stream network without first reaching the shallow aquifer. Lateral flow can be estimated as (Neitsch et al., 2011):

$$Q_{lat} = K_{sat} \times S_{slope} \times SW \tag{4.7}$$

where Q_{lat} is the lateral flow (mm), S_{slope} is the slope gradient, and SW is the soil water content. Percolation occurs when water moves below the root zone and contributes to groundwater recharge.

The amount and timing of percolation are controlled by soil-water storage, saturated hydraulic conductivity, soil depth, and evapotranspiration demand (Neitsch et al., 2011). Groundwater processes in SWAT are represented using shallow and deep aquifer components. Baseflow from the shallow aquifer is commonly represented using an exponential recession equation (Neitsch et al., 2011):

$$Q_{gw} = Q_{gw,prev} \times e^{-\alpha_{bf}} + R_{gw} \tag{4.8}$$

where Q_{gw} is the groundwater flow (mm), $Q_{gw,prev}$ is the previous groundwater flow, α_{bf} is the baseflow recession constant, and R_{gw} is the groundwater recharge. Groundwater contribution to streamflow depends on parameters such as groundwater delay, baseflow recession, threshold water depth in the shallow aquifer for return flow, and groundwater re-evaporation coefficient (Neitsch et al., 2011).

After water is generated from HRUs and subbasins, SWAT routes flow through the channel network. Channel routing is often based on the variable storage or Muskingum routing method (Neitsch et al., 2011):

$$\mathrm{Q}_{out} = K_1\mathrm{Q}_{in} + K_2\mathrm{Q}_{in,prev} + K_3\mathrm{Q}_{out,prev} \tag{4.9}$$

where Q_{out} is the outflow, Q_{in} is the inflow, and K_1, K_2, K_3 are the routing coefficients. Flow velocity in channels is influenced by Manning's equation (Neitsch et al., 2011):

$$V = \frac{1}{n}R^{2/3}S^{1/2} \tag{4.10}$$

where V is the velocity (m/s), n is the Manning's roughness coefficient, R is the hydraulic radius, and S is the channel slope. Channel routing affects the timing and magnitude of downstream flow peaks, which in turn control sediment transport capacity and nutrient delivery.

Reservoir routing is also important in the Nueces River Watershed because Choke Canyon Reservoir and Lake Corpus Christi regulate downstream flow. Reservoir water balance can be expressed as (Neitsch et al., 2011):

$$V_t = V_{t-1} + Q_{in} - Q_{out} - E - S \tag{4.11}$$

where V_t is the reservoir storage, Q_{in} is the inflow, Q_{out} is the outflow, E = evaporation loss, and S is the seepage loss. Reservoirs can store inflow, reduce peak discharge, increase travel time, alter seasonal flow patterns, and affect downstream sediment and nutrient transport (Neitsch et al., 2011).

In the Nueces River Watershed, streamflow is strongly controlled by rainfall variability, soil-water storage, evapotranspiration, groundwater response, channel transmission, and reservoir operations. During dry periods, low precipitation and high evapotranspiration reduce runoff and streamflow. During wet periods, especially high-intensity rainfall events, surface runoff and channel flow can increase rapidly, producing large flow peaks. These high-flow periods are especially important because they drive much of the annual sediment, nitrogen, and phosphorus transport (Thomas et al., 2019).

4.2.2 Relevant Processes Governing Sediment Load Simulations in SWAT

Sediment simulation was conducted after flow calibration because sediment generation and transport in SWAT are directly controlled by runoff volume, peak runoff rate, channel flow, soil erodibility, land cover, and channel routing. In the Nueces River Watershed, sediment loading is important because sediment affects channel morphology, reservoir storage, turbidity, aquatic habitat, and the transport of sediment-associated nutrients and pollutants to the Nueces and Corpus Christi Bay system. Sediment may also serve as a carrier for particulate phosphorus, organic nitrogen, pesticides, metals, and other associated pollutants. Therefore, an acceptable sediment simulation was necessary before evaluating nutrient dynamics and sediment-control management scenarios.

Sediment yield in SWAT is simulated using the Modified Universal Soil Loss Equation (MUSLE), which estimates sediment generation from hydrologic energy rather than rainfall energy alone. Unlike the original Universal Soil Loss Equation, MUSLE uses surface runoff volume and peak runoff rate to estimate sediment yield from each hydrologic response unit. This means at the HRU scale, SWAT estimates sediment yield using MUSLE, which replaces the rainfall energy term in the Universal Soil Loss Equation with a runoff energy term. This allows sediment yield to be calculated on an event basis and links erosion directly to surface runoff volume and peak runoff rate rather than rainfall amount alone. Thus, it makes sediment generation in SWAT strongly dependent on the accuracy of the hydrologic simulation. The major factors affecting sediment yield include runoff, soil erodibility, slope length and steepness, land cover, support practices, and coarse fragment content (Williams, 1975; Neitsch et al., 2011).

The daily sediment yield is computed as:

$$\mathrm{Sed} = 11.8\left(Q_{\mathrm{surf}} \times q_{\mathrm{peak}} \times A_{\mathrm{hru}}\right)^{0.56} \times K_{\mathrm{USLE}} \times C_{\mathrm{USLE}} \times P_{\mathrm{USLE}} \times LS_{\mathrm{USLE}} \times \mathrm{CFRG} \quad (4.12)$$

where Sed is the sediment yield on a given day (metric tons), Q_{surf} is the surface runoff volume (mm H_2O ha^{-1}), q_{peak} is the peak runoff rate (m^3 s^{-1}), A_{hru} is the HRU area (ha), K_{USLE} is the soil erodibility factor, C_{USLE} is the cover and management factor, P_{USLE} is the support practice factor, LS_{USLE} is the topographic factor for slope length and steepness, and CFRG is the coarse fragment factor. This equation implies that sediment detachment and export are driven primarily by runoff energy.

The formulation assumes that land cover, soil condition, topography, and management effects can be represented through multiplicative factors, and that the computed value corresponds to the net sediment yield leaving the HRU, rather than gross soil detachment within the HRU. Because HRUs are conceptual and spatially lumped units, SWAT does not explicitly resolve internal redistribution of sediment within each HRU.

The soil erodibility factor (USLE_K) is calculated from soil properties, including particle-size distribution, organic matter content, soil structure, and permeability. In SWAT, organic matter may be estimated from soil organic carbon as (Neitsch et al., 2011; Williams, 1975):

$$OM = 1.72 \times orgC \tag{4.13}$$

where OM is the soil organic matter content (%) and $orgC$ is the soil organic carbon content (%). This relationship assumes that standard soil database properties are adequate to characterize erodibility where direct erosion measurements are unavailable.

Within SWAT, sediment detachment and transport from the landscape are not simulated as fully separate processes at sub-HRU scale. Instead, MUSLE provides the net sediment delivered from the HRU to the reach for each runoff event. Therefore, the HRU is treated as a homogeneous unit with respect to land use, soil, slope, and management. This is a watershed-scale simplification that supports efficient simulation but assumes that spatially variable within-field erosion and deposition can be represented as an aggregated response. For interpretation, this means that HRU sediment output should be treated as the sediment contribution exported from that HRU, not as a direct plot-scale estimate of erosion at every point on the hillslope. This assumption is especially important when discussing sediment-associated organic nitrogen transport, because organic nitrogen loads depend on the amount of sediment actually delivered to the stream system rather than the amount detached locally.

After sediment enters the stream network, SWAT routes it through the channel system using a transport-capacity approach. The model assumes that two competing processes occur in each reach: deposition, when the flow cannot carry all incoming sediment, and degradation or re-entrainment, when the transport capacity exceeds the incoming sediment load. Transport capacity is estimated from peak channel velocity (Neitsch et al., 2011):

$$v_{\mathrm{ch,pk}} = \frac{q_{\mathrm{ch,pk}}}{A_{\mathrm{ch}}} \tag{4.14}$$

where $v_{\mathrm{ch,pk}}$ is the peak channel velocity (m s^{-1}), $q_{\mathrm{ch,pk}}$ is the peak channel flow rate (m^3 s^{-1}), and A_{ch} is the flow cross-sectional area in the channel (m^2). The peak channel flow rate is related to the average channel flow by (Neitsch et al., 2011):

$$q_{\mathrm{ch,pk}} = \mathrm{prf} \times q_{\mathrm{ch}} \tag{4.15}$$

where prf is the peak rate adjustment factor, and q_{ch} is the average channel flow rate. Using the peak velocity, the maximum sediment concentration that can be transported by the reach is estimated as (Neitsch et al., 2011):

$$\mathrm{conc}_{\mathrm{sed,ch,mx}} = c_{\mathrm{sp}} \times v_{\mathrm{ch,pk}}^{\mathrm{spexp}} \tag{4.16}$$

where $\mathrm{conc}_{\mathrm{sed,\,ch,\,mx}}$ is the maximum sediment concentration transportable by the flow, c_{sp} is the channel sediment routing coefficient, and spexp is the channel sediment routing exponent.

This approach assumes that sediment transport capacity in the reach is controlled primarily by flow hydraulics, especially peak flow velocity, rather than by detailed grain-size mechanics. If the incoming sediment concentration exceeds transport capacity, sediment deposition occurs (Neitsch et al., 2011):

$$\mathrm{sed}_{\mathrm{dep}} = \left(\mathrm{conc}_{\mathrm{sed,ch,i}} - \mathrm{conc}_{\mathrm{sed,ch,mx}}\right) \times V_{\mathrm{ch}} \tag{4.17}$$

where $\mathrm{sed}_{\mathrm{deg}}$ is the sediment deposited in the reach (metric tons), $\mathrm{conc}_{\mathrm{sed,ch,i}}$ is the sediment concentration at the start of the time step, and V_{ch} is the volume of water in the reach. If the sediment concentration is below transport capacity, channel degradation or re-entrainment occurs (Neitsch et al., 2011):

$$\mathrm{sed_{deg}} = \left(\mathrm{conc_{sed,ch,mx}} - \mathrm{conc_{sed,ch,i}}\right) \times V_{\mathrm{ch}} \times K_{\mathrm{CH}} \times C_{\mathrm{CH}} \tag{4.18}$$

where $\mathrm{sed_{deg}}$ is the sediment re-entrained from the channel bed or banks (metric tons), K_{CH} is the channel erodibility factor, and C_{CH} is the channel cover factor. The final sediment stored in the reach is then estimated as (Neitsch et al., 2011):

$$\mathrm{sed_{ch}} = \mathrm{sed_{ch,i}} - \mathrm{sed_{dep}} + \mathrm{sed_{deg}} \tag{4.19}$$

and sediment leaving the reach, $\mathrm{Sed_{out}}$, is calculated as:

$$\mathrm{sed_{out}} = \mathrm{sed_{ch}} \times \left(\frac{V_{\mathrm{out}}}{V_{\mathrm{ch}}}\right) \tag{4.20}$$

where $\mathrm{sed_{ch}}$ is the sediment remaining in the reach after deposition and degradation, $\mathrm{sed_{ch,i}}$ is the initial sediment stored in the reach, and V_{out} is the outflow volume during the time step.

These equations assume that sediment within the reach is sufficiently mixed over the routing time step so that outgoing sediment can be represented in proportion to the fraction of water leaving the reach.

In this study, sediment was evaluated at the monthly time scale using observed sediment load estimates derived from measured total suspended sediment (TSS) concentration and streamflow. SWAT sediment output was compared with the observed monthly sediment load in tons per month. The sediment simulation was calibrated after streamflow calibration to ensure that the hydrologic basis for sediment transport was reasonable.

4.2.3 Relevant Processes Governing TN and TP Load Simulations in SWAT

Nitrogen and phosphorus simulation was conducted after flow and sediment calibration because their transport is controlled by hydrologic pathways, soil-water movement, plant uptake, fertilizer application, mineralization, and organic matter transport. In SWAT, nitrogen may move in dissolved form, especially as nitrate, or in organic form associated with soil particles and organic matter. Phosphorus may be transported in dissolved form with surface runoff or in particulate form attached to eroded sediment. Because sediment-associated phosphorus can represent an important part of total phosphorus loading, the phosphorus simulation was interpreted together with sediment calibration and sediment-control scenarios.

4.2.3.1 Nitrogen Processes in SWAT

Nitrogen cycling in SWAT is represented through several organic and mineral nitrogen pools. Organic nitrogen is associated with soil organic matter, crop residue, and sediment-bound material, while mineral nitrogen is represented primarily through ammonium and nitrate forms. Nitrate is highly mobile and can be transported with surface runoff, lateral flow, percolation, tile drainage where applicable, and groundwater return flow. Organic nitrogen is less mobile in dissolved form and is more closely linked to soil erosion and sediment transport (Neitsch et al., 2011).

The initialization of soil nitrogen is a required first step in SWAT because daily nitrogen transformations depend on the initial distribution of nitrate and organic nitrogen within the soil profile. The principal initialization variables are SOL_NO3, which defines the initial nitrate concentration in each soil layer, and SOL_ORGN, which defines the initial humic organic nitrogen concentration in each soil layer. For nitrogen-focused studies, the initial nitrate and humic organic nitrogen pools may be defined from measured soil data or estimated from soil organic matter and related pedologic properties when direct measurements are unavailable. The model assumes that these initial conditions reasonably represent the starting soil nitrogen status at the beginning of simulation.

SWAT simulates net mineralization and immobilization using routines adapted from the PAPRAN mineralization model. Mineralization is controlled by soil temperature, soil water content, and the quality of residue and humus pools. The underlying assumption is that residue quality governs whether nitrogen is released or immobilized. In SWAT, this is represented through the residue carbon-to-nitrogen ratio. Residue with a low C:N ratio promotes net mineralization, whereas residue with a high C:N ratio promotes immobilization. Soil temperature and moisture further regulate the rate at which these transformations occur (Neitsch et al., 2011; Seligman and van Keulen, 1981). Mineralization from the active humus organic nitrogen pool to the nitrate pool is computed as (Neitsch et al., 2011):

$$N_{mina,ly} = \beta_{min} \times \gamma_{tmp,ly} \times \gamma_{sw,ly}^{1/2} \times orgN_{act,ly} \tag{4.21}$$

where $N_{mina,ly}$ is the nitrogen mineralized from the active humus organic N pool in layer ly (kg N ha^{-1}), β_{min} is the humus mineralization rate coefficient, $\gamma_{tmp,ly}$ is the nutrient cycling temperature factor, $\gamma_{sw,ly}$ is the nutrient cycling soil water factor, and $orgN_{act,ly}$ is the active organic nitrogen in the soil layer.

Decomposition and mineralization of fresh residue organic nitrogen are allowed only in the first soil layer. The nitrogen mineralized from the fresh organic pool is calculated as (Neitsch et al., 2011):

$$N_{minf,ly} = 0.8 \times \delta_{ntr,ly} \times orgN_{frsh,ly} \tag{4.22}$$

and the nitrogen decomposed from the fresh organic pool and transferred to the active humus pool is (Neitsch et al., 2011):

$$N_{dec,ly} = 0.2 \times \delta_{ntr,ly} \times orgN_{frsh,ly} \tag{4.23}$$

where $N_{minf,ly}$ is the nitrogen mineralized from the fresh organic N pool (kg N ha^{-1}), $N_{dec,ly}$ is the nitrogen decomposed from the fresh organic N pool (kg N ha^{-1}), $\delta_{ntr,ly}$ is the residue decay rate constant, and $orgN_{frsh,ly}$ is the fresh organic nitrogen in the residue pool.

SWAT calculates the amount of ammonium converted by nitrification and volatilization together using a first-order kinetic expression. The total transformed ammonium is then partitioned into nitrification and volatilization fractions. This formulation assumes that both processes compete for the same ammonium pool and that their rates are controlled by environmental regulators, primarily temperature, water content, and soil/fertilizer placement conditions. The total ammonium removed through the two competing processes is computed as (Neitsch et al., 2011):

$$N_{nit/vol,ly} = NH_{4,ly} \times \left[1 - \exp\left(-\eta_{nit,ly} - \eta_{vol,ly}\right)\right] \tag{4.24}$$

where $N_{nit/vol,ly}$ is the ammonium transformed by nitrification and volatilization (kg N ha^{-1}), $NH_{4,ly}$ is the ammonium in layer ly, $\eta_{nit,ly}$ is the nitrification regulator, and $\eta_{vol,ly}$ is the volatilization regulator. SWAT simulates denitrification as nitrate loss under warm, wet, carbon-rich conditions.

This formulation assumes that denitrification is negligible until a moisture threshold is exceeded and that carbon availability constrains the process. SWAT therefore treats denitrification as a lumped nitrate sink rather than a fully mechanistic microbial redox model. The amount of nitrogen lost to denitrification is estimated as (Neitsch et al., 2011):

$$N_{denit,ly} = NO_{3,_{ly}} \times \left[1 - \exp\left(-\beta_{denit} \times \gamma_{tmp,ly} \times orgC_{ly}\right)\right]$$

$$if\ \gamma_{sw,ly} \geq \gamma_{sw,thr} \tag{4.25}$$

$$N\_denit, ly = 0 \quad if\ \gamma_{sw,ly} < \gamma_{sw,thr} \tag{4.26}$$

where $N_{denit,ly}$ is the nitrogen lost to denitrification (kg N ha^{-1}), $NO_{3,ly}$ is the nitrate in layer ly, β_{denit} is the denitrification rate coefficient, $\gamma_{tmp,ly}$ is the temperature factor, $\gamma_{sw,ly}$ is the soil water factor, $\gamma_{sw,thr}$ is the threshold soil water factor for denitrification, and $orgC_{ly}$ is the soil organic carbon content.

Plant nitrogen uptake in SWAT is estimated using a supply-demand approach linked to crop growth. The model calculates optimal plant nitrogen concentration as a function of growth stage and biomass, then removes nitrogen from the soil profile according to root distribution and crop demand. This means plant uptake is not prescribed as a constant value, but emerges dynamically from crop development, rooting depth, and nitrogen availability within the soil layers. The main modeling assumption is that crop demand curves and rooting patterns adequately represent actual plant nitrogen extraction.

SWAT treats nitrate as a dissolved and mobile anion. The model assumes that nitrate moves with mobile soil water and is not strongly adsorbed to soil particles. The concept of anion exclusion is used to account for the fact that negatively charged nitrate ions are repelled from negatively charged soil particle surfaces and therefore move through a reduced fraction of the pore space. This effect is controlled by ANION_EXCL, while nitrate retention during percolation is controlled by NPERCO (nitrate percolation coefficient). Organic nitrogen in surface runoff is simulated separately and is associated with sediment transport rather than dissolved water movement. Nitrate movement to the underlying layer by percolation is calculated as (Neitsch et al., 2011):

$$NO_{3perc,ly} = concNO_{3mobile} \times w_{perc,ly} \tag{4.27}$$

where $NO_{3perc,ly}$ is the nitrate moved to the underlying soil layer (kg N ha^{-1}), $concNO_{3mobile}$ is the nitrate concentration in mobile water (kg N mm^{-1} H_2O), and $w_{perc,ly}$ is the amount of percolating water (mm H_2O).

In SWAT, nitrate that moves below the root zone with recharge water may enter the shallow aquifer. The groundwater nitrogen routine is linked directly to the hydrologic groundwater balance; therefore, nitrate transport through groundwater depends on recharge, aquifer storage, and groundwater return flow. SWAT assumes that nitrate entering the shallow aquifer is transported in dissolved form with recharge water and may later re-enter the stream through baseflow. Nitrate loss in the shallow aquifer is simulated using first-order decay kinetics (Neitsch et al., 2011):

$$NO_{3sh,t} = NO_{3sh,0} \times \exp\left(-k_{NO_3,sh} \times t\right) \tag{4.28}$$

where $NO_{3sh,t}$ is the nitrate in the shallow aquifer at time t (kg N ha^{-1}), $NO_{3sh,0}$ is the initial nitrate amount in the shallow aquifer (kg N ha^{-1}), $k_{NO3,sh}$ is the nitrate removal rate constant in the shallow aquifer (day^{-1}), and t is the elapsed time (days). The rate constant is related to the nitrate half-life in the shallow aquifer by:

$$k_{NO3,sh} = \frac{0.693}{t_{1/2,NO_3,sh}} \tag{4.29}$$

where $t_{1/2,NO3,sh}$ is the half-life of nitrate in the shallow aquifer. This half-life is a lumped parameter representing the net effects of bacterial uptake, redox-driven transformations, and other chemical or biological attenuation processes in groundwater.

As a result, SWAT does not explicitly resolve detailed aquifer biogeochemistry, but instead represents nitrate loss in groundwater through an effective first-order decay assumption (Neitsch et al., 2011).

After nitrogen leaves the HRUs and enters the channel network, SWAT routes it through stream reaches where additional transformations may occur. The in-stream nitrogen routines are based on the QUAL2E framework and simulate nitrogen species in the water column as functions of temperature, travel time, biological activity, and settling behavior. SWAT includes in-stream transformation of organic nitrogen, ammonium, nitrite, and nitrate, as well as nitrogen uptake by algae (Brown & Barnwell, 1987; Neitsch et al., 2011).

Organic nitrogen in reaches may be converted to ammonium by hydrolysis and may also be removed from the water column by settling. The relevant parameters include BC3, the local hydrolysis rate constant for organic nitrogen to ammonium, and RS4, the local settling rate for organic nitrogen at 20°C. The settling rate is temperature-adjusted within the stream water-quality calculations (Brown & Barnwell, 1987; Neitsch et al., 2011).

Ammonium in the reach may be oxidized to nitrite and then to nitrate. These reactions are controlled by BC1, the rate constant for biological oxidation of ammonia nitrogen, and BC2, the rate constant for biological oxidation of nitrite to nitrate. In addition, RS3 represents a benthic source of ammonium from the streambed sediment. These terms allow SWAT to account for transformation and release of inorganic nitrogen within stream channels (Brown & Barnwell, 1987; Neitsch et al., 2011).

Algae are explicitly linked to in-stream nitrogen cycling in SWAT. The parameter AI1 defines the fraction of algal biomass that is nitrogen, while P_N defines the algal preference factor for ammonia nitrogen. These parameters allow the model to represent nitrogen assimilation into algal biomass and preferential uptake of ammonium relative to nitrate. This formulation assumes that algal nitrogen dynamics can be represented through simplified kinetic relationships rather than site-specific ecological community structure (Neitsch et al., 2011).

4.2.3.2 Phosphorus Processes in SWAT

Phosphorus cycling in SWAT is represented through interacting organic and mineral phosphorus pools in the soil profile, plant system, surface runoff, sediment, groundwater, and stream network. Unlike nitrate, which is highly mobile in water, phosphorus is generally less mobile and is strongly influenced by soil adsorption, plant uptake, erosion, and sediment transport. Therefore, phosphorus simulation in SWAT depends on both hydrologic processes and sediment-routing processes. This is especially important in the Nueces River Watershed, where high-flow events transport both dissolved phosphorus in runoff and particulate phosphorus attached to eroded sediment (Carpenter et al., 1998; Neitsch et al., 2011).

SWAT uses several simplifying assumptions to represent phosphorus cycling at the watershed scale. Soil phosphorus is divided into organic and inorganic pools. Organic phosphorus is associated with fresh residue and humus organic matter, while inorganic phosphorus is represented through solution, active mineral, and stable mineral pools. Soluble phosphorus is considered the most available form for plant uptake and runoff transport. Particulate phosphorus transport is linked to erosion and sediment delivery, while in-stream transformations follow simplified kinetics.

The initialization of soil phosphorus pools is an important step because daily transformations depend on the initial conditions. The principal phosphorus pools include soluble (labile), active mineral, stable mineral, fresh organic, and humic organic phosphorus. In SWAT inputs, soluble phosphorus may be represented as SOL_SOLP or SOL_LABP, while organic phosphorus is represented as SOL_ORGP. These initial conditions determine phosphorus availability for plant uptake, runoff transport, sediment attachment, and long-term cycling (Neitsch et al., 2011).

Phosphorus transformations include mineralization, immobilization, sorption, desorption, plant uptake, runoff transport, and sediment-associated transport. Organic phosphorus mineralization converts organic phosphorus to mineral forms, while immobilization transfers mineral phosphorus back into organic matter. These processes are controlled by soil temperature, moisture, organic matter, and biological activity (Neitsch et al., 2011).

The inorganic phosphorus cycle is governed by exchanges among three main pools:

$$P_{solution} \leftrightarrow P_{active} \leftrightarrow P_{stable} \tag{4.30}$$

where $P_{solution}$ is the soluble (labile) phosphorus, P_{active} is the active mineral phosphorus, and P_{stable} is the stable mineral phosphorus. This relationship shows that phosphorus availability depends on the exchange between readily available and less available pools. Model parameters such as PSP (phosphorus availability index) and PHOSKD (partition coefficient) control these exchanges (Neitsch et al., 2011).

Plant phosphorus uptake in SWAT is simulated using a supply-demand approach. Uptake depends on plant growth stage, biomass, rooting depth, and optimal phosphorus concentration. Phosphorus is removed from different soil layers based on root distribution and soil phosphorus availability.

Dissolved phosphorus transport primarily occurs through surface runoff. A simplified representation is (Neitsch et al., 2011):

$$P_{\text{runoff}} = f(P_{\text{solution}}, Q_{\text{surf}}, K_d) \tag{4.31}$$

where P_{runoff} is the dissolved phosphorus in runoff, $P_{solution}$ is the soil solution phosphorus, Q_{surf} is the surface runoff, and K_d is the partitioning coefficient. This shows that dissolved phosphorus export increases with higher runoff and higher solution phosphorus but decreases with stronger soil adsorption. Particulate phosphorus transport is directly linked to erosion and sediment movement (Neitsch et al., 2011):

$$P_{sed} = S_{ed} \times P_{soil} \times ER \tag{4.32}$$

where P_{sed} is the sediment-associated phosphorus load, S_{ed} is the sediment yield, P_{soil} is the phosphorus concentration in soil, and ER is the enrichment ratio. The enrichment ratio accounts for preferential transport of fine, phosphorus-rich particles. In SWAT, this process is influenced by the ERORGP parameter, the phosphorus enrichment ratio for loading with sediment.

Phosphorus percolation is usually limited because phosphorus is strongly adsorbed to soil particles. However, SWAT represents limited leaching using a percolation coefficient:

$$P_{perc} = PPERCO \times W_{perc} \times P_{solution} \tag{4.33}$$

where P_{perc} is the percolated phosphorus, PPERCO is the phosphorus percolation coefficient, W_{perc} is the percolating water, and $P_{solution}$ is the soluble phosphorus. Although typically small, phosphorus leaching may increase in coarse soils or highly saturated conditions.

After entering the stream network, phosphorus is routed through channels and reservoirs. Transformations include the settling of particulate phosphorus and the transport of dissolved phosphorus. Reservoir water balance influences phosphorus retention and can be expressed as (Neitsch et al., 2011):

$$P_{\text{out}} = P_{\text{in}} - P_{\text{settle}} - P_{\text{react}} \tag{4.34}$$

where P_{out} is the phosphorus outflow, P_{in} is the phosphorus inflow, P_{settle} is the phosphorus lost through settling, and P_{react} is the phosphorus transformed or retained. Reservoirs such as Choke Canyon and Lake Corpus Christi reduce sediment-associated phosphorus transport and alter downstream loading.

In the Nueces River Watershed, phosphorus transport is expected to be strongly event-driven because high-flow months can generate both runoff and sediment transport. During low-flow periods, phosphorus export is generally limited by low hydrologic transport capacity. During wet months, surface runoff and sediment movement can increase total phosphorus delivery. Therefore, phosphorus simulation was interpreted together with flow and sediment results, especially for evaluating sediment-control practices that may reduce particulate phosphorus transport.

4.3 Materials and Methods

The SWAT modeling component of this study was designed to quantify streamflow, sediment, total nitrogen, and total phosphorus loading from the Nueces River Watershed and to evaluate the effects of selected management scenarios on nutrient and sediment delivery to the Nueces-Corpus Christi Bay system. The methodology consisted of five major steps: (1) representation of the Nueces River Watershed in SWAT, (2) organization of spatial, weather, hydrologic, and water-quality input datasets, (3) processing of observed streamflow and concentration data into monthly load estimates, (4) calibration and validation of flow, sediment, nitrogen, and phosphorus using SWAT-CUP, and (5) simulation of baseline and management scenarios to evaluate relative changes in sediment and nutrient loading.

4.3.1 Description of the Study Area

The Nueces River Watershed is located in South Texas and drains toward Nueces Bay and Corpus Christi Bay (Figure 4.1). The river extends for more than 300 miles before reaching the coastal bay system near Corpus Christi. The watershed is an important source of freshwater inflow for downstream reservoirs, municipal water supply, agriculture, and ecological systems. The basin is characterized by semi-arid to subtropical climatic conditions, with rainfall that is highly variable seasonally and annually. This variability produces alternating low-flow and high-flow periods, which strongly influence sediment and nutrient delivery (Thomas et al., 2019).

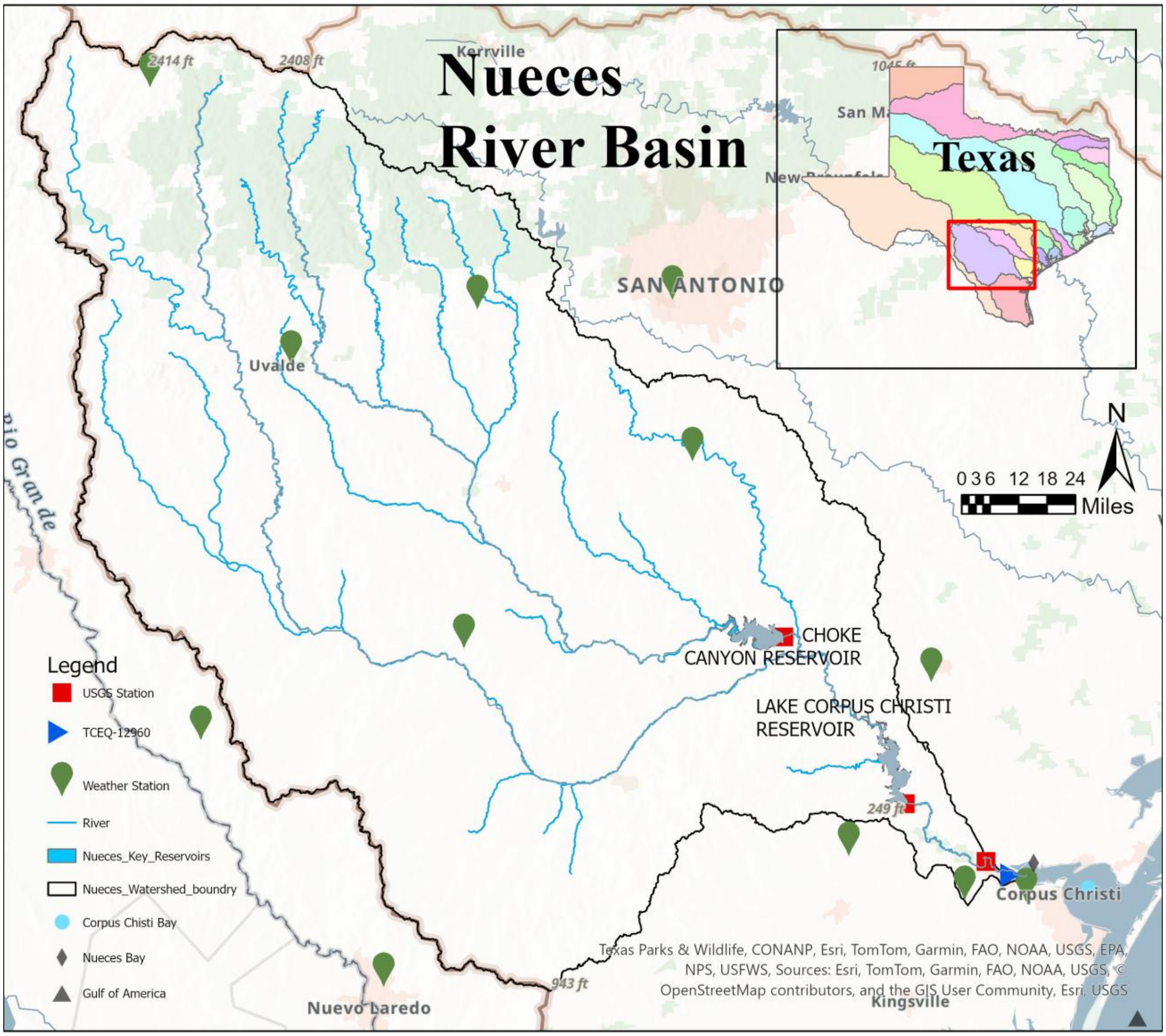

Figure 4.1. Study area map of the Nueces River Watershed, showing water bodies, stream network, and monitoring stations.

4.3.2 SWAT Model Setup and Watershed Representation

An existing SWAT model of the Nueces River Watershed was used as the starting point for this study and was updated for sediment and nutrient loading simulations. The model was processed using ArcSWAT, ArcGIS Pro, and SWAT-CUP. The watershed model also included the major reservoir system in the Nueces River Basin, including Choke Canyon Reservoir and Lake Corpus Christi. Reservoir representation is important in the Nueces system because reservoirs can modify downstream flow timing, attenuate peak flows, retain sediment, alter nutrient transport, and influence the delivery of sediment and nutrients to downstream river reaches and bays. Reservoir input parameters were reviewed and updated where available, including reservoir surface area, storage volume, initial sediment concentration, equilibrium sediment concentration, hydraulic conductivity, evaporation coefficient, release rate, and outflow operation parameters.

Figure 4.2 illustrates the overall workflow used to develop and apply the Nueces River Watershed SWAT model. The process begins with the compilation of watershed data, followed by watershed delineation, hydrologic response unit definition, weather-data preparation, and model parameterization. The model is then calibrated and validated using observed hydrologic and water-quality data. Finally, the calibrated model is used to evaluate management scenarios and support recommendations for reducing sediment and nutrient loading to the Nueces/Corpus Christi Bay system.

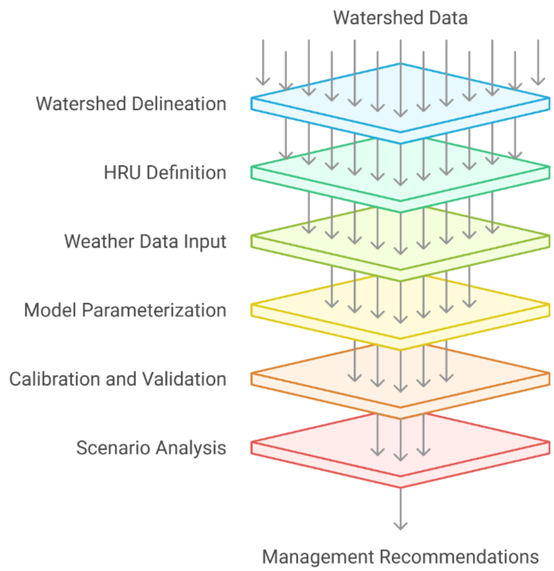

Figure 4.2. Conceptual framework used to develop the Nueces River Watershed SWAT model.

4.3.2.1 Model Input Data

Spatial input datasets were compiled to represent watershed boundary, topography, stream network, land use, soils, and management conditions. The watershed boundary was based on the Watershed Boundary Dataset, and stream network information was derived from the National Hydrography Dataset (Table 4.1). Figure 4.3 describes the DEM with a spatial resolution of 100 m from the USGS National Elevation Dataset (NED) used for terrain analysis, watershed delineation, slope delineation, and flow-routing definition. Land-use data were based on the National Land Cover Dataset, and soil data were obtained from the STATSGO2 database of the Natural Resources Conservation Service and United States Department of Agriculture.

Weather and hydrologic datasets were prepared to support long-term SWAT simulation (Table 4.1). Precipitation data were obtained from National Oceanic and Atmospheric Administration and National Centers for Environmental Information sources. Temperature inputs were derived from NOAA sources and supplemental gridded temperature datasets where needed.

Table 4.1. Input data sources used for SWAT model development and simulation.

	Data Type	Source with Links
GIS Data for SWAT model	Watershed Boundary	10-digit Hydrologic Unit Codes (HUC 10) from Watershed boundary Dataset (WBD), https://www.usgs.gov/national-hydrography/watershed-boundary-dataset
	Stream Network	Texas Geographic Information Office (TxGIO) https://tnris.org/
	Land Surface Elevation	Digital Elevation Model (DEM) from National Elevation Dataset (NED), https://www.usgs.gov/3d-elevation-program
	Land Use	National Land Cover Dataset (NLCD), https://www.mrlc.gov/
	Soil Data	United States general soil map (STATSGO2), from National Resources Conservation Service (NRCS),_United States Department of Agriculture (USDA), https://ippc2.orst.edu/soil_data/TX/
Weather Time Series Data	Precipitation	National centers for environmental information (NCEI), https://www.ncei.noaa.gov/
	Temperature	NOAA and CHIRTS-daily is a quasi-global (60°S – 70°N), high-resolution (0.05° x 0.05°, approx. 5km) data set of daily maximum and minimum temperatures, https://www.ncei.noaa.gov/
	Wind Speed	NLDAS-2 and WXGEN COOP (USDA ARS), https://www.ncei.noaa.gov/
	Solar Radiation	Weather generator tool in SWAT (WXGEN) using Cooperative Observed Network (COOP) datasets for the contiguous United States https://swat.tamu.edu/media/99082/cfsr_world.zip
	Relative Humidity	Weather generator tool in SWAT (WXGEN) using Cooperative Observed Network (COOP) datasets for the contiguous United States https://swat.tamu.edu/media/99082/cfsr_world.zip
Flow and Transport data for Simulation	Streamflow Measurements	USGS Streamflow (USGS NWIS) https://waterdata.usgs.gov/
	Sediment Load Data	National Water Quality Monitoring Council from TCEQ https://www.waterqualitydata.us/provider/STORET/TCEQMAIN/TCEQMAIN-12960/
	Nutrient Concentration Data	National Water Quality Monitoring Council from TCEQ https://www.waterqualitydata.us/provider/STORET/TCEQMAIN/TCEQMAIN-12960/

Additional weather variables, including wind speed, solar radiation, and relative humidity, were represented using available weather generator and regional climate datasets (Table 4.1). Streamflow observations were obtained from the United States Geological Survey National Water Information System. Sediment and nutrient concentration data were compiled from available water-quality monitoring sources, including the National Water Quality Monitoring Council from TCEQ.

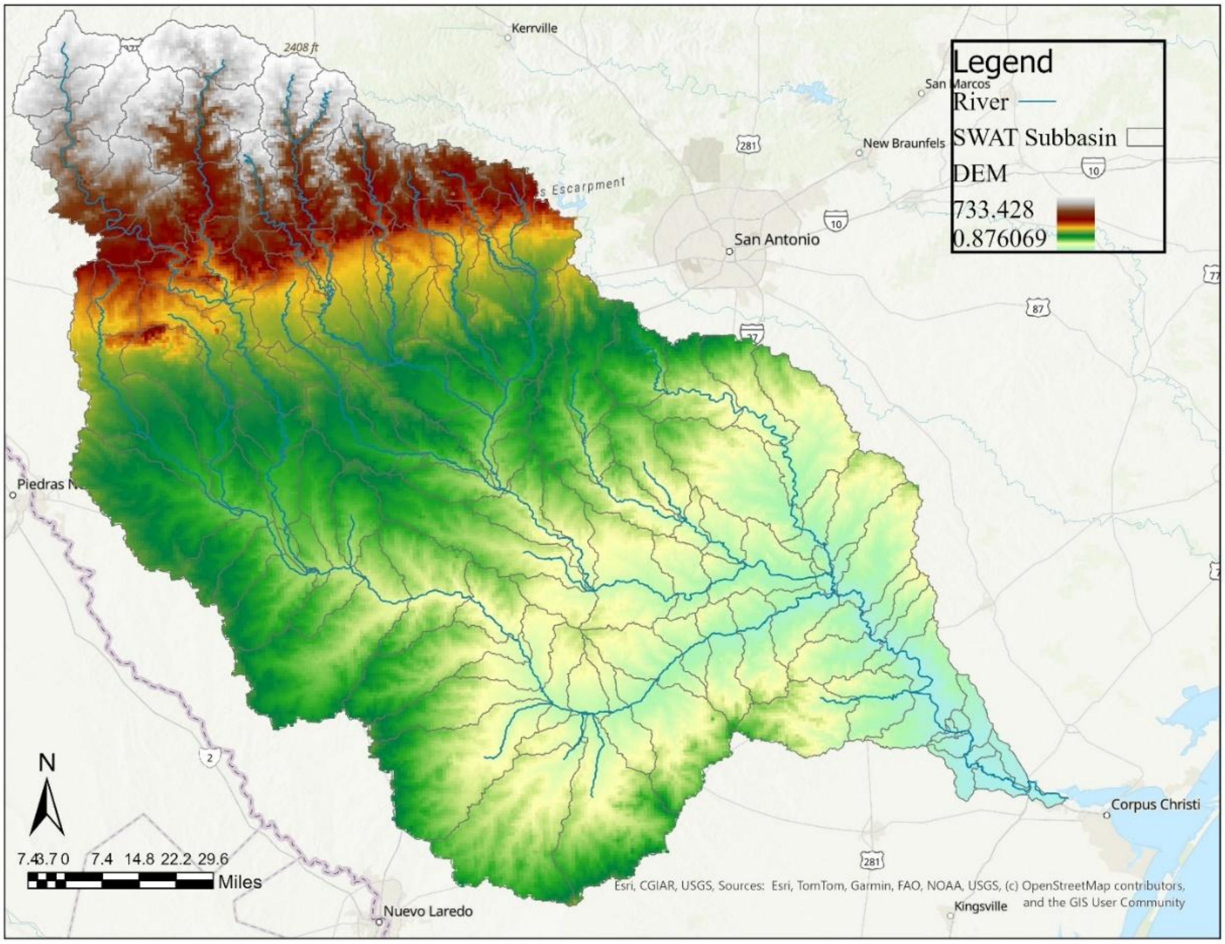

Figure 4.3. Digital elevation model of the Nueces River Basin at 100-m resolution. (Source: https://www.usgs.gov/3d-elevation-program).

Figure 4.3 shows the spatial distribution of elevation across the Nueces River Basin using a 100-m-resolution digital elevation model obtained from the U.S. Geological Survey 3D Elevation Program. The elevation data were used to support watershed delineation, slope classification, drainage-network development, and surface-flow routing within the SWAT model. Table 4.2 summarizes the elevation characteristics of the Nueces River Watershed based on the digital elevation model. Elevation ranges from 0 to 733 m, with a mean elevation of 237.25 m and a standard deviation of 166.09 m, indicating substantial topographic variability across the watershed. Table 4.3 presents the distribution of watershed area among ten elevation ranges. Approximately 63.47% of the watershed occurs below 219 m, with the largest proportion located between 146 and 219 m. The remaining area is distributed across progressively higher elevation classes, with approximately 3.60% of the watershed located between 660 and 733 m.

Table 4.2. Elevation statistics for the Nueces River Watershed DEM.

Statistics	**All elevations reported in meters**
Min.	Elevation: 0
Max.	Elevation: 733
Mean.	Elevation: 237.25
Standard Deviation	Deviation: 166.09

Table 4.3. Elevation-area distribution for the Nueces River Watershed.

Bracket	**Elevation Range**	**% Watershed**	**Cumulative % Area Below Upper Limit**
1	0–72	5.70	5.70
2	73–145	27.59	33.30
3	146–219	30.19	63.47
4	220–292	13.16	76.63
5	293–366	5.58	82.18
6	367–439	3.43	85.66
7	440–512	3.54	89.17
8	513–586	3.40	92.56
9	587–659	3.80	96.37
10	660–733	3.60	100.00

Figure 4.4 below shows the STATSGO2 soil map used to define soil attributes in the Nueces River Watershed SWAT model. Table 4.4 shows the soil summary that was developed by combining watershed-level soil area information with the corresponding Texas STATSGO soil database used in SWAT. The watershed area percentages were taken from the watershed soil-area file, while the soil attributes, including soil type, hydrologic group (HYD_GRP),

texture, bulk density (SOL_BD), available water capacity (SOL_AWC), and saturated hydraulic conductivity (SOL_K), were obtained from the corresponding Texas STATSGO soil records. For each major STATSGO map unit, the dominant soil component was selected to represent the map unit in the table. Because STATSGO map units often contain more than one soil component, the component with the largest percentage within each map unit was used as the representative soil. In addition, the listed soil physical properties were taken from the top soil layer of the dominant component, as this provides a consistent and practical basis for preparing a SWAT-style watershed soil summary table.

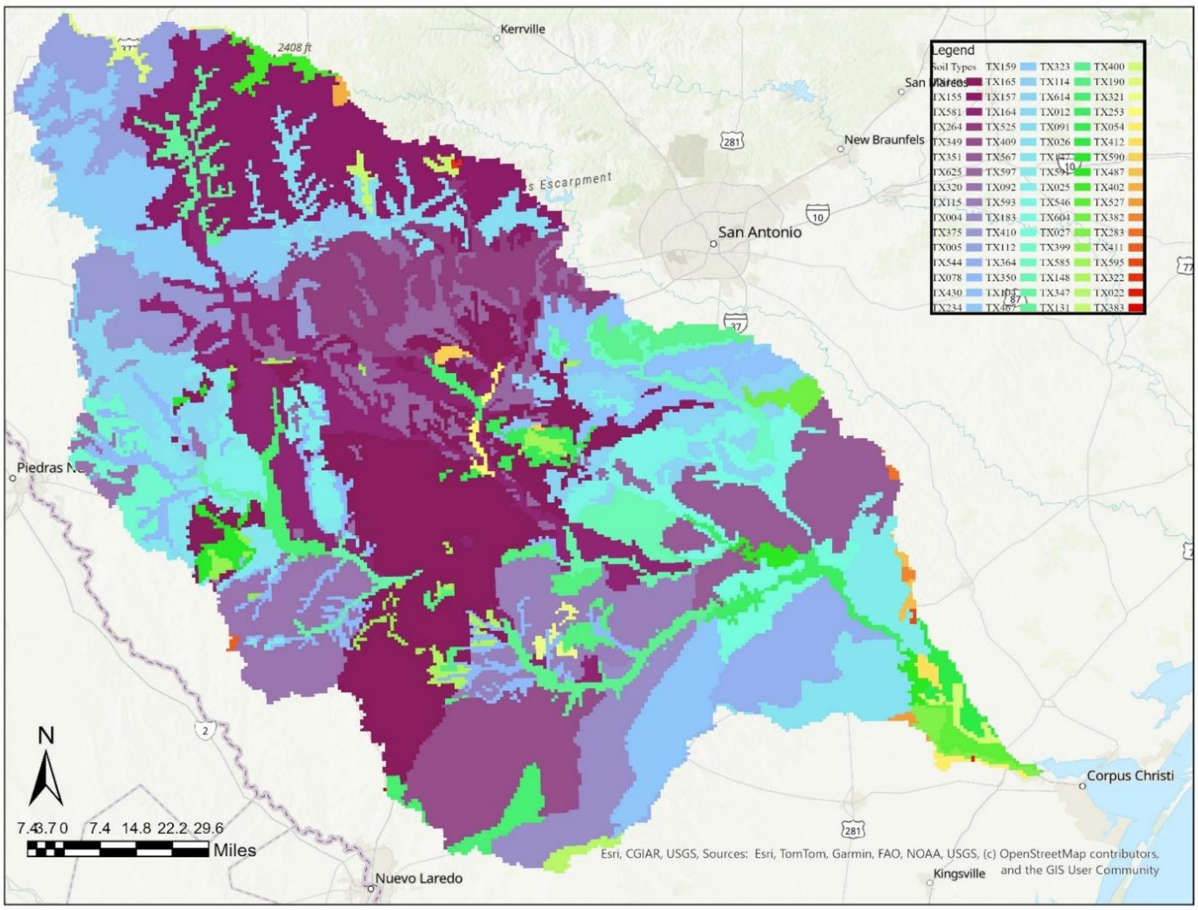

Figure 4.4. STATSGO2 soil map of the Nueces River Watershed (source: https://ippc2.orst.edu/soil_data/TX/).

Table 4.4. Major STATSGO2 soil map units and representative soil properties used in SWAT.

STATSGO Map Unit	Soil Types	Watershed area (%)	HYD_ GRP	Texture	SOL_BD (g/cm^3)	SOL_AWC (mm/mm)	SOL_K (mm/hr)
TX149	Duval	11.98	B	FSL	1.55	0.10	73.0
TX155	Eckrant	7.98	D	CBV-C	1.45	0.12	2.30
TX581	Uvalde	6.17	B	CL	1.30	0.19	8.00
TX264	Knippa	4.42	C	C	1.38	0.16	1.10
TX349	Montell	4.27	D	C	1.38	0.15	0.616
TX351	Monteola	4.15	D	C	1.33	0.16	0.873
TX625	Yologo	3.42	D	GRV-L	1.45	0.09	13.0
TX320	Maverick	3.32	C	C	1.45	0.14	0.864
TX115	Cotulla	2.91	D	C	1.27	0.14	0.531
—	Others	51.38	—	—	—	—	—

Note: HYD_GRP = Hydrologic Soil Group; SOL_BD = Soil Bulk Density; SOL_AWC = Available Water Capacity; SOL_K = Saturated Hydraulic Conductivity. Soil properties were derived from the dominant soil component of each STATSGO map unit using the Texas STATSGO database used in SWAT. Surface texture classes were expanded from SWAT abbreviations where FSL = Fine Sandy Loam, CL = Clay Loam, C = Clay, and GRV-L = Gravelly Loam. The "Other" category combines the remaining 59 minor soil map units within the watershed (Source: https://ippc2.orst.edu/soil_data/TX/).

STATSGO2 soil map units in the watershed include a mixture of fine sandy loam, clay loam, clay, cobbly clay, and gravelly loam textures. Major soil types include Duval, Eckrant, Uvalde, Knippa, Montell, Monteola, Yologo, Maverick, and Cotulla(Table 4.4). Hydrologic soil groups range primarily from B to D, indicating spatial variability in infiltration capacity, runoff potential, and erosion susceptibility (Table 4.4).

Figure 4.5 shows the spatial distribution of land-use and land-cover classes across the Nueces River Watershed. The watershed is dominated by rangeland, particularly range-brush and range-grasses, with smaller areas of agricultural land, hay, forest, wetlands, water, and urban development. These land-cover patterns were used in SWAT to define HRUs and represent differences in runoff generation, evapotranspiration, soil erosion, and nutrient transport.

Table 4.5 summarizes the area and percentage of each land-use and land-cover class in the Nueces River Watershed. Range-brush is the dominant class, covering 60.53% of the watershed, followed by range-grasses at 10.32% and hay at 8.55%. Agricultural row crops and evergreen forest account for 5.77% and 5.58%, respectively. Combined rangeland classes cover approximately 71% of the watershed, while developed land represents a comparatively small proportion of the total area. These land-cover conditions influence runoff generation, soil erosion, plant uptake, nutrient cycling, and channel delivery (Arnold et al., 1998; Neitsch et al., 2011).

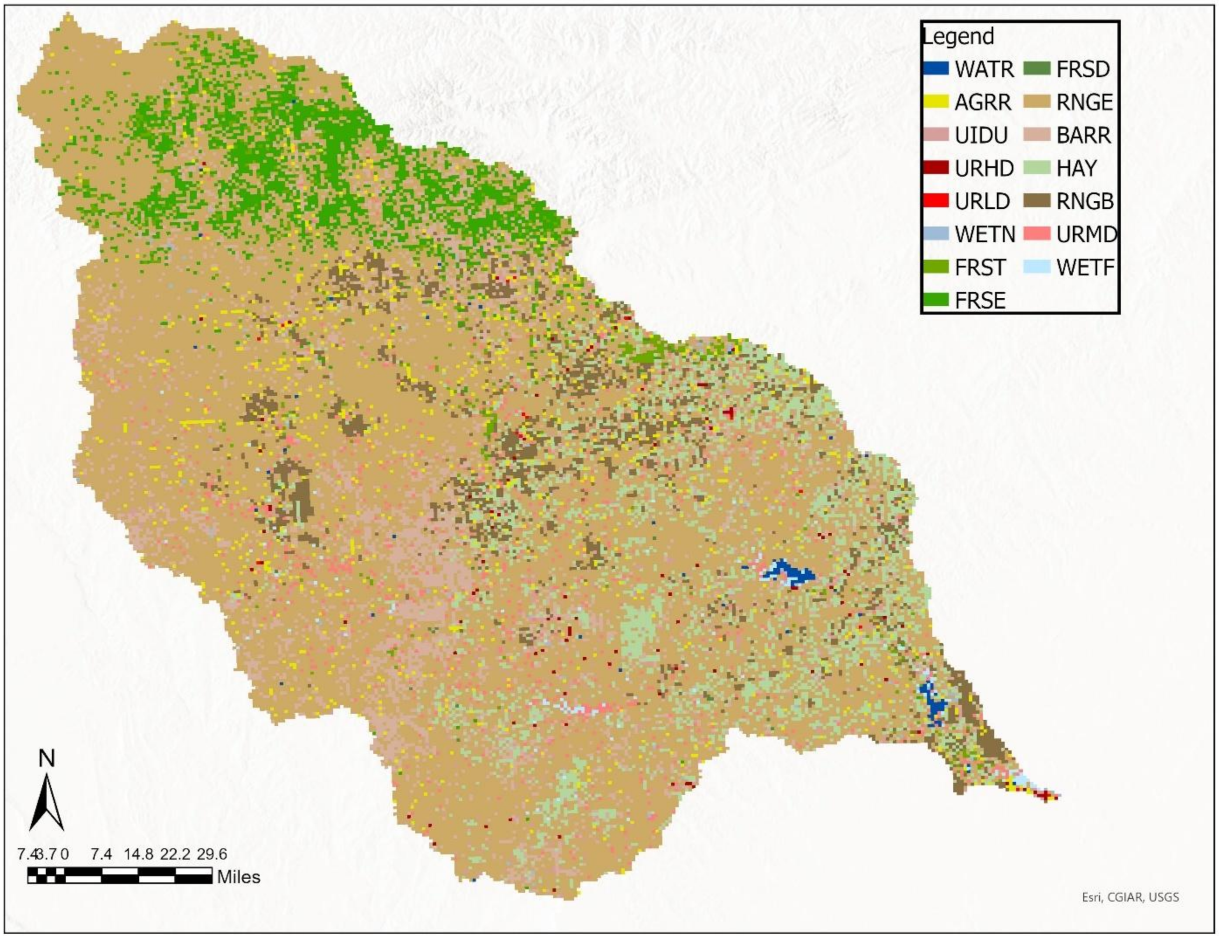

Figure 4.5. Land-use and land-cover map of the Nueces River Watershed (Source: https://www.mrlc.gov/).

Rangeland and brush-dominated areas affect interception, surface roughness, evapotranspiration, and runoff response, while agricultural and hay areas are important for nutrient management because fertilizer application and soil disturbance may increase nitrogen and phosphorus export. The combination of semi-arid rainfall variability, rangeland dominance, agricultural land, urban development, reservoir regulation, and variable soil properties creates complex hydrologic and water-quality responses that require a process-based modeling approach (Sharpley et al., 2003; EPA, 2026).

Table 4.5. Land-use and land-cover distribution for the Nueces River Watershed.

No.	**Land Use**	**Abbreviation**	**Area (ha)**	**Area (acres)**	**% Area**
1	Water	WATR	12001.38	29656	0.28
2	Residential-Low Density	URLD	114265.2	282355.1	2.64
3	Residential-Medium Density	URMD	62931.59	155507.1	1.45
4	Forest-Deciduous	FRSD	79572.16	196626.8	1.84
5	Range-Brush	RNGB	2622251	6479712	60.53
6	Range-Grasses	RNGE	447177.4	1104998	10.32
7	Agricultural Land-Row Crops	AGRR	249810.2	617293.5	5.77
8	Wetlands-Forested	WETF	92279.5	228027.3	2.13
9	Industrial	UIDU	1512.779	3738.152	0.03
10	Southwestern US (Arid) Range	SWRN	6555.374	16198.66	0.15
11	Forest-Evergreen	FRSE	241842.9	597605.9	5.58
12	Residential-High Density	URHD	10791.15	26665.48	0.25
13	Hay	HAY	370328.2	915099.5	8.55
14	Wetlands-Non-Forested	WETN	16035.45	39624.41	0.37
15	Forest-Mixed	FRST	5143.448	12709.72	0.12

Figure 4.6 shows the SWAT subbasins, stream network, and model outlets for the Nueces River Basin. The watershed was represented using 129 subbasins and 3,387 hydrologic response units (HRUs) (Figure 4.6) by setting the land-use, soil, and slope thresholds to zero so that all unique combinations of the three factors were represented. Table 4.6 summarizes the model

setup, including DEM resolution, delineation tools, watershed area, number of subbasins, and number of HRUs.

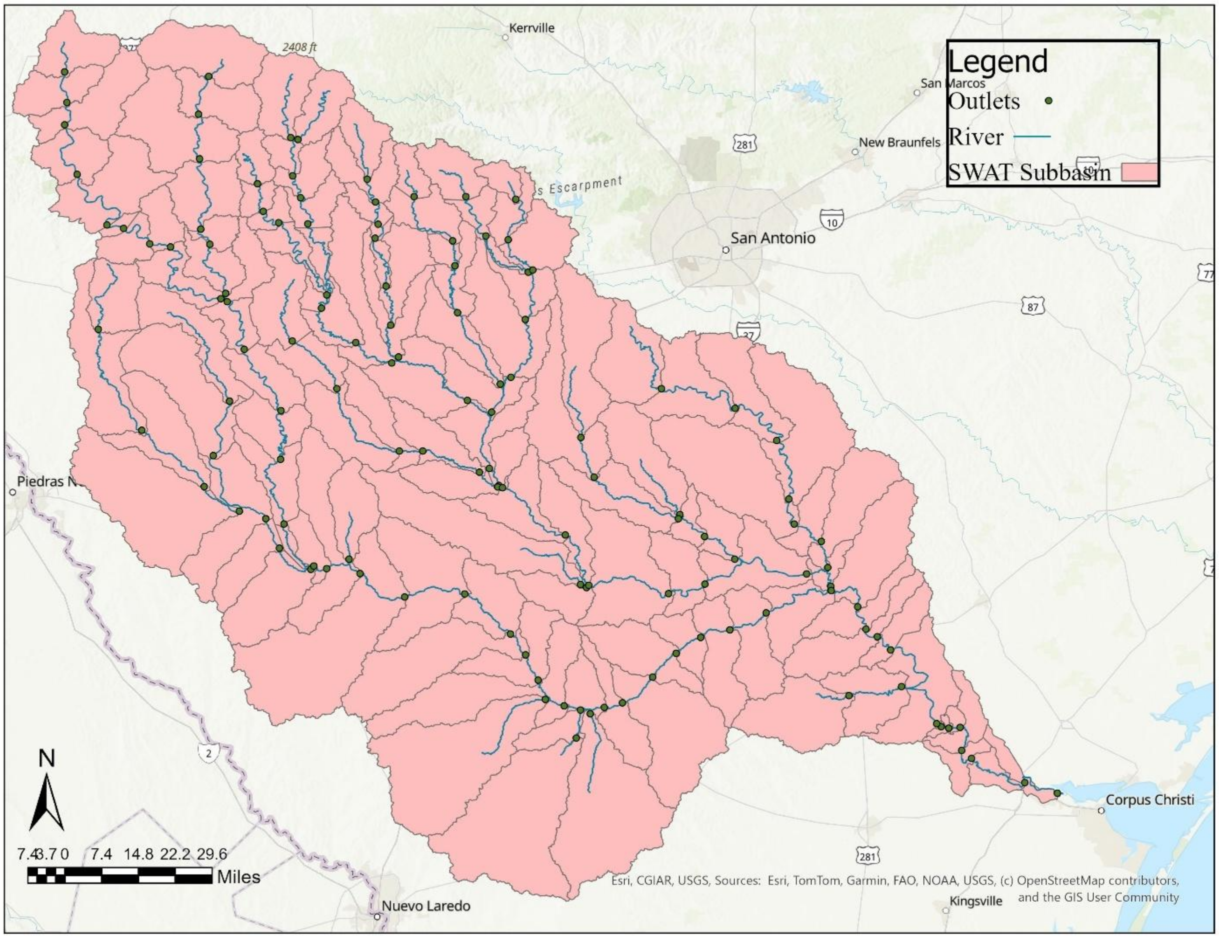

Figure 4.6. SWAT subbasins, stream network, and outlets for the Nueces River Basin.

Table 4.6. SWAT model setup summary for the Nueces River Watershed.

No.	Parameter	Details
1.	DEM Model Grid Size	100 m x 100 m
2.	Watershed Delineation Tool	ArcSWAT, ArcGIS Pro
3.	Total Watershed Area	43,300 km²
4.	Number of Sub-basins	129
5.	Number of Hydrologic Response Units (HRUs)	3387
6.	HRU Grid Size	17.5 km x 17.5 km

4.3.2.2 Preparation of Input Data Files

The base/default SWAT input parameters are listed in Appendix A. Precipitation and temperature inputs were spatially processed using the Thiessen polygon method to assign weather-station influence areas across the Nueces River Watershed. Twelve weather stations were selected to represent the spatial variability of precipitation and temperature across the basin (Figure 4.1). Thiessen polygons were generated around the selected stations, and each polygon was used to define the area of the watershed most closely associated with a given station. This approach allowed daily precipitation and temperature records to be distributed spatially across the watershed rather than applying a single station uniformly to the entire model domain. The use of multiple stations was important because rainfall in South Texas can be highly variable over space and time, particularly during convective storm events. By assigning precipitation and temperature data based on Thiessen polygon coverage, the SWAT model was able to better represent spatial differences in weather forcing among subbasins and HRUs.

Reservoir input data were reviewed and incorporated for the two major reservoirs represented in the Nueces River Watershed model: Choke Canyon Reservoir and Lake Corpus Christi. The reservoir parameter inputs included operational start indicator, year of reservoir operation, emergency spillway surface area and volume, principal spillway surface area and volume, initial reservoir volume, initial sediment concentration, equilibrium sediment concentration, median sediment particle size, bottom hydraulic conductivity, lake evaporation coefficient, outflow simulation option, principal spillway release rate, and flood-season timing parameters (Table 4.7). These parameters were used to represent storage, release, evaporation, seepage, sediment settling, and routing behavior within the reservoir system.

Table 4.7. Reservoir input parameters used for Choke Canyon Reservoir and Lake Corpus Christi in the Nueces River Watershed SWAT model.

No.	SWAT field label	Parameter description	Lake Corpus Christi	Choke Canyon	Data source
1	MORES	Model month in which the reservoir becomes operational	Jan	Jan	Arnold et al. (2012)
2	IYRES	Model year in which the reservoir becomes operational	2008	2008	Arnold et al. (2012)
3	RES_ESA*	Emergency spillway surface area (ha)	7,568	10,294	Texas Water Development Board (2017, 2013); Arnold et al. (2012)
4	RES_EVOL*	Emergency spillway volume (10^4 m^3)	31,421	81,757	Texas Water Development Board (2017, 2013); Arnold et al. (2012)
5	RES_PSA*	Principal spillway surface area (ha)	7,992	10,388	Texas Water Development Board (2017, 2013); Arnold et al. (2012)
6	RES_PVOL*	Principal spillway volume (10^4 m^3)	31,619	85,727	Texas Water Development Board (2017, 2013); Arnold et al. (2012)
7	RES_VOL*	Initial reservoir volume on January 1, 2011 (10^4 m^3)	23,100	65,900	U.S. Geological Survey (n.d.-a, n.d.-b); Texas Water Development Board (2017, 2013)
8	RES_SED*	Initial sediment concentration (mg/L)	42	20	Arnold et al. (2012); model initialization
9	RES_NSED*	Equilibrium sediment concentration (mg/L)	8	3	Arnold et al. (2012); model initialization
10	RES_D50	Median sediment particle size (µm)	5	7.5	Arnold et al. (2012); model initialization
11	RES_K	Reservoir-bottom hydraulic conductivity (mm/h)	1.2	0.15	Arnold et al. (2012); model initialization
12	EVRSV	Lake evaporation coefficient	0.82	0.76	Arnold et al. (2012); model initialization
13	IRESCO	Reservoir outflow simulation option	2	2	Arnold et al. (2012)

14	RES_RR	Principal spillway release rate (m^3/s)	20	10	Arnold et al. (2012); U.S. Geological Survey (n.d.-c) for Choke Canyon discharge
15	IFLOD1R	Beginning month of the non-flood season	11	11	Arnold et al. (2012)
16	IFLOD2R	Ending month of the non-flood season	4	4	Arnold et al. (2012)
17	NDTARGR	Number of days required to release flood-pool storage	2	4	Arnold et al. (2012)
18	PSETLR1	Phosphorus settling rate, January–June (m/year)	4	3.5	Arnold et al. (2012)
19	PSETLR2	Phosphorus settling rate, July–December (m/year)	4	3.5	Arnold et al. (2012)
20	NSETLR1	Nitrogen settling rate, January–June (m/year)	2.2	2	Arnold et al. (2012)
21	NSETLR2	Nitrogen settling rate, July–December (m/year)	2.2	2	Arnold et al. (2012)
22	CHLAR	Chlorophyll-*a*-to-algal-biomass ratio	1	1	Arnold et al. (2012)
23	SECCIR	Secchi-disk light-extinction coefficient	1	1	Arnold et al. (2012)
24	RES_ORGP	Initial organic phosphorus concentration (mg/L)	0.065	0.025	Arnold et al. (2012)
25	RES_SOLP	Initial soluble phosphorus concentration (mg/L)	0.028	0.008	Arnold et al. (2012)
26	RES_ORGN	Initial organic nitrogen concentration (mg/L)	1.1	0.6	Arnold et al. (2012)
27	RES_NO3	Initial nitrate concentration (mg/L)	0.3	0.06	Arnold et al. (2012)
28	RES_NH3	Initial ammonium concentration (mg/L)	0.05	0.025	Arnold et al. (2012)

29	RES_NO2	Initial nitrite concentration (mg/L)	0.01	0.005	Arnold et al. (2012)

*Reservoir surface-area and storage-volume inputs were developed using available Texas Water Development Board volumetric surveys and U.S. Geological Survey reservoir records. Arnold et al. (2012) was used to define the SWAT reservoir and lake-water-quality parameters. Values identified as model initialization or operation assumptions were assigned during model development where direct site-specific measurements were unavailable. These values should not be described as observed data unless a separate monitoring or operational source can be documented.

The reservoir inputs were developed for the corresponding SWAT reservoir subbasins and were adjusted using available reservoir-operation information, such as the volume and outflow rate, which were calculated from the data available to compute the model input requirements. Data from USGS station 08210500 near Mathis, Texas, were used in the simulation of Lake Corpus Christi, while data from USGS station 08206910 near Three Rivers, Texas, were used to simulate Choke Canyon Reservoir.

4.3.3 Observed Data Processing and Load Estimation

Observed streamflow, sediment, and nutrient data were processed at the monthly time scale to match the SWAT model output frequency used for calibration and validation. Streamflow data were obtained from USGS station 08211500 (Nueces River at Calallen, Texas), and sediment and nutrient observations were obtained from the EPA Water Quality Portal and TCEQ monitoring station TCEQMAIN-12960. The datasets and load units used in the analysis are summarized in Table 4.8.

Nutrient loads were estimated from observed nitrogen and phosphorus concentration data and streamflow using consistent load-conversion procedures. SWAT sediment output was evaluated in metric tons per month using SED_OUT, while nutrient outputs were evaluated in kilograms per month. Monthly load estimation was necessary because concentration sampling was discontinuous, while SWAT output and streamflow data were available at regular time steps. The use of monthly aggregation reduced the effect of short-term sampling variability and allowed calibration to focus on seasonal and interannual loading patterns.

Table 4.8. Summary of observed streamflow, sediment, nitrogen, and phosphorus data used for monthly load estimation and calibration.

Station	TCEQMAIN-12960, NUECES RIVER N OF VIOLA BASIN
Discharge source	USGS-08211500 daily mean discharge
Discharge conversion	$m^3/s = ft^3/s \times 0.0283$
Sediment load formula	metric tons/month = mean monthly TSS (mg/L) × sum (daily Q (m^3/s)) × 0.0864
Nutrient load formula	kg/month = mean monthly concentration (mg/L) × sum (daily Q (m^3/s)) × 86.4
SWAT units used	Sediment: metric tons/month for SED_OUT; nutrients: kg/month

Note: For months with more than one TSS sample, the monthly mean concentration was used. Sources: USGS National Water Information System, station 08211500; EPA Water Quality Portal; and TCEQ surface-water-quality monitoring data, station TCEQMAIN-12960. (Source: https://www.waterqualitydata.us/provider/STORET/TCEQMAIN/TCEQMAIN-12960/).

4.3.4 Model Calibration, Validation, and Performance Evaluation

Model calibration and uncertainty analysis were conducted using SWAT-CUP with the Sequential Uncertainty Fitting algorithm. SWAT-CUP was used to adjust selected parameters during calibration and to quantify prediction uncertainty. For validation, the final calibrated parameter set was applied without further adjustment, and validation statistics were calculated for the independent period (Abbaspour, 2015; Arnold et al., 2012).

The calibration period extended from January 2015 through December 2017, and the validation period extended from January 2018 through December 2019. These periods included hydrologically important wet years and high-flow events needed to evaluate model response under conditions that dominate sediment and nutrient transport. Monthly observed and simulated values were compared for streamflow, sediment load, total nitrogen load, and total phosphorus load.

Model performance was evaluated using statistical measures commonly applied in watershed modeling, including the coefficient of determination (R^2), Nash–Sutcliffe efficiency (NSE), Kling–Gupta efficiency (KGE), percent bias where applicable, and the SWAT-CUP uncertainty measures p-factor and r-factor. R^2 measures the strength of the linear association between observed and simulated values, NSE evaluates model predictions relative to the observed mean, and KGE combines correlation, bias, and variability. The p-factor represents the percentage of observed values bracketed by the model prediction uncertainty band, whereas the r-factor indicates the average width of that band relative to the standard deviation of the observed data. In other words, p-factor shows how many observed values fall within the 95% prediction uncertainty range, while the r-factor shows how wide that uncertainty range is. Generally, higher p-factor and a lower r-factor indicate better model uncertainty performance with p-factor of 0.70-0.30 is acceptable and r-factor of <1.50 is acceptable. Model performance was interpreted using commonly applied watershed-modeling guidance (Abbaspour, 2015; Arnold et al., 2012; Moriasi et al., 2007; Gupta et al., 2009). Table 4.9 summarizes the performance classes used for monthly calibration and validation. Separate thresholds were applied to streamflow and to sediment and nutrient loads because water-quality variables generally exhibit greater temporal variability and observational uncertainty. Accordingly, R^2, NSE, and KGE were considered collectively when evaluating overall model performance.

Table 4.9. Model performance rating criteria used for monthly calibration and validation (adapted from Moriasi et al., 2007; Gupta et al., 2009).

Variable	Metric	Very Good	Good	Satisfactory	Unsatisfactory
Flow	**R^2**	> 0.85	0.75–0.85	0.60–0.75	< 0.60
	NSE	> 0.75	0.65–0.75	0.50–0.65	< 0.50
	KGE	> 0.75	0.60–0.75	0.50–0.60	< 0.50
Sediment & Nutrient	**R^2**	> 0.80	0.65–0.80	0.50–0.65	< 0.50
	NSE	> 0.65	0.50–0.65	0.30–0.50	< 0.30
	KGE	> 0.65	0.50–0.65	0.30–0.50	< 0.30

Note: R^2 measures agreement in observed and simulated trends, NSE evaluates performance relative to the observed mean, and KGE combines correlation, bias, and variability. Lower thresholds were used for sediment and nutrients because these variables are more event-driven and variable than streamflow.

4.3.4.1 Flow Calibration Parameters

Flow calibration focused on parameters controlling surface runoff generation, soil-water storage, evapotranspiration, groundwater contribution, and channel routing. The selected hydrologic parameters included the curve number (CN2), soil evaporation compensation factor (ESCO), groundwater threshold depth for return flow (GWQMN), groundwater revap coefficient (GW_REVAP), soil available water capacity (SOL_AWC), baseflow recession constant (ALPHA_BF), groundwater delay time (GW_DELAY), surface runoff lag coefficient (SURLAG), main channel hydraulic conductivity (CH_K2), canopy storage (CANMX), saturated hydraulic conductivity (SOL_K), overland Manning's roughness coefficient (OV_N), plant uptake compensation factor (EPCO), and main channel Manning's roughness coefficient (CH_N2) (Table 4.10).

The curve number parameter controls the partitioning of rainfall into surface runoff and infiltration. A decrease in CN2 generally reduces direct surface runoff and increases infiltration, while an increase in CN2 increases runoff generation. Soil parameters such as SOL_AWC and SOL_K affect soil-water storage, infiltration, percolation, and lateral movement of water through the soil profile. Evapotranspiration-related parameters, including ESCO and EPCO, influence the ability of the model to extract soil water from different depths and to represent plant-water uptake. Groundwater parameters, including ALPHA_BF, GW_DELAY, GWQMN, and GW_REVAP, control the timing, magnitude, and persistence of baseflow contributions to the stream network. Channel parameters, including CH_K2 and CH_N2, affect transmission losses, channel routing, flow resistance, and the movement of water through the main channel system (Neitsch et al., 2011; Arnold et al., 2012).

The flow calibration parameters were selected because the Nueces River Watershed has strong seasonal rainfall variability, substantial rangeland and brush cover, reservoir regulation, and variable soil hydraulic properties. As a result, realistic flow simulation required adjustment of parameters representing both quick runoff response and delayed subsurface or groundwater contribution (Arnold et al., 2012; Neitsch et al., 2011).

Table 4.10. Calibration parameters used for monthly streamflow simulation in the Nueces River Watershed and comparisons with previous work.

Change Code	Parameter	Description	Previous calibration rang[1]	Previous calibrated value[2]	Current Model
v	ALPHA_BF	Baseflow recession constant; controls groundwater/baseflow response	0.0384–0.8322	0.73	0.31
v	CANMX	Maximum canopy storage; controls rainfall interception by vegetation	0.765–14.715	—	3.95
v	CH_K2	Effective hydraulic conductivity of main channel; controls channel transmission loss/seepage	1.0872–205.65	—	53.25
r	CN2	Curve number; controls surface runoff generation	-0.3057–-0.0203	0.13	-0.01
v	ESCO	Soil evaporation compensation factor; controls soil evaporation from lower soil layers	0.6623–0.9668	0.58	1
v	GWQMN	Threshold water depth in shallow aquifer required for return flow	585.75–5000	2625	1331.88
v	GW_DELAY	Groundwater delay time; controls lag between recharge and stream contribution	11.1495–179.255	87.5	431.34
v	GW_REVAP	Groundwater revap coefficient; controls movement from shallow aquifer to root zone	0.0359–0.1807	—	0.08
r	SOL_AWC	Soil available water capacity; controls soil water storage	0.0014–0.1196	0.08	0.2
r	SOL_K	Saturated hydraulic conductivity; controls infiltration and percolation	0.3083–0.3083	850	-0.09
v	SURLAG	Surface runoff lag coefficient; controls timing/smoothing of runoff	—	21.01	3.52
v	OV_N	Manning's n for overland flow; controls surface roughness and runoff velocity	—	17.25	1.28
v	EPCO	Plant uptake compensation factor; controls plant water uptake distribution	—	0.03	0.49
v	CH_N2	Manning's n for main channel; controls channel flow resistance/routing	—	—	0.05

Note: [1]Bassam and Ren (2018); [2]Rony et al. (2020); v = replace with absolute value; r = relative change [multiplied by (1 +{value}); a = absolute change (added to existing value). Relative adjustments (r) are used for spatial inputs to preserve baseline landscape heterogeneity.

4.3.4.2 Sediment Calibration Parameters

Sediment calibration focused on parameters controlling upland erosion, soil erodibility, channel erosion, channel protection, and sediment routing. The selected parameters included

USLE_P, USLE_K, CH_COV1, CH_COV2, SPEXP, and PRF_BSN (Table 4.11). These parameters were selected because they affect the detachment, delivery, deposition, and re-entrainment of sediment in SWAT (Arnold et al., 2012; Neitsch et al., 2011).

The USLE_P parameter represents the support practice factor and is used to account for the effect of erosion-control or conservation support practices on upland soil erosion. The USLE_K parameter represents soil erodibility and controls the susceptibility of soil particles to detachment and transport. Channel-related parameters included CH_COV1 and CH_COV2. CH_COV1 represents the protective effect of channel cover on channel bed and bank erosion, while CH_COV2 controls channel erodibility or resistance to erosion. The SPEXP parameter controls the sediment routing exponent and affects the sensitivity of sediment re-entrainment and transport to flow. PRF_BSN is the peak rate adjustment factor for sediment routing and is especially important during high-flow events.

Table 4.11. Sediment calibration parameters used in the Nueces River Watershed SWAT model.

Change code	Parameter	Description	Calibrated value
v	USLE_P	Support practice factor; represents erosion-control/support practice effects on soil erosion	0.9576
r	USLE_K	Soil erodibility factor; controls susceptibility of soil particles to detachment and erosion	0.2045
v	CH_COV1	Channel cover factor; represents protection of channel bed/banks from erosion	0.3153
v	CH_COV2	Channel erodibility factor; controls channel resistance to erosion	0.263
v	SPEXP	Sediment routing exponent; controls sediment re-entrainment and transport response to flow	1.229
v	PRF_BSN	Peak rate adjustment factor for sediment routing; affects sediment transport during high-flow events	1.5853

Note: v = replace with absolute value; r = relative change [multiplied by (1 +{value}); a = absolute change (added to existing value). Relative adjustments (r) are used for spatial inputs to preserve baseline landscape heterogeneity.

4.3.4.3 Nitrogen Calibration Parameters

Nitrogen calibration focused on parameters controlling atmospheric nitrogen input, mineralization, denitrification, nitrate percolation, plant uptake distribution, soil-moisture controls on denitrification, and initial soil nitrate concentration. The calibrated parameters included RCN, CDN, CMN, N_UPDIS, NPERCO, SDNCO, and SOL_NO3 (Table 4.12).

The RCN parameter represents the concentration of nitrogen in rainfall and accounts for the atmospheric nitrogen contribution to the watershed. CDN is the denitrification exponential rate coefficient and controls the rate of denitrification in the soil. CMN is the rate factor for humus mineralization of active organic nutrients and affects the conversion of organic nitrogen into mineral nitrogen. N_UPDIS controls the depth distribution of plant nitrogen uptake and therefore affects how nitrogen is removed from the soil profile by vegetation. NPERCO controls nitrate movement with percolating water and is important for nitrate leaching and subsurface transport. SDNCO is the denitrification threshold water-content factor and controls the soil-moisture condition required for denitrification. SOL_NO3 represents the initial nitrate concentration in the soil layer and affects the initial nitrate pool available for transport (Arnold et al., 1998; Neitsch et al., 2011).

Table 4.12. Nitrogen calibration parameters used in the Nueces River Watershed SWAT model.

Change code	Parameter	Description	Calibrated value
v	RCN	Concentration of nitrogen in rainfall; represents atmospheric nitrogen contribution	12.8203
v	CDN	Denitrification exponential rate coefficient; controls denitrification rate in soil	0.2297
v	CMN	Rate factor for humus mineralization of active organic nutrients	0.000019
v	N_UPDIS	Nitrogen uptake distribution parameter; controls depth distribution of plant nitrogen uptake	63.2031
v	NPERCO	Nitrogen percolation coefficient; controls nitrate movement with percolating water	0.9613
v	SDNCO	Denitrification threshold water-content factor; controls soil-moisture condition needed for denitrification	1.1516
r	SOL_NO3	Initial nitrate concentration in soil layer; controls initial soil nitrate pool	0.4672

Note: v = replace with absolute value; r = relative change [multiplied by (1 +{value}); a = absolute change (added to existing value). Relative adjustments (r) are used for spatial inputs to preserve baseline landscape heterogeneity.

4.3.4.4 Phosphorus Calibration Parameters

Phosphorus calibration focused on parameters controlling soluble phosphorus movement, phosphorus partitioning between soil and solution, soil phosphorus availability, plant uptake distribution, organic phosphorus enrichment, and initial soil phosphorus pools. The selected phosphorus calibration parameters included PPERCO, PHOSKD, PSP, P_UPDIS, ERORGP, SOL_SOLP, and SOL_ORGP (Table 4.13).

The PPERCO parameter is the phosphorus percolation coefficient and controls the movement of soluble phosphorus from the soil layer to lower layers. PHOSKD is the phosphorus soil partitioning coefficient and controls phosphorus sorption and partitioning between soil and solution. PSP is the phosphorus availability index and affects the availability of phosphorus in the soil solution. P_UPDIS controls the depth distribution of plant phosphorus uptake. ERORGP is the organic phosphorus enrichment ratio and controls the amount of organic phosphorus attached to eroded sediment. SOL_SOLP represents the initial soluble or labile phosphorus concentration in the soil layer, while SOL_ORGP represents the initial organic phosphorus concentration in the soil layer.

In some SWAT input structures, the available phosphorus pool may be represented using SOL_LABP rather than SOL_SOLP. Therefore, phosphorus parameterization should be interpreted based on the available SWAT input-file structure. In this study, the phosphorus calibration was based on the available soil phosphorus variables in the model setup and was interpreted with consideration of the relationship between soil phosphorus pools, sediment transport, and total phosphorus loading.

Table 4.13. Calibrated phosphorus parameters used in the Nueces River Watershed SWAT model.

Change code	Parameter	Description	Calibrated value
v	PPERCO	Phosphorus percolation coefficient; controls soluble phosphorus movement from soil layer to lower layers	12.3658
v	PHOSKD	Phosphorus soil partitioning coefficient; controls phosphorus sorption/partitioning between soil and solution	114.3436
v	PSP	Phosphorus availability index; controls phosphorus availability in soil solution	0.6429
v	P_UPDIS	Phosphorus uptake distribution parameter; controls depth distribution of plant phosphorus uptake	18.6456
v	ERORGP	Organic phosphorus enrichment ratio; controls organic phosphorus attached to eroded sediment	5.1134
v	SOL_SOLP	Initial soluble/labile phosphorus concentration in soil layer	53.0396
v	SOL_ORGP	Initial organic phosphorus concentration in soil layer	14.3311

Note: v = replace with absolute value; r = relative change [multiplied by (1 +{value}); a = absolute change (added to existing value). Relative adjustments (r) are used for spatial inputs to preserve baseline landscape heterogeneity.

4.3.5 Simulations of Management Scenarios

After calibration and validation, the calibrated model was used to simulate selected management scenarios. The baseline scenario, S0, represented the calibrated watershed condition with the existing land-management operations, reservoir settings, and auto-fertilization assumptions retained in the model (Table 4.14). Management scenarios were developed to evaluate changes in streamflow, sediment loading, and nutrient transport.

Table 4.14. Management scenarios simulated using the calibrated SWAT model.

ID	Name/practice	Scenario group and SWAT process affected	Parameter or management change
S0 SED0	Calibrated baseline condition	Baseline: Flow, sediment, nitrogen, and phosphorus processes	Calibrated SWAT model with existing land-use and management assumptions; auto-fertilization active with elemental nitrogen represented.
F1 N1 P1	Brush clearing, 50%	Flow, nitrogen, and phosphorus response: Runoff generation, canopy storage, overland-flow resistance, evapotranspiration, and nutrient transport	CN2 reduced by 5%; CANMX reduced by 50%; OV_N reduced by 20%; ESCO reduced by 15%; EPCO reduced by 15%.
F2	Brush clearing, 85%	Flow response: Runoff generation, canopy storage, overland-flow resistance, and evapotranspiration	CN2 reduced by 10%; CANMX reduced by 85%; OV_N reduced by 30%; ESCO reduced by 15%; EPCO reduced by 15%.
F3	Grassed waterways—30% channel-cover adjustment	Flow response: Channel roughness, concentrated-flow control, channel protection, sediment routing, and sediment-associated nutrient transport	CH_N2 increased by 50%, from 0.047 to 0.070; CH_COV1 reduced by 30%, from 0.315 to 0.221; CH_COV2 reduced by 30%, from 0.263 to 0.184.
SED1	Filter strips	Sediment control: Sediment trapping and reduction of sediment delivery from upland areas to the stream channel	FILTERW.mgt set to 6 m.
SED2 N4	Streambank stabilization	Sediment and nitrogen response: Channel erosion, sediment routing, and transport of sediment-associated organic nitrogen	CH_N2 increased by 50%; CH_COV1 reduced by 50%; CH_COV2 reduced by 50%.
SED3 N2 P2	Grassed waterways—90% channel-cover adjustment	Sediment, nitrogen, and phosphorus response: Concentrated-flow control, channel protection, sediment routing, and sediment-associated nutrient transport	CH_N2 increased by 50%; CH_COV1 reduced by 90%; CH_COV2 reduced by 90%.
SED4	Contour farming	Sediment control: Surface-runoff generation and upland soil erosion	CN2 reduced by 20%; USLE_P adjusted to 0.600.
SED5	Terracing	Sediment control: Runoff reduction and upland erosion control	CN2 adjusted to represent reduced runoff; USLE_P adjusted to 0.120.

SED6 N3 P3	Strip cropping	Sediment, nitrogen, and phosphorus response: Upland erosion, organic nitrogen movement, and particulate phosphorus transport	CN2 adjusted to represent altered runoff; USLE_P adjusted to 0.300.
SED7	Grade stabilization	Sediment control: Channel slope, channel erosion, and sediment-transport capacity	CH_COV1 reduced by 20%; CH_COV2 reduced by 20%; CH_S2 reduced by 80%.

Note: Scenario effects were evaluated relative to the baseline condition, S0. Parameter-based BMP scenarios represent simplified watershed-scale management assumptions and should be interpreted as relative scenario responses rather than exact field-scale predictions.

4.3.5.1 Brush-Clearing for Flow Response Scenarios

Brush-clearing scenarios were developed to evaluate how changes in vegetation cover and watershed roughness may influence streamflow response in the Nueces River Watershed. Because range-brush is the dominant land-cover category in the watershed, changes in brush cover can affect canopy interception, evapotranspiration, soil-water storage, surface roughness, and runoff generation. In SWAT, these effects can be represented through selected hydrologic parameters that control surface runoff, canopy storage, overland flow resistance, evaporation, and plant uptake. To evaluate the effects of the brush-clearing, the following parameters were modified, including the SCS runoff curve number (CN2.mgt), maximum canopy storage (CANMX.hru), Manning's roughness coefficient for overland flow (OV_N.hru), soil evaporation compensation factor (ESCO.hru), and plant uptake compensation factor (EPCO.hru). CN2 controls the amount of precipitation converted to surface runoff, whereas CANMX represents the maximum amount of water that can be intercepted and stored by the vegetation canopy. OV_N controls resistance to overland flow. ESCO affects the distribution of soil evaporation with depth, and EPCO influences the ability of plants to obtain water from lower soil layers. Reductions in these parameters were used to represent the assumed effects of reduced brush cover, canopy interception, surface resistance, and plant-water use.

Two brush-clearing scenarios (F1 and F2) were evaluated (Table 4.14). F1 represented a moderate brush-clearing condition, while F2 represented a more intensive brush-clearing condition. The brush-clearing scenarios (F1 and F2) simulated here represent hypothetical management responses. Brush clearing can produce complex hydrologic responses depending on soil depth, rainfall intensity, vegetation regrowth, slope, antecedent moisture, and spatial location within the watershed. In some areas, reducing woody vegetation may increase water yield by reducing evapotranspiration and interception. In other areas, reduced surface cover may increase runoff and erosion risk if not paired with soil-conservation practices. Therefore, brush-clearing scenarios simulated here were evaluated only as process-based sensitivity scenarios designed to estimate the relative magnitude of flow response.

The F3 grassed-waterway scenario represents a moderate channel-protection best management practice (BMP). It increases CH_N2 by 50% to represent greater channel roughness and slower flow velocity. It also reduces CH_COV1 and CH_COV2 by 30%, to represent improved channel cover and reduced channel erodibility. Overall, F3 is expected to have little effect on streamflow but may reduce sediment and sediment-associated nitrogen and phosphorus transport.

4.3.5.2 Sediment-Control Practice Scenarios

Several sediment-control practice scenarios were developed to evaluate potential reductions in sediment loading relative to the calibrated sediment baseline. These scenarios included filter strips, streambank stabilization, grassed waterways, contour farming, terracing, strip cropping, and grade stabilization. Each scenario was represented by modifying SWAT parameters associated with sediment trapping, channel protection, support practices, curve number, channel erodibility, channel cover, or channel slope.

Sediment-control scenarios modified the edge-of-field filter-strip width (FILTERW.mgt), USLE support-practice factor (USLE_P.mgt), main-channel Manning's roughness coefficient (CH_N2.rte), channel erodibility factor (CH_COV1.rte), channel cover factor (CH_COV2.rte), and main-channel slope (CH_S2.rte). FILTERW represents the width of the vegetated filter strip through which surface runoff passes before entering the channel. USLE_P represents the effectiveness of erosion-control support practices, with lower values indicating greater erosion reduction. CH_N2 controls channel-flow resistance and routing velocity. CH_COV1 and CH_COV2 control channel erodibility and protection from erosion, respectively, while CH_S2 represents the average slope of the main channel. The parameter adjustments were used to represent filter strips, streambank stabilization, grassed waterways, contour farming, terracing, strip cropping, and grade-stabilization practices (Arnold et al., 2012).

The scenario labeled SED0/S0 represented the calibrated sediment baseline (Table 4.14). SED1 represented filter strips using the FILTERW parameter. SED2 represented streambank stabilization by increasing channel roughness and reducing channel erodibility and channel cover factors. SED3 represented grassed waterways using a stronger reduction in channel erodibility and channel cover parameters. SED4 represented contour farming through modification of CN2 and USLE_P. SED5 represented terracing by modifying CN2 and USLE_P. SED6 represented strip cropping by modifying CN2 and USLE_P. SED7 represented grade stabilization through changes in channel cover, channel erodibility, and channel slope.

Sediment loading itself was not directly modified as an input parameter. Instead, it was evaluated as a model response using SED_OUT, which represents the amount of sediment transported out of a reach during the simulation time step. Monthly SED_OUT values at the selected watershed outlet were aggregated and reported in metric tons per month. Consequently, the management parameters altered sediment generation, trapping, channel erosion, deposition, and routing, whereas SED_OUT quantified the resulting change in sediment loading.

4.3.5.3 Nitrogen and Phosphorus-response Scenarios

The nitrogen- and phosphorus-response scenarios did not directly modify nitrogen- or phosphorus-process parameters. Instead, selected hydrologic and sediment-control parameter sets were applied while the baseline fertilizer and nutrient-management assumptions were retained. Changes in total nitrogen and total phosphorus loads therefore represented the indirect effects of altered runoff, plant-water use, erosion, sediment trapping, and channel routing. Sediment-related practices were expected to affect particulate organic nitrogen and phosphorus more directly because these nutrient forms are transported with eroded sediment.

4.3.5.3.1 Nitrogen-related Management Scenarios

Nitrogen-related management scenarios were evaluated relative to the calibrated baseline condition. The baseline scenario, S0, represented the calibrated model condition with the existing management setup. In the current model configuration, auto-fertilization was active and elemental nitrogen fertilizer was represented. Therefore, nitrogen scenario results were interpreted relative to this baseline assumption.

The nitrogen BMP scenarios analyzed included brush clearing, grassed waterways, strip cropping, and streambank stabilization. Although some of these practices primarily affect flow or sediment transport, they can also influence nitrogen loading by changing runoff generation, vegetation uptake, channel transport, and organic nitrogen movement. Scenario N1 represented brush clearing at 50%, implemented through changes in CN2, CANMX, OV_N, ESCO, and EPCO (Table 4.14). Scenario N2 represented grassed waterways through changes in CH_N2, CH_COV1, and CH_COV2. Scenario N3 represented strip cropping designed based on slope, implemented through changes in CN2 and USLE_P. Scenario N4 represented streambank stabilization through changes in CH_N2, CH_COV1, and CH_COV2.

4.3.5.3.2 Phosphorus-related Management Scenarios

Phosphorus management scenarios were evaluated relative to the calibrated baseline condition. The scenarios included brush clearing, grassed waterways, and strip cropping (Table 4.14). Although these scenarios were not all direct phosphorus fertilizer scenarios, they can influence phosphorus loading by modifying runoff generation, sediment transport, channel stability, and erosion control.

Scenario P1 represented brush clearing at 50% (Table 4.14). This scenario modified CN2, CANMX, OV_N, ESCO, and EPCO. These parameter changes represented reductions in canopy storage, surface roughness, soil evaporation compensation, and plant-water uptake. Because brush clearing can affect runoff generation, it may also affect phosphorus transport. If runoff increases after brush clearing, dissolved and particulate phosphorus transport may increase unless the practice is paired with erosion-control measures. Therefore, brush clearing must be interpreted carefully in relation to both water-yield response and sediment-control needs.

Scenario P2 represented grassed waterways. This scenario increased channel roughness and reduced channel cover and channel erodibility parameters. Grassed waterways can reduce phosphorus loading by slowing concentrated flow, increasing deposition, reducing channel detachment, and decreasing sediment transport capacity. Because particulate phosphorus is closely tied to sediment transport, grassed waterways may be particularly effective for reducing sediment-associated phosphorus delivery.

Scenario P3 represented strip cropping designed based on slope. This scenario modifies CN2 and USLE_P. Strip cropping can reduce runoff energy, slow overland flow, and reduce upland soil erosion. By reducing erosion and sediment delivery, strip cropping may reduce particulate phosphorus transport. However, dissolved phosphorus may not decline as strongly unless fertilizer inputs, soil phosphorus availability, and runoff timing are also managed.

All management scenarios were compared with the S0 baseline condition. Scenario outputs were evaluated at the monthly time scale using streamflow (FLOW_OUT), sediment loading (SED_OUT), total nitrogen loading, and total phosphorus loading.

4.4 Results

This section presents the SWAT model results for streamflow, sediment, total nitrogen, and total phosphorus. The results include model calibration and validation performance, baseline loading patterns, and the simulated effects of selected best management practice scenarios.

4.4.1 Model Calibration and Validation

Model calibration and validation were evaluated by comparing simulated and observed monthly streamflow, sediment, total nitrogen, and total phosphorus values. Model performance was assessed using R^2, NSE, KGE, and SWAT-CUP uncertainty measures to determine the model's ability to reproduce observed temporal patterns and load magnitudes.

4.4.1.1 Flow Calibration and Validation Results

During the calibration period, the monthly simulated flow showed strong agreement with observed monthly discharge (Figure 4.7 and Table 4.15). The model captured the general timing and magnitude of major flow events, including the high-flow response associated with wet months. The calibration statistics indicated that the model was able to reproduce monthly discharge patterns within an acceptable to very good performance range for watershed-scale hydrologic modeling (Table 4.15). The p-factor and r-factor showed that uncertainty remained in the simulation. Recalling that the p-factor shows how many observed values fall within the 95%

prediction uncertainty range, while the r-factor shows how wide that uncertainty range is. In general, a higher p-factor and a lower r-factor indicate better model uncertainty performance. A p-factor greater than 0.50 and an r-factor less than 1.50 are commonly used as general guidelines, especially for streamflow calibration; however, since these are guidance values, they are not strict pass–fail criteria. The calibrated model was considered suitable for subsequent sediment and nutrient calibration with the noted uncertainties, which could be further improved in future work.

During the validation period, the model maintained acceptable agreement with observed flow based on R^2 and NSE (Figure 4.7 and Table 4.15). However, validation performance was weaker than calibration, especially based on KGE. This indicates that although the model was able to represent the overall monthly flow pattern, some differences remained in flow bias, variability, and timing during the independent validation period. The weaker validation performance is expected in large semi-arid watersheds where runoff response can be dominated by short-duration storms, reservoir operations, and spatial variability in rainfall that may not be fully captured by the available weather input data (Pulighe et al., 2019; Thomas et al., 2019).

Table 4.15. Monthly streamflow calibration and validation performance at USGS-08211500 Nueces River at Calallen, Texas.

Period	**p-factor**	**r-factor**	**R^2**	**NSE**	**KGE**	**General interpretation**
Calibration, 2015–2017	0.67	6.06	0.87	0.86	0.88	Very good monthly flow simulation
Validation, 2018–2019	—	—	0.69	0.61	0.40	Acceptable by R^2/NSE; weaker by KGE

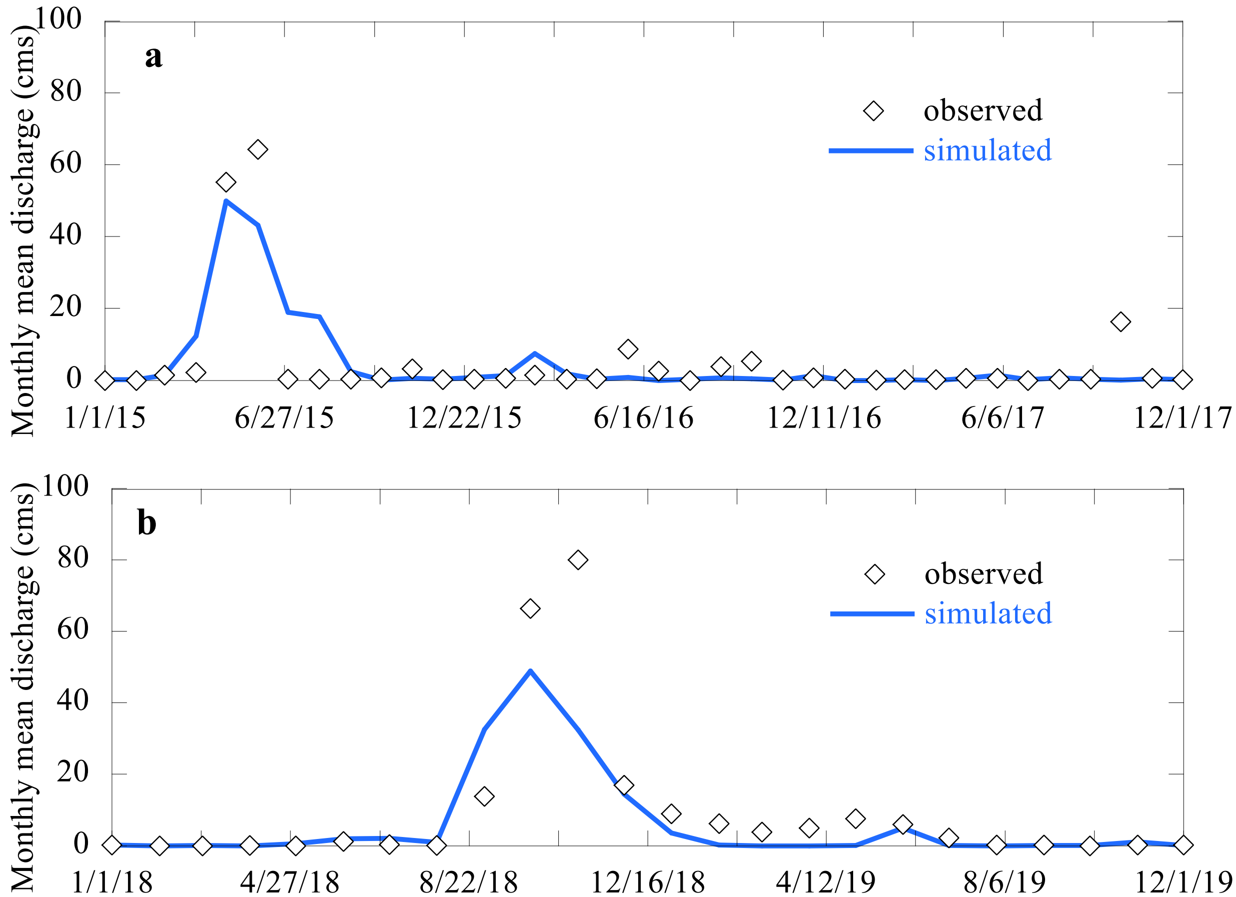

Figure 4.7. Observed and simulated monthly streamflow during: (a) the calibration period, 2015-2017, and (b) the validation period, 2018-2019.

4.4.1.2 Sediment Calibration and Validation Results

During calibration, the sediment model reproduced the overall monthly sediment-loading pattern and captured the dominant sediment peak during the calibration period. The calibration statistics indicated strong model performance, with the model falling within a very good performance range based on commonly used sediment model evaluation criteria (Table 4.16 and Figure 4.8). The calibration p-factor was 0.39 and the r-factor was 1.40, indicating that the prediction uncertainty band did not capture all observations, but the overall simulated pattern and magnitude were reasonable. The calibration R^2, NSE, and KGE values were 0.92, 0.92, and 0.77, respectively.

During validation, the model also showed strong agreement with observed monthly sediment loads. The validation R^2 and NSE values were 0.99 and 0.93, respectively, indicating that the model captured the observed validation trend and magnitude well. The validation KGE value was 0.61, which indicates acceptable performance but also suggests some remaining uncertainty in bias, variability, or timing. Overall, the sediment model was considered suitable for evaluating baseline sediment loading and comparing sediment-control management scenarios.

Table 4.16. Sediment calibration and validation performance for the Nueces River Watershed SWAT model.

Period	**p-factor**	**r-factor**	**R^2**	**NSE**	**KGE**	**General interpretation**
Calibration, 2015–2017	0.39	1.40	0.92	0.92	0.77	Very good sediment simulation
Validation, 2018–2019	—	—	0.99	0.93	0.61	Very good by R^2/NSE; acceptable by KGE

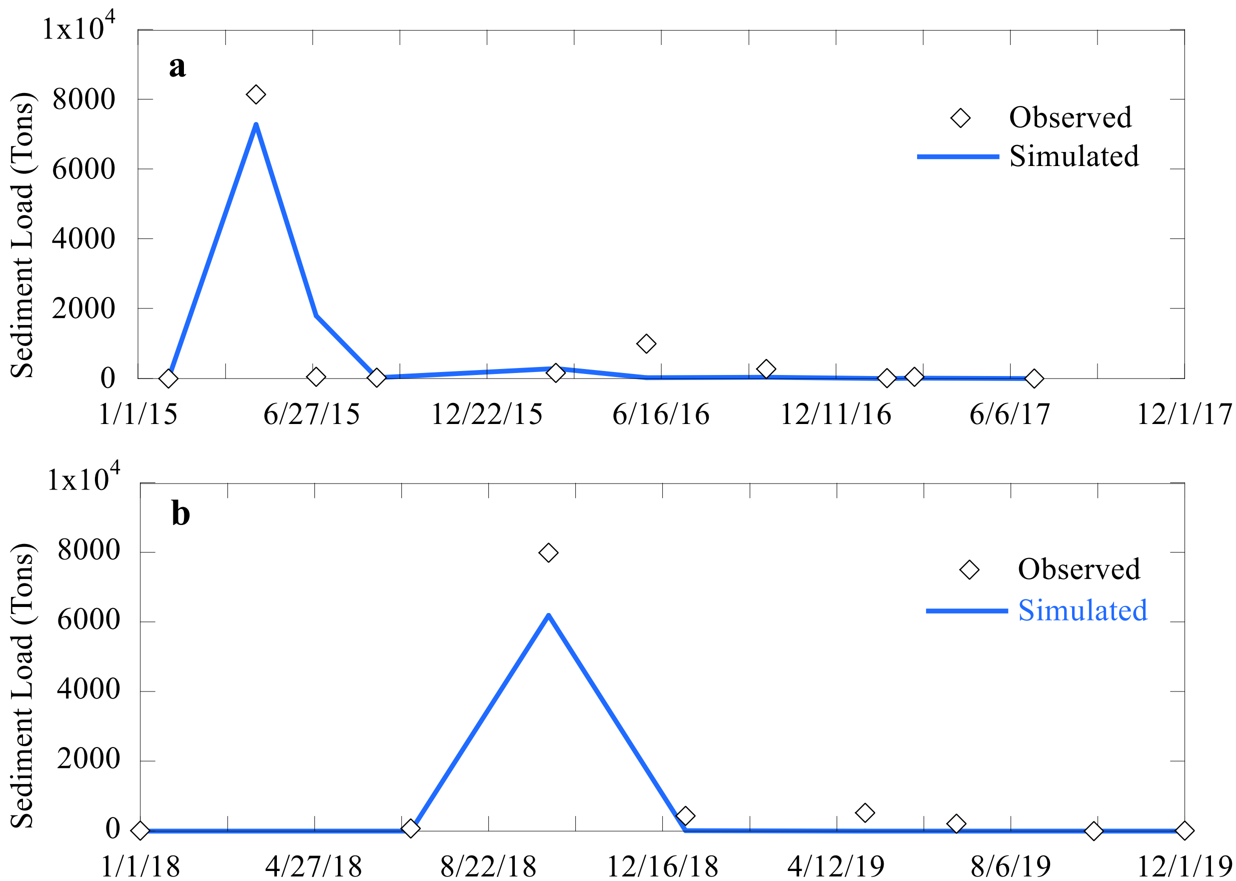

Figure 4.8. Observed and simulated monthly sediment load during: (a) the calibration period, 2015–2017, and (b) the validation period, 2018–2019.

4.4.1.3 Nutrients Calibration and Validation Results

Nutrient calibration and validation were evaluated by comparing simulated and observed monthly total nitrogen and total phosphorus loads. The results were used to assess the model's ability to reproduce seasonal patterns, event-driven peaks, and overall nutrient transport behavior. Greater uncertainty was associated with nutrient simulations than with streamflow because water-quality observations were more limited and nutrient loads were strongly influenced by episodic runoff and sediment transport.

4.4.1.3.1 Nitrogen Calibration and Validation Results

For total nitrogen calibration, the model was evaluated by comparing observed and simulated monthly total nitrogen loads in kilograms per month. The calibration period included a large nitrogen-loading peak, which was important for testing whether the model could represent event-driven nitrogen transport during high-flow conditions. During calibration, the model reproduced the dominant nitrogen-loading pattern and captured the major peak in the observed record. The calibration statistics showed very good performance, with a p-factor of 0.50, r-factor of 1.18, R^2 of 0.93, NSE of 0.93, and KGE of 0.90 (Table 4.17 and Figure 4.9). These results indicate that the calibrated nitrogen model represented monthly total nitrogen loading well during the calibration period.

During validation, the model maintained strong agreement based on R^2 and acceptable agreement based on NSE. The validation R^2 was 0.99 and the NSE was 0.76, indicating that the model captured the overall pattern of observed nitrogen loading during the independent validation period. However, the validation KGE was 0.35, which indicates remaining uncertainty in the model's ability to reproduce bias, variability, or the exact magnitude of monthly nitrogen loads. This suggests that nitrogen validation should be interpreted carefully even though the model performed well according to R^2 and NSE.

Table 4.17. Total nitrogen calibration and validation performance for the Nueces River Watershed SWAT model.

Period	**p-factor**	**r-factor**	**R^2**	**NSE**	**KGE**	**General interpretation**
Calibration, 2015–2017	0.50	1.18	0.93	0.93	0.90	Very good nitrogen simulation
Validation, 2018–2019	—	—	0.99	0.76	0.35	Acceptable by R^2/NSE; uncertain by KGE

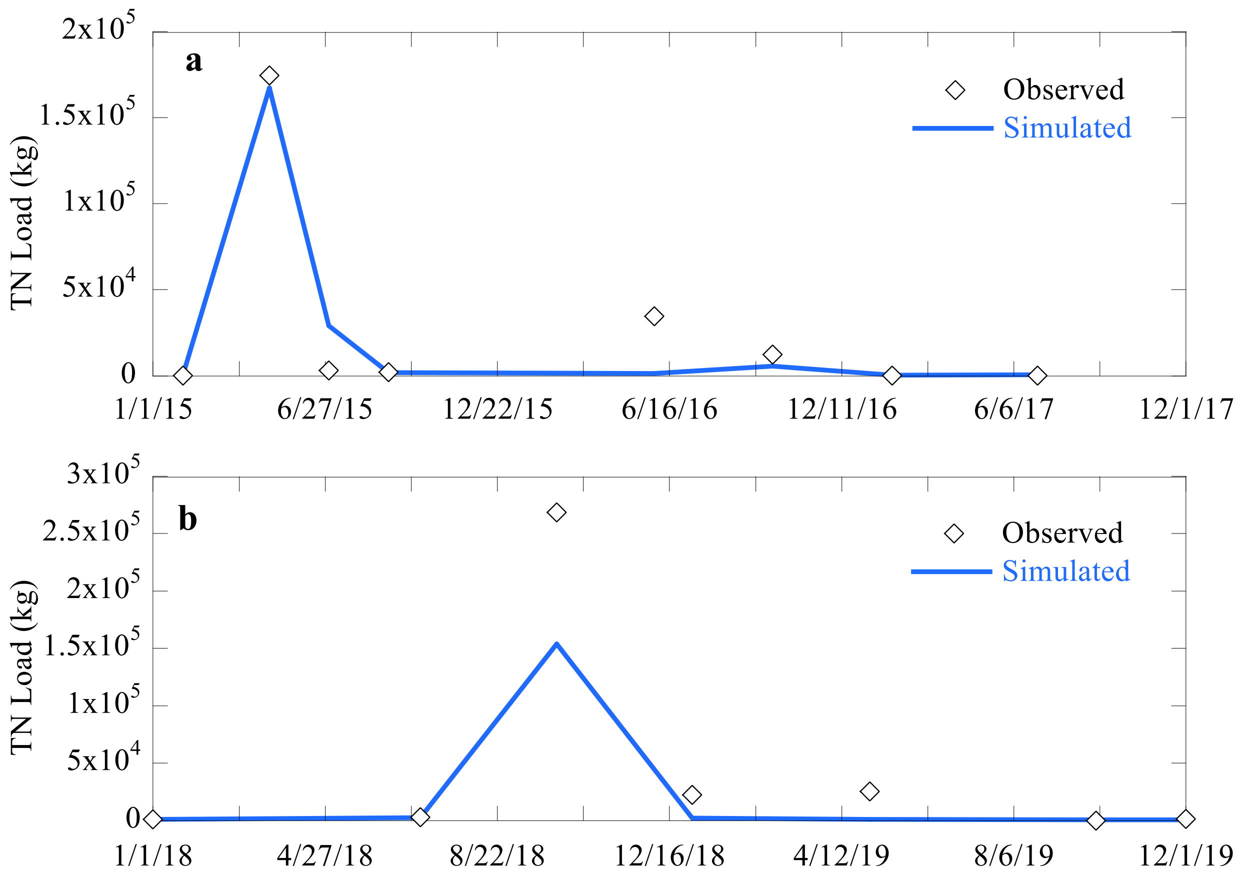

Figure 4.9. Observed and simulated monthly total nitrogen load during: (a) the calibration period, 2015-2017; (b) the validation period, 2018-2019.

4.4.1.3.2 Phosphorus Calibration and Validation Results

Total phosphorus calibration was conducted by comparing observed and simulated monthly total phosphorus loads in kilograms per month. Because phosphorus transport is strongly linked to sediment and runoff, the phosphorus calibration depended on the previously calibrated flow and sediment components.

During calibration, the model reproduced the dominant phosphorus-loading pattern and captured the major phosphorus peak during the calibration period. The calibration p-factor was 0.50, and the r-factor was 1.68 (Table 4.18 and Figure 4.10). The calibration R^2, NSE, and KGE values were 0.94, 0.94, and 0.92, respectively. These values indicate very good model performance during the calibration period.

During validation, the model showed strong correlation based on R^2, but the NSE and KGE values were weak. The validation R^2 was 0.99, indicating that the model followed the general trend in the observed phosphorus data. However, the validation NSE was 0.29, and the validation KGE was -0.09. These results indicate that the model did not reliably reproduce the magnitude, variability, or bias of observed total phosphorus loads during the independent validation period. Therefore, phosphorus results should be interpreted cautiously, especially for absolute load prediction.

Table 4.18. Total phosphorus calibration and validation performance for the Nueces River Watershed SWAT model.

Period	p-factor	r-factor	R^2	NSE	KGE	General interpretation
Calibration, 2015–2017	0.50	1.68	0.94	0.94	0.92	Very good phosphorus calibration
Validation, 2018–2019	—	—	0.99	0.29	-0.09	mixed performance for validation; use cautiously

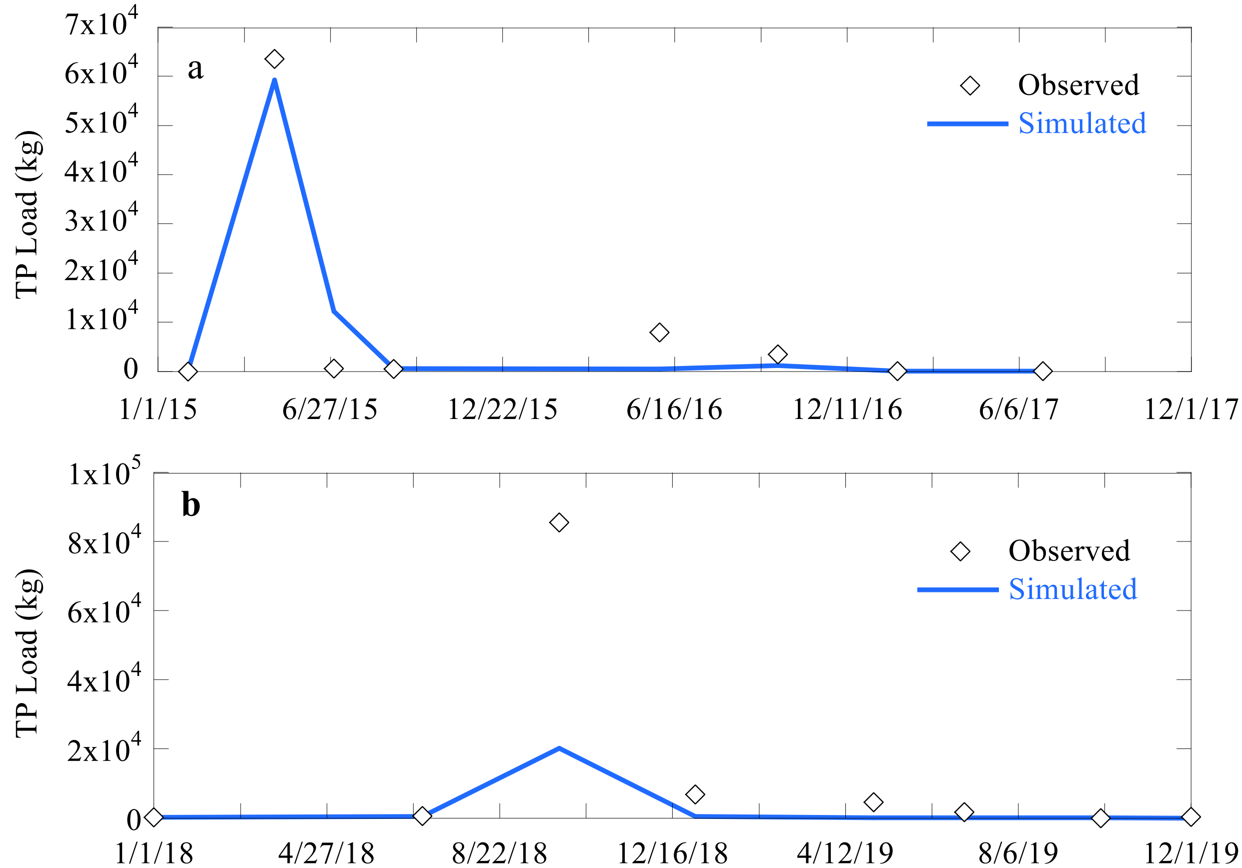

Figure 4.10. Observed and simulated monthly total phosphorus load during: (a) the calibration period, 2015-2017, and (b) the validation period, 2018-2019.

4.4.2 Simulations of Various BMP Scenarios

The calibrated model was used to simulate selected BMP scenarios representing brush clearing, filter strips, grassed waterways, streambank stabilization, contour farming, terracing, strip cropping, and grade stabilization. Scenario results were compared with the calibrated baseline to quantify relative changes in streamflow, sediment, nitrogen, and phosphorus loading.

4.4.2.1 Baseline Simulations

The streamflow calibration results (Figure 4.7a) indicate that the model reproduced the major hydrologic behavior of the Nueces River Watershed at the monthly time scale. The model was able to simulate low-flow periods as well as the general response to wet months. This is important because the Nueces River Watershed is characterized by strong temporal variability, with long dry periods interrupted by high-intensity rainfall events. In such watersheds, a small number of wet months can contribute a large portion of annual flow and pollutant export. Therefore, capturing the magnitude and timing of high-flow months is more important for sediment and nutrient modeling than matching every low-flow month.

The validation results (Figure 4.7b) show that model performance declined during the independent period, particularly when evaluated using KGE. This suggests that the model may not fully reproduce the observed variability and bias in all validation months. Several factors may explain this behavior. First, rainfall in semi-arid watersheds can be highly localized, and a limited weather-station network may not fully represent storm distribution across a large watershed. Second, reservoir storage and release operations can affect downstream flow timing and magnitude. Third, small errors in simulating high-flow events can strongly influence performance statistics because monthly flows vary over several orders of magnitude between dry and wet periods.

4.4.2.2 Simulations of Responses from the Two Reservoirs

Figures 4.11 and 4.12 show that Choke Canyon Reservoir and Lake Corpus Christi responded strongly to major wet years, especially 2015 and 2018. The plotted inflow and outflow patterns indicate event-driven routing of flow, sediment, nitrogen, and phosphorus through the reservoir system. Sediment inflow and outflow increased during high-flow years. Because the plotted sediment inflow and outflow patterns were similar, the reservoirs appeared to route much of the event-driven sediment load downstream during these periods rather than acting as strong sediment sinks in the plotted results.

Lake Corpus Christi showed a similar pattern, with the largest flow, sediment, total nitrogen, and total phosphorus responses occurring during high-flow years. The reservoir results indicate that Lake Corpus Christi received and routed substantial loads during wet periods, especially when inflows increased sharply. Sediment and nutrient loads were much lower during dry years, which supports that pollutant delivery in the Nueces River Watershed is event driven.

For the nutrient, TOT_N and TOT_P represent the outgoing nutrient loads from the reservoir. In the SWAT output file, total nitrogen is reported as the sum of organic nitrogen (NO_3) and nitrate nitrogen (ORGN). Similarly, total phosphorus is reported as the sum of organic phosphorus (ORGP) and mineral phosphorus (MINP). Therefore, the nitrogen and phosphorus values shown for the reservoir outflow represent the combined nutrient load leaving the reservoir, not only one individual nutrient form.

Nitrogen and phosphorus load through Choke Canyon Reservoir and Lake Corpus Christi showed strong event-driven behavior, similar to streamflow and sediment. Total nitrogen and total phosphorus generally increased during wet years and high-flow periods, especially when larger inflows moved through the reservoir system. The similarity between inflow and outflow nutrient patterns suggests that both reservoirs routed a substantial portion of the incoming nutrient load downstream during major runoff events. This indicates that reservoir nutrient export was closely controlled by hydrologic conditions, with higher flow periods increasing the transport of both dissolved and sediment-associated nitrogen and phosphorus. It should also be noted that both total nitrogen and total phosphorus exhibited some storage, indicating load loss when rioting through the two reservoirs. Further studies elucidating the mechanisms, combined with field data, can help validate this potential phenomenon.

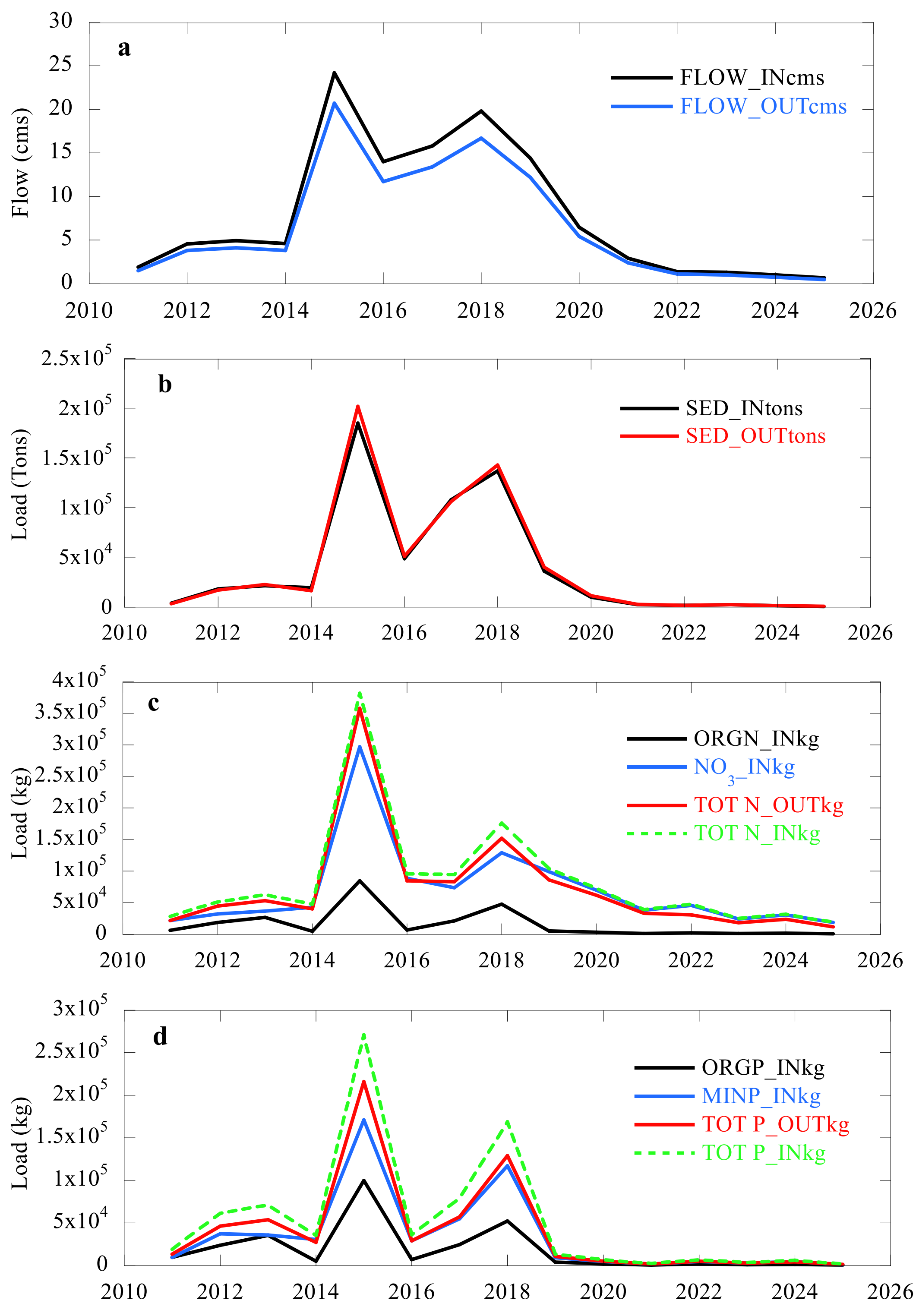

Figure 4.11. (a) Simulated reservoir inflow & outflow, (b) annual sediment in and out load, (c) annual nitrogen load, and (d) annual phosphorus load for Choke Canyon Reservoir.

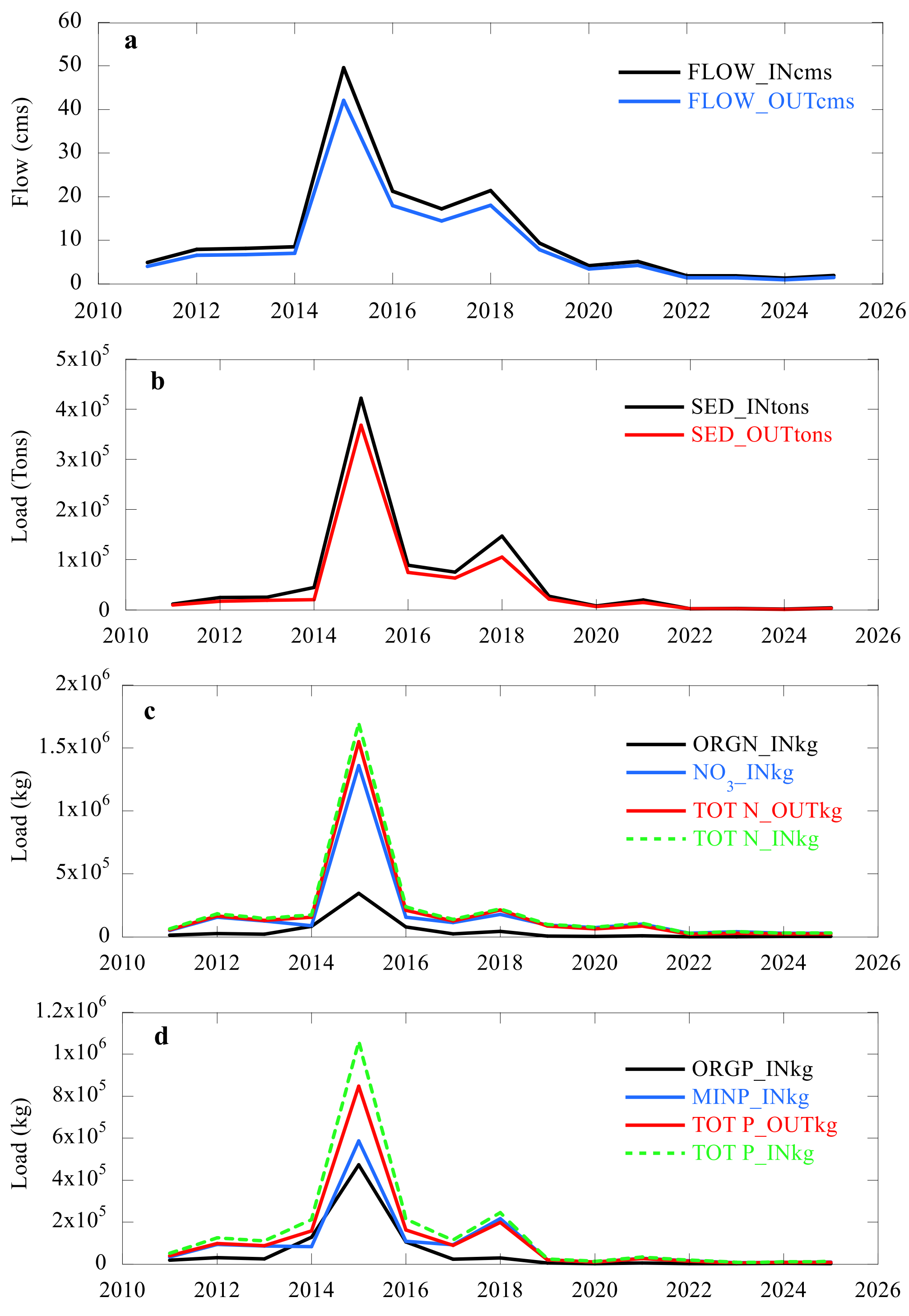

Figure 4.12. (a) Simulated reservoir inflow & outflow, (b) annual sediment in and out load, (c) annual nitrogen load, and (d) annual phosphorus load for Lake Corpus Christi.

4.4.2.3 Simulations of Brush-Clearing / Flow-Response Scenarios

Figure 4.13 compares observed and simulated monthly streamflow under the baseline, 50% brush-clearing (F1), 85% brush-clearing (F2), and grassed-waterway/channel-protection (F3) scenarios (Table 4.14). The F1 and F2 scenarios generally followed the timing of the baseline hydrograph but produced larger discharge peaks during major runoff events. The 85% brush-clearing scenario (F2) produced the strongest response, followed by the 50% brush-clearing scenario (F1), indicating that greater reductions in canopy storage and overland roughness increased simulated streamflow. In contrast, the F3 scenario closely overlapped the baseline throughout the simulation period, indicating little or no effect on monthly discharge. These results suggest that brush clearing may increase high-flow discharge and could increase sediment and nutrient transport unless it is combined with erosion-control and revegetation practices.

In Figure 4.13, sediment, total nitrogen, and total phosphorus generally followed the same event-driven pattern as streamflow. The largest sediment and nutrient loads occurred during high-flow months, indicating that runoff peaks were the main drivers of sediment detachment, channel transport, and nutrient export. In Figure 4.13b, the brush-clearing scenarios increased sediment load during major runoff events, with F2 producing the highest sediment peaks and F1 producing a smaller but still noticeable increase relative to the baseline. A similar pattern was observed for total nitrogen and total phosphorus in Figure 4.13c and Figure 4.13d, where increased runoff under the brush-clearing scenarios resulted in greater nutrient transport, especially during wet periods. The F3 scenario showed a much smaller response compared with F1 and F2 because it primarily represented channel-protection and grassed-waterway adjustments rather than a major change in runoff generation. Overall, Figure 4.13b–d indicates that brush clearing may increase sediment and nutrient export when increased flow is not paired with adequate erosion-control measures, while the F3 scenario had a limited effect on monthly discharge and therefore produced comparatively smaller changes in sediment, total nitrogen, and total phosphorus loads.

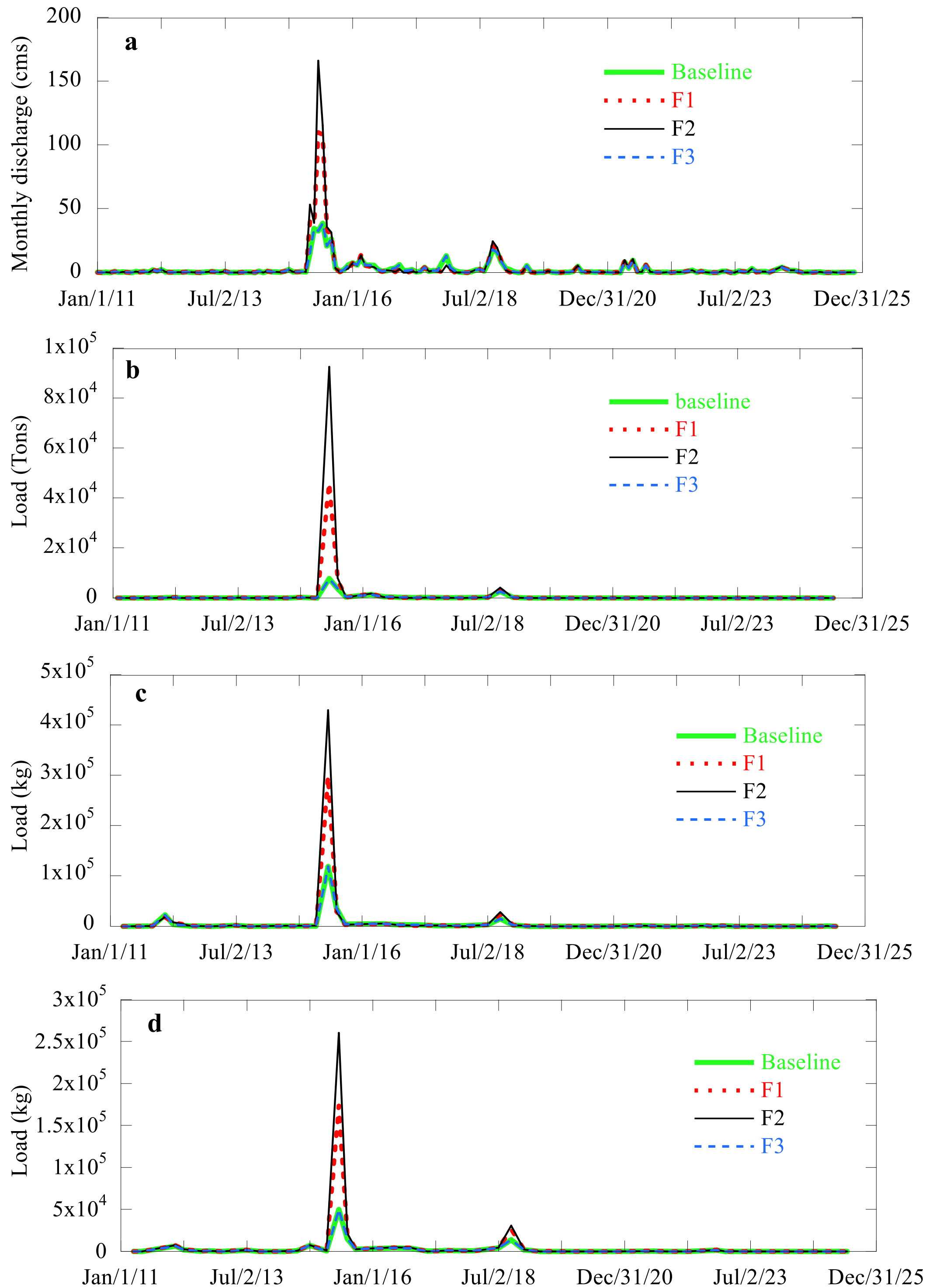

Figure 4.13. Simulation Comparison of Brush-Clearing / Flow-Response Scenarios: (a) streamflow, (b) sediment load, (c) total N load, and (d) total P load.

4.4.2.4 Simulations of Grassed Waterway / Sediment-Control Practice Scenarios

Figure 4.14 compares the observed and simulated monthly streamflow, sediment load, total nitrogen load, and total phosphorus load under the calibrated baseline condition and sediment-control BMP scenarios. The evaluated scenarios included filter strips (SED1), streambank stabilization (SED2), grassed waterways (SED3), contour farming (SED4), terracing (SED5), strip cropping (SED6), and grade stabilization (SED7) as summarized in Table 4.14.

Figure 4.14a shows that the sediment-control BMP scenarios generally followed the same monthly streamflow pattern as the calibrated baseline condition (S0). This indicates that most sediment-control practices had limited influence on overall monthly discharge because they were designed primarily to reduce erosion, sediment delivery, and channel sediment transport rather than to substantially alter watershed runoff volume. Minor differences in streamflow may occur in scenarios such as contour farming (SED4) and terracing (SED5) because these practices can affect runoff generation through changes in curve number and surface-flow response. However, the overall hydrograph pattern remained similar to the baseline, suggesting that sediment BMPs have minimal influence on the timing or magnitude of monthly streamflow.

Figure 4.14b shows that sediment loads remained low during most months but increased sharply during high-flow periods. The largest differences among scenarios occurred during major sediment-producing months, indicating that BMP effectiveness was most visible during event-driven sediment pulses. This pattern is expected because practices such as filter strips (SED1), grassed waterways (SED3), contour farming (SED4), terracing (SED5), streambank stabilization (SED2), strip cropping (SED6), and grade stabilization (SED7) are most relevant when runoff and channel flow are high enough to mobilize sediment.

Among the sediment-control scenarios, practices that directly reduced upland erosion or channel sediment detachment produced the most visible reductions during large sediment peaks. Terracing (SED5) and contour farming (SED4) reduced sediment loading by lowering the support practice factor and modifying runoff response. Grassed waterways (SED3) and streambank stabilization (SED2) reduced channel-related sediment transport by increasing channel roughness and decreasing channel erodibility factors. Filter strips (SED1) provided a trapping mechanism for sediment before delivery to the channel network. Grade stabilization (SED7) represented a reduction in channel slope and channel erosion potential, which can reduce sediment transport capacity in affected reaches.

The grassed waterway scenario (SED3) is especially relevant because it links flow routing and sediment reduction. Increasing channel roughness can reduce flow velocity and promote deposition, while reducing channel erodibility and improving channel cover can decrease the potential for channel sediment detachment. In the context of the Nueces River Watershed, this type of scenario may be most effective in areas where sediment delivery is controlled by concentrated flow paths, ephemeral channels, drainageways, or unstable streambanks. Because phosphorus can be transported with sediment, grassed waterways (SED3) and related sediment-control practices may also reduce particulate phosphorus delivery to downstream water bodies.

Figure 4.14c shows that total nitrogen loads generally responded to the same high-flow periods that produced sediment peaks. Although the sediment-control scenarios were not designed primarily as nitrogen-reduction practices, reductions in sediment movement can also reduce sediment-associated organic nitrogen transport. Scenarios such as grassed waterways (SED3), streambank stabilization (SED2), strip cropping (SED6), and grade stabilization (SED7) may therefore reduce total nitrogen export during event-driven periods when organic nitrogen is attached to eroded soil particles or transported through channel sediment movement. However, because total nitrogen also includes soluble forms such as nitrate, the reduction in total nitrogen was not expected to be as direct or consistent as the reduction in sediment load. Future work focusing on separating total nitrogen into its dissolved and sediment-associated fractions can help better evaluate BMP effectiveness.

Figure 4.14d shows that total phosphorus was more closely linked to sediment-control responses than total nitrogen because phosphorus transport in SWAT is strongly associated with particulate phosphorus attached to eroded sediment. Therefore, scenarios that reduced sediment detachment and delivery also reduced total phosphorus loads during major runoff events. Grassed waterways (SED3), streambank stabilization (SED2), terracing (SED5), contour farming (SED4), strip cropping (SED6), and grade stabilization (SED7) are expected to reduce phosphorus export most visibly during high-flow months when sediment-associated phosphorus transport is greatest. This result supports the interpretation that sediment-control BMPs can provide water-quality benefits beyond sediment reduction by also lowering particulate phosphorus delivery to the Nueces Bay and Corpus Christi Bay system.

The sediment-control results should be interpreted as relative scenario responses rather than exact field-scale predictions. SWAT parameter-based BMP representation simplifies actual conservation practice design, maintenance, spatial placement, and effectiveness. Field-scale BMP performance depends on local slope, soil texture, vegetation establishment, drainage area, rainfall intensity, land management, and maintenance condition. However, the scenario results provide useful guidance for comparing which types of sediment-control practices may be most effective in reducing sediment and sediment-associated nutrient delivery to the Nueces Bay and Corpus Christi Bay system.

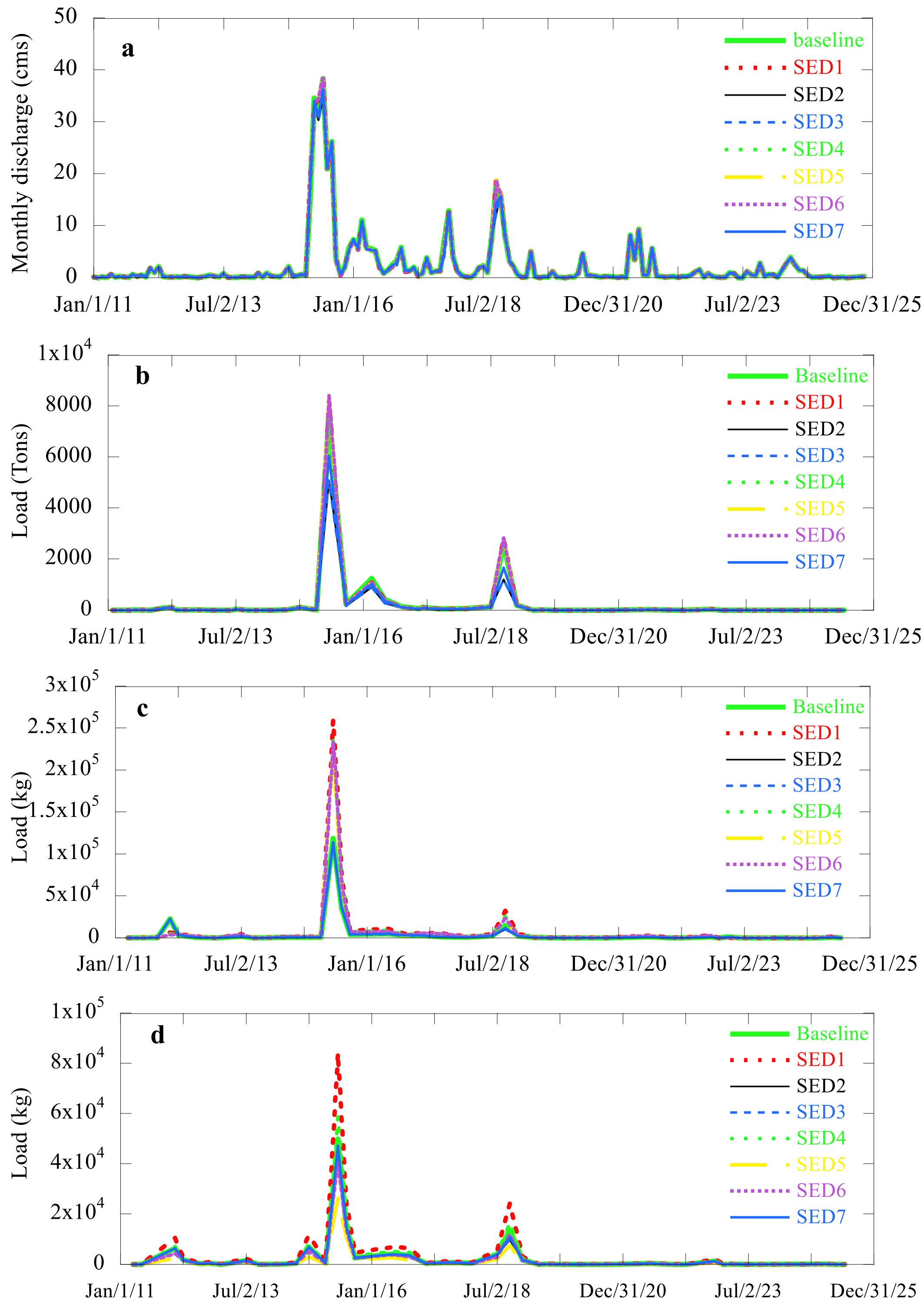

Figure 4.14. Simulation Comparison of Grassed Waterway / Sediment-Control Scenario: (a) streamflow, (b) sediment load, (c) total N load, and (d) total P load.

4.4.2.5 Simulations of Nitrogen Management Scenarios

Figure 4.15a shows that the streamflow response under the nitrogen management scenarios generally followed the same timing as the calibrated baseline condition (S0). The largest streamflow difference was associated with the brush-clearing scenario (N1) because brush clearing can reduce canopy interception, reduce overland roughness, and alter evapotranspiration, which may increase runoff during wet periods. In contrast, grassed waterways (N2), strip cropping (N3), and streambank stabilization (N4) produced smaller changes in monthly streamflow because these practices mainly target erosion control, sediment routing, and nutrient transport rather than directly changing watershed-scale runoff volume. This indicates that the nitrogen-management scenarios influenced the hydrologic response mainly through the N1 scenario.

Figure 4.15b shows that sediment load remained low during most months but increased sharply during major runoff events. The differences among nitrogen scenarios were most visible during high-flow and high-sediment months, when sediment detachment and transport were greatest. Brush clearing (N1) increased sediment loading during storm-driven periods when increased runoff increased erosion and sediment transport capacity. In contrast, grassed waterways (N2), strip cropping (N3), and streambank stabilization (N4**)** reduce sediment movement by slowing concentrated flow, reducing upland erosion, improving channel protection, and decreasing channel sediment detachment. This sediment response is important for nitrogen analysis because part of the total nitrogen load is transported in organic or sediment-associated form.

Figure 4.15c shows that most differences among nitrogen management scenarios occurred during high-loading months. This indicates that management practices had the greatest effect when hydrologic conditions were sufficient to mobilize and transport nitrogen. The observed and simulated scenario lines show that total nitrogen loading remained relatively low in many months but increased sharply during major runoff periods. Therefore, management practices should be evaluated based on their ability to reduce nitrogen peaks during wet months as well as their effect on long-term average loading. Brush clearing (N1) increased nitrogen loading. This is expected because brush clearing can change canopy interception, evapotranspiration, overland roughness, and runoff generation. If brush clearing increases runoff, nitrogen transport may also increase during storm-driven periods unless paired with conservation practices. Grassed waterways (N2) and streambank stabilization (N4) decreased total nitrogen load, which might be because these two BMPs can reduce nitrogen associated with sediment and organic matter through channel erosion reduction and an increase in deposition. Since strip cropping (N3) may reduce upland erosion and runoff energy, thus reducing sediment-bound organic nitrogen transport, the total nitrogen load was lower compared with that simulated for the N1 scenario. However, because nitrate is highly mobile in dissolved form, practices that only reduce sediment may not fully reduce dissolved nitrate loading. For this reason, additional fertilizer-management scenarios, such as reduced nitrogen application rates or changes in application timing, could be further examined in future work.

Figure 4.15d shows that total phosphorus also responded to the nitrogen management scenarios, especially during high-flow months. This response occurred because phosphorus transport is closely linked to runoff and sediment movement. Brush clearing (N1) may increase total phosphorus export during wet periods if increased runoff causes greater sediment detachment and particulate phosphorus transport. In contrast, grassed waterways (N2), strip cropping (N3), and streambank stabilization (N4) can reduce phosphorus loading by decreasing upland erosion, reducing channel erosion, and limiting sediment-associated phosphorus movement. Therefore, although these scenarios were evaluated as nitrogen-management scenarios, they also produced phosphorus-related responses because nitrogen, phosphorus, sediment, and runoff are connected within the SWAT transport processes.

Overall, brush clearing (N1) can affect nitrogen loading by changing canopy interception, evapotranspiration, overland roughness, and runoff generation. If brush clearing increases runoff, nitrogen transport may also increase during storm-driven periods unless paired with conservation practices. Grassed waterways (N2) and streambank stabilization (N4) may reduce nitrogen associated with sediment and organic matter by reducing channel erosion and promoting deposition. Strip cropping (N3) may reduce upland erosion and runoff energy, thereby reducing sediment-bound organic nitrogen transport. However, because nitrate is highly mobile in dissolved form, practices that only reduce sediment may not fully reduce dissolved nitrate loading. For this reason, additional fertilizer-management scenarios, such as reduced nitrogen application rates or changes in application timing, should be included where supported by the final management dataset.

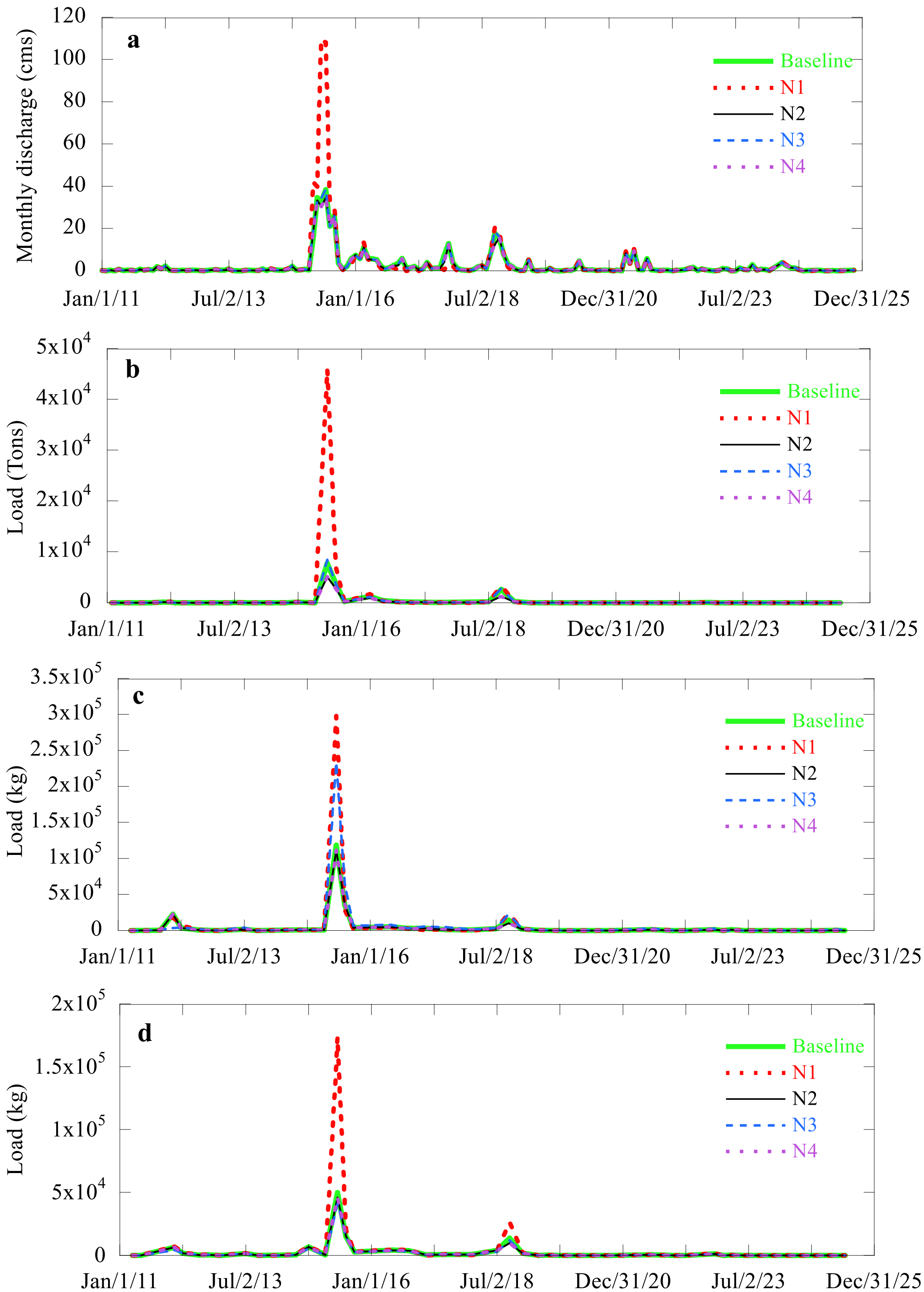

Figure 4.15. Simulation Comparison of Nitrogen Management Scenarios: (a) Streamflow, (b) sediment load, (c) total N load, and (d) total P load.

4.4.2.6 Simulations of Phosphorus and Sediment-Associated Nutrient Response

Figure 4.16a shows that the streamflow response under the phosphorus management scenarios generally followed the same seasonal and event-driven pattern as the calibrated baseline condition (S0). The largest streamflow difference was associated with the brush-clearing scenario (P1) because brush clearing can reduce canopy interception, reduce overland roughness, and alter evapotranspiration, which may increase runoff during wet periods. In contrast, grassed waterways (P2) and strip cropping (P3) produced comparatively smaller changes in monthly streamflow because these practices primarily affect sediment transport and erosion processes rather than strongly altering watershed-scale discharge. This indicates that the phosphorus-related scenarios influenced the hydrologic change mainly visible under P1.

Figure 4.16b shows that sediment loads remained low during most months but increased sharply during high-flow periods. The largest differences among scenarios occurred during major sediment-producing months, indicating that BMP effectiveness was most visible during event-driven sediment pulses. Brush clearing (P1) may increase sediment loading during wet periods if increased runoff leads to greater erosion and sediment transport. In contrast, grassed waterways (P2) and strip cropping (P3) reduced sediment delivery by decreasing runoff energy, slowing concentrated flow, and reducing upland or channel-related sediment transport. This sediment response is especially important for phosphorus evaluation because a substantial portion of total phosphorus is transported in sediment-associated form.

Figure 4.16c shows that total nitrogen also responded to the phosphorus-related scenarios, particularly during major runoff events. The largest differences occurred during high-loading months, when hydrologic conditions were sufficient to mobilize both dissolved and sediment-associated nitrogen. Brush clearing (P1) may increase total nitrogen export if increased runoff enhances nitrogen transport during storm-driven periods. In contrast, grassed waterways (P2) and strip cropping (P3) may reduce total nitrogen loads indirectly by reducing sediment transport and associated organic nitrogen movement. However, because nitrates are highly mobile in dissolved form, reductions in sediment do not necessarily produce equally large reductions in total nitrogen. Therefore, the nitrogen response shown in Figure 4.17c should be interpreted as a secondary co-benefit of phosphorus and sediment-control practices rather than as a direct nitrogen-management result.

Figure 4.16d shows that the largest phosphorus load differences among scenarios occurred during high-loading months. This suggests that phosphorus management effectiveness was most visible during periods of high runoff and sediment movement. The baseline and scenario simulations showed sharp phosphorus peaks during wet periods, while most dry or low-flow months had relatively low phosphorus loads. This pattern supports the interpretation that phosphorus delivery from the Nueces River Watershed is event-driven and closely connected to hydrologic and sediment transport conditions.

Among the evaluated scenarios, grassed waterways (P2) and strip cropping (P3) are directly relevant to sediment-associated phosphorus reduction because both practices can reduce sediment delivery. Grassed waterways (P2) primarily reduce concentrated-flow and channel-related sediment movement, while strip cropping (P3) reduces upland erosion and runoff energy. Brush clearing (P1) may have mixed effects. It may increase water yield in some conditions, but it can also increase erosion and phosphorus export if soil exposure or runoff increases. Therefore, brush-clearing practices should be paired with sediment-control or revegetation strategies when phosphorus reduction is a management objective.

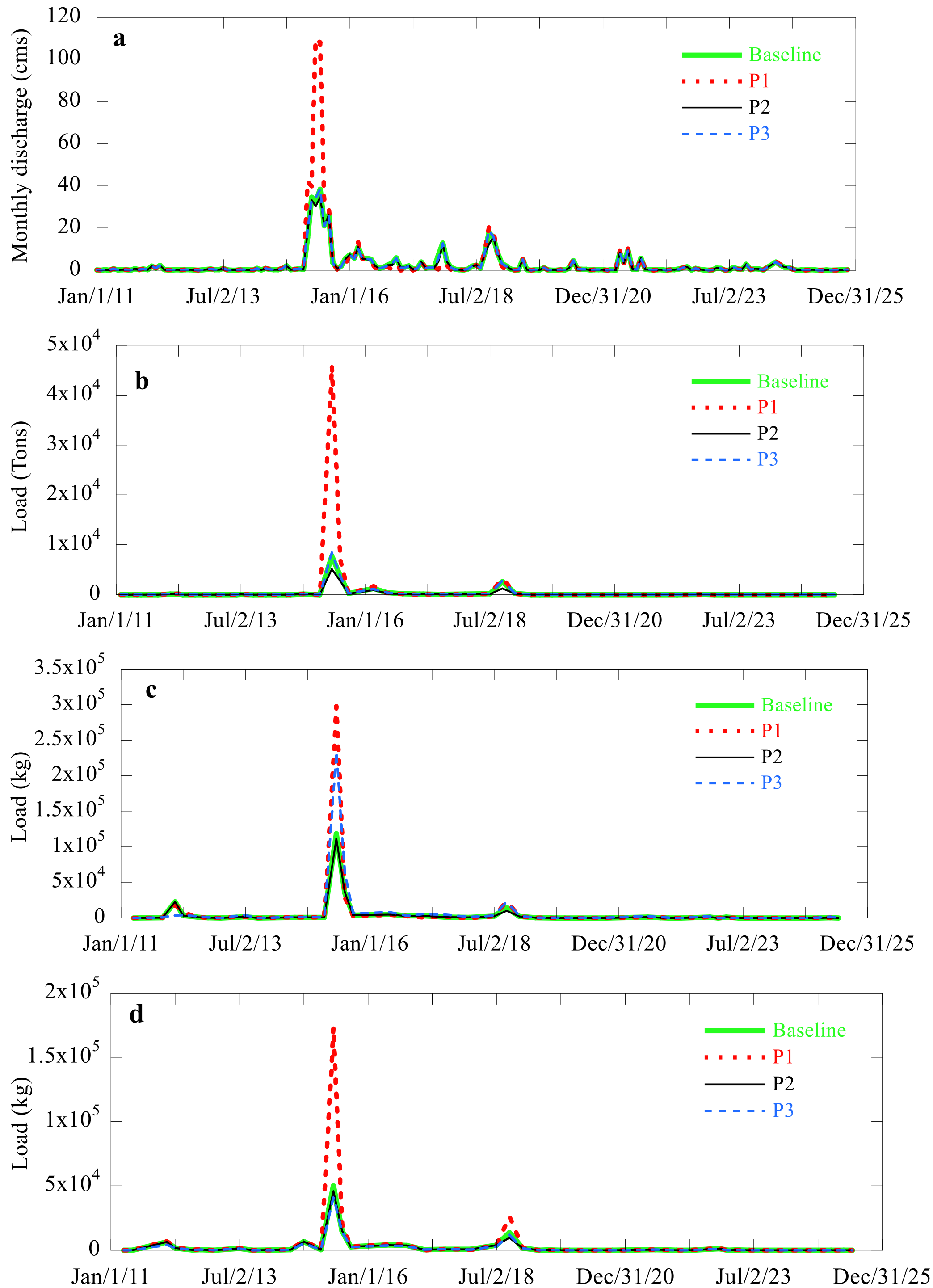

Figure 4.16. Simulations of Phosphorus and Sediment-Associated Nutrient Response scenarios: (a) streamflow, (b) sediment load, (c) total N load, and (d) total P load.

4.5 Recommendations for Best Management Practices

This chapter evaluated streamflow, sediment, total nitrogen, and total phosphorus loading in the Nueces River Watershed using the Soil and Water Assessment Tool (SWAT). The model was calibrated and validated at the monthly time scale and then applied to evaluate selected management scenarios intended to reduce sediment and nutrient delivery to the Nueces-Corpus Christi Bay system. The modeling sequence followed a stepwise approach in which flow was calibrated first, followed by sediment, nitrogen, and phosphorus.

The flow simulation provided the hydrologic foundation for sediment and nutrient modeling. The model produced acceptable to very good streamflow performance during calibration and acceptable performance during validation, although some uncertainty remained in the independent validation period. This uncertainty is expected in a large semi-arid watershed where localized rainfall, reservoir operations, and episodic high-flow events strongly influence monthly discharge. Sediment simulation showed strong calibration and validation performance and was considered suitable for evaluating sediment-control scenarios. Nitrogen simulation also produced acceptable to very good performance during calibration and acceptable validation performance based on R^2 and NSE, although the lower validation KGE indicated uncertainty in magnitude and variability. Phosphorus calibration was strong; however, validation performance was weak, indicating that phosphorus results should be interpreted cautiously, particularly for absolute load prediction.

Overall, the calibrated SWAT model provides a useful process-based framework for comparing relative effects of management decisions on flow, sediment, nitrogen, and phosphorus loading. The model results show that sediment and nutrient transport in the Nueces River Watershed is highly event-driven. Most months produced relatively low loads, while a limited number of wet months and high-flow periods produced large sediment and nutrient pulses. This pattern indicates that effective management should focus on reducing pollutant transport during high-runoff conditions rather than only targeting average annual conditions.

4.5.1 Final BMP Takeaways

The management scenario results indicate that BMP effectiveness depends on the dominant transport pathway being targeted. Practices that modify vegetation cover and runoff response, such as brush-clearing scenarios, primarily affect hydrology by changing canopy interception, evapotranspiration, soil-water use, and overland flow resistance. These scenarios may increase water yield under some conditions, but they may also increase runoff-driven sediment and nutrient transport if not combined with erosion-control practices. Therefore, brush clearing should not be treated as a stand-alone water-quality BMP unless soil protection and revegetation are included in the management plan.

Sediment-control practices showed stronger relevance for reducing sediment and sediment-associated nutrient transport. Grassed waterways, streambank stabilization, grade stabilization, contour farming, terracing, strip cropping, and filter strips were represented through SWAT parameters affecting channel roughness, channel erodibility, channel cover, support practice factors, and runoff response. These practices were most effective during high-flow months when sediment transport was greatest. This suggests that sediment BMPs should be prioritized in areas with concentrated flow, unstable channels, erodible soils, and strong hydrologic connectivity to streams.

Nitrogen-loading scenarios indicated that total nitrogen response was strongly tied to hydrologic conditions. High-flow months produced the largest nitrogen loads and the greatest differences among scenarios. Because nitrate is mobile in water, practices that only reduce sediment may not fully address dissolved nitrogen transport. Therefore, nitrogen reduction should include source-control measures such as fertilizer-rate reduction, improved fertilizer timing, better crop uptake synchronization, and reduction of unnecessary nutrient application in urban or non-agricultural HRUs where applicable.

Phosphorus-loading scenarios were closely linked to sediment transport. Because a portion of total phosphorus is transported in particulate form attached to eroded sediment, sediment-control practices are expected to reduce phosphorus delivery, especially during storm-driven months. However, phosphorus validation uncertainty was higher than for the other model components. Therefore, phosphorus BMP results should be interpreted mainly as relative indicators of likely response rather than exact estimates of phosphorus-load reduction.

4.5.2 Recommended Options to Reduce Loads to Nueces/Corpus Christi Bay

Based on the SWAT scenario results and the dominant transport processes represented in the model, a combined management strategy is recommended for reducing sediment and nutrient delivery to the Nueces-Corpus Christi Bay system. No single BMP is expected to address all pollutant pathways. Instead, management should combine hydrologic, sediment-control, and nutrient-source reduction practices.

First, sediment-control practices should be prioritized in areas with high erosion potential and strong connectivity to the channel network. Grassed waterways are recommended for concentrated flow paths, drainageways, and locations where runoff is likely to transport sediment directly to streams. These practices can slow flow, reduce transport capacity, increase deposition, and reduce channel or drainageway erosion. Streambank stabilization and grade stabilization are recommended where channel erosion contributes to sediment loads. These practices can reduce channel sediment sources and may also reduce particulate phosphorus and organic nitrogen transport.

Second, upland erosion-control practices should be implemented in agricultural and hay-producing areas where runoff and soil disturbance contribute to sediment delivery. Contour farming, terracing, strip cropping, conservation tillage, and filter strips can reduce upland erosion, slow runoff, and trap sediment before it reaches the channel system. These practices are especially important because sediment-associated phosphorus and organic nitrogen are transported with eroded particles.

Third, nitrogen-source management should be included as a separate management priority. Because nitrate can move in dissolved form and may not be fully controlled by sediment BMPs, fertilizer-management practices should be evaluated and implemented where agricultural nitrogen inputs are important. Recommended strategies include reducing nitrogen application rates where appropriate, improving application timing, avoiding application before high-rainfall periods, increasing plant uptake efficiency, and limiting unnecessary auto-fertilization in HRUs where fertilizer application is not realistic or management-relevant.

Fourth, brush management should be applied carefully. Brush clearing may alter flow response and potentially increase water yield, but it may also increase runoff and erosion if vegetation removal leaves soil exposed. Therefore, brush-clearing practices should be paired with soil-stabilization measures, reseeding, contour-based conservation practices, or grassed waterways. Brush management should be targeted only where hydrologic benefits are expected and where erosion risk can be controlled.

Finally, management practices should be prioritized for high-loading periods and high-contributing areas. The model results indicate that large sediment and nutrient loads are concentrated during wet months and high-flow events. Therefore, BMP planning should focus on reducing peak-event transport rather than only reducing average annual loads. Areas that generate high runoff, sediment, or nutrient loads during storm periods should receive priority for implementation.

Chapter 5. Conclusions and Future Work

5.1 Conclusion

5.1.1 Field Data on Sediment, Nutrients, and Pollutants and Its Analysis

This research offers a seasonal and spatial evaluation of water and sediment quality in the Nueces/Corpus Christi Bay estuary system. The findings indicate that seasonal hydrologic fluctuations predominantly dictate water quality dynamics, with dry (low-inflow) periods and wet (high-inflow) events creating markedly different circumstances. Prolonged dry weather resulted in the accumulation of nutrients and contaminants in sediments around the bay. During the following rainy season, severe storm events introduced significant amounts of freshwater, sediment (with SSC increasing by 5–10 times), and nutrients (with ammonium and nitrate loads reaching hundreds of kg/day), resulting in turbidity spikes and a reduction in dissolved oxygen levels. The spatial variations across the five monitoring sites were minimal, since most metrics did not exhibit significant changes by location ($p>0.05$).

Heavy metal analyses indicated that baseline concentrations in water and sediment are typically higher than the criteria, indicative of legacy pollution above chronic risk thresholds and episodic spikes arise in response to seasonal events. Dissolved arsenic and selenium reached their zenith in the dry season, while lead and mercury surged during summer rains, momentarily surpassing state water quality standards. These metals typically migrate and deposit in clusters and cluster analysis verified that the majority of anthropogenic trace metals co-occur on suspended sediments, whereas natural elements (Fe, Al) constitute a distinct group. This coherence suggests shared origins and transport routes (e.g., urban runoff containing multi-metal combinations). Multivariate statistical methods (PCA) elucidated that rainfall-induced flow is the primary factor connecting coarse sediments, suspended solids, and nutrient loads, while low-flow times facilitate elevated dissolved oxygen and salinity levels. The study indicates that the estuary's water quality is influenced by pulses, alternating between periods of calm accumulation and event-driven flushing, exhibiting relatively synchronized patterns across locations.

These findings have significant implications for environmental science and coastal management. This study significantly enhances the temporal resolution of water quality comprehension in a semi-arid Gulf Coast estuary, rectifying identified data deficiencies concerning seasonal dynamics. The work enhances understanding of estuarine responses to climate variability by measuring the extremity of fluctuations, such as around 30 PSU salinity during drought conditions compared to abrupt declines with inflow, and sediment loads changing by two orders of magnitude. The comprehensive investigation of water, sediment, and pollution loading exemplifies a holistic methodology for assessing coastal water quality. The documenting of heavy metal spikes underscores the necessity for continuous contamination monitoring, even when long-term averages appear benign, as acute episodes may provide ecological hazards. The study's innovative contribution is in documenting these transient events and demonstrating their potential effects around bay health.

5.1.2 Remote Sensing Data on Sediment Transport and Its Analysis

This study successfully developed a geospatial framework to estimate Total Suspended Solids (TSS) in the Nueces River, Nueces Bay, and Corpus Christi Bay using MODIS and Landsat 8 satellite imagery. By integrating remote sensing with machine learning, the research addressed the critical gap in continuous sediment monitoring for South Texas coastal waters, fulfilling the primary objective of utilizing remote sensing to extend the spatial and temporal reach of sparse field measurements. The experimental results confirmed the first hypothesis regarding model performance across both the river and bay environments, as the non-parametric

Random Forest regressor significantly outperformed traditional power-form and linear models. The Random Forest model achieved $R_2 = 0.87$ for the combined river and bay system, proving its superior ability to capture the complex, non-linear relationship between spectral reflectance and the optically complex waters of the Nueces Estuary.

The analysis of temporal trends fulfilled the second research objective by identifying clear seasonal patterns within the study area. The data revealed that the highest average TSS concentrations consistently occur during the March–May transition, peaking in April at 36.8 mg/L, while the lowest levels were typically observed in December at 22.8 mg/L. Spatially, the study identified critical hotspots through polygon-based completeness analysis, mapping frequent sediment spikes near the Nueces Bay Causeway, where concentrations often exceed the baseline threshold of 39.88 mg/L.

The hypothesis that precipitation-driven runoff is the primary driver of bay TSS was partially rejected; under normal conditions, the data revealed a "flush-and-dilute" effect, with significant rainfall events diluting existing sediment rather than increasing its concentration. Despite the natural expectation that upstream discharge and precipitation would contribute substantially to sediment loading, this study found that both Pearson ($R = 0.034$) and Spearman ($R = 0.036$) correlations between residue and these hydrometeorological drivers were negligible. Analysis showed that mean residue values increased slightly before a storm, peaking at approximately 33.4 mg/L, but declined sharply to a minimum near 31.5 mg/L by the third day post-event, reflecting a hydraulic reset caused by the influx of freshwater. A weak positive correlation with TSS spikes was observed only during extreme weather events exceeding a 50 mm rainfall threshold, which accounted for only 2% of the variance in sediment response. Consequently, the results suggest that the system's sediment regime is predominantly governed by internal bay dynamics, such as wind-driven resuspension, rather than land-based runoff or freshwater inflow.

A key methodological contribution of this work was the multi-level data validation process, which utilized pixel-level density and polygon-based completeness to ensure mathematical consistency across satellite overpasses. This approach accounted for sensor limitations and atmospheric interference, providing a reliable measure of the water surface area successfully monitored within the river segment polygons. Ultimately, the findings indicate that while the Nueces River is a primary source of sediment, internal bay dynamics, such as wind-driven resuspension and dredging activities, likely exert a greater influence on daily TSS fluctuations than land-based runoff.

For coastal management and economic planning, the hotspot maps and predictive models generated in this study provide a cost-effective tool for prioritizing dredging and ecological restoration efforts within the Corpus Christi Ship Channel and the wider estuary system.

5.1.3 SWAT Modeling and Strategies to Reduce Sediment and Nutrient Loads

The SWAT model was successfully applied to simulate flow, sediment, total nitrogen, and total phosphorus loading in the Nueces River Watershed. The model represented the watershed using subbasins and HRUs based on land use, soil, slope, and management conditions and incorporated major hydrologic and reservoir-routing processes. The calibrated model provided an acceptable basis for evaluating watershed-scale loading and management scenario response.

Flow simulation showed that the model captured the major monthly hydrologic patterns, although validation uncertainty remained. This uncertainty should be considered because flow errors can affect sediment and nutrient simulations. Sediment simulation performed well and was suitable for evaluating sediment-control scenarios. Nitrogen simulation showed strong calibration and acceptable validation based on R^2 and NSE, but the lower KGE during validation indicated uncertainty in bias and variability. Phosphorus simulation showed strong calibration but weak validation, meaning that phosphorus results should be interpreted cautiously.

The modeling results indicate that sediment and nutrient delivery from the Nueces River Watershed is strongly controlled by high-flow events. Large sediment, nitrogen, and phosphorus loads occurred during a small number of wet months, while most low-flow months contributed relatively small loads. This event-driven behavior is important for management because BMPs must be effective under storm-driven runoff conditions to substantially reduce annual pollutant export.

Sediment-control practices such as grassed waterways, streambank stabilization, grade stabilization, contour farming, terracing, strip cropping, and filter strips are recommended for reducing sediment and sediment-associated nutrients. Nitrogen reduction requires additional fertilizer-management strategies because dissolved nitrogen may continue to move with runoff, lateral flow, percolation, and groundwater return flow. Brush-clearing scenarios should be interpreted carefully and should be paired with erosion-control practices if implemented as part of a watershed management strategy.

Overall, the calibrated SWAT model provides a useful decision-support tool for evaluating relative management effects on sediment and nutrient loading to the Nueces Bay and Corpus Christi Bay system. The model should be used to compare management alternatives, identify high-risk hydrologic periods, and support prioritization of BMPs. However, because observed nutrient data were limited and phosphorus validation was weak, the model should not be used as a precise predictor of absolute nutrient loads without further refinement.

5.2 Recommendations for Future Work

While this study has provided valuable insights into the seasonal and spatial dynamics of water and sediment quality around the Nueces/Corpus Christi Bay system, several opportunities remain to enhance understanding of long-term processes and management implications. Future work should aim to integrate continuous monitoring, advanced analytical techniques, and modeling approaches to build upon the findings of this research.

1) Long-Term Monitoring and Trend Analysis: Extending the current study over multiple hydrological years would enable the identification of interannual trends and the quantification of long-term changes in water and sediment quality. Continuous monitoring of parameters such as salinity, nutrients, and suspended sediment concentration (SSC) using in situ sensors would improve temporal resolution and capture short-lived events like storm surges or flash floods that are often missed in periodic sampling. This would help distinguish between natural variability and anthropogenic effects in nutrient and metal loading.
2) Hydrodynamic and Water Quality Modeling: Future studies should incorporate numerical modeling tools such as Deltares Delft Three-Dimensional Hydrodynamic and Water Quality Modeling Suite (Delft3D), Environmental Fluid Dynamics Code (EFDC), and Water Quality Analysis Simulation Program (WASP) to simulate hydrodynamic circulation, sediment transport, and nutrient cycling under different freshwater inflow and climatic scenarios. Model calibration using the dataset from this study can provide predictive capabilities to assess the impacts of altered inflow regimes, sea-level rise, and extreme weather events on water quality and sediment dynamics. These models would also be instrumental in evaluating management interventions aimed at reducing nutrient and sediment inputs.

3) Metal Speciation and Ecological Risk Assessment: Although this research quantified total heavy metal concentrations, future work should focus on metal speciation and bioavailability to better assess ecological risk. Sequential extraction and porewater analyses can help determine the mobility of metals such as Fe, Zn, Cu, and Pb under varying redox conditions. Coupling these data with benthic organism tissue analysis would elucidate bioaccumulation pathways and their implications for food web health and human exposure.
4) Isotopic and Geochemical Tracing of Nutrient Sources: Stable isotope techniques (e.g., $\delta^{15}N$, $\delta^{13}C$, $\delta^{34}S$) could be applied to differentiate between nutrient sources such as agricultural runoff, wastewater effluent, and atmospheric deposition. Combined with geochemical fingerprinting, isotopic tracing would provide a clearer understanding of nutrient transport pathways, transformation processes, and sediment–water interactions, especially during seasonal transitions.
5) Integration of Remote Sensing and Machine Learning: Remote sensing technologies (e.g., Sentinel-2, Landsat 9) offer potential for spatial mapping of turbidity, chlorophyll-a, and sediment distribution across the bay. When integrated with field datasets, machine learning algorithms such as random forest or LSTM models could be trained to predict nutrient and sediment dynamics based on meteorological and hydrological inputs. This data-driven approach would enable early warning systems for eutrophication, sediment resuspension, and pollutant fluxes under varying environmental conditions.
6) Policy and Management Applications: Finally, the outcomes of future studies should be translated into practical management strategies in collaboration with agencies such as the Texas General Land Office (GLO) and Coastal Bend Bays & Estuaries Program (CBBEP).

Scenario modeling and risk-based mapping can help establish nutrient load reduction targets, optimize freshwater inflow management, and guide restoration of sensitive estuarine habitats.

7) Integration of High-Resolution Wind Data: Given that precipitation was found to be a negligible driver of TSS in the bay, future research should incorporate the collection and analysis of localized, high-frequency wind and tidal velocity data. This would enable a formal cross-correlation analysis of wind-driven resuspension and TSS spikes, particularly during the peak months of April and May.

8) Expansion to Sentinel-2 and Landsat 9: To address the temporal gaps in the Landsat archive, future work could utilize a multi-sensor fusion approach. Combining Landsat 8/9 with Sentinel-2's 5-day revisit cycle would significantly improve the probability of capturing transient "first-flush" events that are currently missed by the 16-day Landsat cycle.

9) More Water Quality Data to Improve the Numerical Model: To improve the reliability of nutrient calibration, refining management representation, and strengthening the connection between watershed loading and bay water-quality response, additional observed water-quality data are needed, especially during storm events and high-flow periods. Monthly or occasional grab samples may miss short-duration sediment and nutrient peaks, which can dominate annual loading. More frequent sampling during wet-weather events would improve load estimation and provide stronger calibration data for sediment, nitrogen, and phosphorus.

10) Better characterization of fertilizer management: The current model used auto-fertilization with elemental nitrogen active, which provides a practical baseline but may not fully represent actual fertilizer timing, rates, crop-specific management, or spatial variability in agricultural practices. Improved information on fertilizer application, crop rotations, planting

and harvest dates, tillage operations, and urban nutrient sources would improve nitrogen and phosphorus simulation.

11) A Better Phosphorus Modeling: Because phosphorus validation was weak, additional work is needed to separate dissolved and particulate phosphorus processes, improve soil phosphorus pool initialization, and verify which SWAT phosphorus variables are available in the model input structure. More observed phosphorus data, especially paired with sediment measurements, would improve confidence in phosphorus-load estimates and sediment-associated phosphorus interpretation.

12) Improved Spatial Prioritization: Future work should identify subbasins and HRUs that contribute disproportionately to sediment and nutrient loading. This would allow BMPs to be targeted to the areas where they are most likely to reduce loads. Scenario results should be summarized not only at the watershed outlet but also by subbasin, land-use class, and management category.

13) Link between watershed loading results and downstream bay response where possible: The SWAT model estimates loads delivered through the watershed and river system, but additional estuarine or receiving-water analysis would help evaluate how sediment and nutrient reductions affect conditions in Nueces Bay and Corpus Christi Bay. Combining SWAT outputs with monitoring, remote sensing, and bay-scale water-quality assessment would provide a stronger decision-support framework for reducing nutrient and pollutant impacts in the coastal system.

Acknowledgments

The authors express their sincere gratitude to Texas Water Development Board (TWDB) for the loan of the ADCP at no cost, arranged by Mark A. Lopez at TWDB as well as to Victor G Garcia for the field data collection and analysis.

References

Abbas, S. A., Bailey, R. T., White, J. T., Arnold, J. G., White, M. J., Čerkasova, N., & Gao, J. (2024). A framework for parameter estimation, sensitivity analysis, and uncertainty analysis for holistic hydrologic modeling using SWAT+. *Hydrology and Earth System Sciences, 28*(1), 21–48. https://doi.org/10.5194/hess-28-21-2024

Abbaspour, K. C. (2015). *SWAT-CUP: SWAT calibration and uncertainty programs—A user manual*. Swiss Federal Institute of Aquatic Science and Technology.

Abbaspour, K. C., Rouholahnejad, E., Vaghefi, S. A., Srinivasan, R., Yang, H., & Kløve, B. (2015). A continental-scale hydrology and water quality model for Europe: Calibration and uncertainty of a high-resolution large-scale SWAT model. *Journal of Hydrology, 524*, 733–752. https://doi.org/10.1016/j.jhydrol.2015.03.027

Abbaspour, K. C., Vaghefi, S. A., & Srinivasan, R. (2018). A guideline for successful calibration and uncertainty analysis for Soil and Water Assessment: A review of papers from the 2016 International SWAT Conference. *Water, 10*(1), Article 6. https://doi.org/10.3390/w10010006

Abbaspour, K. C., Vaghefi, S. A., Yang, H., & Srinivasan, R. (2019). Global soil, landuse, evapotranspiration, historical and future weather databases for SWAT applications. *Scientific Data, 6*, Article 263. https://doi.org/10.1038/s41597-019-0282-4

Alparone, L., Aiazzi, B., Baronti, S., & Garzelli, A. (2020). Multispectral and Panchromatic Image Fusion for Marine and Estuarine Sediment Tracking: Feature Extraction and Predictor Set Development. *International Journal of Remote Sensing, 41*(12), 4589-4606. doi:10.1080/01431161.2020.1724332

APHA, A. (2017). *Standard Methods for the Examination of Water and Wastewater.* American Public Health Association. doi:https://www.standardmethods.org/

Applebaum, S., Montagna, P. A., & Ritter, C. (2005). Status and Trends of Dissolved Oxygen in Corpus Christi Bay, Texas, U.S.A. *Environmental Monitoring and Assessment, 107*, 297-311. doi:10.1007/s10661-005-3111-5

Arnold, J. G., Kiniry, J. R., Srinivasan, R., Williams, J. R., Haney, E. B., & Neitsch, S. L. (2012). *Soil and Water Assessment Tool input/output documentation: Version 2012* (Technical Report No. 439). Texas Water Resources Institute. https://swat.tamu.edu/media/69296/swat-io-documentation-2012.pdf

Arnold, J. G., Moriasi, D. N., Gassman, P. W., Abbaspour, K. C., White, M. J., Srinivasan, R., Santhi, C., Harmel, R. D., van Griensven, A., Van Liew, M. W., Kannan, N., & Jha, M. K. (2012). SWAT: Model use, calibration, and validation. *Transactions of the ASABE, 55*(4), 1491–1508. https://doi.org/10.13031/2013.42256

Arnold, J. G., Srinivasan, R., Muttiah, R. S., & Williams, J. R. (1998). Large area hydrologic modeling and assessment part I: Model development. *Journal of the American Water Resources Association, 34*(1), 73–89. https://doi.org/10.1111/j.1752-1688.1998.tb05961.x

Arnold, J. G., Kiniry, J. R., Srinivasan, R., Williams, J. R., Haney, E. B., & Neitsch, S. L. (2009). Soil & Water Assessment Tool. https://swat.tamu.edu/media/19754/swat-io-2009.pdf

Association, A. P., Association, A. W., & Federation, W. E. (2017). *Standard Methods for the Examination of Water and Wastewater.* American Public Health Association.

ASTM International. (2007). *Standard Test Method for Particle-Size Analysis of Soils.* ASTM International.

ASTM International. (2014). *Standard Test Methods for Moisture, Ash, and Organic Matter of Peat and Other Organic Soils.* ASTM International.

Ayana, E. K., Philpot, W. D., Melesse, A. M., & Steenhuis, T. S. (2015). Assessing the Potential of MODIS/Terra Version 5 Images to Improve Near Shore Lake Bathymetric Surveys. *International Journal of Applied Earth Observation and Geoinformation, 37*, 130-136. doi:10.1016/j.jag.2014.10.016

Bailey, S. W., & Werdell, P. J. (2006). A Multi-Sensor Approach for the On-Orbit Validation of Ocean Color Satellite Data Products. *Remote Sensing of Environment, 102*(1-2), 12-23. doi:10.1016/j.rse.2006.01.015

Barbier, E. B., Hacker, S. D., Kennedy, C., Koch, E. W., Adrian, C., & Stier, B. R. (2011). The value of estuarine and coastal ecosystem services. *Ecological Monographs*.

Bassam, S., & Ren, J. (2018). A Decision Support Modeling System for Managing the Water Resources around the Region of Choke Canyon Reservoir of the Nueces River Basin. A Report on integrated SWAT-MODFLOW Model System. (Contract No. 15-0101). City of Corpus Christi.

Beck, M. W., Brumbaugh, R. D., Airoldi, L., Carranza, A., Coen, L., Crawford, C., . . . & Guo, X. (2011). Oyster Reefs at Risk and Recommendations for Conservation, Restoration, and Management. *BioScience, 61*(2), 107-116. doi:10.1525/bio.2011.61.2.5

Berry, W., Rubinstein, N., Melzian, B., & Hill, B. (2003). *The Biological Effects of Suspended and Bedded Sediment (SABS) in Aquatic Systems: A Review.* United States Environmental Protection Agency (U.S. EPA).

Bieger, K., Arnold, J. G., Rathjens, H., White, M. J., Bosch, D. D., Allen, P. M., Volk, M., & Srinivasan, R. (2017). Introduction to SWAT+, a completely restructured version of the

Soil and Water Assessment Tool. *Journal of the American Water Resources Association, 53*(1), 115–130. https://doi.org/10.1111/1752-1688.12482

Bighash, P., & Murgulet, D. (2015). Application of Factor Analysis and Electrical Resistivity to Understand Groundwater Contributions to Coastal Embayments in Semi-Arid and Hypersaline Coastal Settings. *Science of the Total Environment, 532*, 688-701. doi:10.1016/j.scitotenv.2015.06.077

Binding, C. E., Bowers, D. G., & Mitchelson-Jacob, E. G. (2005). Estimating Suspended Sediment Concentrations from Ocean Colour Measurements in Moderately Turbid Waters: The Impact of Variable Particle Scattering Properties. *Remote Sensing of Environment, 94*(3), 373-383. doi:10.1016/j.rse.2004.11.002

Bower, C. E., & Holm-Hansen, O. (1980). A Salicylate-Hypochlorite Method for Determining Ammonia in Seawater. *Canadian Journal of Fisheries and Aquatic Sciences, 37*(5), 794-798. doi:10.1139/f80-106

Breiman, L. (2001). Random Forests. *Machine Learning, 45*(1), 5-32. doi:10.1023/A:1010933404324

Brian , B. B., & Chuanmin , H. (2016). Island Building in the South China Sea: Detection of Turbidity Plumes and Artificial Islands Using Landsat and MODIS Data. *Scientific Reports, 6*, 33194. doi:10.1038/srep33194

Brooks, E., Thomas, V., Wynne, R., & Howard, J. (2014). Fitting the Continuous Change Detection and Classification Algorithm to High-Temporal Frequency Landsat Time Series: Harmonic Seasonal Modeling of Coastal Landscapes. *Hydrological Processes, 28*(13), 4112-4124. doi:10.1002/hyp.7613

Brown, L. C., & Barnwell, T. O., Jr. (1987). *The enhanced stream water quality models QUAL2E and QUAL2E-UNCAS: Documentation and user manual* (EPA/600/3-87/007). U.S. Environmental Protection Agency.

Bugica, K., Sterba-Boatwright, B., & Wetz, M. S. (2020). Water quality trends in Texas estuaries. *152*, 110903. doi:10.1016/j.marpolbul.2020.110903

Carpenter, S. R., Caraco, N. F., Correll, D. L., Howarth, R. W., Sharpley, A. N., & Smith, V. H. (1998). Nonpoint pollution of surface waters with phosphorus and nitrogen. *Ecological Applications, 8*(3), 559–568. https://doi.org/10.1890/1051-0761(1998)008[0559:NPOSWW]2.0.CO;2

Chawanda, C. J., Van Griensven, A., Nkwasa, A., Teran Orsini, J. P., Jeong, J., Choi, S.-K., Srinivasan, R., & Arnold, J. G. (2025). CoSWAT Model v1: A high-resolution global SWAT+ hydrological model. *Hydrology and Earth System Sciences, 29*(23), 6901–6916. https://doi.org/10.5194/hess-29-6901-2025

Chai, T., & Draxler, R. R. (2014). Root Mean Square Error (RMSE) or Mean Absolute Error (MAE)?—Arguments Against Avoiding RMSE in the Literature. *Geoscientific Model Development*, *7*(3), 1247-1250. doi:10.5194/gmd-7-1247-2014

Chen, L., Wu, W., & Xu, J. (2021). Atmospheric and Illumination Normalization of Landsat 8 Surface Reflectance for Suspended Sediment Tracking in Micro-Tidal Estuarine Networks. *Estuarine, Coastal and Shelf Science, 250*. doi:10.1016/j.ecss.2021.107149

Čerkasova, N., White, M., Arnold, J., Bieger, K., Allen, P., Gao, J., Gambone, M., Meki, M., Kiniry, J., & Gassman, P. W. (2023). Field-scale SWAT+ modeling of corn and soybean yields for the contiguous United States: National Agroecosystem Model development. *Agricultural Systems, 210*, Article 103695. https://doi.org/10.1016/j.agsy.2023.103695

Chong, J. (2024). *27 Best & Fun Things to Do in Corpus Christi (Texas)*. Retrieved from Busy Tourist: https://www.busytourist.com/things-to-do-in-corpus-christi-tx/

Cloern, J. E. (2001). Our evolving conceptual model of the coastal eutrophication problem. *Marine Ecology Progress Series, 210*. doi:10.3354/meps210223

Conkle, J., Pinnell, L., & Turner, J. (2022). Microplastic and Suspended Sediment Dynamics Within the Microtidal Estuaries of the Texas Coastal Bend. *Marine Pollution Bulletin, 174*, 113290. doi:10.1016/j.marpolbul.2021.113290

Conrads, P. A., Rodgers, K. D., Passeri, D. L., Prinos, S. T., Smith, C., Swarzenski, C. M., & Middleton, B. A. (2018). *Coastal Estuaries and Lagoons: The Delicate Balance at the Edge of the Sea.* U.S. Geological Survey.

Dakhlalla, A. O., & Parajuli, P. B. (2019). Assessing model parameter sensitivity and uncertainty of streamflow, sediment, and nutrient transport using SWAT. *Information Processing in Agriculture, 6*(1), 61–72. https://doi.org/10.1016/j.inpa.2018.08.007

Da Silva, Y. J., Cantalice, J. R., Nascimento, C. W., Singh, V. P., & Cruz, C. M. (2015). Bedload and Suspended Sediment Transport in a Multicontaminated Watershed in Brazil. *Environmental Earth Sciences, 74*(1), 605-613. doi:10.1007/s12665-015-4063-x

Dai, Y., Yang, S., Zhao, D., Hu, C., Xu, W., Anderson, D. M., . . . Feng, L. (2023). Coastal phytoplankton blooms expand and intensify in the 21st century. *Nature, 615*, 280-284. doi:10.1038/s41586-023-05760-y

Darji, H., & Lodha, P. (2025). Spatiotemporal Variation and Water Quality Assessment of Surface Water Bodies Using Statistical Approaches. *Environmental Monitoring and Assessment, 197*(3). doi:10.1007/s10661-025-13642-x de Morais, G., Rocha, R. C., & Kor, M. G. (2021). Colorimetric Determination of Phosphorus in Soil and Sediment Samples Using Ascorbic Acid as a Reducing Agent: Optimization and Validation. *Microchemical Journal, 164*, 106025. doi:10.1016/j.microc.2021.106025

Dekker, A. G., Vos, R. J., & Peters, S. W. (2002). Analytical Methods for Mapping Water Quality Parameters from Regional to Global Scales. *Proceedings of the 2002 WSSD Satellite Application Conference.*

Demutskaya, L., & Kalinichenko, I. (2010). Photometric Determination of Ammonium Nitrogen with the Nessler Reagent in Drinking Water After Its Chlorination. *Journal of Water Chemistry and Technology, 32*(2), 90-94. doi:10.3103/S1063455X10020049

Dile, Y. T., Daggupati, P., George, C., Srinivasan, R., & Arnold, J. (2016). Introducing a new open source GIS user interface for the SWAT model. *Environmental Modelling & Software, 85*, 129–138. https://doi.org/10.1016/j.envsoft.2016.08.004

Douglas-Mankin, K. R., Srinivasan, R., & Arnold, J. G. (2010). Soil and Water Assessment Tool (SWAT) model: Current developments and applications. *Transactions of the ASABE, 53*(5), 1423–1431. https://doi.org/10.13031/2013.34915

Doxaran, D., Froidefond, J.-M., Castaing, P., & Babin, M. (2009). Dynamics of the Turbidity Maximum Zone in a Macrotidal Estuary (the Gironde, France): Observations from Field and MODIS Satellite Data. *Estuarine, Coastal and Shelf Science, 81*(3), 321-332. doi:10.1016/j.ecss.2008.11.013

Droppo, I. G., Ongley, E. D., & Murthy, C. R. (1992). The Significance of Sediment Activity in Lake and River Systems: Application of Stokes' Law. *Hydrobiologia, 235/236*, 3-11.

Folle, S., Dalzell, B., & Mulla, D. (2007). *Evaluation of best management practices (BMPs) in impaired watersheds using the SWAT model*. Minnesota Department of Agriculture. https://www.mda.state.mn.us/sites/default/files/inline-files/swatmodel.pdf

Feng, L., Hu, C., Chen, X., & Song, Q. (2012). Assessment of MODIS Aqua Intense Blooms Observations in Complex Inland Waters. *Journal of Geophysical Research: Oceans, 117*(C8). doi:10.1029/2012JC007987

Gassman, P. W., Reyes, M. R., Green, C. H., & Arnold, J. G. (2007). The Soil and Water Assessment Tool: Historical development, applications, and future research directions. *Transactions of the ASABE, 50*(4), 1211–1250. https://doi.org/10.13031/2013.23637

Gassman, P. W., Sadeghi, A. M., & Srinivasan, R. (2014). Applications of the SWAT model special section: Overview and insights. *Journal of Environmental Quality, 43*(1), 1–8. https://doi.org/10.2134/jeq2013.11.0466

Glavan, M., Karnez, E., Sagir, H., Golpinar, M. S., Cetin, M., Akgul, M. A., Ibrikci, H., & Pintar, M. (2017, June 28–30). Understanding of water and nitrogen cycle in an irrigated Mediterranean area in southern Turkey [Conference presentation]. *International Soil and Water Assessment Tool Conference*, Warsaw, Poland.

Gitelson, A., Dall'Olmo, G., Moses, W., Rundquist, D., Barrow, T., Inloes, M., & Holz, J. (2008). A Simple Semi-Analytical Model for Remote Estimation of Total Suspended Solids in Turbid Waters: Validation and Linear Regression Frameworks. *Remote Sensing of Environment*, *112*(9), 3582-3593. doi:10.1016/j.rse.2008.04.015

Gorelick, N., Hancher, M., Dixon, M., Ilyushchenko, S., Thau, D., & Moore, R. (2017). Google Earth Engine: Planetary-Scale Geospatial Analysis for Everyone. *Remote Sensing of Environment*, *202*, 18-27. doi:10.1016/j.rse.2017.05.010

Groten, J., Landers, M., & Woodside, C. (2023). *Refinement of Suspended Sediment Sampling Protocols for Small to Medium Rivers.* U.S. Geological Survey.

Gupta, H. V., Kling, H., Yilmaz, K. K., & Martinez, G. F. (2009). Decomposition of the mean squared error and NSE performance criteria: Implications for improving hydrological modelling. *Journal of Hydrology, 377*(1–2), 80–91. https://doi.org/10.1016/j.jhydrol.2009.08.003.

Harris, I., Osborn, T. J., Jones, P., & Lister, D. (2020). Version 4 of the CRU TS monthly high-resolution gridded multivariate climate dataset. *Scientific Data*, *7*, Article 109. https://doi.org/10.1038/s41597-020-0453-3

Harrison, G., & Martin, E. A. (1982). *Heavy-metal contamination of Crassostrea virginica and associated sediments of the Corpus Christi Bay system, Texas.* U.S. Geological Survey.

Helsel, D. R., Hirsch, R. M., Ryberg, K. M., Archfield, S. P., & Gilroy, E. J. (2020). *Statistical Methods in Water Resources.* U.S. Geological Survey. doi:10.3133/tm4A3.

Hill, E. M., & Nicolau, B. A. (2016). *Historical Review of Nueces Bay (Segment 2482) Zinc Total Maximum Daily Load Effectiveness Monitoring.* Texas Commission on Environmental Quality.

Himanshu, S. K., Pandey, A., Yadav, B., & Gupta, A. (2019). Evaluation of best management practices for sediment and nutrient loss control using the SWAT model. *Soil and Tillage Research, 192*, 42–58. https://doi.org/10.1016/j.still.2019.04.016

Horowitz, A. (2010). A Quarter Century of USGS Land-Surface Suspended-Sediment Data: 1. Course-Scale Patterns and Trends. *Hydrological Processes, 24*(12), 1591-1616. doi:10.1002/hyp.7613

Hossain, A., Mathias, C., & Blanton, R. (2021). Remote Sensing of Turbidity in the Tennessee River Using Landsat 8 Satellite. *Remote Sensing*, *3785*(18), 13. doi:10.3390/rs13183785

Howarth, R. W., Sharpley, A., & Walker, D. (2002). Sources of nutrient pollution to coastal waters in the United States: Implications for achieving coastal water quality goals. *Estuaries, 25*, 656–676. doi:10.1007/BF02804898

Hu, C., Chen, Z., Clayton, T. D., Swarzenski, P., Brock, J. C., & Muller-Karger, F. E. (2004). Assessment of Estuarine Water-Quality Indicators Using MODIS Medium-Resolution Bands: Initial Results from Tampa Bay, FL. *Remote Sensing of Environment, 93*(1-2), 423-441. doi:10.1016/j.rse.2004.08.007

Hughes, T. P., Kerry, J. T., Baird, A. H., Connolly, S. R., Dietzel, A., Eakin, C. M., . . . Torda, G. (2018). Global warming transforms coral reef assemblages. *Nature, 556*, 492-496. doi:10.1038/s41586-018-0041-2

Imen, S., Chang, N.-B., & Yang, Y. J. (2015). Developing the Remote Sensing-Based Early Warning System for Monitoring TSS Concentrations in Lake Mead. *Journal of Environmental Management, 160*, 73-89. doi:10.1016/j.jenvman.2015.06.003

Isra, N., Arsyad, U., & Chairuddin, Z. (2023). Sedimentation analysis using the SWAT model (Soil and Water Assessment Tool) in Mamasa Sub-Watershed. *IOP Conference Series: Earth and Environmental Science, 1230*(1), Article 012027. https://doi.org/10.1088/1755-1315/1230/1/012027

Jeter, B., & Wu, J. (2020). Synoptic Climatology of the "Spring Wind Maximum" Over the Western Gulf of Mexico and South Texas Coastal Zone. *Journal of Applied Meteorology and Climatology, 59*(8), 1345-1361. doi:10.1175/JAMC-D-19-0241.1

Jiang, X., Lu, K., Tunnell, J., & Liu, Z. (2021). *Mapping Distribution and Chemical Levels of Nurdles in the Coastal Bend.* Coastal Bend Bays & Estuaries Program.

Jin, L., Higgins, S. J., Thompson, J. A., Strager, M. P., Collins, S. E., & Hubbart, J. A. (2024). SWAT model performance using spatially distributed saturated hydraulic conductivity (Ksat) and varying-resolution DEMs. *Water, 16*(5), Article 735. https://doi.org/10.3390/w16050735

Julien, P. (2010). *Erosion and Sediment Transport.* Cambridge University Press. doi:10.1017/CBO9780511806247

Kadim, M. K., Risjani, Y., Pasisingi, N., Hertika, A., Olii, A., Suciyono, & Hasanuddin, A. (2026). Integrating Metallothionein Expression and Heavy Metal Bioavailability for River Biomonitoring with Cheumatopsyche sp. Larvae. *Journal of Ecological Engineering, 27*(3), 399-415. doi:10.12911/22998993/214172

Keys, R. (1981). Cubic Convolution Interpolation for Digital Image Processing. *IEEE Transactions on Acoustics, Speech, and Signal Processing, 29*(6), 1153-1160. doi:10.1109/TASSP.1981.1163711

Kloiber, S. M., Anderle, T. H., Olmanson, L. G., Bauer, M. E., & Brezonik, P. L. (2002). A Procedure for Regional Assessment of Water Clarity in Lakes Using Landsat Imagery. *Remote Sensing of Environment, 82*(1), 38-47. doi:10.1016/S0034-4257(02)00022-0

Krysanova, V., & White, M. (2015). Advances in water resources assessment with SWAT—An overview. *Hydrological Sciences Journal, 60*(5), 771–783. https://doi.org/10.1080/02626667.2015.1029482

Li, L., Zheng, B., & Liu, S. (2015). Monitoring water presence in a seasonally flooded wetland in southern Spain using MODIS-derived spectral indices. *Remote Sensing*, 7(11), 15433–15456.

Liu, W., Wang, L., Zhou, J., Li, Y., Sun, F., Fu, G., Li, X., & Sang, Y.-F. (2016). A worldwide evaluation of basin-scale evapotranspiration estimates against the water balance method. *Journal of Hydrology*, *538*, 82–95. https://doi.org/10.1016/j.jhydrol.2016.04.006

Lu, C.-M., & Chiang, L.-C. (2019). Assessment of sediment transport functions with the modified SWAT-Twn model for a Taiwanese small mountainous watershed. *Water*, *11*(9), Article 1749. https://doi.org/10.3390/w11091749

MacDonald, D. D., Ingersoll, C. G., & Berger, T. A. (2000). Development and Evaluation of Consensus-Based Sediment Quality Guidelines for Freshwater Ecosystems. *Archives of Environmental Contamination and Toxicology, 39*(1), 20-31. doi:10.1007/s002440010075

Maitra, T., Kumar, S., & Dwivedi, S. B. (2022). Assessment of Water Quality and Hydro-Geochemical Characterization of Surface Water Using Multivariate Statistical Techniques. *Environmental Monitoring and Assessment, 194*(8). doi:10.1007/s10661-022-10214-x

Maurer, E. P., Wood, A. W., Adam, J. C., Lettenmaier, D. P., & Nijssen, B. (2002). A long-term hydrologically based dataset of land surface fluxes and states for the conterminous United States. *Journal of Climate*, *15*(22), 3237–3251. https://doi.org/10.1175/1520-0442(2002)015<3237:ALTHBD>2.0.CO;2

Masterson, J. P. (2004). *Simulated Interaction Between Freshwater and Saltwater and Effects of Ground-Water Pumping and Sea-Level Change, Lower Cape Cod Aquifer System, Massachusetts.* U.S. Geological Survey.

McHugh, C. M., Pekar, S. F., Christie-Blick, N., Ryan, W., Carbotte, S., & Bell, R. (2004). Spatial variations in a condensed interval between estuarine and open-marine settings: Holocene Hudson River estuary and adjacent continental shelf. *Geology, 32*(2), 169–172. doi:10.1130/G20150.1

Mendoza, K., Bawa, A., George, C., Tech, J., Moore, S., & Srinivasan, R. (2025, October 21). HAWQS and HAWQS+: Recent updates and future direction [Conference presentation]. *International SWAT Conference*, Fort Collins, CO, United States. https://swat.tamu.edu/media/ccip0jxz/f2-2.pdf

Miller, R. L., & McKee, B. A. (2004). Using MODIS Terra 250 m Imagery to Map Concentrations of Total Suspended Matter in Coastal Waters. *Remote Sensing of Environment*, *93*(1-2), 259-266. doi:10.1016/j.rse.2004.07.012

Mishra, Y., Nakamura, T., Babel, M. S., Ninsawat, S., & Ochi, S. (2018). Impact of climate change on water resources of the Bheri River Basin, Nepal. *Water*, *10*(2), Article 220. https://doi.org/10.3390/w10020220

Mondejar, M. U., & Tongco, A. F. (2019). Near Infrared Band as a Single-Band Water Index for Mapping Water Bodies Using Landsat 8 Imagery. *International Journal of Environmental Science and Development*, *10*(12), 411-415. doi:10.18178/IJESD.2019.10.12.1207

Montagna, P. A., & Douglas, A. R. (2021). *Freshwater Inflow to Texas Bays and Estuaries.* Texas A&M University–Corpus Christi.

Montagna, P. A., Coffey, D. M., Jose, R. H., & Stunz, G. W. (2021a). *Vulnerability Assessment of Coastal Bend Bays.* Harte Research Institute, Texas A&M University–Corpus Christi.

Montagna, P. A., Li, J., & Street, G. (1995). *A Conceptual Ecosystem Model of the Corpus Christi Bay National Estuary Program Study Area.* Texas Natural Resource Conservation Commission.

Montagna, P. A., Palmer, T. A., & Pollack, J. B. (2012). *Hydrological Changes and Estuarine Dynamics.* Springer Science & Business Media. doi:10.1007/978-1-4614-5833-3

Montagna, P., Palmer, T., & Pollack, J. B. (2013). *Hydrological Changes and Estuarine Dynamics.* Springer Singapore. doi:10.1007/978-94-007-5124-8

Moriasi, D. N., Arnold, J. G., Van Liew, M. W., Bingner, R. L., Harmel, R. D., & Veith, T. L. (2007). Model evaluation guidelines for systematic quantification of accuracy in watershed simulations. *Transactions of the ASABE, 50*(3), 885–900. https://doi.org/10.13031/2013.23153

Neitsch, S. L., Arnold, J. G., Kiniry, J. R., & Williams, J. R. (2011). *Soil and Water Assessment Tool theoretical documentation: Version 2009* (Texas Water Resources Institute Technical Report No. 406). Texas Water Resources Institute. https://swat.tamu.edu/media/99192/swat2009-theory.pdf

Nicolau, B. A., & Hill, E. M. (2013). *Nueces Bay Total Maximum Daily Load Project – Year-seven Implementation Effectiveness Monitoring Data Report.* Texas Commission on Environmental Quality.

Novo, E., Barbosa, C., de Freitas, R., Shimabukuro, Y., Melack, J., & Filho, W. (2006). Seasonal Dynamics of Total Suspended Solids in the Amazon River Floodplain Using Water

Quality Modeling and Log-Linear Satellite Regression. *Earth Surface Processes and Landforms, 31*(11), 1378-1389. doi:10.1002/esp.1339

Nueces River Authority. (2018). *Nueces River Basin Summary Report: An Assessment of Water Quality and Nutrient Dynamics in Nueces Bay.* Texas Clean Rivers Program.

Ockerman, D. (2013). *Hydrologic and Water-Quality Characterization of the Lower Nueces River Basin, Texas, and Development of a Tool for Estimating Constituent Fluxes into the Nueces Estuary.* U.S. Geological Survey.

Ockerman, D. J., & Heitmuller, F. T. (2010). *Simulation of Streamflow and Suspended-Sediment Concentrations and Loads in the Lower Nueces River Watershed, Downstream from Lake Corpus Christi to the Nueces Estuary, South Texas, 1958–2008.* U.S. Geological Survey.

Ockerman, D. J., Heitmuller, F. T., & Wehmeyer, L. L. (2013). *Sources of Suspended-Sediment Loads in the Lower Nueces River Watershed, Downstream from Lake Corpus Christi to the Nueces Estuary, South Texas, 1958–2010.* U.S. Geological Survey.

Olmanson, L. G., Bauer, M. E., & Brezonik, P. L. (2008). A 20-Year Satellite-Based Record of Lake Water Clarity as a Tool for Regional Ecological Assessment. *Remote Sensing of Environment, 112*(10), 3865-3874. doi:10.1016/j.rse.2008.06.001

Owens, P. N., Batalla, R. J., Collins, A. J., Gomez, B., Hicks, D. M., Horowitz, A. J., Kondolf, G. M., Marden, M., Page, M. J., Peacock, D. H., Petticrew, E. L., Salomons, W., & Trustrum, N. A. (2005). Fine-grained sediment in river systems: Environmental significance and management issues. *River Research and Applications*, *21*(7), 693–717. https://doi.org/10.1002/rra.878

Pacific Coastal and Marine Science Center. (2021, November 15). *The Role of Sediment in Coastal Resiliency*. Retrieved from U.S. Geological Survey (USGS): https://www.usgs.gov/centers/pcmsc/news/role-sediment-coastal-resiliency

Paerl, H. W., Hall, N. S., & Calandrino, E. S. (2011). Controlling harmful cyanobacterial blooms in a world experiencing anthropogenic and climatic-induced change. *Science of The Total Environment, 409*(10), 1739-1745. doi:10.1016/j.scitotenv.2011.02.001

Page, B. P., Olmanson, K. A., & Olmanson, L. G. (2019). A Google Earth Engine Architecture for Cloud Computing and Processing of Remote Sensing Data for Lake Water Quality Monitoring. *Remote Sensing, 11*(19). doi:10.3390/rs11192244

Palmer, T. A., Montagna, P. A., Pollack, J. B., Kalke, R. D., & DeYoe, H. R. (2011). The role of freshwater inflow in lagoons, rivers, and bays. *Hydrobiologia, 667*(1), 49–67. doi:10.1007/s10750-011-0637-0

Patro, E. R., De Michele, C., Granata, G., & Biagini, C. (2022). Assessment of Current Reservoir Sedimentation Rate and Storage Capacity Loss: An Italian Overview. *Journal of Environmental Management, 318*, 115826. doi:10.1016/j.jenvman.2022.115826

Paudel, B., Montagna, P. A., & Adams, L. (2019). The relationship between suspended solids and nutrients with variable hydrologic flow regimes. *Regional Studies in Marine Science, 29*, 100657. doi:10.1016/j.rsma.2019.100657

Petus, C., Chust, G., Gohin, F., Doxaran, D., Froidefond, J.-M., & Sagarminaga, Y. (2010). Estimating Turbidity and Total Suspended Matter in the Adour River Plume (South Bay of Biscay) Using MODIS 250-m Imagery. *Continental Shelf Research, 30*(5), 379-392. doi:10.1016/j.csr.2009.12.007

Pulighe, G., Bonati, G., Colangeli, M., Traverso, L., Lupia, F., Altobelli, F., Dalla Marta, A., & Napoli, M. (2019). Predicting streamflow and nutrient loadings in a semi-arid Mediterranean watershed with ephemeral streams using the SWAT model. *Agronomy, 10*(1), Article 2. https://doi.org/10.3390/agronomy10010002

Quality, T. C. (2005). *Historical Review of Water Quality with Emphasis on Heavy Metals and Organic Compounds in the Nueces River Tidal, Nueces Bay, and Corpus Christi Inner Harbor.* Texas Commission on Environmental Quality.

Rabalais, N. N., Turner, R. E., & Wiseman Jr., W. J. (2002). Gulf of Mexico hypoxia. *Annual Review of Ecology and Systematics, 33*(1), 235-263. doi:10.1146/annurev.ecolsys.33.010802.150513

Reisinger, A., Bruesewitz, D., & Wetz, M. (2017). Nutrient and Suspended Sediment Dynamics in a Shallow, Microtidal Estuary: The Role of Wind-Driven Resuspension and Episodic River Discharge. *Estuaries and Coasts, 40*(6), 1549-1564. doi:10.1007/s12237-017-0243-y

Rensselaer Polytechnic Institute. (2024, July 16). *Loss of oxygen in lakes and oceans a major threat to ecosystems, society, and planet*. Retrieved from ScienceDaily: https://www.sciencedaily.com/releases/2024/07/240715135713.htm

Richardson, S. D. (2009). Environmental Mass Spectrometry: Emerging Contaminants and Current Issues. *Analytical Chemistry, 81*(12), 4645-4677. doi:10.1021/ac9008013

Robert, W. H. (1988). Nutrient Limitation of Net Primary Production in Marine Ecosystems. *Annual Review of Ecology and Systematics, 19*, 89-110. doi:10.1146/annurev.es.19.110188.000521

Rony, S.M.S.M., J. Ren, E. Buskey, T. Sinha, and T. Lynn, Modeling Freshwater Inflows, Nutrient Dynamics and their Relationships to Algal Bloom in Nueces Bay, Texas General Land Office, Coastal Management Program, Contract No. 19-045-000-B079, Final Report, Nov. 30, 2020. Available at https://www.glo.texas.gov/coastal-grants/_documents/grant-project/19-045-final-rpt.pdf

Rosati, J. D. (2005). *Coastal Inlet Navigation Channel Shoaling with Deepening and Widening.* U.S. Army Corps of Engineers.

Rouholahnejad, E., Abbaspour, K. C., Srinivasan, R., Bacu, V., & Lehmann, A. (2014). Water resources of the Black Sea Basin at high spatial and temporal resolution. *Water Resources Research, 50*(7), 5866–5885. https://doi.org/10.1002/2013WR014132

Sahoo, D. P., Sahoo, B., & Tiwari, M. K. (2022). MODIS-Landsat Fusion-Based Single-Band Algorithms for TSS and Turbidity Estimation in an Urban-Waste-Dominated River Reach. *Water Research, 224*, 119082. doi:10.1016/j.watres.2022.119082

Santhi, C., Srinivasan, R., Arnold, J. G., & Williams, J. R. (2006). A modeling approach to evaluate the impacts of water quality management plans implemented in a watershed in Texas. *Environmental Modelling & Software, 21*(8), 1141–1157.

Schoenbaechler, C., Guthrie, C. G., Matsumoto, J., Lu, Q., & Negusse, S. (2011). *TxBLEND model calibration and validation for the Nueces estuary.* Texas Water Development Board.

Searle, P. (1984). The Automated Determination of Ammonium in Soil, Plant and Water Extracts by Nessler's Reagent and by Indo-Phenol Blue Methods. *New Zealand Journal of Science, 27*, 101-107.

Seligman, N. G., & van Keulen, H. (1981). PAPRAN: A simulation model of annual pasture production limited by rainfall and nitrogen. In M. J. Frissel & J. A. van Veen (Eds.), *Simulation of nitrogen behaviour of soil-plant systems* (pp. 192–220). Pudoc.

Senent-Aparicio, J., Jimeno-Sáez, P., López-Ballesteros, A., Giménez, J. G., Pérez-Sánchez, J., Cecilia, J. M., & Srinivasan, R. (2021). Impacts of SWAT weather generator statistics from high-resolution datasets on monthly streamflow simulation over Peninsular Spain. *Journal of Hydrology: Regional Studies, 35*, Article 100826. https://doi.org/10.1016/j.ejrh.2021.100826

Shelton, L. R., & Capel, P. D. (1994). *Guidelines for Collecting and Processing Samples of Stream Bed Sediment for Analysis of Trace Elements and Organic Contaminants.* U.S. Geological Survey.

Silva, A., Amaro, V. E., Stattegger, K., Schwarzer, K., Vital, H., & Heise, B. (2015). Spectral Calibration of CBERS 2B Multispectral Satellite Images to Assess Suspended Sediment Concentration. *ISPRS Journal of Photogrammetry and Remote Sensing*, *103*, 48-58. doi:10.1016/j.isprsjprs.2015.02.011

Smith, V. H., Tilman, G. D., & Nekola, J. C. (1999). Eutrophication: Impacts of excess nutrient inputs on freshwater, marine, and terrestrial ecosystems. *Environmental Pollution, 100*(1–3), 179–196. https://doi.org/10.1016/S0269-7491(99)00091-3

Stow, D., Hope, A., McGuire, D., & Phinn, S. (2004). Remote Sensing of Vegetation and Water Quality Parameters in Dynamic Coastal Zones: Predictor Optimization and Modeling Frameworks. *Remote Sensing of Environment, 89*(2), 154-168. doi:10.1016/j.rse.2003.10.008

Stramma, L., Johnson, G. C., Sprintall, J., & Mohrholz, V. (2008). Expanding Oxygen-Minimum Zones in the Tropical Oceans. *Science, 320*(5876), 655-658. doi:10.1126/science.1153847

Sun, W., Yao, X., Cao, N., Xu, Z., & Yu, J. (2016). Integration of soil hydraulic characteristics derived from pedotransfer functions into hydrological models: Evaluation of its effects on simulation uncertainty. *Hydrology Research, 47*(5), 964–978. https://doi.org/10.2166/nh.2016.150

Syvitski, J. P., Vörösmarty, C., Kettner, A., & Green, P. (2005). Impact of Humans on the Flux of Terrestrial Sediment to the Global Coastal Ocean. *Science, 308*(5720), 376-380. doi:10.1126/science.1109454

Tarkegn, T. G., Van Oel, P. R., Chukalla, A. D., Ray, R. L., Tefera, G. W., Haileslassie, A., Taye, M. T., Worqlul, A. W., Adgo, E., Bantider, A., & Dile, Y. T. (2025). Modeling integrated impacts of agro-hydrological interventions on blue and green water and crop yield in SWAT+. *Journal of Hydrology: Regional Studies, 62,* Article 102783. https://doi.org/10.1016/j.ejrh.2025.102783

Texas Commission on Environmental Quality. (2005). *Assessment of Toxic Chemical Contaminants in Fish and Crab Tissues from Nueces Bay and Corpus Christi Bay.* Texas Commission on Environmental Quality.

Texas Commission on Environmental Quality. (2026). *Surface water quality data and reports*. Retrieved July 9, 2026, from https://www.tceq.texas.gov/agency/data/lookup-data/swq-data.html

TxDOT. (2021). *Ship Channel Improvement Report: 2020–2021 Texas Port Mission Plan.* Texas Department of Transportation.

Texas Water Development Board. (2013). *Volumetric and sedimentation survey of Choke Canyon Reservoir: June 2012 survey*. https://www.twdb.texas.gov/hydro_survey/chokecanyon/2012-06/ChokeCanyon2012_FinalReport.pdf

Texas Water Development Board. (2017). *Volumetric survey of Lake Corpus Christi: February 2016 survey*. https://www.twdb.texas.gov/hydro_survey/corpuschristi/2016-02/Corpus2016_FinalReport.pdf

Texas Water Development Board. (2017). *Freshwater Inflow Recommendation for the Nueces River Estuary: A Study of Nutrient Pulses and Salinity Gradients.* Texas Water Development Board.

Thomas, E. D., Venkataraman, K., Chraibi, V., & Kannan, N. (2019). Hydrologic trends in the upper Nueces River Basin of Texas: Implications for water resource management and ecological health. *Hydrology, 6*(1), Article 20. https://doi.org/10.3390/hydrology6010020

Tuppad, P., Kannan, N., Srinivasan, R., Rossi, C. G., & Arnold, J. G. (2010). Simulation of agricultural management alternatives for watershed protection. *Water Resources Management, 24*(12), 3115–3144. https://doi.org/10.1007/s11269-010-9598-8

Turk, J. T. (2001). *Field Guide for Surface-Water Sample and Data Collection.* U.S. Geological Survey.

Uniyal, B., Jha, M. K., Verma, A. K., & Anebagilu, P. K. (2020). Identification of critical areas and evaluation of best management practices using SWAT for sustainable watershed management. *Science of the Total Environment, 744*, Article 140737. https://doi.org/10.1016/j.scitotenv.2020.140737

USACE. (1984). *Shore Protection Manual.* Coastal Engineering Research Center, Waterways Experiment Station.

USACE. (2022). *Waterborne tonnage for principal U.S. ports and all 50 states.* U.S. Army Corps of Engineers.

U.S. States Environmental Protection Agency. (1993a). *Method 300.0: Determination of Inorganic Anions by Ion Chromatography.* U.S. Environmental Protection Agency.

U.S. States Environmental Protection Agency. (1993b). *Method 365.1: Determination of Phosphorus by Semi-Automated Colorimetry.* U.S. Environmental Protection Agency.

U.S. States Environmental Protection Agency. (1994). *Method 200.8: Determination of Trace Elements in Waters and Wastes by Inductively Coupled Plasma–Mass Spectrometry.* U.S. Environmental Protection Agency, Office of Research and Development, Environmental Monitoring Systems Laboratory.

U.S. States Environmental Protection Agency. (1996). *Method 3052: Microwave Assisted Acid Digestion of Siliceous and Organically Based Matrices.* United States Environmental Protection Agency.

U.S. Environmental Protection Agency. (2026). *Basic information on nutrient pollution*. https://www.epa.gov/nutrientpollution/basic-information-nutrient-pollution

U.S. Environmental Protection Agency, & U.S. Geological Survey. (n.d.). *Water Quality Portal*. Retrieved July 9, 2026, from https://www.waterqualitydata.us/

U.S. Geological Survey. (2014). *Water Quality in the West Oso Creek Watershed, Nueces County, Texas.* U.S. Geological Survey.

U.S. Geological Survey. (n.d.-a). *USGS 08206900 Choke Canyon Reservoir near Three Rivers, Texas*. Water Data for the Nation. Retrieved July 9, 2026, from https://waterdata.usgs.gov/nwis/uv?site_no=08206900

U.S. Geological Survey. (n.d.-b). *USGS 08206910 Choke Canyon Reservoir outlet works channel near Three Rivers, Texas*. Water Data for the Nation. Retrieved July 9, 2026, from https://waterdata.usgs.gov/nwis/uv?site_no=08206910

U.S. Geological Survey. (n.d.-c). *USGS 08210500 Lake Corpus Christi near Mathis, Texas*. Water Data for the Nation. Retrieved July 9, 2026, from https://waterdata.usgs.gov/nwis/uv?site_no=08210500

U.S. Geological Survey. (n.d.-d). *Water Data for the Nation: National Water Information System*. Retrieved July 9, 2026, from https://waterdata.usgs.gov/

Vaughan, M., Wetz, M., & Hayes, K. (2021). Wind-Driven Sediment Resuspension Dictates Total Suspended Solids (TSS) Variability in Shallow, Microtidal Bays: Case Study of Nueces and Corpus Christi Bays. *Estuaries and Coasts, 44*(5), 1211-1224. doi:10.1007/s12237-020-00874-y

Vermote, E., El Saleous, N., & Justice, C. O. (2002). Atmospheric Correction of MODIS Data in the Visible to Middle Infrared: First Results. *Remote Sensing of Environment, 83*(1-2), 97-111. doi:10.1016/S0034-4257(02)00095-5

Vincenty, T. (1975). Direct and Inverse Solutions of Geodesics on an Ellipsoid with Application of Nested Equations. *Survey Review*, *23*(176), 88-93. doi:10.1179/sre.1975.23.176.88

Wakwella, A., Wenger, A., Jenkins, A., Lamb, J., Kuempel, C., Claar, D., . . . Jupiter, S. D. (2023). Integrated watershed management solutions for healthy coastal ecosystems and people. *Cambridge Prisms: Coastal Futures, 1*, e27. doi:10.1017/cft.2023.15

Walling, D. E. (2006). Human impact on land–ocean sediment transfer by the world's rivers. *Geomorphology, 79*(3–4), 192–216. https://doi.org/10.1016/j.geomorph.2006.06.019

Wang, C., Gao, G. L., Huang, J. X., Zhang, K. S., Zhong, H., Wang, H. W., . . . Wang, Q. G. (2017). Nutritive Value of Dry Citrus Pulp and Its Effect on Performance in Geese from 35 to 70 Days of Age. *Journal of Applied Poultry Research, 26*(2), 253-259. doi:10.3382/japr/pfw069

Wang, P., Wang, J., & Zhang, Q. (2013). Evaluation of Phosphorus Fractionation in Sediments of Lakes Using the Ascorbic Acid Method. *Environmental Monitoring and Assessment, 185*(6), 4531-4542. doi:10.1007/s10661-012-2886-3

Ward, N. (2024). Seasonal Hydrodynamics and Hydraulic Resets in Shallow Microtidal Estuaries. *Estuarine, Coastal and Shelf Science, 296*. doi:10.1016/j.ecss.2024.108580

Waycott, M., Duarte, C. M., Carruthers, T. J., Orth, R. J., Dennison, W. C., Olyarnik, S., . . . Williams, S. L. (2009). Accelerating loss of seagrasses across the globe threatens coastal ecosystems. *Proceedings of the National Academy of Sciences, 106*(30), 12377-12381. doi:10.1073/pnas.0905620106

Wetz, M. S. (2025). *Nueces River tidal nutrient bioassays: Annual report* (Project No. 2429). Coastal Bend Bays & Estuaries Program. https://www.cbbep.org/manager/wp-content/uploads/Report_Final_Nueces-Bioassay_2429.pdf

Wilde, F. D., Radtke, D. B., Gibs, J., & Iwatsubo, R. T. (2004). *Cleaning of Equipment for Water Sampling.* U.S. Geological Survey.

Williams, J. R. (1975). Sediment-yield prediction with universal equation using runoff energy factor. In *Present and prospective technology for predicting sediment yield and sources*

(ARS-S-40, pp. 244–252). U.S. Department of Agriculture, Agricultural Research Service.

Willmott, C. J., Robeson, S. M., & Matsuura, K. (2012). A Refined Scale-Independent Measure of Model Performance. *International Journal of Climatology*, *32*(13), 2088-2094. doi:10.1002/joc.2419

Willmott, C., & Matsuura, K. (2005). Advantages of the Mean Absolute Error Over the Root Mean Square Error in Assessing Alternative Model Performance. *Climate Research*, *30*(1), 79-82. doi:10.3354/cr030079

Winchell, M., Srinivasan, R., Di Luzio, M., & Arnold, J. G. (2013). *ArcSWAT interface for SWAT2012: User's guide*. Blackland Research and Extension Center, Texas AgriLife Research.

Wilson, K., Carter, S., & Foti, R. (2018). Multi-Temporal Satellite Remote Sensing of Coastal Turbidity: Incorporating Cyclical Harmonic Components to Map Sediment Plumes. *Remote Sensing of Environment*, *216*, 385-398. doi:10.1016/j.rse.2018.07.012

Wu, G., Liu, L., Chen, F., & Fei, T. (2014). Developing MODIS-Based Retrieval Models of Suspended Particulate Matter Concentration in Dongting Lake, China. *International Journal of Applied Earth Observation and Geoinformation*, *32*, 46-53. doi:10.1016/j.jag.2014.03.025

Yazdani, M., Monavari, S. M., Omrani, G. A., Shariat, M., & Hosseini, S. M. (2015). Landfill site suitability assessment by means of geographic information system analysis. *Solid Earth*, *6*(3), 945–956. https://doi.org/10.5194/se-6-945-2015

Yeager, K. M., Santschi, P. H., Schindler, K. J., Andres, M. J., & Weaver, E. A. (2006). The Relative Importance of Terrestrial versus Marine Sediment Sources to the Nueces–

Corpus Christi Estuary, Texas: An Isotopic Approach. *Estuaries and Coasts, 29*(3), 443-454. doi:10.1007/BF02784992

YSI . (2021). *YSI ProDSS User Manual.* YSI Incorporated.

Yuan, Y., & Koropeckyj-Cox, L. (2022). SWAT model application for evaluating agricultural conservation practice effectiveness in reducing phosphorus loss from the Western Lake Erie Basin. *Journal of Environmental Management, 302*, Article 114000. https://doi.org/10.1016/j.jenvman.2021.114000

Yuliati, Y., Sumiarsih, E., Purwanto, E., Adriman, A., Mulyani, I., Nurfathihayati, N., & Nasution, K. R. (2024). Assessment of Pollution Load on Surface Water in the Down-Lower Part of the Tapung Kiri River, Kampar Regency, Riau. *BIO Web of Conferences.* EDP Sciences. doi:10.1051/bioconf/202413605002

Zeiger, S., & Hubbart, J. (2017). An assessment of mean areal precipitation methods on simulated streamflow: A SWAT model performance assessment. *Water, 9*(7), Article 459. https://doi.org/10.3390/w9070459

Zhu, Z., & Woodcock, C. E. (2012). Object-Based Cloud and Cloud Shadow Detection in Landsat Imagery. *Remote Sensing of Environment, 118*, 83-94. doi:10.1016/j.rse.2011.10.028

Appendix A: Base/Default SWAT Input Parameter Tables

The following tables summarize the base parameter values contained in the Nueces River Watershed SWAT input files before model calibration. They document the original model configuration used as the reference condition for evaluating calibration changes and management scenario responses. Values are reported as a single default value when uniform or as a minimum-to-maximum range when they vary among model units.

Appendix A1: Hydrologic Parameters

The hydrologic parameters listed below represent the base or default values contained in the Nueces River Watershed SWAT input files before calibration and before any best management practice scenario was applied. These parameters establish the initial representation of surface runoff, interception, evapotranspiration, soil-water storage, groundwater exchange, snow processes, channel routing, tile drainage, and channel geometry. A single value indicates that the same starting value was used throughout the applicable model units, whereas a range indicates that the parameter varied among HRUs, soil layers, reaches, or subbasins. The table therefore documents the original hydrologic configuration against which calibrated parameter changes and scenario adjustments were evaluated.

Table A1. Base/default hydrologic input parameters used in the Nueces River Watershed SWAT model.

Parameter	Process Group	Description	Base Value/Range
SLSUBBSN.hru	Surface Runoff	Average slope length [m]	91.463–121.951
HRU_SLP.hru	Surface Runoff	Average slope steepness [m/m]	0–0.048
OV_N.hru	Surface Runoff	Manning's n value for overland flow	0.01–0.3
SURLAG_HRU.hru	Surface Runoff	Surface runoff lag time at HRU level [days]	2
CANMX.hru	Interception	Maximum canopy storage [mm]	0.675–14.715
ESCO_HRU.hru	Evapotranspiration	Soil evaporation compensation factor (HRU-level override)	0.6623–0.9668
EPCO_HRU.hru	Evapotranspiration	Plant water uptake compensation factor (HRU-level override)	1
LAT_TTIME.hru	Lateral Flow	Lateral flow travel time [days]	0
SLSOIL.hru	Lateral Flow	Slope length for lateral subsurface flow [m]	0
DEP_IMP.hru	Lateral Flow	Depth to impervious layer in soil profile [mm]	6,000
CN2.mgt	Surface Runoff	Initial SCS curve number for moisture condition II	35–93.582
SOL_Z.sol	Soil	Depth from soil surface to bottom of layer [mm]	25.4–2,438.4
SOL_BD.sol	Soil	Moist bulk density [g/cm³]	0–2.5
SOL_AWC.sol	Soil	Available water capacity, including rock fragments [mm/mm]	0–0.31
SOL_K.sol	Soil	Saturated hydraulic conductivity [mm/h]	0.08–650
SOL_CBN.sol	Soil	Organic carbon content [weight %]	0–2.91
CLAY.sol	Soil	Clay content [weight %]	0–70
SILT.sol	Soil	Silt content [weight %]	0–63.09
SAND.sol	Soil	Sand content [weight %]	0–94.39
SOL_ALB.sol	Soil	Moist soil albedo	0.01–0.23
SHALLST.gw	Groundwater	Initial depth of water in shallow aquifer [mm]	1,000
DEEPST.gw	Groundwater	Initial depth of water in deep aquifer [mm]	2,000
GW_DELAY.gw	Groundwater	Groundwater delay: vadose zone to shallow aquifer [days]	11.149–179.255
ALPHA_BF.gw	Groundwater	Baseflow alpha factor (recession constant) [days]	0.0468–0.8322
GWQMN.gw	Groundwater	Threshold depth in shallow aquifer for return flow [mm]	585.75–5,000
GW_REVAP.gw	Groundwater	Groundwater revap coefficient	0.02–0.2

Parameter	Process Group	Description	Base Value/Range
REVAPMN.gw	Groundwater	Threshold depth for revap [mm]	750
RCHRG_DP.gw	Groundwater	Deep aquifer percolation fraction	0–0.64
GWHT.gw	Groundwater	Initial groundwater height [m]	1
GW_SPYLD.gw	Groundwater	Specific yield of shallow aquifer [m^3/m^3]	0.003
ALPHA_BF_D.gw	Groundwater	Baseflow alpha factor for deep aquifer [days]	0.01
SFTMP.bsn	Snow	Snowfall temperature [°C]	1
SMTMP.bsn	Snow	Snowmelt base temperature [°C]	0.5
SMFMX.bsn	Snow	Melt factor for snow on June 21 [mm H_2O/°C-day]	4.5
SMFMN.bsn	Snow	Melt factor for snow on December 21 [mm H_2O/°C-day]	4.5
TIMP.bsn	Snow	Snowpack temperature lag factor	1
SNOCOVMX.bsn	Snow	Minimum snow-water content for 100% snow cover [mm]	1
SNO50COV.bsn	Snow	Fraction of SNOCOVMX corresponding to 50% snow cover	0.5
ESCO.bsn	Evapotranspiration	Soil evaporation compensation factor	0.95
EPCO.bsn	Evapotranspiration	Plant water uptake compensation factor	1
EVLAI.bsn	Evapotranspiration	Leaf area index at which no evaporation occurs from water surface	3
FFCB.bsn	Water Balance	Initial soil-water storage as fraction of field capacity	0
SURLAG.bsn	Surface Runoff	Surface runoff lag time [days]	2
ICN.bsn	Surface Runoff	Daily curve-number method (0 = soil storage; 1 = soil moisture)	1
CNCOEF.bsn	Surface Runoff	Plant ET curve-number coefficient	2
SMXCO.bsn	Surface Runoff	Adjustment factor for maximum curve-number S factor	1
CN_FROZ.bsn	Surface Runoff	Frozen-soil adjustment parameter for infiltration/runoff	0.000862
IRTE.bsn	Channel Routing	Water routing method (0 = variable travel time; 1 = Muskingum)	0
MSK_CO1.bsn	Channel Routing	Muskingum calibration coefficient for normal flow	0.75
MSK_CO2.bsn	Channel Routing	Muskingum calibration coefficient for low flow	0.25
MSK_X.bsn	Channel Routing	Muskingum weighting factor (inflow versus outflow)	0.2
TRNSRCH.bsn	Channel Routing	Fraction of transmission losses partitioned to deep aquifer	0.15
EVRCH.bsn	Channel Routing	Reach evaporation adjustment factor	1

Parameter	Process Group	Description	Base Value/Range
IUH.bsn	Channel Routing	Unit hydrograph method (1 = triangular; 2 = gamma function)	1
UHALPHA.bsn	Channel Routing	Alpha coefficient for gamma-function unit hydrograph	5
BFLO_DIST.bsn	Channel Routing	Baseflow distribution flag (0 = uniform; 1 = rainfall pattern)	0.75
RE_BSN.bsn	Tile Drainage	Effective radius of drains [mm]	50
SDRAIN_BSN.bsn	Tile Drainage	Distance between drain/tile tubes [mm]	15,000
DRAIN_CO_BSN.bsn	Tile Drainage	Drainage coefficient	10
DEPIMP_BSN.bsn	Tile Drainage	Depth to impervious layer for perched water tables [mm]	0
DDRAIN_BSN.bsn	Tile Drainage	Depth to subsurface drain [mm]	0
TDRAIN_BSN.bsn	Tile Drainage	Time to drain soil to field capacity [h]	0
GDRAIN_BSN.bsn	Tile Drainage	Drain-tile lag time [h]	0
ITDRN.bsn	Tile Drainage	Tile-drainage equations flag	0
IWTDN.bsn	Tile Drainage	Water-table depth algorithms flag	0
CHW2.rte	Channel Geometry	Main-channel width [m]	20.541–780.967
CHD.rte	Channel Geometry	Main-channel depth [m]	0.823–9.303
CH_S2.rte	Channel Geometry	Main-channel slope [m/m]	0.00001–0.008
CH_L2.rte	Channel Geometry	Main-channel length [km]	1.627–48.573
CH_WDR.rte	Channel Geometry	Main-channel width-to-depth ratio [m/m]	24.964–83.945
ALPHA_BNK.rte	Channel Routing	Baseflow alpha factor for bank storage [days]	0
CH_L1.sub	Tributary Channel	Longest tributary-channel length [km]	1.627–48.573
CH_S1.sub	Tributary Channel	Average slope of tributary channel [m/m]	0–0.008
CH_W1.sub	Tributary Channel	Average width of tributary channel [m]	2.227–95.744
CH_K1.sub	Tributary Channel	Effective hydraulic conductivity in tributary channel [mm/h]	0
CH_K2.rte	Tributary Channel	Effective hydraulic conductivity in main-channel alluvium [mm/h]	1.227–153.77
CH_N1.sub	Tributary Channel	Manning's n value for tributary channels	0.014

Appendix A2: Sediment Parameters

The sediment parameters listed below represent the base or default values used in the SWAT model before sediment calibration modification. They define the initial representation of upland soil erosion, support practices, coarse-fragment effects, channel erodibility and cover, sediment re-entrainment, deposition, and sediment routing through the stream network. Parameters with one value were assigned uniformly in the applicable model file, while parameters shown as a range varied spatially among HRUs, soil layers, or channel reaches. These values provide the reference condition from which the calibrated sediment parameters and sediment-control scenarios were developed.

Table A2. Base/default sediment input parameters used in the Nueces River Watershed SWAT model.

Parameter	**Process Group**	**Description**	**Base Value/Range**
SPCON.bsn	Channel Routing	Linear parameter for maximum sediment re-entrained during channel routing	0.0001
SPEXP.bsn	Channel Routing	Exponent used to calculate sediment re-entrainment during channel routing	1
PRF_BSN.bsn	Channel Routing	Peak-rate adjustment factor for sediment routing in the main channel	1
ADJ_PKR.bsn	Subbasin Routing	Peak-rate adjustment factor for sediment routing in tributary channels	1
CH_COV1.rte	Channel Erosion	Channel erodibility factor (stored as CH_COV1 in *.rte)	0
CH_COV2.rte	Channel Erosion	Channel cover factor (stored as CH_COV2 in *.rte)	0
CH_N2.rte	Channel Routing	Manning's n value for the main channel	0.014
CH_K2.rte	Channel Routing	Effective hydraulic conductivity in main channel [mm/h]	0–205.65
USLE_K.sol	Surface Erosion	USLE soil erodibility factor	0.01–0.49
USLE_P.mgt	Surface Erosion	USLE support-practice factor	1
ROCK.sol (CFRG)	Surface Erosion	Rock fragments [vol %]; SWAT computes CFRG = exp(-0.053 × rock %)	0–98
ISED_DET.bsn	Routing	Detached-sediment lag coefficient	0
EROS_SPL.bsn	Sub-daily Erosion	Splash-erosion coefficient	1
RILL_MULT.bsn	Sub-daily Erosion	Rill-erosion multiplier applied to USLE_K	0.7
EROS_EXPO.bsn	Sub-daily Erosion	Exponent in the overland-flow erosion equation	1.2
SUBD_CHSED.bsn	Sub-daily Erosion	Channel-sediment routing flag (0 = off; 1 = Brownlie; 2 = Yang)	0
C_FACTOR.bsn	Sub-daily Erosion	Scaling parameter for the cover-management factor	0.03
CH_D50.bsn	Channel Erosion	Median particle diameter of channel-bed sediment [mm]	50
SIG_G.bsn	Channel Erosion	Geometric standard deviation of particle-size distribution	1.57

Appendix A3: Nitrogen Parameters

The nitrogen parameters listed below represent the base or default values used to initialize nitrogen cycling and transport before calibration. They describe nitrogen inputs from rainfall, humus mineralization, denitrification, plant uptake, nitrate percolation, residue decomposition, soil nitrogen pools, and groundwater nitrogen behavior. A single value represents a uniform starting setting, while a range indicates variability among the applicable soil, groundwater, HRU, or basin records. These values are the original model inputs and should not be interpreted as the final fitted values obtained during nitrogen calibration.

Table A3. Base/default nitrogen input parameters used in the Nueces River Watershed SWAT model.

Parameter	Process Group	Description	Base Value/Range
RCN.bsn	Nitrogen Cycle	Concentration of nitrogen in rainfall [mg N/L]	0
CMN.bsn	Nitrogen Cycle	Rate factor for humus mineralization of active organic nitrogen	0.0003
CDN.bsn	Nitrogen Cycle	Denitrification exponential rate coefficient	1.4
SDNCO.bsn	Nitrogen Cycle	Denitrification threshold water content	1.1
N_UPDIS.bsn	Nutrient Uptake	Nitrogen uptake distribution parameter	20
NPERCO.bsn	Nitrogen Transport	Nitrate percolation coefficient	0.2
RSDCO.bsn	Nitrogen/Phosphorus Cycle	Residue decomposition coefficient	0.05
ANION_EXCL_BSN.bsn	Nitrogen Transport	Fraction of soil porosity from which anions are excluded	0.2
HLIFE_NGW_BSN.bsn	Nitrogen Cycle	Half-life of nitrogen in groundwater [days]	5
RCN_SUB_BSN.bsn	Nitrogen Cycle	Concentration of nitrate in precipitation [ppm]	1
SOL_NO3.chm	Nitrogen Cycle	Initial nitrate concentration in soil layer [mg/kg]	0
SOL_ORGN.chm	Nitrogen Cycle	Initial organic nitrogen concentration in soil layer [mg/kg]	0
SHALLST_N.gw	Nitrogen Cycle	Initial nitrate concentration in shallow aquifer [mg N/L]	0
HLIFE_NGW.gw	Nitrogen Cycle	Half-life of nitrate in shallow aquifer [days]	0

Appendix A4: Phosphorus Parameters

The phosphorus parameters listed below represent the base or default values used to initialize phosphorus cycling and transport before calibration adjustments. They control phosphorus uptake, sorption, percolation, residue decomposition, initial soil phosphorus pools, groundwater phosphorus concentrations, and reservoir-related settling processes. Uniform parameters are reported as single values, whereas spatially variable inputs are reported as ranges. The table documents the original phosphorus configuration of the model and provides the reference condition for interpreting subsequent calibration changes and simulated phosphorus responses under management scenarios.

Table 4.D. Base/default phosphorus input parameters used in the Nueces River Watershed SWAT model.

Parameter	Process Group	Description	Base Value/Range
P_UPDIS.bsn	Nutrient Uptake	Phosphorus uptake distribution parameter	20
PPERCO.bsn	Phosphorus Transport	Phosphorus percolation coefficient	10
PHOSKD.bsn	Phosphorus Transport	Phosphorus soil partitioning coefficient	175
PSP.bsn	Phosphorus Cycle	Phosphorus sorption parameter	0.4
RSDCO.bsn	Nitrogen/Phosphorus Cycle	Residue decomposition coefficient	0.05
RES_STLR_CO.bsn	Reservoir	Reservoir sediment-settling coefficient	0.184
SOL_P_MODEL.bsn	Phosphorus Cycle	Soil phosphorus model flag (0 = default SWAT; 1 = modified EPIC)	0
SOL_SOLP.chm	Phosphorus Cycle	Initial soluble (labile) phosphorus concentration in soil layer [mg/kg]	5
SOL_ORGP.chm	Phosphorus Cycle	Initial organic phosphorus concentration in soil layer [mg/kg]	0
GWSOLP.gw	Phosphorus Cycle	Soluble phosphorus concentration in groundwater contribution [mg P/L]	0